Numerical Modeling of Electromagnetic Problems with the Hybrid Finite Element - Boundary Integral - Multilevel Fast Multipole - Uniform Geometrical Theory of Diffraction Method

Vom Fachbereich Elektrotechnik und Informationstechnik
der Technischen Universität Darmstadt

zur Erlangung
der Würde eines Doktor-Ingenieurs (Dr.-Ing.)
genehmigte

Dissertation

von

Andreas Tzoulis, M.Sc.
geboren am 19. Juli 1976 in München

Darmstadt 2009

Referent:	Prof. Dr.-Ing. Thomas Weiland
Korreferent:	Prof. Dr.-Ing. Thomas Eibert
Tag der Einreichung:	14. Oktober 2008
Tag der mündlichen Prüfung:	20. April 2009

D 17
Darmstädter Dissertation

Στους γονείς μου

To my parents

Abstract

In the present thesis, a hybrid numerical method is presented for the solution of very large and complex radiation and scattering electromagnetic problems, which combines the Finite Element Boundary Integral (FEBI) technique and the Multilevel Fast Multipole Method (MLFMM) with the Uniform Geometrical Theory of Diffraction (UTD). The presented hybrid approach is referred to as FEBI-MLFMM-UTD method and it combines for the first time a local method, a global fast Integral Equation (IE) method, and ray optical asymptotic techniques. The hybridization with UTD is performed in both the Boundary Integral Method (BIM) part, where the Green's function and the incident field are appropriately modified for Combined Field Integral Equation (CFIE), as well as within the matrix-vector multiplications in the various levels of the MLFMM part by approximating ray optical terms of the Green's function with far-field expressions suitable for MLFMM interactions. This results in modification of the translation procedure using a far-field approximation of the translation operator for ray optical contributions. In each case, the Green's function and the incident field are modified according to superposition of all received field contributions. Dielectric regions of FEBI objects are handled efficiently through conventional combination of BIM with the Finite Element Method (FEM), which does not affect the hybridization with UTD. Further, postprocessing near-field computations in the proposed hybrid method are accelerated using MLFMM combining near-field and far-field MLFMM translations for optimum performance. Near-field translations are performed from source groups including currents to receiving groups including nearby observation points, whereas far-field translations are performed for each far-away observation point at the coarsest level on which far-field condition is still satisfied. The optimum level for far-field translations is found for each observation point in the initialization step in a worst-case sense using its shortest distance to the MLFMM domain of the currents. In both domains ray optical contributions due to the presence of UTD objects are taken into account according to hybridization of MLFMM with UTD. In addition, far-field scattering computations are performed by applying Near-Field to Far-Field Transformations (NFFFTs) in the postprocessing stage based on planar near-field scanning techniques. Particularly, the scattered ray optical electric field is first computed in a scanning plane in the near-field region of the involved objects using the postprocessing MLFMM and it is then transformed into far-field regions using plane wave expansions. Direct field contributions are evaluated directly in the far-field of the involved objects using conventional fast techniques and the total far-fields are found by superposition. In the UTD part, double diffracted ray optical fields at arbitrarily oriented straight metallic edges are included using scalar diffraction coefficients of standard UTD. Using the hybrid FEBI-MLFMM-UTD method large scale problems including arbitrarily shaped and electrically large objects can be handled very efficiently saving a large amount in computation and memory requirements, which is demonstrated very clearly with numerical examples.

Zusammenfassung

In der vorliegenden Dissertation wird eine hybride numerische Modellierungsmethode zur Lösung sehr großer und komplexer Antennen- und Streufeldprobleme vorgestellt, die das Finite Element Boundary Integral (FEBI) Verfahren und die Multilevel Fast Multipole Methode (MLFMM) mit der Uniform Geometrical Theory of Diffraction (UTD) verknüpft. Das vorgestellte Verfahren wird als hybride FEBI-MLFMM-UTD-Methode bezeichnet und verknüpft zum ersten Mal eine lokale Methode, ein schnelles globales Integralgleichungsverfahren und strahlenoptische Ansätze. Die Hybridisierung mit der UTD wird sowohl in der Boundary Integral Methode (BIM), wo die Greensche Funktion und das einfallende Feld für die kombinierte Feldintegralgleichung (CFIE) modifiziert werden, als auch innerhalb der Matrix-Vektor-Multiplikationen auf den verschiedenen Leveln der MLFMM durch Näherung strahlenoptischer Terme der Greenschen Funktion mit für MLFMM-Verkopplungen geeigneten Fernfeldausdrücken, durchgeführt. Dies führt zur Modifizierung der Translation mit geeigneten Fernfeldausdrücken des Translationsoperators für strahlenoptische Feldbeiträge. In beiden Fällen wird die Greensche Funktion und das einfallende Feld durch Überlagerung aller empfangenen Feldbeiträge modifiziert. Dielektrische Bereiche werden effizient durch konventionelle Verknüpfung der BIM mit der Finiten Elemente Methode (FEM) ohne Einfluss auf die Hybridisierung mit der UTD behandelt. Außerdem, werden beim Postprocessing Nahfeldberechnungen mit der MLFMM beschleunigt, wobei Nahfeld- und Fernfeldtranslationen für optimale Leistung kombiniert werden. Nahfeldtranslationen werden von Quellgruppen mit Strömen zu Empfangsgruppen mit naheliegenden Beobachtungspunkten durchgeführt, wobei Fernfeldtranslationen für jeden entfernten Beobachtungspunkt auf dem gröbstem Level durchgeführt werden, auf dem die Fernfeldbedingung noch erfüllt wird. Das optimale Level für Fernfeldtranslationen wird für jeden Beobachtungspunkt im Initialisierungsprozess bestimmt, wobei nur der worst-case des kürzesten Abstandes des Beobachtungspunktes zum MLFMM-Bereich der Ströme untersucht wird. Für beide Bereiche werden strahlenoptische Beiträge aufgrund von UTD-Objekten entsprechend der Hybridisierung der MLFMM mit der UTD berücksichtigt. Zudem, wird beim Postprocessing die Berechnung gestreuter Fernfelder mit Hilfe von Nahfeld-Fernfeld-Transformationen (NFFFTs) auf der Grundlage planarer Scanning-Verfahren durchgeführt. Dabei werden strahlenoptische Beiträge des gestreuten Feldes zuerst auf einer planaren Scan-Ebene im Nahfeld abgetastet und danach auf der Grundlage einer Zerlegung in ebene Wellen ins Fernfeld transformiert. Direkte Beiträge werden mit konventionellen schnellen Methoden direkt im Fernfeld der Objekte berechnet. Das gesamte Feld ist die Überlagerung dieser Beiträge. Im UTD-Teil werden zweifach gebeugte strahlenoptische Felder an beliebig orientierten geraden metallischen Kanten mit Hilfe der skalaren Beugungskoeffizienten der UTD berücksichtigt. Mit der hybriden FEBI-MLFMM-UTD-Methode werden Probleme mit beliebig geformten und elektrisch sehr großen Objekten sehr effizient behandelt unter Einsparung beträchtlicher Rechenzeit und Speicheraufwand. Dies wird deutlich mit numerischen Beispielen demonstriert.

Preamble

The present work has been performed in the context of my research work at the Department Antennas and Scattering (AuS) of the Institute for High-Frequency Physics and Radar Techniques (FHR) of FGAN e.V., Wachtberg, Germany, which I have joined in the end of 2002.

I would like to thank Prof. Dr.-Ing. Thomas Eibert for guidance and supervision of my research over the past years. The considerable discussions and his creative suggestions have contributed significantly to the completion of this work. I would also like to thank Prof. Dr.-Ing. Thomas Weiland for giving me the opportunity to submit this thesis at the Department of Electrical Engineering and Information Technology of the Technical University of Darmstadt.

My deep acknowledgment goes to the Directors of the FHR Prof. Dr. Klaus Krücker and Prof. Dr. Joachim Ender as well as to the former Head of the Department AuS Prof. Dr. rer. nat. Christoph von Winterfeld and his followers Prof. Dr.-Ing. Thomas Eibert and Dr. Peter Knott for giving me the opportunity to contribute with my skills to the research activities of the institute. I would additionally like to express my thanks to all my colleagues in the department for being always available for helpful discussions. Special thanks to my colleague Dr. Frank Weinmann for proofreading the manuscript.

Finally, I would like to thank warmly my family and Elisabeth for their tremendous support and precious patience throughout the preparation and completion of this work.

Bonn, 2008

Andreas Tzoulis

Contents

Acronyms

ABC	Absorbing Boundary Condition
AIM	Adaptive Integral Method
BI	Boundary Integral
BIM	Boundary Integral Method
BVP	Boundary Value Problem
CEM	Computational Electromagnetics
CFIE	Combined Field Integral Equation
CNLT	Constant Normal Linear Tangential
EDSB	Edge Diffraction Shadow Boundary
EFIE	Electric Field Integral Equation
EMC	Electromagnetic Compatibility
FAFFA	Fast Far-Field Approximation
FDTD	Finite Difference Time Domain
FE	Finite Element
FEBI	Finite Element Boundary Integral
FEM	Finite Element Method
FFT	Fast Fourier Transform
FIT	Finite Integration Technique
FMM	Fast Multipole Method
FVTD	Finite Volume Time Domain
GTD	Geometrical Theory of Diffraction
GO	Geometrical Optics
IBC	Impedance Boundary Condition
IE	Integral Equation
ISB	Incidence Shadow Boundary
MFIE	Magnetic Field Integral Equation
MLFMM	Multilevel Fast Multipole Method
MoM	Method of Moments
MPIE	Mixed Potential Integral Equation
NFFFT	Near-Field to Far-Field Transformation
PBT	Parasitic Body Technique
PEC	Perfect Electric Conductor
PMC	Perfect Magnetic Conductor
PML	Perfectly Matched Layer
PO	Physical Optics
PWE	Parabolic Wave Equation
P-MLFMM	Postprocessing MLFMM
RWG	Rao-Wilton-Glisson

RSB	Reflection Shadow Boundary
SBR	Shooting and Bouncing Rays
SIE	Surface Integral Equation
SSF	Split-Step Fourier
TDIE	Time Domain Integral Equation
TD-UTD	Time Domain Uniform Geometrical Theory of Diffraction
UTD	Uniform Geometrical Theory of Diffraction

List of Notations

General Mathematical Notations

∇	nabla operator, gradient
$\nabla\cdot$	divergence operator
∇_A	surface gradient operator
$\nabla_A\cdot$	surface divergence operator
$\nabla\times$	rotation (curl) operator
$\bar{\mathbf{I}}$	unit dyad
$f(\cdot)$	function
$F(\cdot)$	Fresnel function, functional
$\mathbb{R}^3$	Hilbert space of real numbers
$\mathbb{C}^3$	Hilbert space of complex numbers
$L^2(V)$	Hilbert space known as Lebesque space containing square integrable functions in V
$O(N)$	complexity of the order N
ϑ	elevation angle in spherical coordinate system
φ	azimuth angle in spherical coordinate system
$\hat{n}$	outward normal unit vector on surface

General Notations in Electromagnetics

$\mathbf{E}$, $\mathbf{H}$	electric and magnetic field intensity
$\mathbf{D}$, $\mathbf{B}$	electric and magnetic flux density
$\mathbf{J}$, $\mathbf{M}$	electric and magnetic current density
$\mathcal{E}$	instantaneous electric field
ϱ_e, ϱ_m	electric and magnetic charge density
$\mathbf{A}$	magnetic vector potential, plane wave spectrum
$\mathbf{F}$	electric vector potential
φ_e, φ_m	electric and magnetic scalar potential
φ	electrostatic scalar potential
ε, $\bar{\bar{\varepsilon}}$	scalar and tensor permittivity (dielectric constant)
ε_r, $\bar{\bar{\varepsilon}}_r$	scalar and tensor relative permittivity
ε_0	permittivity of free space
μ, $\bar{\bar{\mu}}$	scalar and tensor permeability
μ_r, $\bar{\bar{\mu}}_r$	scalar and tensor relative permeability
μ_0	permeability of free space
ω	radial frequency
t	time variable

j	imaginary unit $\sqrt{-1}$, index for edges
f	frequency
λ	wavelength
λ_0	free space wavelength
k	wavenumber, index for various quantities
k_0	wavenumber of free space
Z	wave impedance
Z_0	wave impedance of free space
Y	wave admittance
Y_0	wave admittance of free space

Finite Element Boundary Integral Method

$\mathbf{E}^{inc}$, $\mathbf{E}^{i}$, $\mathbf{H}^{inc}$	incident electric and magnetic field intensity
$\mathbf{E}_a$, $\mathbf{E}^{int}$	electric field intensity inside V_a
$\mathbf{H}_a$, $\mathbf{H}^{int}$	magnetic field intensity inside V_a
$\mathbf{E}_{ad}$, $\mathbf{H}_{ad}$	adjoint electric and magnetic field
$\mathbf{E}^{ext}$, $\mathbf{H}^{ext}$	electric and magnetic field intensity inside V
$\bar{\mathbf{G}}_{J/M}^{E/H}$	dyadic Green's function within V of the electric or magnetic field due to electric and magnetic point source
G	scalar Green's function
$\mathbf{J}_A$, $\mathbf{M}_A$	equivalent electric and magnetic surface current density
ϱ_A^e, ϱ_A^m	equivalent electric and magnetic surface charge density
$\mathbf{r}'$, $\mathbf{r}_n$	position vector of source point
$\mathbf{r}$, $\mathbf{r}_m$	position vector of testing or observation (field) point
V	external solution domain for equivalence principle formulations
V_a	internal domain for equivalence principle formulations, FEM solution domain
A_∞	closed surface placed at infinity surrounding domain V
A_d	closed surface surrounding domain V_a
A_c	infinitesimally thin conducting surfaces within V
A	boundary (Huygens') surface enclosing domain V consisting of A_d, A_c, and A_∞
S	general closed surface for equivalence principle definitions
H_n, E_n	expansion coefficients of electric and magnetic surface currents
E_j^e, H_j^e	expansion coefficients of electric and magnetic field within tetrahedron e
M	number of triangle elements
N	number of BI unknowns
M_{FE}	number of tetrahedral elements
N_{FE}	degrees of freedom within V_a
A_T	surface of triangle element
n	index for various quantities
$\hat{n}_A$	normal unit vector on triangle element
α	CFIE combination parameter
l	index for various quantities
e	index for tetrahedral elements
R	distance between source and testing point

$\hat{e}_R$	direction of gradient of free space scalar Green's function
∂A	boundary of triangle element
$\hat{u}$	outer unit vector normal to ∂A
$\boldsymbol{\beta}_n$	RWG basis functions
$\boldsymbol{\alpha}_j$	zeroth-order edge element basis functions
$[A]$	sparse coupling matrix of FE part
$[B]$	full coupling matrix of BI part
$\{x\}$	vector of expansion coefficients
$\{b\}$	excitation vector

Multilevel Fast Multipole Method

$\left[Z_{J,M}^{CFIE}\right]$	coupling matrix of BI part due to electric and magnetic currents for CFIE
$Z_{mn,J,M}^{MoM}$	near coupling matrix elements for CFIE between non well-separated groups due to electric and magnetic currents
$\{H\}$, $\{E\}$	vector of electric and magnetic surface current expansion coefficients
M_G	number of MLFMM groups at the finest level
N'	number of current elements per MLFMM group at the finest level
$G_{n'}$	index for source (radiating) groups
$G_{m'}$	index for testing (receiving) groups
$G_{Bn'}$	all nearby (not well-separated) groups of the n'-th source group $G_{n'}$ including itself
$\mathbf{r}_{n'}$	position vector of source group center
$\mathbf{r}_{m'}$	position vector of testing group center
$\mathbf{r}_{mn}$	vector from source to testing point
$\mathbf{r}_{nn'}$	vector from center of source group to source point
$\mathbf{r}_{m'n'}$, $\mathbf{D}$	vector from center of source group to center of testing group
$\mathbf{r}_{mm'}$	vector from center of testing group to testing point
$\mathbf{d}$	sum of vectors from the considered current elements to the particular group centers
$\hat{D}$, $\hat{d}$	unit vector in direction of $\mathbf{D}$ and $\mathbf{d}$
j_l	first kind spherical Bessel function of degree l
$h_l^{(2)}$	second kind spherical Hankel function of degree l
P_p^q	Legendre polynomial of degree p and order q
$\mathbf{k}$	propagation (wave) vector
$\hat{k}$	unit vector in direction of $\mathbf{k}$ (propagation direction)
T_L	translation operator of conventional MLFMM
L_m	number of multipoles
L	number of MLFMM levels
ε	relative error
d_a	number of digits of accuracy
J, M	index for electric and magnetic currents
$\tilde{\boldsymbol{\beta}}_n$	$\hat{k}$-space representation of basis functions $\boldsymbol{\beta}_n$
$\tilde{\boldsymbol{\alpha}}_n$	$\hat{k}$-space representation of basis functions $\boldsymbol{\alpha}_n$
Y_{pq}	orthonormalized spherical harmonics
$\mathbf{f}_{pq}^n$	expansion coefficients of spherical harmonics

Uniform Geometrical Theory of Diffraction

$\mathbf{E}_{GO}$, $\mathbf{H}_{GO}$	geometrical optics electric and magnetic field
$\mathbf{E}^r$, $\mathbf{H}^r$	reflected electric and magnetic ray optical field
$\mathbf{E}^d$, $\mathbf{H}^d$	diffracted electric and magnetic ray optical field
Ψ	phase function of ray optical fields
$\hat{X}_1$, $\hat{X}_2$	principal directions of curvature of astigmatic ray tube
ρ_1, ρ_2	radii of curvature in the principal directions $\hat{X}_1$ and $\hat{X}_2$
G_c	Gaussian curvature of the wavefront
O'	source point
P	observation point
Q_R, Q_D	reflection and diffraction point
A	divergence (spreading) factor of ray optical field
A_R, A_D	divergence factor of the reflected and diffracted ray
$\hat{e}$	unit vector tangent to the edge at the point of diffraction
$\hat{e}_s$	unit vector normal to the ray optical fields (direction of power flow)
$\hat{e}^i$	propagation direction of incident ray before reflection
$\hat{e}^r$	propagation direction of reflected ray
$\hat{e}_{s'}$	propagation direction of incident ray before diffraction
$\hat{e}_s$	propagation direction of diffracted ray
ϑ^i	angle of ray incidence before reflection
ϑ^r	angle of reflection
β_0'	angle of ray incidence before diffraction
β_0	angle of diffraction
ρ_1^i, ρ_2^i	principal radii of curvature of the incident wavefront at the reflection point Q_R
ρ_1^r, ρ_2^r	principal radii of curvature of the reflected wavefront at the reflection point Q_R
ρ_c	ray caustic distance of the diffracted field
ρ_c^i	radius of curvature of the incident wavefront at diffraction point in the plane of incidence
s'	distance from source point to phase reference point
s	distance from observation point to phase reference point
$\mathbf{r}_s$	position vector of observation point
$\mathbf{r}_{Q_R}$, $\mathbf{r}_{Q_D}$	position vector of reflection and diffraction point
$\overline{\mathbf{R}}^E$, $\overline{\mathbf{R}}^H$	dyadic reflection coefficient for the electric and magnetic field
$\overline{\mathbf{D}}^E$, $\overline{\mathbf{D}}^H$	dyadic diffraction coefficient for the electric and magnetic field
$R_\parallel$, $R_\perp$	scalar reflection coefficient related to field components parallel and perpendicular to plane of incidence and reflection in ray-fixed coordinate system
$D_\parallel$, $D_\perp$	scalar diffraction coefficient related to field components parallel and perpendicular to plane of incidence and diffraction in edge-fixed coordinate system
$\hat{e}_\parallel^i$, $\hat{e}_\parallel^r$	unit vector in ray-fixed coordinate system parallel to plane of incidence and reflection
$\hat{e}_\perp^i$, $\hat{e}_\perp^r$	unit vector in ray-fixed coordinate system perpendicular to plane of incidence and reflection
$\hat{e}_{\beta_0'}$, $\hat{e}_{\beta_0}$	unit vector in edge-fixed coordinate system parallel to plane of incidence and diffraction

$\hat{e}_{\varphi'}$, $\hat{e}_{\varphi}$	unit vector in edge-fixed coordinate system perpendicular to plane of incidence and diffraction
φ', φ	angle from reference face of the wedge to direction of incidence and diffraction

Hybrid Formulations

$\bar{\mathbf{G}}^{E/H}_{J,tot}$	total Green's functions within V of the electric or magnetic field due to electric surface currents
$\bar{\mathbf{G}}^{E/H}_{M,tot}$	total Green's functions within V of the electric or magnetic field due to magnetic surface currents
$\bar{\mathbf{G}}^{E/H}_{J/M,UTD}$	ray optical terms of Green's functions
G_R	ray optical scalar Green's function for reflection
$\tilde{A}_{R/D}$	factors combining the appropriate divergence and phase factors of ray optical mechanisms
$\mathbf{E}^{inc}_{tot}$, $\mathbf{H}^{inc}_{tot}$	total incident electric and magnetic field
$\mathbf{E}^{inc}_{UTD}$, $\mathbf{H}^{inc}_{UTD}$	ray optical incident electric and magnetic field
$\mathbf{E}^{r,inc}$, $\mathbf{H}^{r,inc}$	reflected term of the ray optical incident electric and magnetic field
$\mathbf{E}^{d,inc}$, $\mathbf{H}^{d,inc}$	diffracted term of the ray optical incident electric and magnetic field
$\mathbf{E}^{dd}$	double diffracted electric field
$\mathbf{E}_{tot}$, $\mathbf{H}_{tot}$	total electric and magnetic field produced by source currents at an observation point
$\mathbf{E}_P$, $\mathbf{H}_P$	direct electric and magnetic field contributions by source currents in absence of UTD objects
$\mathbf{E}_{UTD}$, $\mathbf{H}_{UTD}$	ray optical electric and magnetic field contributions by source currents
$\mathbf{E}^s_{tot}$	scattered electric field produced by equivalent surface currents at observation point
$\mathbf{E}^s$	direct contributions to scattered electric field
$\mathbf{E}^{s,tot}_{UTD}$	ray optical contributions to scattered electric field
$\mathbf{E}^s_{UTD}$	ray optical contributions of surface currents to scattered electric field
$\hat{e}^i$, $\hat{k}_i$, $\hat{r}_{Qn'}$	direction of incident ray
$\hat{e}^r$, $\hat{k}_r$, $\hat{r}_{m'Q}$	direction of reflected ray
$\hat{e}^d$, $\hat{k}_d$, $\hat{r}_{m'Q}$	direction of diffracted ray
$\hat{k}_0$, $\hat{r}_{mn'}$	direction from center of source group to observation point
$\hat{k}_s$, $\hat{r}$,	direction to observation point
O'_{im}	image source point
R_r	scalar reflection coefficient related to radial field components
$\mathbf{r}_{mQ}$	vector from local point on the UTD object to testing or observation point
$\mathbf{r}_{Qn}$	vector from source point to local point on the UTD object
$\mathbf{r}_{m'Q}$	vector from local point on the UTD object to center of testing group
$\mathbf{r}_{Qn'}$	vector from center of source group to local point on the UTD object
$\mathbf{r}_{g_{n'}}$	position vector of gravity center of currents within source group
$\mathbf{r}_{g_{m'}}$	position vector of gravity center of currents within testing group
$\mathbf{r}_{Qg_{n'}}$	vector from gravity center of currents within source group to local point on the UTD object

$\mathbf{r}_{g_{n'}n'}$	vector from source current to gravity center of currents within source group
$\mathbf{r}_{m'g_{m'}}$	vector from gravity center of currents within testing group to testing current
$\mathbf{r}_{mn'}$	vector from center of source group to observation point
$\mathbf{r}_{v_1}$	position vector of the first edge vertex
$\mathbf{r}'_{im}$	position vector of image source point
T_L^{UTD}	ray optical translation operator
T_L^{FF}	direct far-field translation operator
$\left[Z_{J,M,tot}^{CFIE}\right]$	total coupling matrices due to electric and magnetic currents
p	index for sampling points in $\hat{k}$-space
p_t, $p_{t'}$	index for interpolation and anterpolation points
K	number of sampling points in $\hat{k}$-space
K_0	number of interpolation and anterpolation points
w_{p_t}, $w_{p_{t'}}$	interpolation and anterpolation weights
D_l	group dimension at level l
D_1	smallest group dimension at lowest level
r_{UTD}	condition for ray optical translations
r_{far}	condition for far-field translations
$d_{l_{FMM}}$	translation region around source group for conventional MLFMM
$d_{l_{UTD}}$	extended translation region around source group for ray optical translations
d_m	multiplier controlling the extension width of ray optical translation domain
d_R	distance of reflection surface from origin of the coordinate system
p_R	parameter defined on ray trajectory
p_D	parameter defined on edge
l_e	edge length
h_1	distance of source point from edge
h_2	distance of observation point from edge
x_d	distance of projection of source point from diffraction point
x_1	distance of projection of source point from first vertex of edge
x_2	distance of projection of observation point from first vertex of edge
U	index for UTD objects
P	number of observation points
T_1, T_2	spectrum density functions of outgoing waves

Chapter 1

Introduction

Solution of large and complex radiation and scattering problems is an important topic in electromagnetics and is found nowadays in many applications like analysis and design of antenna systems, analysis of installed antenna performance on large and complex platforms, signature prediction of radar targets, remote sensing, geoelectromagnetics, biomedical engineering, Electromagnetic Compatibility (EMC) investigations in communication systems, etc. In each case the electromagnetic solution is achieved by means of solving Maxwell's equations for the given radiation and scattering system. Since exact analytical solutions of electromagnetic field problems are given only for systems with canonical geometries, Computational Electromagnetics (CEM) has become the most important approach in the last decades for solving large and complex electromagnetic radiation and scattering problems.

There is a variety of numerical methods available these days for the formulation and solution of problems associated with electromagnetic radiation and scattering phenomena [1]-[4]. Various approaches are used for solving the field problem, starting either with exact differential or integral formulations providing solutions in the time or frequency domain, or using high-frequency approximations for the field formulations providing asymptotic solutions. Each of these methods has advantages and disadvantages when it is used to solve electromagnetic field problems. The essential factors for their applicability are the shape and the material properties as well as the dimensions with respect to the wavelength of the involved objects. However, none of the existing methods can handle with acceptable efficiency all possible electromagnetic problems for the whole frequency range of interest. As a consequence the advantages of the various numerical approaches are combined within *hybrid methods*. It will be an essential task of today's and tomorrow's CEM to suitably combine numerical techniques within one hybrid tool, which can be efficiently applied to many different kinds of electromagnetic problems from very low up to very high frequencies.

An important step into this direction is given with the present thesis, which combines for the first time a fast and powerful integral equation method with ray optical asymptotic techniques together with the ability of fast and efficient postprocessing near-field and far-field scattering computations including ray optical fields. Additionally, double diffracted ray optical fields at arbitrarily oriented straight edges are included. In the following, an overview over the available numerical modeling methods and the outline of the present work will be given.

1.1 Overview over Numerical Modeling Methods

Numerical modeling methods of electromagnetic problems can be divided into *exact* and *asymptotic* methods [5] as shown in Fig. 1.1. Exact methods start with the exact Maxwell's equations to provide field formulations in either differential or integral form and to obtain a numerical solution. On the other hand, asymptotic methods use an approximation of the field equations, which is accurate for very small wavelengths providing accurate asymptotic solutions of electromagnetic fields in the high-frequency limit, where the dimensions of the objects can be assumed very large as compared to the wavelength. According to this distinction, exact numerical methods are also known as *low-frequency* methods, whereas asymptotic methods are referred to as *high-frequency* methods.

Another class of approximate methods is derived using a parabolic approximation of the Helmholtz wave equation known as Parabolic Wave Equation (PWE), which is widely used in electromagnetic wave propagation analysis [6]. The primary limitation of the PWE approach is the neglect of backscattered fields, so that accurate calculations are restricted to near-horizontal propagation directions. Numerical solution of PWE formulations can be achieved with the Split-Step Fourier (SSF) algorithm [7], [8]. Finally, formulations for slowly varying electromagnetic fields are derived from Maxwell's equations using quasistatic approximations, in which the field coupling resulting from either the magnetic induction or the electric displacement current is neglected [9].

Exact methods can be further divided into *local* and *global* methods. Local methods start directly from Maxwell's equations to obtain the field formulations. The field equations are discretized in the whole solution domain resulting in local dependencies between the discrete field quantities. Most common local techniques are the Finite Difference Time Domain (FDTD) method [10], [11], the Finite Volume Time Domain (FVTD) method [12], [13], the Finite Integration Technique (FIT) [14] and the Finite Element Method (FEM) [15]-[17]. Due to the local nature of these methods, they are best suited for modeling closed inhomogeneous volumes, which are not too large as compared to the wavelength. In general, the FEM is more attractive for modeling complex dielectric structures with arbitrary shapes due to its variational formulation and the flexible volume meshing.

Global methods are based on Integral Equation (IE) formulations, where equivalent current densities are defined according to the equivalence principle. The field distributions of these equivalent source currents have a global effect in the whole solution domain. The IEs can be line, surface, or volume IEs according to the geometry of the object and they are mainly solved by the Method of Moments (MoM) [18], [19]. In particular, the formulation of the fields using surface IEs over the boundaries of the involved objects is in general known as Boundary Integral Method (BIM). A description of numerical methods based on the solution of Time Domain Integral Equations (TDIEs) can be found in [20]. The main advantage of global methods is that due to the global effect of the equivalent current sources radiation and scattering computations can be done in a more effective way compared to local methods, where the whole solution domain must be discretized or appropriately truncated. On the other hand, the main disadvantage is the rapidly increasing computation and memory complexity with growing dimensions of the involved structures. This problem has been relieved by introducing fast integral equation methods like the Adaptive Integral Method (AIM) [21], pre-corrected Fast Fourier Transform (FFT) methods [22] and the Fast Multipole Method (FMM) [23] along with its multilevel versions, known as the *Multilevel Fast Multipole Method* (MLFMM) [4], [24]-[26] resulting in low computation and memory complexity. Using fast

IE solution techniques, large and complex electromagnetic field problems are handled very efficiently up to the point imposed by currently available computational resources.

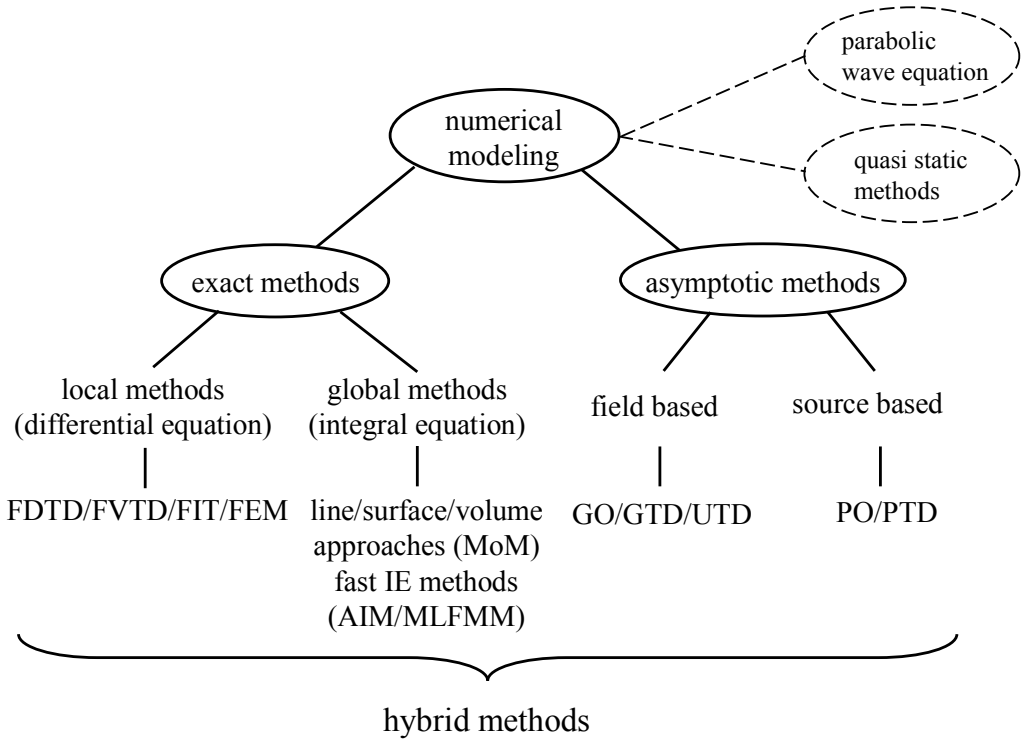

Figure 1.1: Numerical methods for modeling electromagnetic radiation and scattering problems.

In addition, asymptotic methods can be *field* or *source based*. The first describe the electromagnetic fields according to ray concepts of classical Geometrical Optics (GO) [27], [28] and ray optical diffraction theories such as the Geometrical Theory of Diffraction (GTD) introduced 1951 by Keller [29] and its uniform version developed by Kouyoumjian and Pathak [30], [31], which is known as the *Uniform Geometrical Theory of Diffraction* (UTD). The Time Domain Uniform Geometrical Theory of Diffraction (TD-UTD) has been developed in [32]. The main advantage of ray optical high-frequency methods is that there is no need to discretize electrically large objects providing solutions with very low computational effort, but on the other hand, ray optical formulations are restricted to objects with relatively simple geometries. Further drawbacks of these methods is their failure to predict electromagnetic fields at caustics as well as the fact that fields can be evaluated only in specular ray directions.

Source based asymptotic methods use a GO approximation for the surface currents on the objects according to the Physical Optics (PO) together with the evaluation of the appropriate radiation integral in order to calculate the electromagnetic fields in all spatial directions. A systematic extension of the PO for objects with edges has been developed by Ufimtsev [33], which is known as Physical Theory of Diffraction (PTD). Similar approaches using equivalent edge currents have been developed by Knott and Senior [34] and Michaeli [35]. The PTD is very useful for estimating the fields in regions having confluence of the transition regions associated with ray caustics and shadow boundaries, where UTD fails. However, the PO and PTD require integration over the currents, which can be very inefficient for large scale problems.

It is obvious, that all available methods have drawbacks, which restrict more or less their applicability under certain conditions. *Hybrid methods* combine the advantages of the various numerical techniques providing improved performance and applicability. Within exact methods a hybrid approach combining a local and a global technique in the frequency domain is the *Finite Element Boundary Integral* (FEBI) method, [16], [17], [36]-[40], where the solution of the Boundary Integral (BI) part is nowadays routinely accelerated by MLFMM resulting in a FEBI-MLFMM technique [41]. Combination of local and global methods in the time domain can be found in [42]-[48]. Within asymptotic methods a powerful hybrid ray tracer with ray density normalization combining GO/UTD with PO/PTD was recently developed [49], [50]. However, for successful treatment of problems involving both arbitrarily shaped objects with relatively large electrical sizes as well as electrically very large objects with relatively simple shapes, combination of exact with asymptotic methods is needed.

Hybrid approaches combining exact and asymptotic methods in the frequency domain have been developed since the 70's mainly including combinations of conventional MoM based global methods for conducting objects with current based (PO) and field based (GO, GTD, UTD) high-frequency techniques [51]-[61]. A hybrid approach combining the FEM with high-frequency methods was introduced in [62]. Corresponding combinations in the time domain can be found in [63]-[66]. Recently, hybridization of the FIT with UTD was developed by Skarlatos et al. for both the frequency as well as the time domain [67], [68]. A very promising hybrid technique was developed in 2002 by Alaydrus et al. [69], where the FEBI was combined with UTD giving full electromagnetic coupling between dielectric and electrically large conducting objects within a common environment. However, the hybrid FEBI-UTD method developed in [69] is restricted to conventional BI formulation without fast IE solution. Therefore, modeling flexibility is not good and UTD must often be applied to moderately large objects that should be modeled within the BI part.

In the present thesis, the hybrid FEBI-UTD technique is extended by a novel hybrid approach, which combines the multipole field representations of MLFMM with the ray optical fields of UTD [70]-[73]. This extends significantly the applicability of the hybrid method. The hybridization is performed within the FEBI-MLFMM framework resulting in a hybrid FEBI-MLFMM-UTD method, which combines for the first time a local method, a global fast IE method, and ray optical asymptotic techniques. Further, postprocessing near-field computations in the hybrid method are accelerated using MLFMM, where near-field and far-field translations are combined in order to achieve optimum performance [74]-[78]. Thereby, ray optical contributions due to the presence of electrically very large UTD objects are taken into account within each translation domain according to the presented hybridization of MLFMM with UTD [79], [80]. Also, far-field scattering computations are performed by applying Near-Field to Far-Field Transformation (NFFFT) based on planar near-field scanning techniques to ray optical field contributions [81]-[84]. Additionally, double diffracted ray optical fields at arbitrarily oriented straight metallic edges are included using scalar diffraction coefficients of standard UTD [85], [86]. With the presented novel hybrid method large scale problems including arbitrarily shaped and electrically very large objects can be handled efficiently by saving a large amount of computation and memory requirements.

After giving a short overview over existing numerical modeling techniques for solving electromagnetic problems and the motivation of the present thesis, the outline of the document will be given in the next section.

1.2 Outline

The present thesis is outlined as follows: First, an introduction to the three methods combined in the hybrid FEBI-MLFMM-UTD approach will be given. In particular, the FEBI technique is described in Chapter 2. A discussion on various possible formulations is also given. In Chapter 3 the MLFMM is discussed with focus given on the diagonal multipole field representations and the memory efficient implementation by spherical harmonics expansion of the $\hat{k}$-space representation of the basis functions. Also, in Chapter 4 the UTD is described, where ray optical asymptotic field representations are given and reflection and diffraction mechanisms are described.

After that, the combination of MLFMM with UTD is presented in Chapter 5 and details in the numerical implementation including double diffractions are discussed. In Chapter 6 the implementation of MLFMM in the postprocessing stage for fast computation of near-fields is presented combining near-field and far-field MLFMM translations for optimum performance including ray optical contributions. Also, in Chapter 7 far-field scattering computations using near-field to far-field transformations are described based on planar near-field scanning techniques. Finally, in Chapter 8 numerical results are shown, where the applicability of the overall hybrid method and the advantages of the novel approaches can be clearly seen. The thesis is closing with summary and conclusions in Chapter 9.

Chapter 2

The Finite Element Boundary Integral Method

The Finite Element Boundary Integral method is a numerical technique combining the advantages of the local Finite Element Method and the global Boundary Integral Method. With this approach efficient numerical solutions of electromagnetic problems containing arbitrarily shaped objects with complex materials is achieved. In this chapter, the basic theoretical concepts of the involved methods and the formulation of the combined approach will be given.

2.1 Theoretical Introduction

2.1.1 The Vector Wave Equation

Consider the general case of a linear, inhomogeneous, and anisotropic medium with constitutive parameters $\bar{\bar{\varepsilon}}(\mathbf{r})$, $\bar{\bar{\mu}}(\mathbf{r})$, which are in general complex in order to consider material losses. Assuming time-harmonic dependence $e^{j\omega t}$, the complex electric and magnetic field vectors are governed by *Maxwell's field equations*

$$\nabla \times \mathbf{E}(\mathbf{r}) = -j\omega \mathbf{B}(\mathbf{r}) - \mathbf{M}(\mathbf{r}), \tag{2.1}$$
$$\nabla \times \mathbf{H}(\mathbf{r}) = j\omega \mathbf{D}(\mathbf{r}) + \mathbf{J}(\mathbf{r}), \tag{2.2}$$
$$\nabla \cdot \mathbf{D}(\mathbf{r}) = \varrho_e(\mathbf{r}), \tag{2.3}$$
$$\nabla \cdot \mathbf{B}(\mathbf{r}) = \varrho_m(\mathbf{r}), \tag{2.4}$$

where $\mathbf{E}, \mathbf{H}$ are the electric and magnetic field intensity, $\mathbf{D}, \mathbf{B}$ the electric and magnetic flux density, $\mathbf{J}, \mathbf{M}$ the electric and magnetic current density and ϱ_e, ϱ_m the electric and magnetic charge density, respectively. Equations (2.1)-(2.4) are the mathematical expressions in differential form of Faraday's and Ampere-Maxwell's law as well as Gauss's law for the electric and magnetic field, respectively. The magnetic sources $\mathbf{M}$ and ϱ_m do not exist in nature and they are only introduced through the generalized current concept for symmetry purposes [87]. In addition, taking the divergence of (2.2) and using (2.3), the *continuity equation* for the electric charge

$$\nabla \cdot \mathbf{J}(\mathbf{r}) = -j\omega \varrho_e(\mathbf{r}) \tag{2.5}$$

is derived, which connects the divergence of the electric current density with the electric charge density and states for the conversation of electric charge. Although the magnetic counterparts of current and charge do not exist in nature, the continuity equation for the magnetic charge

$$\nabla \cdot \mathbf{M}(\mathbf{r}) = -j\omega\varrho_m(\mathbf{r}) \tag{2.6}$$

can also be derived in the same way for symmetry purposes.

The effect of the considered medium on the electromagnetic fields is taken into account by the *constitutive relations*

$$\mathbf{B}(\mathbf{r}) = \mu_0 \bar{\bar{\mu}}_r(\mathbf{r}) \cdot \mathbf{H}(\mathbf{r}), \tag{2.7}$$
$$\mathbf{D}(\mathbf{r}) = \varepsilon_0 \bar{\bar{\varepsilon}}_r(\mathbf{r}) \cdot \mathbf{E}(\mathbf{r}), \tag{2.8}$$

which reduce equations (2.1)-(2.4) to

$$\nabla \times \mathbf{E}(\mathbf{r}) = -j\omega\mu_0 \bar{\bar{\mu}}_r(\mathbf{r}) \cdot \mathbf{H}(\mathbf{r}) - \mathbf{M}(\mathbf{r}), \tag{2.9}$$
$$\nabla \times \mathbf{H}(\mathbf{r}) = j\omega\varepsilon_0 \bar{\bar{\varepsilon}}_r(\mathbf{r}) \cdot \mathbf{E}(\mathbf{r}) + \mathbf{J}(\mathbf{r}), \tag{2.10}$$
$$\nabla \cdot \bar{\bar{\varepsilon}}_r(\mathbf{r}) \cdot \mathbf{E}(\mathbf{r}) = \varepsilon_0^{-1}\varrho_e(\mathbf{r}), \tag{2.11}$$
$$\nabla \cdot \bar{\bar{\mu}}_r(\mathbf{r}) \cdot \mathbf{H}(\mathbf{r}) = \mu_0^{-1}\varrho_m(\mathbf{r}). \tag{2.12}$$

The first two Maxwell's equations (2.9) and (2.10), which give the rotation of the electromagnetic fields, are first-order differential equations, in which the electric and magnetic fields are coupled. These two equations can be transformed by eliminating $\mathbf{E}$ and $\mathbf{H}$ into a single second-order differential wave equation in terms of only the electric or magnetic field, which is known as *vector wave equation* [17]. In particular, taking the rotation of (2.9) assuming that $\bar{\bar{\mu}}_r(\mathbf{r})$ is invertible yields

$$\nabla \times \bar{\bar{\mu}}_r^{-1}(\mathbf{r}) \cdot \nabla \times \mathbf{E}(\mathbf{r}) = -j\omega\mu_0 \nabla \times \mathbf{H}(\mathbf{r}) - \nabla \times \bar{\bar{\mu}}_r^{-1}(\mathbf{r}) \cdot \mathbf{M}(\mathbf{r}) \tag{2.13}$$

and using (2.10) gives

$$\nabla \times \bar{\bar{\mu}}_r^{-1}(\mathbf{r}) \cdot \nabla \times \mathbf{E}(\mathbf{r}) = -j\omega\mu_0 \big[j\omega\varepsilon_0 \bar{\bar{\varepsilon}}_r(\mathbf{r}) \cdot \mathbf{E}(\mathbf{r}) + \mathbf{J}(\mathbf{r})\big] - \nabla \times \bar{\bar{\mu}}_r^{-1}(\mathbf{r}) \cdot \mathbf{M}(\mathbf{r}) \Rightarrow$$
$$\nabla \times \bar{\bar{\mu}}_r^{-1}(\mathbf{r}) \cdot \nabla \times \mathbf{E}(\mathbf{r}) = \omega^2\varepsilon_0\mu_0 \bar{\bar{\varepsilon}}_r(\mathbf{r}) \cdot \mathbf{E}(\mathbf{r}) - j\omega\mu_0 \mathbf{J}(\mathbf{r}) - \nabla \times \bar{\bar{\mu}}_r^{-1}(\mathbf{r}) \cdot \mathbf{M}(\mathbf{r}).$$

Finally, by taking into account the wavenumber $k_0 = \omega\sqrt{\varepsilon_0\mu_0}$ and the wave impedance $Z_0 = \sqrt{\mu_0/\varepsilon_0} \Rightarrow k_0 Z_0 = \omega\mu_0$ of free space, we have

$$\nabla \times \bar{\bar{\mu}}_r^{-1}(\mathbf{r}) \cdot \nabla \times \mathbf{E}(\mathbf{r}) - k_0^2 \bar{\bar{\varepsilon}}_r(\mathbf{r}) \cdot \mathbf{E}(\mathbf{r}) = -jk_0 Z_0 \mathbf{J}(\mathbf{r}) - \nabla \times \bar{\bar{\mu}}_r^{-1}(\mathbf{r}) \cdot \mathbf{M}(\mathbf{r}). \tag{2.14}$$

The above equation is the *vector wave equation for the electric field*. Similarly, by taking the rotation of (2.10) assuming that $\bar{\bar{\varepsilon}}_r(\mathbf{r})$ is invertible and using (2.9) results in

$$\nabla \times \bar{\bar{\varepsilon}}_r^{-1}(\mathbf{r}) \cdot \nabla \times \mathbf{H}(\mathbf{r}) - k_0^2 \bar{\bar{\mu}}_r(\mathbf{r}) \cdot \mathbf{H}(\mathbf{r}) = -jk_0 Y_0 \mathbf{M}(\mathbf{r}) + \nabla \times \bar{\bar{\varepsilon}}_r^{-1}(\mathbf{r}) \cdot \mathbf{J}(\mathbf{r}), \tag{2.15}$$

where $Y_0 = 1/Z_0 = \sqrt{\varepsilon_0/\mu_0} \Rightarrow k_0 Y_0 = \omega\varepsilon_0$ is the wave admittance of free space. This is the *vector wave equation for the magnetic field*.

It is noticed, that the wave equations (2.14) and (2.15) are incorporating the divergence conditions imposed by Maxwell's equations (2.3) and (2.4), respectively. This can be easily shown by taking the divergence of both sides of (2.14) and (2.15) using the continuity equations (2.5) and (2.6), respectively, as well as applying the vector identity

$$\nabla \cdot \nabla \times \mathbf{E} = 0, \tag{2.16}$$

which says that the divergence of the curl of any vector is always zero. In the special case of source free regions ($\mathbf{J} = 0, \mathbf{M} = 0$), the corresponding divergenceless (solenoidal) condition is incorporated in the vector wave equation for all but static fields.

A very important theorem in electromagnetics that is involved in the numerical approaches described in this chapter is the equivalence principle, which will be discussed in the following subsection.

2.1.2 The Equivalence Principle

Two sources are assumed to be equivalent in a specific region if they produce the same fields within that region. The equality of the fields produced by given sources in a certain specified region with the fields produced by appropriate equivalent sources placed over the boundaries of that region is expressed by *field equivalence theorems* [88]. The primary equivalence theorem is stated with Kirchhoff's formula, which gives the field outside (or inside) a closed surface S in terms of the field function and its normal derivatives on S. This formula involves scalar functions and is applied in static problems. Application of original Kirchhoff's formula to the components of an electromagnetic field vector results in a solution that does not satisfy Maxwell's equations. Vector analog of Kirchhoff's formula was derived by Love [89], Schelkunoff [88] and Stratton and Chu [9]. These formulations represent the *equivalence principle* in electromagnetics, which expresses the fields outside (or inside) a closed surface S in terms of equivalent current densities on S, which are actually tangential field components on S. The equivalence principle is a more rigorous formulation of the Huygens' principle[1]. Formulations of the equivalence principle for more general configurations are given in [87] in a descriptive manner based on uniqueness theorem[2]. A detailed mathematical formulation and proof of the equivalence principle in electromagnetics was given by Chen [90] and Monzon [91] for homogeneous regions and inhomogeneous bianisotropic media, respectively.

For the formulation of the equivalence principle, the configuration shown in Fig. 2.1 is assumed, which is excited by a plane wave $\mathbf{E}^{inc}, \mathbf{H}^{inc}$. The considered solution domain is the region V with linear, homogeneous, and isotropic material properties ε, μ, which can be in general complex parameters. The domain V is enclosed by the surface A_∞ placed at infinity and it comprises the region outside the closed surface A_d up to infinity surrounding the internal domain V_a. Within V, infinitesimally thin conducting surfaces A_c are allowed to exist, on

[1] The Huygens' principle states that each point on a primary wavefront can be considered to be a source of a new secondary spherical wave and that a secondary wavefront can be constructed as the envelope of these secondary spherical waves [27].

[2] According to uniqueness theorem, a field in a lossy region is uniquely defined by the sources within the region plus the tangential components of the electric field over the boundary, or the tangential components of the magnetic field over the boundary, or the former over part of the boundary and the latter over the rest of the boundary [27]. The above statement remains the same for lossless regions, if the frequency is not equal to the resonant frequency of the region surrounded by the boundary surface. Otherwise, the derivative of the tangential components of the field over the boundary with respect to the frequency should also be given in order to obtain the unique field [92].

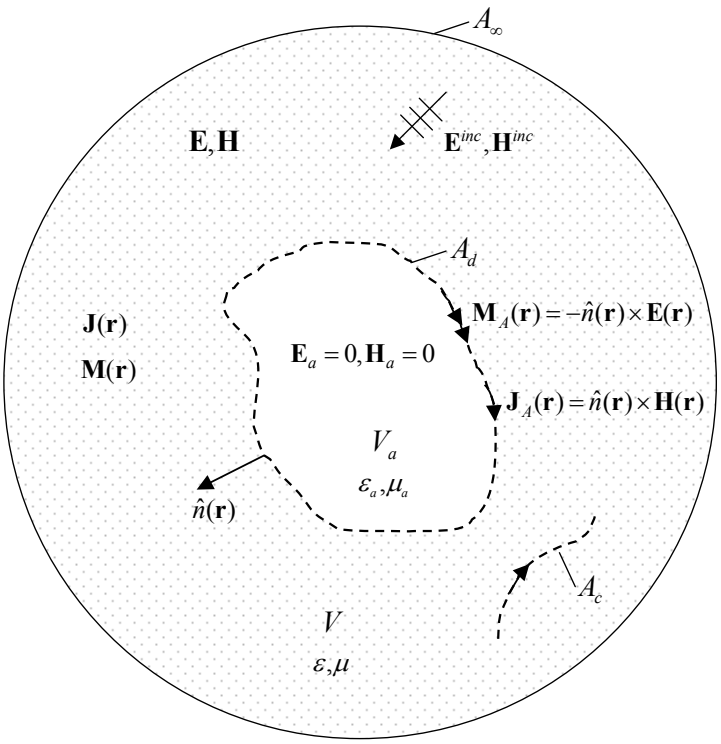

Figure 2.1: The equivalence principle.

which abrupt changes on the material properties of V are introduced. Thus, the boundary surface A enclosing the domain V consists of the closed surface A_d, the conducting surface A_c, and the surface A_∞ placed at infinity as shown in Fig. 2.1, thus $A \rightarrow A_d + A_c + A_\infty$. The fields of the original problem in the solution domain V surrounded by the boundary surface A are denoted by $\mathbf{E}, \mathbf{H}$. In the equivalent problem, the boundary surface A is replaced by source current densities, which produce under the absence of the boundary surface the same fields $\mathbf{E}, \mathbf{H}$ within the solution domain V. In addition, the fields within the internal domain V_a are zero ($\mathbf{E}_a = 0, \mathbf{H}_a = 0$) and the whole internal region V_a can be filled with the same material ε, μ as the solution domain to make the whole space homogeneous. Starting from Maxwell's equations for the particular configuration, the essential expressions of the equivalent current densities on the boundary surface are derived and the results are fully conformal to uniqueness theorem. In the following, the derivation is given for a source free ($\mathbf{J} = 0, \mathbf{M} = 0$) region V. Detailed derivation of the equivalence principle equations for the general case of impressed current densities $\mathbf{J}, \mathbf{M}$ within V is given in [37].

The fields within the solution domain V satisfy Maxwell's equations (2.9)-(2.12), which are reduced for the source free ($\varrho_e = 0, \mathbf{J} = 0, \varrho_m = 0, \mathbf{M} = 0$) homogeneous ε, μ region to

$$\nabla \times \mathbf{E}(\mathbf{r}) = -j\omega\mu\mathbf{H}(\mathbf{r}), \tag{2.17}$$

$$\nabla \times \mathbf{H}(\mathbf{r}) = j\omega\varepsilon\mathbf{E}(\mathbf{r}), \tag{2.18}$$

$$\nabla \cdot \varepsilon\mathbf{E}(\mathbf{r}) = 0, \tag{2.19}$$

$$\nabla \cdot \mu\mathbf{H}(\mathbf{r}) = 0. \tag{2.20}$$

Further, auxiliary fields $\mathbf{E}_g(\mathbf{r}), \mathbf{H}_g(\mathbf{r})$ are defined, which are field responses of electric and magnetic point sources placed at $\mathbf{r}'$ with amplitudes c_e and c_m, respectively. These fields

also satisfy Maxwell's curl equations (2.9) and (2.10) within V, which are written in this case as

$$\nabla \times \mathbf{E}_g(\mathbf{r}) = -j\omega\mu\mathbf{H}_g(\mathbf{r}) - c_m\hat{e}_m\delta(\mathbf{r}-\mathbf{r}'), \tag{2.21}$$
$$\nabla \times \mathbf{H}_g(\mathbf{r}) = j\omega\varepsilon\mathbf{E}_g(\mathbf{r}) - c_e\hat{e}_e\delta(\mathbf{r}-\mathbf{r}'). \tag{2.22}$$

Taking the dot product of (2.22) with $\mathbf{E}$, of (2.17) with $\mathbf{H}_g$, of (2.21) with $\mathbf{H}$, of (2.18) with $\mathbf{E}_g$ and subtracting the resulting equations we get

$$\nabla \cdot \big[\mathbf{H}(\mathbf{r}) \times \mathbf{E}_g(\mathbf{r}) - \mathbf{H}_g(\mathbf{r}) \times \mathbf{E}(\mathbf{r})\big] = c_m\mathbf{H}(\mathbf{r}) \cdot \hat{e}_m\delta(\mathbf{r}-\mathbf{r}') - c_e\mathbf{E}(\mathbf{r}) \cdot \hat{e}_e\delta(\mathbf{r}-\mathbf{r}'). \tag{2.23}$$

Now, the Gauss's theorem is applied to equation (2.23) for the solution domain V excepting points on the conducting surface A_c, over which we find abrupt changes of the material properties. The resulting integral contributions over A_c are zero as described in [91]. It is also assumed, that the point sources at $\mathbf{r}'$ lie within V, except on the boundary surface A. Applying Gauss's theorem to equation (2.23) for this domain results for $c_m = 0$ and $c_e = 1$ to

$$\mathbf{E}(\mathbf{r}') \cdot \hat{e}_e = \oiint_A \big[\hat{n}(\mathbf{r}) \times \mathbf{H}(\mathbf{r}) \cdot \mathbf{E}_{g_e}(\mathbf{r}) - \mathbf{H}_{g_e}(\mathbf{r}) \cdot \mathbf{E}(\mathbf{r}) \times \hat{n}(\mathbf{r})\big] da, \tag{2.24}$$

with

$$\mathbf{E}_{g_e}(\mathbf{r}) = \bar{\mathbf{G}}_J^E(\mathbf{r},\mathbf{r}') \cdot \hat{e}_e, \tag{2.25}$$
$$\mathbf{H}_{g_e}(\mathbf{r}) = \bar{\mathbf{G}}_J^H(\mathbf{r},\mathbf{r}') \cdot \hat{e}_e, \tag{2.26}$$

and for $c_m = 1$ and $c_e = 0$ to

$$-\mathbf{H}(\mathbf{r}') \cdot \hat{e}_m = \oiint_A \big[\hat{n}(\mathbf{r}) \times \mathbf{H}(\mathbf{r}) \cdot \mathbf{E}_{g_m}(\mathbf{r}) - \mathbf{H}_{g_m}(\mathbf{r}) \cdot \mathbf{E}(\mathbf{r}) \times \hat{n}(\mathbf{r})\big] da, \tag{2.27}$$

with

$$\mathbf{E}_{g_m}(\mathbf{r}) = \bar{\mathbf{G}}_M^E(\mathbf{r},\mathbf{r}') \cdot \hat{e}_m, \tag{2.28}$$
$$\mathbf{H}_{g_m}(\mathbf{r}) = \bar{\mathbf{G}}_M^H(\mathbf{r},\mathbf{r}') \cdot \hat{e}_m. \tag{2.29}$$

Thereby, $\hat{n}(\mathbf{r})$ is the outward normal unit vector on A_d and $\bar{\mathbf{G}}_{J/M}^{E/H}(\mathbf{r},\mathbf{r}')$ are the Green's functions within V of the electric or magnetic field due to electric and magnetic point sources, respectively, which are solutions of the wave equations

$$\nabla \times \mu^{-1}\nabla \times \bar{\mathbf{G}}_J^{E/H}(\mathbf{r},\mathbf{r}') - \omega^2\varepsilon\bar{\mathbf{G}}_J^{E/H}(\mathbf{r},\mathbf{r}') = -j\omega\,\bar{\mathbf{I}}\delta(\mathbf{r}-\mathbf{r}'), \tag{2.30}$$
$$\nabla \times \mu^{-1}\nabla \times \bar{\mathbf{G}}_M^{E/H}(\mathbf{r},\mathbf{r}') - \omega^2\varepsilon\bar{\mathbf{G}}_M^{E/H}(\mathbf{r},\mathbf{r}') = -j\nabla \times\, \bar{\mathbf{I}}\delta(\mathbf{r}-\mathbf{r}'). \tag{2.31}$$

The above wave equations are obtained using (2.21) and (2.22) and following the procedure of Section 2.1.1. In free space regions, the solutions of (2.30) and (2.31) are given by

$$\bar{\mathbf{G}}_J^E(\mathbf{r},\mathbf{r}') = \frac{\mu}{\varepsilon}\bar{\mathbf{G}}_M^H(\mathbf{r},\mathbf{r}') = -j\frac{\omega\mu}{4\pi}\left(\bar{\mathbf{I}} + \frac{1}{k^2}\nabla\nabla'\right)\frac{\mathrm{e}^{-jk|\mathbf{r}-\mathbf{r}'|}}{|\mathbf{r}-\mathbf{r}'|}, \tag{2.32}$$
$$\bar{\mathbf{G}}_M^E(\mathbf{r},\mathbf{r}') = -\bar{\mathbf{G}}_J^H(\mathbf{r},\mathbf{r}') = -\frac{1}{4\pi}\nabla \times\, \bar{\mathbf{I}}\frac{\mathrm{e}^{-jk|\mathbf{r}-\mathbf{r}'|}}{|\mathbf{r}-\mathbf{r}'|}, \tag{2.33}$$

where

$$G(\mathbf{r},\mathbf{r}') = \frac{\mathrm{e}^{-jk|\mathbf{r}-\mathbf{r}'|}}{|\mathbf{r}-\mathbf{r}'|} \tag{2.34}$$

is the scalar Green's function of free space. Substituting (2.25) and (2.26) into (2.24) as well as (2.28) and (2.29) into (2.27) using $\bar{\mathbf{G}}_M^E(\mathbf{r}',\mathbf{r}) = -\bar{\mathbf{G}}_J^H(\mathbf{r},\mathbf{r}')$ and $\bar{\mathbf{G}}_J^E(\mathbf{r}',\mathbf{r}) = \bar{\mathbf{G}}_J^E(\mathbf{r},\mathbf{r}')$ after changing primed and unprimed coordinates we finally get

$$\mathbf{E}(\mathbf{r}) = \iint_A \bar{\mathbf{G}}_J^E(\mathbf{r},\mathbf{r}')\cdot\mathbf{J}_A(\mathbf{r}')da' + \iint_A \bar{\mathbf{G}}_M^E(\mathbf{r},\mathbf{r}')\cdot\mathbf{M}_A(\mathbf{r}')da', \tag{2.35}$$

$$\mathbf{H}(\mathbf{r}) = \iint_A \bar{\mathbf{G}}_J^H(\mathbf{r},\mathbf{r}')\cdot\mathbf{J}_A(\mathbf{r}')da' + \iint_A \bar{\mathbf{G}}_M^H(\mathbf{r},\mathbf{r}')\cdot\mathbf{M}_A(\mathbf{r}')da', \tag{2.36}$$

with $\mathbf{r}\in V$. Thereby, $\mathbf{r}'$ stands for the source point position vector and $\mathbf{r}$ for the position vector of the observation point within V. It is noticed, that the fields at infinity satisfy the Sommerfeld radiation condition, so that the integration over A_∞ in (2.35) and (2.36) returns zero. In the general case of impressed current densities $\mathbf{J},\mathbf{M}$ within V the resulting equations for the equivalence principle are

$$\mathbf{E}(\mathbf{r}) = \iint_A \bar{\mathbf{G}}_J^E(\mathbf{r},\mathbf{r}')\cdot\mathbf{J}_A(\mathbf{r}')da' + \iint_A \bar{\mathbf{G}}_M^E(\mathbf{r},\mathbf{r}')\cdot\mathbf{M}_A(\mathbf{r}')da' + \mathbf{E}^{inc}(\mathbf{r}), \tag{2.37}$$

$$\mathbf{H}(\mathbf{r}) = \iint_A \bar{\mathbf{G}}_J^H(\mathbf{r},\mathbf{r}')\cdot\mathbf{J}_A(\mathbf{r}')da' + \iint_A \bar{\mathbf{G}}_M^H(\mathbf{r},\mathbf{r}')\cdot\mathbf{M}_A(\mathbf{r}')da' + \mathbf{H}^{inc}(\mathbf{r}), \tag{2.38}$$

where the incident fields $\mathbf{E}^{inc}(\mathbf{r}),\mathbf{H}^{inc}(\mathbf{r})$ represent in short form volume integration over V of the impressed current densities [37]. In the above expressions,

$$\mathbf{J}_A(\mathbf{r}') = \hat{n}(\mathbf{r}')\times\mathbf{H}(\mathbf{r}'), \tag{2.39}$$

$$\mathbf{M}_A(\mathbf{r}') = -\hat{n}(\mathbf{r}')\times\mathbf{E}(\mathbf{r}') \tag{2.40}$$

are the *equivalent surface currents* with $\mathbf{r}'\in A$ representing tangential field components on the boundary surface A.

The equations (2.37)-(2.40) represent the formal expressions of the *equivalence principle*. According to them, integration of the equivalent currents over the boundary surface A together with the incident excitation field gives the exact electromagnetic fields everywhere in the considered solution domain. This result is fully conformal to the uniqueness theorem. Detailed derivation and proof of the equivalence principle for inhomogeneous bianisotropic media can be found in [91]. The equivalence principle can be formulated in the same way for the internal domain V_a enclosed by surface A_d. In this case, the external domain is free of fields and it can be filled with the same material as the internal domain. For general configurations, where fields exist in all domains of Fig. 2.1, the equivalence principle is similarly formulated by additionally taking into account transition conditions over the closed surface A_d [87].

The equivalence principle can alternatively be expressed using electromagnetic potentials. This issue will be discussed in the following subsection.

2.1.3 Equivalence Principle Formulation Using Electromagnetic Potentials

According to potential theory in electromagnetics, fields can be expressed by superposition of independent terms due to electromagnetic vector and scalar potentials. Among many engineers, the vector potentials are strictly mathematical tools in electromagnetics and they do not have any physical meaning [93], in contrast to the scalar electrostatic potential, which is closely related to the required work for moving the positive unit of electric charge between two points within an electrostatic field. The electromagnetic potentials are determined from conditions imposed directly from Maxwell's equations resulting in an exact field representation in the desired solution domain.

Within a region, which is free of magnetic sources ($\varrho_m = 0, \mathbf{M} = 0$), the magnetic flux $\mathbf{B} = \mu\mathbf{H}$ is divergenceless, or solenoidal, as imposed by Maxwell's divergence equation (2.20). Since the divergence of the curl of a vector is by identity (2.16) zero, the magnetic flux is expressed by the rotation of the *magnetic vector potential* $\mathbf{A}$ according to

$$\mathbf{B}(\mathbf{r}) = \mu\mathbf{H}(\mathbf{r}) = \nabla \times \mathbf{A}(\mathbf{r}), \tag{2.41}$$

where $\mathbf{r}$ is the observation point within the considered domain. So, the magnetic field due to $\mathbf{A}$ is given by

$$\mathbf{H}_A(\mathbf{r}) = \frac{1}{\mu}\nabla \times \mathbf{A}(\mathbf{r}). \tag{2.42}$$

Substituting (2.42) into the Maxwell's curl equation (2.17) we get

$$\nabla \times \big[\mathbf{E}(\mathbf{r}) + j\omega\mathbf{A}(\mathbf{r})\big] = 0. \tag{2.43}$$

Now, using the vector identity

$$\nabla \times \nabla\varphi = 0, \tag{2.44}$$

which states that the curl of the gradient of any scalar function is always zero, we can write (2.43) as

$$\mathbf{E}(\mathbf{r}) = -j\omega\mathbf{A}(\mathbf{r}) - \nabla\varphi_e(\mathbf{r}), \tag{2.45}$$

using the *electric scalar potential* φ_e. The rotation of $\mathbf{A}$ is defined in (2.41) and we are free to define the divergence of $\mathbf{A}$, which is independent of its rotation. That way, the vector potential $\mathbf{A}$ is uniquely defined according to Helmholtz theorem[3]. This is done by the Lorentz gauge condition

$$\nabla \cdot \mathbf{A}(\mathbf{r}) = -j\omega\varepsilon\mu\varphi_e(\mathbf{r}). \tag{2.46}$$

So, the electric field due to $\mathbf{A}$ is given by

$$\mathbf{E}_A(\mathbf{r}) = -j\omega\mathbf{A}(\mathbf{r}) - \nabla\varphi_e(\mathbf{r}) = -j\omega\mathbf{A}(\mathbf{r}) - j\frac{1}{\omega\varepsilon\mu}\nabla\big[\nabla \cdot \mathbf{A}(\mathbf{r})\big]. \tag{2.47}$$

[3]The Helmholtz theorem states that any vector field is uniquely defined if its divergence and its rotation are properly given.

Similarly, within a region free of electric sources ($\varrho_e = 0, \mathbf{J} = 0$), the electric flux $\mathbf{D} = \varepsilon\mathbf{E}$ is solenoidal, as imposed by Maxwell's divergence equation (2.19). In this case, the electric flux is expressed by the rotation of the *electric vector potential* $\mathbf{F}$ according to

$$\mathbf{D}(\mathbf{r}) = \varepsilon\mathbf{E}(\mathbf{r}) = -\nabla \times \mathbf{F}(\mathbf{r}). \tag{2.48}$$

The divergence of $\mathbf{F}$ is defined by the condition

$$\nabla \cdot \mathbf{F}(\mathbf{r}) = -j\omega\varepsilon\mu\varphi_m(\mathbf{r}), \tag{2.49}$$

using the *magnetic scalar potential* φ_m. Thus, the electric and magnetic fields due to $\mathbf{F}$ are given by

$$\mathbf{E}_F(\mathbf{r}) = -\frac{1}{\varepsilon}\nabla \times \mathbf{F}(\mathbf{r}) \tag{2.50}$$

and

$$\mathbf{H}_F(\mathbf{r}) = -j\omega\mathbf{F}(\mathbf{r}) - \nabla\varphi_m(\mathbf{r}) = -j\omega\mathbf{F}(\mathbf{r}) - j\frac{1}{\omega\varepsilon\mu}\nabla\big[\nabla \cdot \mathbf{F}(\mathbf{r})\big], \tag{2.51}$$

respectively.

The total electromagnetic fields within the considered domain are given by superposition of the field terms (2.42), (2.47) due to $\mathbf{A}$ and the field terms (2.50), (2.51) due to $\mathbf{F}$. This finally results in the mixed potential field expressions

$$\mathbf{E}(\mathbf{r}) = -j\omega\mathbf{A}(\mathbf{r}) - j\frac{1}{\omega\varepsilon\mu}\nabla\big[\nabla \cdot \mathbf{A}(\mathbf{r})\big] - \frac{1}{\varepsilon}\nabla \times \mathbf{F}(\mathbf{r}),$$
$$\mathbf{H}(\mathbf{r}) = -j\omega\mathbf{F}(\mathbf{r}) - j\frac{1}{\omega\varepsilon\mu}\nabla\big[\nabla \cdot \mathbf{F}(\mathbf{r})\big] + \frac{1}{\mu}\nabla \times \mathbf{A}(\mathbf{r}),$$

or

$$\mathbf{E}(\mathbf{r}) = -j\omega\mathbf{A}(\mathbf{r}) - \nabla\varphi_e(\mathbf{r}) - \frac{1}{\varepsilon}\nabla \times \mathbf{F}(\mathbf{r}), \tag{2.52}$$

$$\mathbf{H}(\mathbf{r}) = -j\omega\mathbf{F}(\mathbf{r}) - \nabla\varphi_m(\mathbf{r}) + \frac{1}{\mu}\nabla \times \mathbf{A}(\mathbf{r}). \tag{2.53}$$

The equivalence principle given in (2.37)-(2.40) for the solution region V can alternatively be expressed using electromagnetic potentials. Substituting the Green's functions (2.32)-(2.34) into the expressions (2.37) and (2.38) and applying the identity $\bar{\mathbf{I}} \cdot f\mathbf{A} = f\mathbf{A} \cdot \bar{\mathbf{I}} = f\mathbf{A}$ as well as using the vector identity $\nabla \times f\mathbf{A} = f\nabla \times \mathbf{A} + \nabla f \times \mathbf{A}$ with $\nabla \times \mathbf{J}(\mathbf{r}') = \nabla \times \mathbf{M}(\mathbf{r}') = 0$, since in the third term of the right hand side of the above equations the curl operator is applied to the surface current densities with respect to unprimed coordinates, we finally get for the equivalence principle the formulations

$$\begin{aligned}\mathbf{E}(\mathbf{r}) = &- j\frac{\omega\mu}{4\pi}\iint_A G(\mathbf{r},\mathbf{r}')\mathbf{J}_A(\mathbf{r}')da' - j\frac{1}{4\pi\omega\varepsilon}\nabla\iint_A G(\mathbf{r},\mathbf{r}')\nabla'_A \cdot \mathbf{J}_A(\mathbf{r}')da' \\ &- \frac{1}{4\pi}\iint_A \nabla G(\mathbf{r},\mathbf{r}') \times \mathbf{M}_A(\mathbf{r}')da' + \mathbf{E}^{inc}(\mathbf{r}), \qquad \forall\, \mathbf{r} \in V,\end{aligned} \tag{2.54}$$

$$\begin{aligned}\mathbf{H}(\mathbf{r}) = &- j\frac{\omega\varepsilon}{4\pi}\iint_A G(\mathbf{r},\mathbf{r}')\mathbf{M}_A(\mathbf{r}')da' - j\frac{1}{4\pi\omega\mu}\nabla\iint_A G(\mathbf{r},\mathbf{r}')\nabla'_A \cdot \mathbf{M}_A(\mathbf{r}')da' \\ &+ \frac{1}{4\pi}\iint_A \nabla G(\mathbf{r},\mathbf{r}') \times \mathbf{J}_A(\mathbf{r}')da' + \mathbf{H}^{inc}(\mathbf{r}), \qquad \forall\, \mathbf{r} \in V.\end{aligned} \tag{2.55}$$

Thereby, $\nabla'_A\cdot$ is the surface component of the divergence operator applied to the surface currents with respect to primed coordinates. Also, the equivalent surface current densities $\mathbf{J}_A(\mathbf{r}')$ and $\mathbf{M}_A(\mathbf{r}')$ on the boundary surface A are given in (2.39) and (2.40), respectively. Comparing the equivalence principle formulations in (2.54) and (2.55) with the mixed potential field expressions in (2.52) and (2.53), respectively, we observe that these are identical for vector potentials given by

$$\mathbf{A}(\mathbf{r}) = \frac{\mu}{4\pi}\iint\limits_A G(\mathbf{r},\mathbf{r}')\mathbf{J}_A(\mathbf{r}')da', \tag{2.56}$$

$$\mathbf{F}(\mathbf{r}) = \frac{\varepsilon}{4\pi}\iint\limits_A G(\mathbf{r},\mathbf{r}')\mathbf{M}_A(\mathbf{r}')da' \tag{2.57}$$

and for scalar potentials given by

$$\varphi_e(\mathbf{r}) = \frac{j}{4\pi\omega\varepsilon}\iint\limits_A G(\mathbf{r},\mathbf{r}')\nabla'_A\cdot\mathbf{J}_A(\mathbf{r}')da', \tag{2.58}$$

$$\varphi_m(\mathbf{r}) = \frac{j}{4\pi\omega\mu}\iint\limits_A G(\mathbf{r},\mathbf{r}')\nabla'_A\cdot\mathbf{M}_A(\mathbf{r}')da', \tag{2.59}$$

which are connected to the corresponding equivalent surface charges $\varrho^e_A(\mathbf{r}')$ and $\varrho^m_A(\mathbf{r}')$ on A through the continuity equations (2.5) and (2.6), respectively, according to

$$\varphi_e(\mathbf{r}) = \frac{1}{4\pi\varepsilon}\iint\limits_A G(\mathbf{r},\mathbf{r}')\varrho^e_A(\mathbf{r}')da', \tag{2.60}$$

$$\varphi_m(\mathbf{r}) = \frac{1}{4\pi\mu}\iint\limits_A G(\mathbf{r},\mathbf{r}')\varrho^m_A(\mathbf{r}')da'. \tag{2.61}$$

It is noticed, that the mixed potential formulation of the equivalence principle according to (2.52)-(2.53) and (2.56)-(2.59) corresponds to the originally introduced equivalence principle by Schelkunoff [88].

The equivalence principle formulation using electromagnetic potentials is used to provide field expressions in the Boundary Integral Method as it will be described in the following section.

2.2 The Boundary Integral Method

The *Boundary Integral Method* (BIM) is a global numerical modeling technique for the solution of Boundary Value Problems (BVPs). These kind of problems are formulated in general using differential or integral operators in a specific domain together with appropriate boundary or transition conditions on the boundaries of the domain. In this particular case, the BVP is formulated with surface integrals over the boundaries of the involved objects using equivalent surface current densities according to equivalence principle. Placing observation points on the boundaries of the objects and considering tangential field components on the

boundary surfaces, the surface integral expressions are transformed into Surface Integral Equations (SIEs), whose solution gives the unknown equivalent surface current densities all over the boundary surfaces. These equivalent currents are sources for the scattered field in the solution domain everywhere outside (or inside) the boundary surfaces. In the present work, surface integral representation using electromagnetic potentials is applied resulting in Mixed Potential Integral Equations (MPIEs). These Integral Equations (IEs) are solved by the Method of Moments (MoM) expanding the unknown surface currents in terms of appropriate basis functions on discrete surface elements and using Galerkin's testing. The basic concepts of derivation and solutions of the IEs according to BIM will be described more in detail in the following subsections.

2.2.1 Integral Equations

The surface integral expressions (2.54) and (2.55) give the exact electromagnetic fields for observation points in V in terms of the equivalent surface current densities (2.39) and (2.40). However, for a given configuration the equivalent current densities are in general unknown vector functions and they must be computed in the first place to obtain a field solution. For this purpose, an MPIE for the unknown surface currents is formulated starting from the field expressions (2.54) and (2.55). The IE is obtained by placing the observation points on the boundary surface A and considering tangential field components on A.

In order to formulate the IE, it must be guaranteed, that the field expressions (2.54) and (2.55) remain valid for observation points placed on the boundary surface A, since the original derivation requires $\mathbf{r}$ to be inside of V and the Green's function (2.34) becomes singular according to

$$G(\mathbf{r},\mathbf{r}') \sim \frac{1}{|\mathbf{r}-\mathbf{r}'|} \to \infty, \quad \forall\, \mathbf{r}=\mathbf{r}'. \tag{2.62}$$

For this purpose, the boundary surface is deformed in the vicinity of the observation point using a hemispherical extension assuming that the boundary surface is a smooth surface. The integral contribution over the hemispherical surface is evaluated analytically for the limiting case of its radius going to zero, whereas the remaining integral contributions are taken into account in terms of Cauchy principle values. This procedure is described in detail in [37] and results in the expressions

$$\begin{aligned}\frac{1}{2}\mathbf{E}(\mathbf{r}) = &- j\frac{\omega\mu}{4\pi}\iint_A G(\mathbf{r},\mathbf{r}')\mathbf{J}_A(\mathbf{r}')da' - j\frac{1}{4\pi\omega\varepsilon}\nabla\iint_A G(\mathbf{r},\mathbf{r}')\nabla'_A\cdot\mathbf{J}_A(\mathbf{r}')da' \\ &- \frac{1}{4\pi}\iint_A \nabla G(\mathbf{r},\mathbf{r}')\times\mathbf{M}_A(\mathbf{r}')da' + \mathbf{E}^{inc}(\mathbf{r}), \qquad \forall\,\mathbf{r}\in A, \end{aligned}\tag{2.63}$$

$$\begin{aligned}\frac{1}{2}\mathbf{H}(\mathbf{r}) = &- j\frac{\omega\varepsilon}{4\pi}\iint_A G(\mathbf{r},\mathbf{r}')\mathbf{M}_A(\mathbf{r}')da' - j\frac{1}{4\pi\omega\mu}\nabla\iint_A G(\mathbf{r},\mathbf{r}')\nabla'_A\cdot\mathbf{M}_A(\mathbf{r}')da' \\ &+ \frac{1}{4\pi}\iint_A \nabla G(\mathbf{r},\mathbf{r}')\times\mathbf{J}_A(\mathbf{r}')da' + \mathbf{H}^{inc}(\mathbf{r}), \qquad \forall\,\mathbf{r}\in A. \end{aligned}\tag{2.64}$$

Starting from the equivalence principle formulation for the electric field (2.63) assuming observation points placed on the boundary surface A and taking the $\hat{n}(\mathbf{r})\times\hat{n}(\mathbf{r})\times$ product

with equation (2.63) by considering tangential components on A along with using (2.40) for the left hand side we get

$$\begin{aligned}\frac{1}{2}\hat{n}(\mathbf{r})\times\mathbf{M}_A(\mathbf{r}) &= \hat{n}(\mathbf{r})\times\hat{n}(\mathbf{r})\times\Bigg\{j\frac{\omega\mu}{4\pi}\iint\limits_A G(\mathbf{r},\mathbf{r}')\mathbf{J}_A(\mathbf{r}')da' \\ &+ j\frac{1}{4\pi\omega\varepsilon}\nabla\iint\limits_A G(\mathbf{r},\mathbf{r}')\nabla'_A\cdot\mathbf{J}_A(\mathbf{r}')da' \\ &+ \frac{1}{4\pi}\iint\limits_A\nabla G(\mathbf{r},\mathbf{r}')\times\mathbf{M}_A(\mathbf{r}')da' - \mathbf{E}^{inc}(\mathbf{r})\Bigg\}, \qquad \forall\,\mathbf{r}\in A, \end{aligned} \tag{2.65}$$

where the surface integrals should be understood as principal values. The equation (2.65) is the *Electric Field Integral Equation* (EFIE) for the unknown surface current densities $\mathbf{J}_A(\mathbf{r}')$, $\mathbf{M}_A(\mathbf{r}')$. The EFIE given in (2.65) is only valid for tangential field components on A.

Similarly, starting from the equivalence principle formulation for the magnetic field (2.64) and taking the $\hat{n}(\mathbf{r})\times$ product with equation (2.64) along with using (2.39) for the left hand side we get

$$\begin{aligned}\frac{1}{2}\mathbf{J}_A(\mathbf{r}) &= \hat{n}(\mathbf{r})\times\Bigg\{-j\frac{\omega\varepsilon}{4\pi}\iint\limits_A G(\mathbf{r},\mathbf{r}')\mathbf{M}_A(\mathbf{r}')da' - j\frac{1}{4\pi\omega\mu}\nabla\iint\limits_A G(\mathbf{r},\mathbf{r}')\nabla'_A\cdot\mathbf{M}_A(\mathbf{r}')da' \\ &+ \frac{1}{4\pi}\iint\limits_A\nabla G(\mathbf{r},\mathbf{r}')\times\mathbf{J}_A(\mathbf{r}')da' + \mathbf{H}^{inc}(\mathbf{r})\Bigg\}, \qquad \forall\,\mathbf{r}\in A, \end{aligned} \tag{2.66}$$

where the surface integrals should be understood as principal values. The equation (2.66) is the *Magnetic Field Integral Equation* (MFIE) for the unknown surface current densities $\mathbf{J}_A(\mathbf{r}')$, $\mathbf{M}_A(\mathbf{r}')$.

A disadvantage of the above MPIEs is the problem of *interior resonances*. According to this, the IEs fail to produce accurate results near the frequencies, which correspond to the resonant frequencies of the cavity formed by covering the boundary surface A with a PEC surface after filling the interior domain V_a with the homogeneous material of the exterior region V [94]. In particular, for those resonant frequencies, the operators in the integral equations (2.65) and (2.66) become singular. This problem is overcome using the linear combination of EFIE and MFIE according to

$$Z(1-\alpha)MFIE - \alpha EFIE = 0, \tag{2.67}$$

where α is the combination parameter with values from 0 to 1 and

$$Z = \sqrt{\frac{\mu}{\varepsilon}} \tag{2.68}$$

is the wave impedance in the considered solution domain. The IE obtained by (2.67) is called *Combined Field Integral Equation* (CFIE) and it does not suffer from the problem of interior resonances [95]. An alternative approach to overcome the problem of interior resonances in SIEs is to introduce small losses in the propagation constant associated with

the SIE in order to move the resonant frequency away from the real frequency axis [96]. However, for efficient elimination of interior resonances in particular problems high losses may be needed resulting in strong modification from the original configuration. Further, using the augmented electric and magnetic field integral equations introduced in [97], additional normal field components are considered in the formulations providing an alternative remedy to this issue. Finally, according to the Parasitic Body Technique (PBT) introduced in [98], a parasitic lossy body is considered in the internal domain V_a, which interacts only with the resonant fields attenuating them without influencing the field distribution in the exterior region V.

2.2.2 Solution of the Integral Equations

In order to solve the IEs, the boundary surface A is discretized with surface elements and the unknown current densities are expanded in terms of appropriate basis functions with unknown expansion coefficients on the discrete surface elements. After that, applying appropriate testing approaches, the integral equation is transformed into its algebraic analog system of equations, whose solution finally gives the unknown current expansion coefficients. This approach for solving integral equations in electromagnetics is in general known as method of moments [18].

In particular, the boundary surface A is discretized with triangles. The numbering of nodes, edges and edge vectors is performed according to Fig. 2.2 a). Each triangle element has three degrees of freedom associated to its edges, whereas the degrees of freedom are shared between adjacent triangle elements. Hence, discretizing the boundary surface A with M triangle elements assuming that A is a closed surface results in $N = 1.5M$ total degrees of freedom on A, since each degree of freedom is shared by two triangle elements. For open surfaces the degrees of freedom are slightly less, since currents normal to free edges of the open surface are set to zero based on current transition conditions. Further, the unknown surface current densities are expanded in terms of Rao-Wilton-Glisson (RWG) basis functions according to

$$\mathbf{J}_A(\mathbf{r}) = \sum_{n=1}^{N} H_n \boldsymbol{\beta}_n(\mathbf{r}), \tag{2.69}$$

$$\mathbf{M}_A(\mathbf{r}) = -\sum_{n=1}^{N} E_n \boldsymbol{\beta}_n(\mathbf{r}), \tag{2.70}$$

where H_n, E_n are the unknown coefficients of the expansion of electric and magnetic currents on the discrete surface triangles corresponding to unknown tangential magnetic and electric fields, respectively. Also, N is the number of surface edges. The RWG basis functions $\boldsymbol{\beta}_n(\mathbf{r})$ enforce normal continuity of the currents on triangular common edges as shown in Fig. 2.2 b) and they are the triangular rooftop functions introduced in [19]. According to this, each basis function is defined on the common edge j of two adjacent triangles by

$$\boldsymbol{\beta}_j(\mathbf{r}) = \mp \frac{\mathbf{r} - \mathbf{r}_{4-j}}{2A_T} \left[\hat{n}_A \cdot \hat{n}(\mathbf{r})\right] \begin{cases} -, \; j = 1,3 \\ +, \; j = 2 \end{cases} . \tag{2.71}$$

Thereby, $\mathbf{r}_{4-j}$ are the position vectors of the triangle vertices, A_T is the surface of the triangle element and $\hat{n}_A$ is the normal unit vector on the particular triangle. It can be seen,

that the RWG functions have a constant normal and a linear tangential component on the common edge as shown in Fig. 2.2 b) and they are also referred to as Constant Normal Linear Tangential (CNLT) elements [99]. Further, RWG basis functions have constant divergence on the corresponding triangular element with zero total charge associated with the triangle pair and they represent *divergence conforming* basis functions.

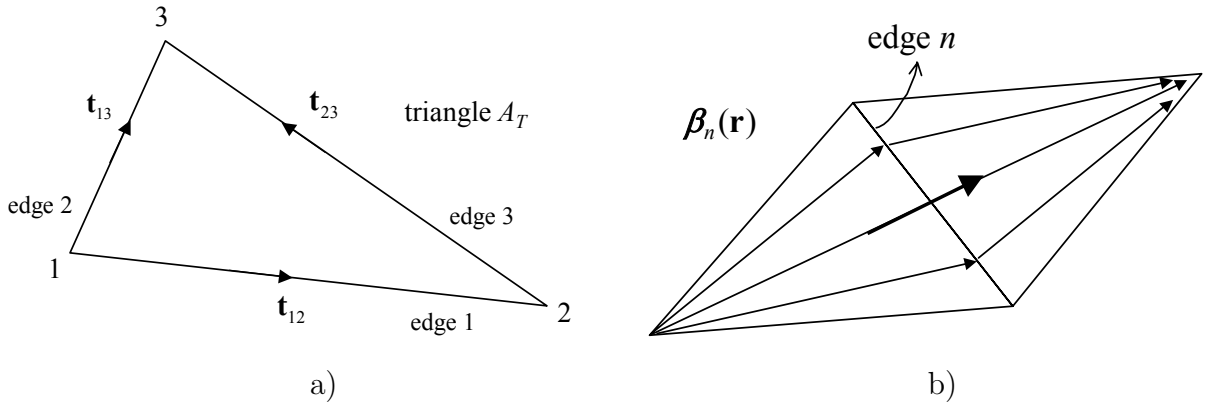

Figure 2.2: a) Discrete triangle surface element. b) RWG basis functions.

The final step of the IE solution by MoM is to perform the testing procedure by multiplying the IEs with appropriate testing functions on the same triangular mesh and integrating over the corresponding testing elements. In Galerkin's testing, the same functions (2.71) are used for testing as the basis functions used for current expansions. So, for each testing function, one equation is obtained for all expansion functions containing the total reaction of the source currents on the particular testing current according to the integral formulation given in (2.65), (2.66), and (2.67). Repeating this procedure for all testing functions results in a linear system of equations.

EFIE

Applying the MoM with Galerkin's testing to the EFIE (2.65) for testing points $\mathbf{r} = \mathbf{r}_m$ and source points $\mathbf{r}' = \mathbf{r}_n$ on the boundary surface A results in

$$
\begin{aligned}
&\frac{1}{2}\sum_{n=1}^{N} E_n \iint\limits_{A} \boldsymbol{\beta}_m(\mathbf{r}_m)\cdot\left[\boldsymbol{\beta}_n(\mathbf{r}_n)\times\hat{n}(\mathbf{r}_m)\right]da \\
&+j\frac{\omega\mu}{4\pi}\sum_{n=1}^{N} H_n \left\{\iint\limits_{A}\boldsymbol{\beta}_m(\mathbf{r}_m)\cdot\left[\iint\limits_{A'} G(\mathbf{r}_m,\mathbf{r}_n)\boldsymbol{\beta}_n(\mathbf{r}_n)da'\right]da\right\} \\
&+j\frac{1}{4\pi\omega\varepsilon}\sum_{n=1}^{N} H_n \left\{\iint\limits_{A}\nabla_A\cdot\boldsymbol{\beta}_m(\mathbf{r}_m)\left[\iint\limits_{A'} G(\mathbf{r}_m,\mathbf{r}_n)\nabla'_A\cdot\boldsymbol{\beta}_n(\mathbf{r}_n)da'\right]da\right\} \\
&+\frac{1}{4\pi}\sum_{n=1}^{N} E_n \left\{\iint\limits_{A}\boldsymbol{\beta}_m(\mathbf{r}_m)\cdot\left[\iint\limits_{A'}\nabla G(\mathbf{r}_m,\mathbf{r}_n)\times\boldsymbol{\beta}_n(\mathbf{r}_n)da'\right]da\right\} \\
&\quad=\iint\limits_{A}\boldsymbol{\beta}_m(\mathbf{r}_m)\cdot\mathbf{E}^{inc}(\mathbf{r}_m)da, \qquad \forall\ \mathbf{r}_m,\mathbf{r}_n\in A,
\end{aligned}
\tag{2.72}
$$

where m, n are the testing and source edge, respectively, with $m = 1, 2, \ldots, N$. The surface divergence of the RWG basis functions is given in [19] and the gradient of the free space scalar Green's function is equal to

$$\nabla G(\mathbf{r}_m, \mathbf{r}_n) = -\left(\frac{1}{R} + jk\right) G(\mathbf{r}_m, \mathbf{r}_n)\hat{e}_R = -\nabla' G(\mathbf{r}_m, \mathbf{r}_n) \tag{2.73}$$

with

$$R = |\mathbf{r}_m - \mathbf{r}_n| \tag{2.74}$$

being the distance between source and testing point in the direction of $\hat{e}_R = \frac{\mathbf{r}_m - \mathbf{r}_n}{|\mathbf{r}_m - \mathbf{r}_n|}$. The elements of equation (2.72) are given in matrix form in the Appendix B.1. It is noticed, that the expression in (2.72) of the form

$$\iint_A \boldsymbol{\beta}(\mathbf{r}_m) \cdot \mathbf{E}^{inc}(\mathbf{r}_m) da$$

can be understood, from the mathematical point of view, as the moment of the exciting incident vector field $\mathbf{E}^{inc}(\mathbf{r}_m)$ around the weighting function $\boldsymbol{\beta}(\mathbf{r}_m)$. This is typical for discrete solution of integral equations in electromagnetics by method of moments.

MFIE

Similarly, applying the MoM with Galerkin's testing to the MFIE (2.66) results in

$$\begin{aligned}
&\frac{1}{2}\sum_{n=1}^{N} H_n \iint_A \boldsymbol{\beta}_m(\mathbf{r}_m) \cdot \boldsymbol{\beta}_n(\mathbf{r}_n) da \\
&+ j\frac{\omega\varepsilon}{4\pi}\sum_{n=1}^{N} E_n \left\{ \iint_A \left[\hat{n}(\mathbf{r}_m) \times \boldsymbol{\beta}_m(\mathbf{r}_m)\right] \cdot \left[\iint_{A'} G(\mathbf{r}_m, \mathbf{r}_n)\boldsymbol{\beta}_n(\mathbf{r}_n) da' \right] da \right\} \\
&+ j\frac{1}{4\pi\omega\mu}\sum_{n=1}^{N} E_n \left\{ \iint_A \nabla_A \cdot \left[\hat{n}(\mathbf{r}_m) \times \boldsymbol{\beta}_m(\mathbf{r}_m)\right] \left[\iint_{A'} G(\mathbf{r}_m, \mathbf{r}_n)\nabla'_A \cdot \boldsymbol{\beta}_n(\mathbf{r}_n) da' \right] da \right\} \\
&- \frac{1}{4\pi}\sum_{n=1}^{N} H_n \left\{ \iint_A \left[\hat{n}(\mathbf{r}_m) \times \boldsymbol{\beta}_m(\mathbf{r}_m)\right] \cdot \left[\iint_{A'} \nabla G(\mathbf{r}_m, \mathbf{r}_n) \times \boldsymbol{\beta}_n(\mathbf{r}_n) da' \right] da \right\} \\
&\quad = \iint_A \left[\hat{n}(\mathbf{r}_m) \times \boldsymbol{\beta}_m(\mathbf{r}_m)\right] \cdot \mathbf{H}^{inc}(\mathbf{r}_m) da, \qquad \forall\ \mathbf{r}_m, \mathbf{r}_n \in A,
\end{aligned} \tag{2.75}$$

with $m = 1, 2, \ldots, N$. The elements of equation (2.75) are given in matrix form in the Appendix B.2.

CFIE

Obviously, solution of CFIE is achieved by applying (2.72) and (2.75) in the linear combination given in (2.67).

For successful solution of the above SIEs, accurate evaluation of singular potential integrals is an essential task. This issue will be discussed in the following subsection.

2.2.3 Treatment of Singular Integrals

The situation of singular potential integrals applies if the testing point $\mathbf{r}_m$ comes near the source point $\mathbf{r}_n$. In this case, the surface potential integral kernels become singular due to the involved free space Green's function because of (2.62). By looking at the EFIE and MFIE formulations in (2.72) and (2.75), respectively, integral kernels with singularities of order $1/R$ and $\nabla(1/R)$ must be considered, where R is the distance between source and testing point given in (2.74). In particular, for the EFIE part the integrals

$$I_1^{EFIE} = \iint\limits_A \boldsymbol{\beta}_m(\mathbf{r}_m) \cdot \big[\boldsymbol{\beta}_n(\mathbf{r}_n) \times \hat{n}(\mathbf{r}_m)\big] da, \tag{2.76}$$

$$I_2^{EFIE} = \iint\limits_A \boldsymbol{\beta}_m(\mathbf{r}_m) \cdot \left[\iint\limits_{A'} G(\mathbf{r}_m, \mathbf{r}_n) \boldsymbol{\beta}_n(\mathbf{r}_n) da' \right] da, \tag{2.77}$$

$$I_3^{EFIE} = \iint\limits_A \nabla_A \cdot \boldsymbol{\beta}_m(\mathbf{r}_m) \left[\iint\limits_{A'} G(\mathbf{r}_m, \mathbf{r}_n) \nabla'_A \cdot \boldsymbol{\beta}_n(\mathbf{r}_n) da' \right] da, \tag{2.78}$$

$$I_4^{EFIE} = \iint\limits_A \boldsymbol{\beta}_m(\mathbf{r}_m) \cdot \left[\iint\limits_{A'} \nabla G(\mathbf{r}_m, \mathbf{r}_n) \times \boldsymbol{\beta}_n(\mathbf{r}_n) da' \right] da \tag{2.79}$$

must be evaluated, whereas the MFIE part requires calculation of the integrals

$$I_1^{MFIE} = \iint\limits_A \boldsymbol{\beta}_m(\mathbf{r}_m) \cdot \boldsymbol{\beta}_n(\mathbf{r}_n) da, \tag{2.80}$$

$$I_2^{MFIE} = \iint\limits_A \big[\hat{n}(\mathbf{r}_m) \times \boldsymbol{\beta}_m(\mathbf{r}_m)\big] \cdot \left[\iint\limits_{A'} G(\mathbf{r}_m, \mathbf{r}_n) \boldsymbol{\beta}_n(\mathbf{r}_n) da' \right] da, \tag{2.81}$$

$$I_3^{MFIE} = \iint\limits_A \nabla_A \cdot \big[\hat{n}(\mathbf{r}_m) \times \boldsymbol{\beta}_m(\mathbf{r}_m)\big] \left[\iint\limits_{A'} G(\mathbf{r}_m, \mathbf{r}_n) \nabla'_A \cdot \boldsymbol{\beta}_n(\mathbf{r}_n) da' \right] da, \tag{2.82}$$

$$I_4^{MFIE} = \iint\limits_A \big[\hat{n}(\mathbf{r}_m) \times \boldsymbol{\beta}_m(\mathbf{r}_m)\big] \cdot \left[\iint\limits_{A'} \nabla G(\mathbf{r}_m, \mathbf{r}_n) \times \boldsymbol{\beta}_n(\mathbf{r}_n) da' \right] da. \tag{2.83}$$

The integrals I_1 for the EFIE and MFIE part are regular and they are evaluated analytically as described in [37]. The integrals I_2 and I_3 for the EFIE and MFIE parts contain in the integrand the Green's function and singularities of order $1/R$ must be considered when the observation point is near the source point. Finally, the integrals I_4 for the EFIE and MFIE parts contain in the integrand the gradient of the Green's function and singularities of order $\nabla(1/R) \to 1/R^2$ must be considered.

In this work, *singularity extraction method* is applied to overcome this problem [100], [101]. According to this, the surface integrals are regularized by extracting the singular static term from the Green's function as follows:

$$G(\mathbf{r}_m, \mathbf{r}_n) = \left(G(\mathbf{r}_m, \mathbf{r}_n) - \frac{1}{R} \right) + \frac{1}{R}. \tag{2.84}$$

Due to this, the gradient of the Green's function becomes

$$\nabla G(\mathbf{r}_m, \mathbf{r}_n) = \nabla \left(G(\mathbf{r}_m, \mathbf{r}_n) - \frac{1}{R} \right) + \nabla \frac{1}{R}. \tag{2.85}$$

The terms in parentheses of (2.84) and (2.85) are regular and the extracted term includes the singularity. Applying this extraction to the integrals I_2-I_4 for the EFIE and MFIE parts, the inner source integral of the singular extracted term can be calculated in any case in closed form in primed coordinates using the formulas in [101]-[103]. The remaining function is regular and the outer testing integral is calculated numerically in unprimed coordinates. Further, singular self-coupling terms of I_2^{EFIE} and I_3^{EFIE} can be calculated in closed form, if the test and source integrals coincide [102], [103].

Difficulties in this approach may arise due to the following two reasons: First, after extracting the singular term from the Green's function, the remaining function in the parentheses of (2.84) has a discontinuous derivative at $R = 0$. This discontinuity means that a straightforward application of a numerical integration routine for the testing integral may lead to an inaccurate solution. Second, difficulties may occur in the case of $\nabla(1/R)$ (integrals I_4 for EFIE and MFIE part), when the source and test triangles have common points and are not in the same plane. In particular, although it is possible in this case to calculate the inner source integral of the extracted singular term $\nabla(1/R)$ analytically using the formulas in [101], a logarithmic singularity still remains in the outer testing integral. Therefore, if higher accuracy is required, the testing integral cannot be calculated by a standard numerical calculation technique.

The above difficulties are avoided in the present thesis by applying the singularity treatment presented in [104]. In order to avoid the discontinuity of the remaining function in the parentheses of (2.84), an additional term is extracted from the Green's function as follows:

$$G(\mathbf{r}_m, \mathbf{r}_n) = \left(G(\mathbf{r}_m, \mathbf{r}_n) - \frac{1}{R} + \frac{k^2}{2} R \right) + \frac{1}{R} - \frac{k^2}{2} R. \tag{2.86}$$

Due to this, the gradient of the Green's function becomes

$$\nabla G(\mathbf{r}_m, \mathbf{r}_n) = \nabla \left(G(\mathbf{r}_m, \mathbf{r}_n) - \frac{1}{R} + \frac{k^2}{2} R \right) + \nabla \frac{1}{R} - \frac{k^2}{2} \nabla R. \tag{2.87}$$

Now the terms in parentheses of (2.86) and (2.87) have a continuous derivative at $R = 0$ and calculation of source and testing integrals of these terms can be done easily with standard numerical procedures. The two extracted terms can be integrated analytically over the source triangle in primed coordinates for all integrals I_2-I_4 using the formulas in [101] and [104]. The formulas for analytical integration presented in [104] are recursive and allow for the extraction of any number of terms from the singular kernel and integration of these terms over the source triangle in closed form.

Thereafter, the last term of (2.86) and (2.87) is integrated numerically over the testing triangle in unprimed coordinates for all integrals I_2-I_4, because the outer integrand for this term is regular. The testing integral of the second term of (2.86) can also be calculated numerically in unprimed coordinates for integrals I_2 and I_3 of the EFIE and MFIE part, because the outer integrand for this term is regular, too. The problem is to calculate the testing integral of the second term of (2.87), because in the outer integrand of this term a logarithmic singularity remains when the source and testing triangles have common points

and are not on the same plane. This singularity exists in integrals I_4 of the EFIE and MFIE part. In particular, for analytical calculation of the source integral of the term $\nabla(1/R)$ in primed coordinates the gradient is divided into normal and surface components and the integral of the surface component over the source triangle is transformed with Gauss's theorem into a line integral, which means that

$$\iint_{A'} \nabla \frac{1}{R} da' = \iint_{A'} \nabla_n \frac{1}{R} da' + \int_{\partial A'} \hat{u}(\mathbf{r}_n) \frac{1}{R} dl', \tag{2.88}$$

where $\partial A'$ is the boundary of the source triangle and $\hat{u}(\mathbf{r}_n)$ is the outer unit vector normal to $\partial A'$. Now, according to [101], the analytical expression of the line integral in the above equation has a logarithmic term, which causes the logarithmic singularity in the outer testing integral. It is noticed, that the same logarithmic singularity exists also in the integrals I_4 when applying the single extraction of equation (2.84).

In order to avoid this singularity, after the source integral of the surface component of the singular term $\nabla(1/R)$ is transformed into a line integral, the order of integration is changed [104]. Particularly, for the EFIE part, the remaining term of integral I_4^{EFIE}, which produces the logarithmic singularity after applying the singularity extraction of either (2.84) or (2.86), has the form

$$I_4^{EFIE} = \iint_{A} (\mathbf{r}_m - \mathbf{p}) \cdot \left[\iint_{A'} (\mathbf{r}_n - \mathbf{q}) \times \nabla' \frac{1}{R} da' \right] da, \tag{2.89}$$

where $\mathbf{p}$ is the position vector of the free vertex of the testing triangle and $\mathbf{q}$ is the position vector of the free vertex of the source triangle. It is noticed, that in the above equation the identity $\nabla(1/R) = -\nabla'(1/R)$ has been used. Applying the substitution

$$\mathbf{r}_n - \mathbf{q} = (\mathbf{r}_n - \mathbf{r}_m) + (\mathbf{r}_m - \mathbf{p}) + (\mathbf{p} - \mathbf{q}), \tag{2.90}$$

which is obtained by intervening in the source path $\mathbf{r}_n - \mathbf{q}$ the testing point with position vector $\mathbf{r}_m$ as well as the free vertex of the testing triangle with position vector $\mathbf{p}$, along with separating the normal and surface derivatives, equation (2.89) can be written as

$$\begin{aligned} I_4^{EFIE} &= \iint_{A} (\mathbf{r}_m - \mathbf{p}) \cdot \left[\iint_{A'} (\mathbf{p} - \mathbf{q}) \times \nabla'_n \frac{1}{R} da' \right] da \\ &+ \iint_{A} (\mathbf{r}_m - \mathbf{p}) \cdot \left[\iint_{A'} (\mathbf{p} - \mathbf{q}) \times \nabla'_s \frac{1}{R} da' \right] da. \end{aligned} \tag{2.91}$$

To avoid the logarithmic singularity in the testing integral of the surface gradient terms after using the Gauss's theorem to translate the integral of the surface gradient over the source triangle into a line integral, the order of integration is changed and the surface component of (2.91) is written as

$$\begin{aligned} I_{4_s}^{EFIE} &= \iint_{A} (\mathbf{r}_m - \mathbf{p}) \cdot \left[(\mathbf{p} - \mathbf{q}) \times \int_{\partial A'} \hat{u}(\mathbf{r}_n) \frac{1}{R} dl' \right] da \\ &= \int_{\partial A'} \left[(\mathbf{p} - \mathbf{q}) \times \hat{u}(\mathbf{r}_n) \right] \cdot \left[\iint_{A} \frac{(\mathbf{r}_m - \mathbf{p})}{R} da \right] dl'. \end{aligned} \tag{2.92}$$

Now, the inner testing integral is calculated analytically in unprimed coordinates using the formulas in [104]. In those formulas the logarithmic term is canceled. As a result, the outer source line integral has a regular integrand and allows numerical integration in primed coordinates. Hence, by considering the normal and surface gradients separately and changing the order of integration, the logarithmic singularity on the outer testing integral is avoided.

The same procedure is applied to the integral I_4^{MFIE} of the MFIE part. In this case, the remaining term of integral I_4^{MFIE}, which produces the logarithmic singularity after applying the singularity extraction of either (2.84) or (2.86), has the form

$$I_4^{MFIE} = \iint\limits_A \big[\hat{n}(\mathbf{r}_m) \times (\mathbf{r}_m - \mathbf{p})\big] \cdot \left[\iint\limits_{A'} (\mathbf{r}_n - \mathbf{q}) \times \nabla' \frac{1}{R} da' \right] da. \tag{2.93}$$

Applying the same procedure leads to a surface component of (2.93) given by

$$\begin{aligned} I_{4_s}^{MFIE} &= \int\limits_{\partial A'} \big[(\mathbf{p} - \mathbf{q}) \times \hat{u}(\mathbf{r}_n)\big] \cdot \left[\hat{n}(\mathbf{r}_m) \times \iint\limits_A \frac{(\mathbf{r}_m - \mathbf{p})}{R} da \right] dl' \\ &- \int\limits_{\partial A'} \hat{u}(\mathbf{r}_n) \cdot \hat{n}(\mathbf{r}_m) \left[\iint\limits_A \frac{|\mathbf{r}_m - \mathbf{p}|^2}{R} da \right] dl'. \end{aligned} \tag{2.94}$$

Note that due to the cross product with the normal unit vector of surface A the last term of (2.94) must additionally be calculated. The inner testing integral of this term is calculated analytically in unprimed coordinates as reported in [104] and the outer source line integral has a regular integrand and is calculated numerically in primed coordinates.

Alternatively, *singularity cancellation methods* can be used, like the Duffy transformation [105], where the source triangle is divided into three subtriangles with common vertex at the singular point. Then, the integrals over each subtriangle are transformed into integration over a square. This procedure cancels the singularity. Duffy's transformation has three main disadvantages: First, it is accurate only for sufficiently regular triangles. Second, new integration points on the source integral have to be generated for each integration point on the testing integral. This increases the computation time. Third, singularities of order $\nabla(1/R)$ cannot be easily evaluated, because Duffy's transformation is derived for functions having a point singularity of order $1/R$. A novel singularity cancellation method for singular potential integrals was presented in [106] and it was extended to an adaptive singularity cancellation technique in [107]. Thereby, unnecessary computations are avoided through appropriate subdivision of the source triangular domain and the effect of accuracy by variations in height of observation point above the plane of source domain is removed. Additionally, an optimum selection criterion for the distribution of quadrature samples is presented. Reviews of singularity treatment for surface integral equation solved by MoM can be found in [108], [109].

After introducing in the previous sections the basic concepts of the BIM, the Finite Element Method will be introduced in the following section, which is the second numerical method that is involved in the combined Finite Element Boundary Integral approach.

2.3 The Finite Element Method

The *Finite Element Method* (FEM) is a local numerical modeling technique for the solution of BVPs, which are formulated with the vector wave equation for a closed domain containing an inhomogeneous and anisotropic material. The used boundary conditions are simple homogeneous Dirichlet boundary conditions. The solution of the differential equation is achieved with finite elements using a variational method, which seeks a stationary point of a variational formulation of the BVP called *functional*[4]. The solution of the differential equation, with which the BVP is formulated, corresponds to this stationary point, which is found by minimizing the functional. The basic concepts of functional formulation and its solution according to FEM will be given in the following subsections.

2.3.1 Variational Formulation

The configuration for Finite Element (FE) modeling is shown in Fig. 2.3 consisting of the volume domain V_a with lossy, linear, inhomogeneous, and anisotropic material properties $\bar{\bar{\varepsilon}}(\mathbf{r}), \bar{\bar{\mu}}(\mathbf{r})$, which is enclosed by the surface A_d and placed within free space. The corresponding BVP for the domain V_a is formulated by the vector wave equation for the electric field (2.14) using homogeneous Dirichlet boundary conditions on A_d. The boundary conditions impose known tangential field components $\hat{n}(\mathbf{r}) \times \mathbf{E}(\mathbf{r})$ and $\hat{n}(\mathbf{r}) \times \mathbf{H}(\mathbf{r})$ on A_d.

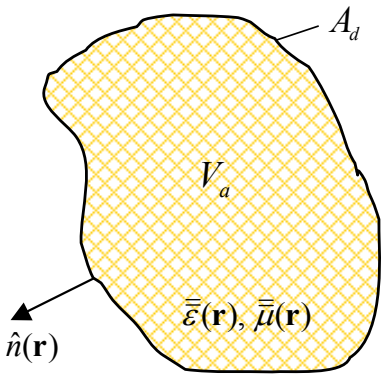

Figure 2.3: Configuration for FE modeling.

The FEM solution of the field problem for the domain V_a is achieved using a *generalized variational principle for anisotropic media* [16], [37], [110]-[112], where the differential equation of the original BVP is expressed with a functional using complex-valued (or real-type) inner product definition and introducing the homogeneous adjoint[5] field problem. According to this, using Green's first identity of vector analysis in the vector wave equation (2.14) and

[4] A functional is a mapping of a space of functions to the complex numbers. It's usually an integral containing an unknown function. The result of the integration is a simple number in contrast to an IE, which maps the function into an other function.

[5] Given an operator $\mathcal{L}$ of an equation expressing a BVP, the adjoint operator $\mathcal{L}^\dagger$ is defined by the relation $\langle \mathcal{L}\phi, \psi \rangle = \langle \phi, \mathcal{L}^\dagger \psi \rangle$, where ϕ, ψ are arbitrary functions and $\langle \cdot, \cdot \rangle$ denotes any inner product definition. Using the adjoint operator $\mathcal{L}^\dagger$, an adjoint equation to the original boundary value equation can be introduced. It is obvious, that the operator $\mathcal{L}$ is self-adjoint if $\mathcal{L} = \mathcal{L}^\dagger$. The adjoint operator is commonly used in Sturm-Liouville theory.

assuming zero impressed magnetic sources within V_a ($\mathbf{M} = 0$) the functional

$$\begin{aligned} F(\mathbf{E}_{ad}, \mathbf{E}) &= \iiint_{V_a} \Big[\nabla \times \mathbf{E}_{ad}(\mathbf{r}) \cdot \bar{\bar{\mu}}_r^{-1}(\mathbf{r}) \cdot \nabla \times \mathbf{E}(\mathbf{r}) - k_0^2 \mathbf{E}_{ad}(\mathbf{r}) \cdot \bar{\bar{\varepsilon}}_r(\mathbf{r}) \cdot \mathbf{E}(\mathbf{r}) \\ &\qquad + jk_0 Z_0 \mathbf{E}_{ad}(\mathbf{r}) \cdot \mathbf{J}(\mathbf{r}) \Big] dv \\ &+ jk_0 Z_0 \oiint_{A_d} \mathbf{E}_{ad}(\mathbf{r}) \cdot \big[\mathbf{H}(\mathbf{r}) \times \hat{n}(\mathbf{r}) \big] da \end{aligned} \tag{2.95}$$

is derived, which is stationary with respect to both the electric field $\mathbf{E}(\mathbf{r})$ of the original field problem as well as the adjoint electric field $\mathbf{E}_{ad}(\mathbf{r})$, which is a solution of the homogeneous adjoint field problem. Also, $\mathbf{J}(\mathbf{r})$ is an impressed electric current density in the volume domain V_a.

The definition of a complex-valued inner product allows consideration of losses in the material of V_a, since the resulting functional is a complex quantity, that is applicable to complex problems. Further, in the general case of arbitrary anisotropy the differential operator in (2.14) is non-self-adjoint even for complex-valued inner product definition resulting in an non-self-adjoint (or non-Hermitian) system of equations, which is asymmetric and indefinite and consequently very difficult to solve with iterative solution techniques. However, introducing the adjoint field problem the functional (2.95) is derived by building a complex-valued inner product in terms of the adjoint and original fields and discretization with finite elements results into a system of equations, which is symmetric in case of symmetric material properties. For definition of terms related with linear algebra, the reader is referred to Section A.1 in the Appendix A.

The functional (2.95) is derived in terms of the adjoint and original electric field $(\mathbf{E}_{ad}, \mathbf{E})$. The formulation of the FE functional using this approach is known as *E-formulation*. The FE functional can be expressed in the same way in terms of the adjoint and original magnetic field $(\mathbf{H}_{ad}, \mathbf{H})$, which is known as *H-formulation*. Both formulations are *field formulations*, since they are derived in terms of field quantities. Alternative variational formulations for FEM are *potential formulations*, which are using a vector potential $\mathbf{A}$ and a scalar potential V. The resulting formulations can be gauged or ungauged and are referred to as $\mathbf{A}$-V-*formulations* [113], [114]. Using an ungauged $\mathbf{A}$-V-formulation, better convergence within iterative solvers can be achieved. However, an obvious disadvantage of $\mathbf{A}$-V-formulations is that the additional scalar potential increases the computation and memory requirements per iteration compared to the standard E-formulation.

As mentioned in Section 2.1.1, solutions to the vector wave equations (2.14) and (2.15) satisfy the divergence conditions imposed by Maxwell's equations. This is true for continuous functions with continuous first derivatives in the Hilbert space[6] $\mathbb{R}^3$. Functions with continuous first derivatives are denoted in mathematics as $\mathbf{C^1}$ functions. This means that the electric and magnetic fields must be differentiable twice with continuous rotations and in this case they satisfy the governing vector wave equation in a strong sense. However, using the variational formulation of the BVP given in (2.95), the first derivatives of the solutions

[6] A Hilbert space is a vector space with an inner product $\langle f, g \rangle$, such that the norm defined by $|f| = \sqrt{\langle f, f \rangle}$ turns the space into a complete metric space. Examples of finite-dimensional Hilbert spaces include the real numbers $\mathbb{R}^3$ and the complex numbers $\mathbb{C}^3$.

do not need to be differentiable (continuous) any more but only integrable. In this case, the electric and magnetic fields must be square integrable[7]. This is true for field solutions within V_a defined in the space $H(curl; V_a) = \{\mathbf{u} \in [L^2(V_a)]^3 | \nabla \times \mathbf{u} \in [L^2(V_a)]^3\}$, where $\mathbf{u}$ is any vector field function. These field solutions satisfy the governing vector wave equation in a weak sense, which means that the variational formulation in (2.95) is a *weak formulation* of the BVP.

2.3.2 Discretization

In order to solve the FE functional (2.95) for the unknown fields, the solution domain V_a is discretized into volume finite elements and the unknown fields within V_a are expanded in terms of appropriate basis functions defined on the discrete elements. Enforcing the FE functional to be stationary, a system of equations for the unknown coefficients of the field expansion on the volume elements is derived.

For expanding the fields within the volume finite elements, the basis functions must be linearly independent and they should satisfy the continuity conditions imposed by Maxwell's equations. Thus, tangential electric field components must be continuous allowing normal electric field components to be discontinuous along the interfaces of finite elements. Further, in order to avoid *spurious modes*[8], the basis functions must properly approximate static electric field solutions, which are referred to as *gradient fields*, since they are associated to gradients of the scalar electrostatic potential function φ according to

$$\mathbf{E} = -\nabla\varphi. \tag{2.96}$$

These solutions are eigenvectors of the governing vector wave equation with zero eigenvalue $k_0 = 0$ and are forming the infinite dimensional nullspace of the curl operator, since for static electric fields

$$\nabla \times \mathbf{E} = \nabla \times \nabla\varphi = 0. \tag{2.97}$$

In order to satisfy the above requirements, vector basis functions are used for field expansion, in which the degrees of freedom are associated to edges of the volume finite elements. Such basis functions are known in literature as *tangential vector finite elements*, or *edge elements* [115]-[119]. Particularly, these vector basis functions have only tangential components along the corresponding edge on which they are defined. Therefore, they give an approximation of $\mathbf{E}$, which has continuous tangential components but discontinuous normal components along the interfaces of finite elements. Edge element basis functions have zero divergence and constant curl within the volume finite element on which they are defined and they represent *curl conforming* basis functions [17], [116], in contrast to RWG basis functions, which are divergence conforming as stated in Section 2.2.2. Also, in order to satisfy the condition (2.96) for static field solutions, only tangential continuity of $\nabla\varphi$ is required, which

[7] In mathematics, the Hilbert space containing square integrable functions is known as Lebesque space L^2 and its subset, in which finite L^2 norm is imposed for the functions and their weak derivatives is the standard Sobolev space H^2.

[8] Spurious modes are parasitic, nonphysical eigensolutions of the eigenvalue problem corresponding to the considered BVP, which are caused by inconsistent approximation of static solutions to the wave equation. Since each field solution can be expanded in terms of the eigensolutions, spurious modes can be contained in field solutions of excitation problems.

is true if φ is continuous without the need for continuity of the normal derivative of φ. The required continuity of the scalar potential φ is automatically achieved with tangential vector finite elements giving an exact representation of the static eigensolutions without spurious modes.

An alternative approach is to use scalar basis functions with continuous derivatives for field expansion, in which the degrees of freedom are associated to nodes of volume finite elements. Such basis functions are referred to as $\mathbf{C^1}$ finite elements [119], [120]. In this case, the approximation of $\mathbf{E}$ provides both tangential as well as normal continuity along interfaces of adjacent finite elements. Using $\mathbf{C^1}$ finite elements, the condition (2.96) for static field solutions is satisfied providing an exact representation of the nullspace of the curl operator without spurious modes. However, $\mathbf{C^1}$ basis functions are not commonly found in finite elements, since they do not exist in general over an arbitrary mesh and may need to be explicitly derived for the particular case. Therefore, $\mathbf{C^1}$ finite elements are not a favorable approach in finite element electromagnetic solutions.

In this work, tetrahedral volume finite elements are used to discretize the solution domain V_a as shown in Fig. 2.4 a). Within each tetrahedron, homogeneous material properties are assumed. Also, zeroth-order edge element basis functions $\boldsymbol{\alpha}_j(\mathbf{r})$ are defined on the tetrahedral elements [37]. According to the order of interpolation that these functions are introducing on the discrete elements, they are often also referred to as 0.5-th order basis functions, since the order of interpolation perpendicular to the corresponding edge on which they are defined is 1 and the order of interpolation along that edge is 0. Each tetrahedral element has six degrees of freedom associated to its edges, whereas the degrees of freedom are shared between adjacent tetrahedral elements. Hence, discretizing the solution domain V_a with M_{FE} tetrahedral elements results in $N_{FE} = 2M_{FE}$ total degrees of freedom within V_a, since each degree of freedom is shared by three tetrahedral elements.

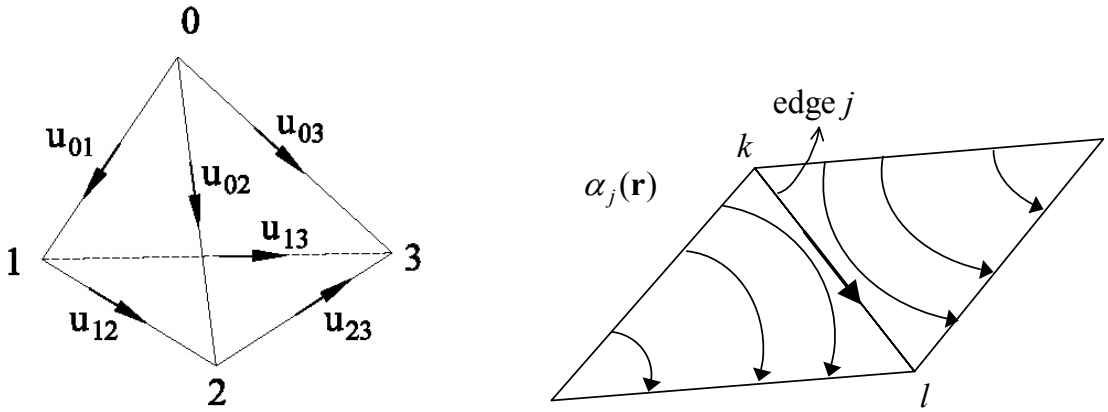

Figure 2.4: a) Tetrahedral finite element with associated degrees of freedom. b) Edge element basis functions.

Using volume simplex coordinates[9] [17], [37], the zeroth-order edge element basis function associated to the edge from node k to node l is described by

$$\boldsymbol{\alpha}_j(\mathbf{r}) = \boldsymbol{\alpha}_{kl}(\mathbf{r}) = \lambda_k \nabla \lambda_l - \lambda_l \nabla \lambda_k. \tag{2.98}$$

[9]Components of a local coordinate system within the corresponding tetrahedral element, which is introduced by dividing the element for each observation point in its interior into four subtetrahedrons.

Vector functions defined by (2.98) have tangential field components only at the edge on which they are defined as well as on faces containing those edges, whereas at all other faces they have only normal components. This gives the required tangential field continuity as shown in Fig. 2.4 b) allowing normal field components to be discontinuous along the interfaces of adjacent tetrahedral elements as previously discussed.

The field quantities in the variational formulation (2.95) are expanded within the discrete tetrahedral element e in terms of edge element basis functions $\boldsymbol{\alpha}_j(\mathbf{r})$ according to

$$\mathbf{E}(\mathbf{r}) = \sum_{j=1}^{n} E_j^e \boldsymbol{\alpha}_j^e(\mathbf{r}), \tag{2.99}$$

$$\mathbf{E}_{ad}(\mathbf{r}) = \sum_{j=1}^{n} E_{j,ad}^e \boldsymbol{\alpha}_j^e(\mathbf{r}), \tag{2.100}$$

$$\mathbf{H}(\mathbf{r}) = \sum_{j=1}^{n} H_j^e \boldsymbol{\alpha}_j^e(\mathbf{r}), \tag{2.101}$$

with E_j^e, H_j^e being the unknown expansion coefficients within the tetrahedron e, associated to electric and magnetic field quantities, respectively. Also, n denotes the number of edges comprising the tetrahedral element e.

Using the expansions (2.99)-(2.101) of the field quantities in the functional (2.95) for the tetrahedral finite element e and applying the functional to be stationary, results in a *local system of equations* for the unknown coefficients of the field expansions within the tetrahedron e given by

$$[R^e]\{E^e\} - k_0^2[S^e]\{E^e\} + jk_0Z_0[T^e]\{H^e\} = -jk_0Z_0\{w^e\}, \tag{2.102}$$

with the local system matrices

$$[R_{ij}^e] = \iiint\limits_{V_a} \left[\nabla \times \boldsymbol{\alpha}_i^e(\mathbf{r})\right] \cdot \bar{\bar{\mu}}_r^{-1} \cdot \left[\nabla \times \boldsymbol{\alpha}_j^e(\mathbf{r})\right] dv, \tag{2.103}$$

$$[S_{ij}^e] = \iiint\limits_{V_a} \boldsymbol{\alpha}_i^e(\mathbf{r}) \cdot \bar{\bar{\varepsilon}}_r \cdot \boldsymbol{\alpha}_j^e(\mathbf{r}) dv, \tag{2.104}$$

$$[T_{ij}^e] = \oiint\limits_{A_d} \boldsymbol{\alpha}_i^e(\mathbf{r}) \cdot \left[\boldsymbol{\alpha}_j^e(\mathbf{r}) \times \hat{n}(\mathbf{r})\right] da, \tag{2.105}$$

and the local vector of excitation coefficients

$$\{w_i^e\} = \iiint\limits_{V_a} \boldsymbol{\alpha}_i^e(\mathbf{r}) \cdot \mathbf{J}_i^e dv. \tag{2.106}$$

In the discrete equations (2.103)-(2.106), the material parameters $\bar{\bar{\mu}}_r$, $\bar{\bar{\varepsilon}}_r$ as well as the impressed electric current density $\mathbf{J}_i^e$ are assumed to be constant over the working tetrahedral element e and the corresponding position vector dependence in (2.103)-(2.106) is neglected. The equations for computation of matrix and vector elements (2.103)-(2.106) can be found in [17], [37].

The *global system of equations* in FEM is obtained by summing the local equations (2.102) with matrix and vector elements given in (2.103)-(2.106) over all volume finite elements. This process is called *assembly* and results in the global FE system of equations

$$[R]\{E\} - k_0^2[S]\{E\} + jk_0Z_0[T]\{H\} = -jk_0Z_0\{w\}. \tag{2.107}$$

2.3.3 Truncation of the Solution Domain

The FE system of equations obtained by (2.107) is a system of N_{FE} equations, where N_{FE} is the number of basis functions used to expand $\mathbf{E}$. The number of system equations equals to the number of unknowns if the FE problem is uniquely defined, which is true if the problem is completely decoupled from the domain external to V_a. This is done by determination of the tangential components of the electric and magnetic field or by defining a specific relationship between them on the closed surface A_d surrounding the solution domain V_a.

In FE problems, where the solution domain V_a is terminated physically by the geometry itself, the required tangential field components at the closed surface A_d are determined by the natural conditions imposed by the boundary walls. These can be the conditions of a Perfect Electric Conductor (PEC) or Perfect Magnetic Conductor (PMC). The tangential field components can also be determined by the relationship imposed by an Impedance Boundary Condition (IBC) [17], [121], [122]. However, for the solution of open region radiation and scattering electromagnetic problems using FEM truncation of the infinite solution domain is required to limit the size of the computational domain.

This can be achieved using an artificial boundary, which allows waves to pass through them without reflection. Thus, such an artificial boundary does not perturb the field that is incident upon it. The resulting boundary condition is generally referred to as Absorbing Boundary Condition (ABC). Perfect absorption without reflection of incident fields at the artificial boundary is achieved with an ABC of infinite order. However, since this is impractical, ABCs of finite order must be used. Typically, ABCs of second and higher order are utilized for accurate results. A review of ABCs can be found in [123].

An alternative approach that can be used to truncate the infinite FEM solution domain is to use artificial material absorbers known as Perfectly Matched Layer (PML). It consists in general of an interface between two spaces, one of which is lossy, and absorbs an electromagnetic wave for a specific range of frequencies, angle of incidence and polarization, while it is perfectly matched to the FE solution domain. An insight into PMLs is given in [124]-[126].

The main disadvantage of the above truncation approaches is the significant additional computational domain needed for accurate results. The FEM solution domain is efficiently truncated using BIM formulated at the boundaries of the radiation and scattering objects as described in Section 2.2. In this case, the truncation is exact, since the BI approach incorporates the Sommerfeld radiation condition at infinity through the use of the appropriate Green's function. This kind of truncation is done without any additional computational domain outside the involved objects.

In this work, the BIM is used to solve for the fields in the domains exterior to the involved objects and it is combined with the FEM to handle interior inhomogeneous dielectric regions of the objects providing an efficient truncation of the FEM solution domain. This combination results in a Finite Element Boundary Integral (FEBI) formulation, which will be described more in detail in the following section.

2.4 Combined Finite Element - Boundary Integral Formulation

The configuration of the combined FEBI approach is shown in Fig. 2.5. It consists of composite metallic/dielectric objects with arbitrary shape, where the dielectric regions can be in general inhomogeneous. The surface A_d surrounding the dielectric regions V_a consists of the closed surfaces A_{d_1} and A_{d_2}.

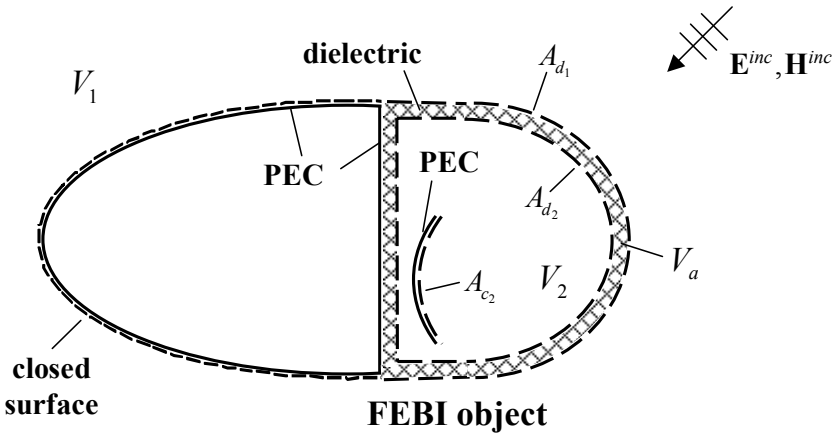

Figure 2.5: Combined FEBI configuration.

Fields in exterior regions are treated by BIM as described in Section 2.2, which is applied to the boundary surface $A \rightarrow A_1 + A_2$ consisting of A_{d_1}, A_{d_2} and any infinitesimally thin open conducting surface like the surface A_{c_2} shown in Fig. 2.5. In particular, the solution domain for the BIM applied to the boundary surface $A_1 \rightarrow A_{d_1} + A_\infty$ is the homogeneous region V_1 exterior to A_{d_1} up to infinity. In this case, CFIE expressions are obtained by substituting the EFIE

$$\hat{n}(\mathbf{r}) \times \left\{ \frac{1}{2}\mathbf{M}_{A_1}(\mathbf{r}) - \hat{n}(\mathbf{r}) \times \left[j\frac{\omega\mu}{4\pi} \iint_{A_1} G(\mathbf{r},\mathbf{r}')\mathbf{J}_{A_1}(\mathbf{r}')da' \right.\right.$$
$$\left.\left. + j\frac{1}{4\pi\omega\varepsilon}\nabla \iint_{A_1} G(\mathbf{r},\mathbf{r}')\nabla'_{A_1} \cdot \mathbf{J}_{A_1}(\mathbf{r}')da' + \frac{1}{4\pi}\iint_{A_1} \nabla G(\mathbf{r},\mathbf{r}') \times \mathbf{M}_{A_1}(\mathbf{r}')da' - \mathbf{E}^{inc}(\mathbf{r}) \right] \right\}$$
$$= 0, \qquad \forall\, \mathbf{r} \in A_1 \tag{2.108}$$

and the MFIE

$$\frac{1}{2}\mathbf{J}_{A_1}(\mathbf{r}) + \hat{n}(\mathbf{r}) \times \left[j\frac{\omega\varepsilon}{4\pi} \iint_{A_1} G(\mathbf{r},\mathbf{r}')\mathbf{M}_{A_1}(\mathbf{r}')da' + j\frac{1}{4\pi\omega\mu}\nabla \iint_{A_1} G(\mathbf{r},\mathbf{r}')\nabla'_{A_1} \cdot \mathbf{M}_{A_1}(\mathbf{r}')da' \right.$$
$$\left. - \frac{1}{4\pi}\iint_{A_1} \nabla G(\mathbf{r},\mathbf{r}') \times \mathbf{J}_{A_1}(\mathbf{r}')da' - \mathbf{H}^{inc}(\mathbf{r}) \right] = 0, \qquad \forall\, \mathbf{r} \in A_1 \tag{2.109}$$

into the linear combination (2.67). In addition, the solution domain of the BIM applied to the boundary surface $A_2 \rightarrow A_{d_2} + A_{c_2}$ is the interior homogeneous region V_2, where no

incident fields $\mathbf{E}^{inc}$, $\mathbf{H}^{inc}$ are available. In this case, the corresponding EFIE and MFIE expressions are

$$\hat{n}(\mathbf{r}) \times \left\{ \frac{1}{2}\mathbf{M}_{A_2}(\mathbf{r}) - \hat{n}(\mathbf{r}) \times \left[j\frac{\omega\mu}{4\pi} \iint_{A_2} G(\mathbf{r},\mathbf{r}')\mathbf{J}_{A_2}(\mathbf{r}')da' \right.\right.$$
$$\left.\left. + j\frac{1}{4\pi\omega\varepsilon}\nabla \iint_{A_2} G(\mathbf{r},\mathbf{r}')\nabla'_{A_2} \cdot \mathbf{J}_{A_2}(\mathbf{r}')da' + \frac{1}{4\pi}\iint_{A_2} \nabla G(\mathbf{r},\mathbf{r}') \times \mathbf{M}_{A_2}(\mathbf{r}')da' \right] \right\}$$
$$= 0, \qquad \forall\, \mathbf{r} \in A_2 \tag{2.110}$$

and

$$\frac{1}{2}\mathbf{J}_{A_2}(\mathbf{r}) + \hat{n}(\mathbf{r}) \times \left[j\frac{\omega\varepsilon}{4\pi} \iint_{A_2} G(\mathbf{r},\mathbf{r}')\mathbf{M}_{A_2}(\mathbf{r}')da' + j\frac{1}{4\pi\omega\mu}\nabla \iint_{A_2} G(\mathbf{r},\mathbf{r}')\nabla'_{A_2} \cdot \mathbf{M}_{A_2}(\mathbf{r}')da' \right.$$
$$\left. - \frac{1}{4\pi}\iint_{A_2} \nabla G(\mathbf{r},\mathbf{r}') \times \mathbf{J}_{A_2}(\mathbf{r}')da'(\mathbf{r}) \right] = 0, \qquad \forall\, \mathbf{r} \in A_2, \tag{2.111}$$

respectively. Thereby, CFIE is used for all segments of A_1 and A_2 except for the open surface A_{c_2}, where EFIE is used due to reasons which are discussed in Section 2.5. In general, the material parameters of the homogeneous domain V_1 can be different from those of the region V_2.

On the other hand, fields within interior dielectric regions are treated by FEM as described in Section 2.3.1 resulting in the field expression

$$\iiint_{V_a} \nabla \times \mathbf{E}^{int}_{ad}(\mathbf{r}) \cdot \bar{\bar{\mu}}_r^{-1}(\mathbf{r}) \cdot \nabla \times \mathbf{E}^{int}(\mathbf{r})dv - \iiint_{V_a} k_0^2 \mathbf{E}^{int}_{ad}(\mathbf{r}) \cdot \bar{\bar{\varepsilon}}_r(\mathbf{r}) \cdot \mathbf{E}^{int}(\mathbf{r})dv$$
$$+ jk_0 Z_0 \oiint_{A_d} \mathbf{E}^{int}_{ad}(\mathbf{r}) \cdot \big[\mathbf{H}^{int}(\mathbf{r}) \times \hat{n}(\mathbf{r})\big]da = \iiint_{V_a} jk_0 Z_0 \mathbf{E}^{int}_{ad}(\mathbf{r}) \cdot \mathbf{J}(\mathbf{r})dv, \quad \forall\, \mathbf{r} \in V_a. \tag{2.112}$$

The solution domain of the FEM part is the dielectric region V_a, which is surrounded by the surface $A_d \rightarrow A_{d_1} + A_{d_2}$.

The solution of the above equations is obtained by following procedures described in Section 2.2.2 and Section 2.3.2, whereas the field expressions in the various solution domains must be coupled. This is done by combining in equations (2.108)-(2.112) the involved fields of the interior and exterior regions on the boundary surfaces A_1 and A_2. The coupling is performed at the dielectric segments of the boundary surfaces via the field continuity conditions

$$\hat{n}(\mathbf{r}) \times \mathbf{E}^{ext}(\mathbf{r}) = \hat{n}(\mathbf{r}) \times \mathbf{E}^{int}(\mathbf{r}), \qquad \forall\, \mathbf{r} \in A_{1,2}, \tag{2.113}$$
$$\hat{n}(\mathbf{r}) \times \mathbf{H}^{ext}(\mathbf{r}) = \hat{n}(\mathbf{r}) \times \mathbf{H}^{int}(\mathbf{r}), \qquad \forall\, \mathbf{r} \in A_{1,2}. \tag{2.114}$$

Considering the expressions (2.39) and (2.40) for the equivalent surface currents, the field continuity conditions become

$$\mathbf{J}_{A_{1,2}}(\mathbf{r}) = \hat{n}(\mathbf{r}) \times \mathbf{H}^{ext}(\mathbf{r}) = \hat{n}(\mathbf{r}) \times \mathbf{H}^{int}(\mathbf{r}), \qquad \forall\, \mathbf{r} \in A_{1,2}, \tag{2.115}$$
$$\mathbf{M}_{A_{1,2}}(\mathbf{r}) = -\hat{n}(\mathbf{r}) \times \mathbf{E}^{ext}(\mathbf{r}) = -\hat{n}(\mathbf{r}) \times \mathbf{E}^{int}(\mathbf{r}), \qquad \forall\, \mathbf{r} \in A_{1,2}, \tag{2.116}$$

which finally result in the coupling expressions

$$\mathbf{J}_{A_{1,2}}(\mathbf{r}) = \sum_{n=1}^{N} H_n \boldsymbol{\beta}_n(\mathbf{r}) = \sum_{n=1}^{N} H_n \big[\hat{n}(\mathbf{r}) \times \boldsymbol{\alpha}_n(\mathbf{r})\big], \qquad \forall\, \mathbf{r} \in A_{1,2}, \tag{2.117}$$

$$\mathbf{M}_{A_{1,2}}(\mathbf{r}) = -\sum_{n=1}^{N} E_n \boldsymbol{\beta}_n(\mathbf{r}) = -\sum_{n=1}^{N} E_n \big[\hat{n}(\mathbf{r}) \times \boldsymbol{\alpha}_n(\mathbf{r})\big], \qquad \forall\, \mathbf{r} \in A_{1,2}. \tag{2.118}$$

Thereby, the expansions (2.69), (2.70) and (2.99), (2.101) were taken into account by also considering that the edge element basis functions $\boldsymbol{\alpha}(\mathbf{r})$ are the tangential counterpart of RWG basis functions $\boldsymbol{\beta}(\mathbf{r})$ on the boundary surface, thus

$$\boldsymbol{\beta}(\mathbf{r}) = \hat{n}(\mathbf{r}) \times \boldsymbol{\alpha}(\mathbf{r}), \qquad \forall\, \mathbf{r} \in A_{1,2}. \tag{2.119}$$

It is noticed, that electric fields within FEM are expanded in terms of edge element basis functions according to (2.99) only on the dielectric parts of the boundary surface A, since on the PEC parts of A the tangential electric field vanishes. Further, magnetic currents within BIM exist only in the dielectric parts of the boundary surface A, since on the PEC parts of A magnetic currents vanish due to (2.40) along with the boundary condition imposing zero tangential components of the electric field on PEC surfaces. Electric currents, however, exist all over the boundary surface A. Obviously, the BIM degrees of freedom in the dielectric segments of A are identical to those of the FEM field expansion. It is finally noticed, that the IEs applied to A_1 and A_2 are decoupled and its MoM solution leads to two independent sets of linear equations. Coupling of the two IEs is given through the FEM on the dielectric segments of A_{d_1} and A_{d_2} according to the above expressions.

Applying the FEBI approach to the configuration shown in Fig. 2.5 results in a coupled linear system of equations according to

$$[A + B]\,\{x\} = \{b\}, \tag{2.120}$$

where $[A]$ is the sparse FE coupling matrix of interior regions, $[B]$ is the full coupling matrix of the BI part, $\{b\}$ is the excitation vector and $\{x\}$ is the unknown vector of expansion coefficients. In general, linear system of equations can be solved numerically using either *direct* or *iterative* solvers. The first provide a numerically exact solution of the equation system and they are in general based on Gaussian elimination, whereas the second are typically used for large problems and start from an initial guess of the solution and intend to converge to the exact solution with acceptable numerical accuracy through iteration steps. The convergence of iterative solvers is strongly influenced by the condition number of the system matrix, which can be improved using preconditioning techniques. The general idea of preconditioners is to multiply the system of equations with an appropriate matrix, in order to obtain a new equation system, which is easier to solve with iterative techniques. The most common preconditioning approaches include diagonal, block diagonal and near neighbor preconditioners. More on iterative solvers and preconditioning can be found in [16], [127].

In this work, the FEBI linear system of equations (2.120) is solved by a recursive iterative solution technique using a multilevel iterative preconditioning strategy with several nested iteration loops. For more detailed description of the equation system solution algorithm the reader is referred to [78], [128].

2.5 Discussion

The IEs given in Section 2.2.1 show different behavior when applied to an infinitesimally thin open metallic surface A_c. In order to discuss this difference, it is assumed that the open ends of A_c are connected by any fictitious extension to form a closed surface A_c'. The volume produced that way enclosed by A_c' has the same material parameters as the external domain. Then, the IEs are applied to both sides of the closed surface A_c' (interior and exterior problem), whereas at the fictitious part of A_c' both electric and magnetic equivalent surface currents are considered. The corresponding IEs for the interior and exterior problem are subtracted so that the contributions from the fictitious part of A_c' are eliminated since they are identical, whereas appropriate boundary conditions are considered at the original surface A_c. Applying this approach for EFIE results in proper modeling, since the tangential electric field is equal to zero on both sides of A_c, thus it is continuous across A_c. This means, that the same electric field exist on A_c on both sides of it, so that EFIE can be used properly on both sides of the infinitesimally thin surface. However, applying this approach for MFIE results in improper modeling, since tangential magnetic field components are discontinuous across A_c by the amount of the surface electric current density on A_c. Consequently, the tangential magnetic field jumps on the open conducting surface and additional unknowns are needed for proper modeling of the magnetic field on both sides of the open surface, which are not provided using MFIE for both sides of A_c. It is obvious, that the same limitations also exist when applying CFIE for modeling of open conducting surfaces, since it involves the MFIE according to (2.67). This is the reason why EFIE is used for modeling the open surface A_{c_2} shown in Fig. 2.5. A detailed discussion on this issue can be found in [129].

Moreover, the EFIE and MFIE were derived in Section 2.2.1 assuming observation points placed on the boundary surface A and considering tangential field components on A. Thereby, the $\hat{n}\times\hat{n}\times$ product with equation (2.63) was taken for EFIE formulation and the $\hat{n}\times$ product with equation (2.64) for MFIE formulation. This results in both cases in components tangential to A. In particular, denoting the unit vector of the $\hat{n}\times$ product by $\hat{t}'$ and the unit vector of the $\hat{n}\times\hat{n}\times$ product by $\hat{t}=\hat{n}\times\hat{t}'$ results in a set of unit vectors $\hat{n},\hat{t}',\hat{t}$, which lie orthogonal to each other with $\hat{t},\hat{t}'$ being tangential to the boundary surface A. This means, that the $\hat{n}\times\hat{n}\times$ product with (2.63) corresponds to $\hat{t}\cdot\mathbf{E}$ formulation and the $\hat{n}\times$ product with (2.64) to $\hat{n}\times\mathbf{H}$ formulation. So, following the notation used in [130], the EFIE given in Section 2.2.1 corresponds to TE formulation, which can be assumed as testing with RWG functions. Similarly, the MFIE corresponds to NH formulation, which can be assumed as testing with $\hat{n}\times$RWG functions. Consequently, the CFIE given in (2.67) corresponds to TENH formulation. Alternative CFIE formulations include TETH, NETH, and NENH formulations as described in [130]. Additionally, a TENENH formulation was proposed in [130] for improved efficiency and accuracy, which can be assumed as testing the EFIE part with both RWG as well as $\hat{n}\times$RWG functions. However, as discussed in [131] this is not necessarily important, since it turns out that accurate evaluation of BI integrals is the most important task for accurate FEBI results. Especially accurate computation of singularities of the Green's function must be handled carefully as reported in Section 2.2.3.

In the present thesis, the matrix-vector multiplications of the BIM part are accelerated within the iterative solver using a very powerful implementation of the Multilevel Fast Multipole Method, which will briefly described in the following chapter.

Chapter 3

The Multilevel Fast Multipole Method

The *Multilevel Fast Multipole Method* (MLFMM) is a global numerical modeling technique, where field contributions are expressed by spherical multipole expansions. At this point, it is used to accelerate the matrix-vector product computations reported in iterative solutions of equation systems, which are obtained in field problems solved by IE techniques. It is actually the multilevel version of the originally introduced Fast Multipole Method (FMM), in which far interactions between surface current elements are represented using two basic steps: In the first step, the current elements are collected into groups reducing that way the number of radiation centers. The radiated fields of the basis functions are expanded in terms of spherical multipoles located at the center of the groups. Coupling between source and testing elements imposed by MoM solution in BIM is computed by translating multipoles from the coordinate system of source groups to the coordinate system of testing groups using an appropriate translation matrix. The second step is the expansion of the spherical wave functions included in the multipole expansion into plane waves. This provides diagonalization of the translation operator and reduces significantly the complexity for the matrix-vector multiplications within each iteration step of the BIM solution. In this chapter, the basic theoretical concepts of FMM and MLFMM as well as the necessary formulations for CFIE will be given.

3.1 The Fast Multipole Method

The FMM was originally proposed by Greengard and Rokhlin to solve static IEs rapidly [132] and was extended by Rokhlin to solve acoustic wave scattering problems [133] as well as by many research groups to solve electromagnetic scattering problems [23], [134], [135]. The FMM reduces the computation complexity and memory requirements of the BI matrix-vector product from $O(N^2)$ to $O(N^{3/2})$, where N is the number of BI unknowns. In the following subsections, field representations by multipole expansions and diagonalization of translation operator according to FMM will be discussed.

3.1.1 Field Representation by Multipole Expansions

The system of equations obtained by MoM solution of CFIE in the BI part of the FEBI technique is written as

$$\left[Z_J^{CFIE}\right]\{H\} + \left[Z_M^{CFIE}\right]\{E\} = \{b\}, \tag{3.1}$$

where $\{H\}, \{E\}$ are vectors containing the unknown electric and magnetic surface current expansion coefficients, respectively, and $\{b\}$ is the excitation vector due to an incident plane wave or an impressed voltage on the boundary surface A through a delta-gap voltage source [136]. Also, $\left[Z_{J,M}^{CFIE}\right]$ are the coupling matrices due to electric and magnetic currents, respectively. For conventional MoM computations, the elements of those matrices are given in Section 2.2.2. The conventional MoM coupling matrices are dense resulting in bad computational complexity of the matrix-vector products in (3.1). An alternative expression of the MoM matrix elements for CFIE, which is used for FMM formulations, is given by

$$\begin{aligned} Z_{mn,J}^{CFIE} = \; & + \; c_1 \iint\limits_A \boldsymbol{\beta}_m(\mathbf{r}_m) \cdot \iint\limits_{A'} \left(\bar{\mathbf{I}} + \frac{1}{k^2}\nabla\nabla' \right) G(\mathbf{r}_m, \mathbf{r}_n) \cdot \boldsymbol{\beta}_n(\mathbf{r}_n) da' da \\ & + \; c_2 \iint\limits_A \left[\nabla \times \boldsymbol{\alpha}_m(\mathbf{r}_m)\right] \cdot \iint\limits_{A'} G(\mathbf{r}_m, \mathbf{r}_n) \boldsymbol{\beta}_n(\mathbf{r}_n) da' da, \end{aligned} \tag{3.2}$$

$$\begin{aligned} Z_{mn,M}^{CFIE} = \; & + \; c_3 \iint\limits_A \left[\nabla \times \boldsymbol{\beta}_m(\mathbf{r}_m)\right] \cdot \iint\limits_{A'} G(\mathbf{r}_m, \mathbf{r}_n) \boldsymbol{\beta}_n(\mathbf{r}_n) da' da \\ & + \; c_4 \iint\limits_A \boldsymbol{\alpha}_m(\mathbf{r}_m) \cdot \iint\limits_{A'} \left(\bar{\mathbf{I}} + \frac{1}{k^2}\nabla\nabla' \right) G(\mathbf{r}_m, \mathbf{r}_n) \cdot \boldsymbol{\beta}_n(\mathbf{r}_n) da' da, \end{aligned} \tag{3.3}$$

respectively, with $m, n = 1, 2, \ldots, N$ and $\mathbf{r}_m, \mathbf{r}_n \in A$. The coefficients c_1 to c_4 are given by

$$c_1 = -j\frac{\omega\mu}{4\pi}\alpha, \tag{3.4}$$

$$c_2 = Z\frac{1}{4\pi}(1-\alpha), \tag{3.5}$$

$$c_3 = \frac{1}{4\pi}\alpha, \tag{3.6}$$

$$c_4 = jZ\frac{\omega\varepsilon}{4\pi}(1-\alpha), \tag{3.7}$$

where α is the CFIE combination parameter and Z is the wave impedance in the considered solution domain given by (2.68). Also,

$$k = \omega\sqrt{\varepsilon\mu} = \frac{2\pi}{\lambda} \tag{3.8}$$

is the wavenumber in the considered solution domain with λ being the wavelength. The scalar Green's function $G(\mathbf{r}_m, \mathbf{r}_n)$ is given by (2.34) for $\mathbf{r} = \mathbf{r}_m$ and $\mathbf{r}' = \mathbf{r}_n$.

For fast computation of the matrix-vector product in (3.1), the N current elements on the boundary surface A are collected into M_G groups labeled by G_p with $p = 1, 2, \ldots, M_G$, so that each group is supporting $N' = N/M_G$ basis functions. Assuming that $\mathbf{r}' = \mathbf{r}_n$ is a source point within the group $G_{n'}$, which is centered at the point $\mathbf{r}_{n'}$, and $\mathbf{r} = \mathbf{r}_m$ is a testing point

within the group $G_{m'}$, which is centered at the point $\mathbf{r}_{m'}$ as shown in Fig. 3.1, the direct coupling path $\mathbf{r}_{mn} = \mathbf{r}_m - \mathbf{r}_n$ between source and field point is written as

$$\begin{aligned} \mathbf{r} - \mathbf{r}' = \mathbf{r}_m - \mathbf{r}_n &= (\mathbf{r}_m - \mathbf{r}_{m'}) + (\mathbf{r}_{m'} - \mathbf{r}_{n'}) + (\mathbf{r}_{n'} - \mathbf{r}_n) \\ &= \mathbf{r}_{mm'} + \mathbf{r}_{m'n'} - \mathbf{r}_{nn'}, \end{aligned} \tag{3.9}$$

by intervening the center points of the groups in the coupling path.

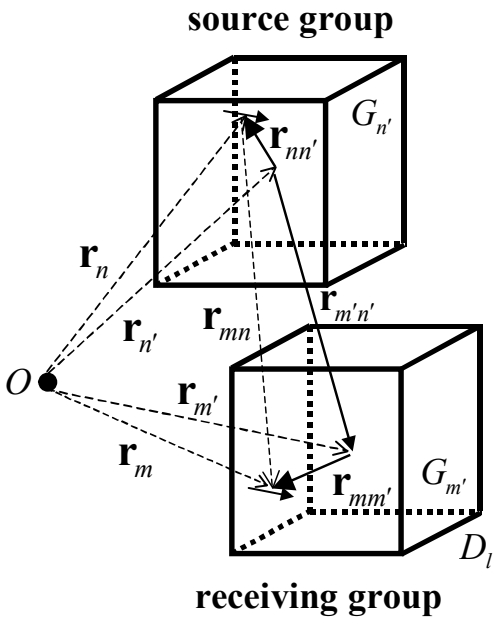

Figure 3.1: Coupling path from source point $\mathbf{r}' = \mathbf{r}_n$ to testing point $\mathbf{r} = \mathbf{r}_m$ split into three sections $\mathbf{r}_{nn'}$, $\mathbf{r}_{m'n'}$ and $\mathbf{r}_{mm'}$.

Then, a spherical multipole expansion is applied to the free space scalar Green's function using Gegenbauer's addition theorem [137]. According to this, the scalar Green's function from a source current element placed at $\mathbf{r}_n$ in the source group $G_{n'}$ to a testing current element placed at $\mathbf{r}_m$ in the testing group $G_{m'}$ is expanded in terms of spherical wave functions including dynamic multipoles located at the center of the corresponding groups $\mathbf{r}_{n'}$ and $\mathbf{r}_{m'}$, respectively, according to

$$\frac{\mathrm{e}^{-jk|\mathbf{D}+\mathbf{d}|}}{|\mathbf{D}+\mathbf{d}|} = -jk \sum_{l=0}^{\infty} (-1)^l (2l+1) j_l(kd) h_l^{(2)}(kD) P_l(\hat{d} \cdot \hat{D}), \tag{3.10}$$

where

$$\mathbf{D} = \mathbf{r}_{m'n'} \tag{3.11}$$

is the vector between the centers of the groups containing the considered current elements [23]. Also,

$$\mathbf{d} = \mathbf{r}_{mm'} - \mathbf{r}_{nn'} \tag{3.12}$$

is the sum of the vectors from the considered current elements to the particular group centers with

$$D > d. \tag{3.13}$$

Thus, using (3.9) we get

$$\mathbf{D}+\mathbf{d}=\mathbf{r}_m-\mathbf{r}_n. \tag{3.14}$$

Also, j_l is the first kind spherical Bessel function of degree l, $h_l^{(2)}$ is the second kind spherical Hankel function of degree l and P_l is the Legendre polynomial of degree l.

Applying the spherical multipole expansion (3.10) to the BIM equations given in (3.1)-(3.3), the field contributions associated with source and testing elements are transformed into new coordinate systems placed at the center of the corresponding groups containing those elements. The collected field contributions at the center of the source groups are transformed into the center of the testing groups by translating dynamic multipoles from the coordinate system of the former to the coordinate system of the latter. This procedure results in a representation, where the translation operator is a fully populated matrix. This is typical for multipole expansions in electromagnetic problems, where dynamic multipoles carry information about the source along distance[1]. Hence, long distance interactions in electromagnetics are replaced in general by multipole-to-multipole interactions. However, a full translation matrix does not reduce the computational complexity of the matrix-vector multiplication. Therefore, diagonalization of the translation operator is performed for electromagnetic problems. This will be described in the following subsection.

3.1.2 Diagonalization of Translation Operator

The matrix representation of the translation operator using dynamic multipoles as a basis results in a full translation matrix and does not reduce the computational complexity of the matrix-vector products in (3.1). The success of FMM in electromagnetic problems relies in the diagonal factorization of the translation operator. The spherical translation operators have diagonal representations when expressed in terms of their plane wave spectra [139]. From the point of view of group theory in physics, the existence of diagonal representations of the translation operator can be found in the commutative identity of the translational groups, which is a direct consequence of translational invariance of Maxwellian free space field solutions [4]. The diagonal translation theory was summarized in [140]. A different derivation based on plane wave expansions was given in [141].

The spherical wave functions included in (3.10) are expanded in terms of plane waves using the identity [9]

$$4\pi(-1)^l j_l(kd)P_l(\hat{d}\cdot\hat{D})=\oiint \mathrm{e}^{-j\mathbf{k}\cdot\mathbf{d}}P_l(\hat{k}\cdot\hat{D})d\hat{k}^2, \tag{3.15}$$

where the integration is performed over the Ewald sphere with

$$\mathbf{k}=k\hat{k}. \tag{3.16}$$

Thus, equation (3.10) becomes

$$\frac{\mathrm{e}^{-jk|\mathbf{D}+\mathbf{d}|}}{|\mathbf{D}+\mathbf{d}|}=-\frac{jk}{4\pi}\oiint\left\{\mathrm{e}^{-j\mathbf{k}\cdot\mathbf{d}}\sum_{l=0}^{\infty}(-1)^l(2l+1)h_l^{(2)}(kD)P_l(\hat{k}\cdot\hat{D})\right\}d\hat{k}^2, \tag{3.17}$$

[1]This can be clearly seen e.g. by looking at the radiation pattern produced by a radiating element compared to the one produced by an array of the same elements. The lobes and nulls observed in long distance (far-field) are different in both cases giving information about the source of the radiation. The same behavior can be found in dynamic multipoles [138].

where the order of integration and summation has been exchanged. The infinite series in equation (3.17) is truncated at the term $l = L_m$ and using (3.11)-(3.14) we finally get the representation of the free space scalar Green's function given by

$$G(\mathbf{r}_m, \mathbf{r}_n) = \frac{\mathrm{e}^{-jk|\mathbf{r}_m - \mathbf{r}_n|}}{|\mathbf{r}_m - \mathbf{r}_n|} \approx \oiint \mathrm{e}^{-j\mathbf{k}\cdot\mathbf{r}_{mm'}} T_L(\hat{k}\cdot\hat{r}_{m'n'}) \mathrm{e}^{j\mathbf{k}\cdot\mathbf{r}_{nn'}} d\hat{k}^2, \tag{3.18}$$

where

$$T_L(\hat{k}\cdot\hat{r}_{m'n'}) = -\frac{jk}{4\pi}\sum_{l=0}^{L_m}(-1)^l(2l+1)h_l^{(2)}(kr_{m'n'})P_l(\hat{k}\cdot\hat{r}_{m'n'}) \tag{3.19}$$

is the *translation operator*. This operator is a diagonal matrix, which translates radiated plane waves from the center of the source group to received plane waves at the center of the testing group. The factorization of the Green's function according to (3.18) is valid outside a sufficient radius from the groups due to the limitation (3.13) provided by the addition theorem. Groups for which this criterion is valid are referred to as *well-separated groups*. Particularly, groups are assumed to be well-separated, if they are separated by at least one group, so that the addition theorem criterion (3.13) remains valid.

The truncation of the multipole series expansion at the term L_m is a controllable error source in FMM. It was shown in [4], that truncation of the infinite series at the term

$$L_m \approx kd + 1.8d_a^{2/3}(kd)^{1/3} \tag{3.20}$$

results in a relative error of $\varepsilon = 10^{-d_a}$, where d_a is the number of digits of accuracy. It is noticed, that the above accuracy approximation was obtained under far field conditions, which may not be necessarily the case in near domains, thus for small groups.

The $\hat{k}$-space numerical integration over the Ewald sphere is also a controllable error source in FMM. The $2(L_m+1)$ trapezoidal quadrature rule in the interval $[0, 2\pi]$ is typically used for integration over φ, due to periodicity over φ with a period of 2π. The numerical integration over ϑ is performed using Gauss-Legendre quadrature rule with (L_m+1) integration points in the interval $[0, \pi]$. This results in a total number of $2(L_m+1)^2$ integration points in the $\hat{k}$-space, where L_m is the number of multipoles [142].

3.1.3 Matrix Elements

Substituting the factorized Green's function (3.18) in the matrix elements for CFIE given in (3.2) and (3.3) we get the FMM matrix elements

$$\begin{aligned} Z_{mn,J}^{FMM} = & - jZ\frac{k}{4\pi}\alpha \oiint \widetilde{\boldsymbol{\beta}}_m^*(\hat{k})\cdot T_L(\hat{k}\cdot\hat{r}_{m'n'})\left(\bar{\mathbf{I}} - \hat{k}\hat{k}\right)\cdot\widetilde{\boldsymbol{\beta}}_n(\hat{k})\, d\hat{k}^2 \\ & + jZ\frac{k}{4\pi}(1-\alpha)\oiint \left[\hat{k}\times\widetilde{\boldsymbol{\alpha}}_m^*(\hat{k})\right]\cdot T_L(\hat{k}\cdot\hat{r}_{m'n'})\widetilde{\boldsymbol{\beta}}_n(\hat{k})\, d\hat{k}^2, \end{aligned} \tag{3.21}$$

$$\begin{aligned} Z_{mn,M}^{FMM} = & + j\frac{k}{4\pi}\alpha \oiint \left[\hat{k}\times\widetilde{\boldsymbol{\beta}}_m^*(\hat{k})\right]\cdot T_L(\hat{k}\cdot\hat{r}_{m'n'})\widetilde{\boldsymbol{\beta}}_n(\hat{k})\, d\hat{k}^2 \\ & + j\frac{k}{4\pi}(1-\alpha)\oiint \widetilde{\boldsymbol{\alpha}}_m^*(\hat{k})\cdot T_L(\hat{k}\cdot\hat{r}_{m'n'})\left(\bar{\mathbf{I}} - \hat{k}\hat{k}\right)\cdot\widetilde{\boldsymbol{\beta}}_n(\hat{k})\, d\hat{k}^2, \end{aligned} \tag{3.22}$$

where

$$j\frac{\omega\mu}{4\pi} = jZ\frac{k}{4\pi}, \tag{3.23}$$

$$jZ\frac{\omega\varepsilon}{4\pi} = j\frac{k}{4\pi} \tag{3.24}$$

have been used to express the corresponding constants. Thereby, the substitution $\nabla \rightarrow -j\mathbf{k}$ was used, which is valid for application of the ∇ operator on elementary plane wave functions $\mathrm{e}^{-j\mathbf{k}\cdot\mathbf{r}}$ in the $\hat{k}$-space. Also,

$$\widetilde{\boldsymbol{\beta}}_n(\hat{k}) = \iint\limits_A \boldsymbol{\beta}_n(\mathbf{r}_n)\mathrm{e}^{j\mathbf{k}\cdot\mathbf{r}_{nn'}}da', \tag{3.25}$$

$$\widetilde{\boldsymbol{\alpha}}_n(\hat{k}) = \iint\limits_A \boldsymbol{\alpha}_n(\mathbf{r}_n)\mathrm{e}^{j\mathbf{k}\cdot\mathbf{r}_{nn'}}da' \tag{3.26}$$

are the $\hat{k}$-space representations of the basis functions with * denoting complex conjugation and $T_L(\hat{k}\cdot\hat{r}_{m'n'})$ is the translation operator given in (3.19).

Equations (3.21) and (3.22) are used for FMM computations among well-separated groups. The coupling terms between nearby groups, which are not well-separated, are computed by conventional MoM approaches as described in Section 2.2.2. Hence, we can rewrite the matrix-vector product of equation system (3.1) for electric currents as

$$\begin{aligned}\sum_{n=1}^{N} Z_{mn,J}^{CFIE}H_n = &\sum_{n'\in G_{Bn'}}\sum_{n\in G_{n'}} Z_{mn,J}^{MoM}H_n \\ &-jZ\frac{k}{4\pi}\alpha \oiint \widetilde{\boldsymbol{\beta}}_m^*(\hat{k})\cdot\sum_{n'\notin G_{Bn'}} T_L(\hat{k}\cdot\hat{r}_{m'n'})\left(\bar{\mathbf{I}}-\hat{k}\hat{k}\right)\cdot\sum_{n\in G_{n'}} H_n\widetilde{\boldsymbol{\beta}}_n(\hat{k})\,d\hat{k}^2 \\ &+jZ\frac{k}{4\pi}(1-\alpha)\oiint\left[\hat{k}\times\widetilde{\boldsymbol{\alpha}}_m^*(\hat{k})\right]\cdot\sum_{n'\notin G_{Bn'}} T_L(\hat{k}\cdot\hat{r}_{m'n'})\sum_{n\in G_{n'}} H_n\widetilde{\boldsymbol{\beta}}_n(\hat{k})\,d\hat{k}^2,\end{aligned} \tag{3.27}$$

for $m \in G_{m'}$, where $G_{m'}$ is the m'-th testing group. Also, $G_{Bn'}$ denotes all nearby (not well-separated) groups of the n'-th source group $G_{n'}$ including itself. Similarly, the matrix-vector product of equation system (3.1) for magnetic currents is written as

$$\begin{aligned}\sum_{n=1}^{N} Z_{mn,M}^{CFIE}E_n = &\sum_{n'\in G_{Bn'}}\sum_{n\in G_{n'}} Z_{mn,M}^{MoM}E_n \\ &+j\frac{k}{4\pi}\alpha\oiint\left[\hat{k}\times\widetilde{\boldsymbol{\beta}}_m^*(\hat{k})\right]\cdot\sum_{n'\notin G_{Bn'}} T_L(\hat{k}\cdot\hat{r}_{m'n'})\sum_{n\in G_{n'}} E_n\widetilde{\boldsymbol{\beta}}_n(\hat{k})\,d\hat{k}^2 \\ &+j\frac{k}{4\pi}(1-\alpha)\oiint\widetilde{\boldsymbol{\alpha}}_m^*(\hat{k})\cdot\sum_{n'\notin G_{Bn'}} T_L(\hat{k}\cdot\hat{r}_{m'n'})\left(\bar{\mathbf{I}}-\hat{k}\hat{k}\right)\cdot\sum_{n\in G_{n'}} E_n\widetilde{\boldsymbol{\beta}}_n(\hat{k})\,d\hat{k}^2.\end{aligned} \tag{3.28}$$

Thereby, $Z_{mn,J,M}^{MoM}$ are the near coupling matrix elements for CFIE between non well-separated groups due to electric and magnetic currents, respectively, which are evaluated by conventional MoM using equations (2.67), (2.72), and (2.75). The near coupling matrices must be

explicitly built and stored in memory, in order to be used within the iterative solver. These matrices are sparse and can be stored efficiently in a compressed format. They can also be used for a near neighbor preconditioning approach [78], [128]. However, the FMM part of the matrix-vector products are computed in each iteration step using the above equations.

By looking at the equations (3.27) and (3.28) it can be observed, that FMM consists of three processes, which are illustrated in Fig. 3.2:

- *Aggregation Process*

  In the aggregation process, the radiation patterns of the source groups are evaluated by collecting the radiation patterns of the basis functions at the center of the groups. The radiation patterns of the current elements are Fourier transformed basis functions for several $\hat{k}$-directions, namely the $\hat{k}$-space representations given in (3.25) and (3.26). The main term of this process is the function $\mathrm{e}^{j\mathbf{k}\cdot\mathbf{r}_{nn'}}$, which expresses the far-field radiation pattern of the current element n in the source group $G_{n'}$.

- *Translation Process*

  In the translation process, the radiated plane waves by the source group $G_{n'}$ are translated into received plane waves at the center of the testing group $G_{m'}$. The main term of this process is the diagonal translation operator $T_L(\hat{k}\cdot\hat{r}_{m'n'})$ given in (3.19).

- *Disaggregation Process*

  In the disaggregation process, the received field contribution at the center of the testing group $G_{m'}$ are computed at the testing point m by multiplying them with the receiving pattern of the current element at the testing point. The main term of this process is the function $\mathrm{e}^{-j\mathbf{k}\cdot\mathbf{r}_{mm'}}$, which expresses the far-field receiving pattern of the current element m in the testing group $G_{m'}$.

3.2 The Multilevel FMM

The MLFMM is the multilevel version of the FMM and was implemented for CFIE by Song and Chew [24], [25] with $O(N \log N)$ complexity and memory requirements for computation of the BI matrix-vector products. Further saving of a considerable amount of memory without compromising accuracy and numerical speed is achieved by expanding the $\hat{k}$-space representation of the basis functions into spherical harmonics introduced by Eibert [26]. The basic concepts of MLFMM concerning the numerical algorithm, interpolation and anterpolation issues as well as spherical harmonics expansion of the basis functions' far-fields will be addressed briefly in the following subsections.

3.2.1 Numerical Algorithm

In order to extend the FMM in a multilevel principle and to achieve additional reduction of computational requirements for the BI matrix-vector product computation, the groups are combined into multiple levels using a tree structure. At each level, the groups have in every dimension twice the size of the groups at the level directly below. Empty groups that may arise through the grouping process are ignored at each level. Non empty groups containing

BI current elements are collected and numbered at every level. Thereby, the lowest level containing the finest groups (smallest group size) is labeled with 1 and the highest level containing the coarsest group (largest group size) is labeled with L.

The basic multilevel algorithm for the matrix-vector multiplication consists of two steps, which are illustrated in Fig. 3.2:

- First, the aggregation process is performed. The $\hat{k}$-space representations of the basis functions are computed for the corresponding $\hat{k}$-directions at the lowest level. Using these representations, the radiation patterns of the source groups are computed at the lowest level and they are stored in memory. Through shifting and interpolation the corresponding radiation patterns of the groups on higher levels are performed. In particular, assuming that $\mathbf{r}_{n_l'}$ and $\mathbf{r}_{n_{l-1}'}$ are the group centers at levels l and $l-1$, respectively, the $\hat{k}$-space representation of the basis function at the level l is given by

$$\tilde{\boldsymbol{\beta}}_{n_l}(\hat{k}) = \mathrm{e}^{-j\mathbf{k}\cdot\mathbf{r}_{n_l'n_{l-1}'}}\tilde{\boldsymbol{\beta}}_{n_{l-1}}(\hat{k}), \tag{3.29}$$

  where

$$\mathbf{r}_{n_l'n_{l-1}'} = \mathbf{r}_{n_l'} - \mathbf{r}_{n_{l-1}'} \tag{3.30}$$

  is the vector difference of the source group centers at the particular levels. At the higher level l, the group size is larger than the group size at the lower level $l-1$ resulting in larger spectral content, so that more $\hat{k}$-directions are needed at level l to perform the numerical integration over the Ewald sphere. The radiation patterns are evaluated for the additional $\hat{k}$-directions at level l using interpolation between the known values for the $\hat{k}$-directions at the lower level $l-1$. More on interpolation in MLFMM will be discussed in Section 3.2.2.

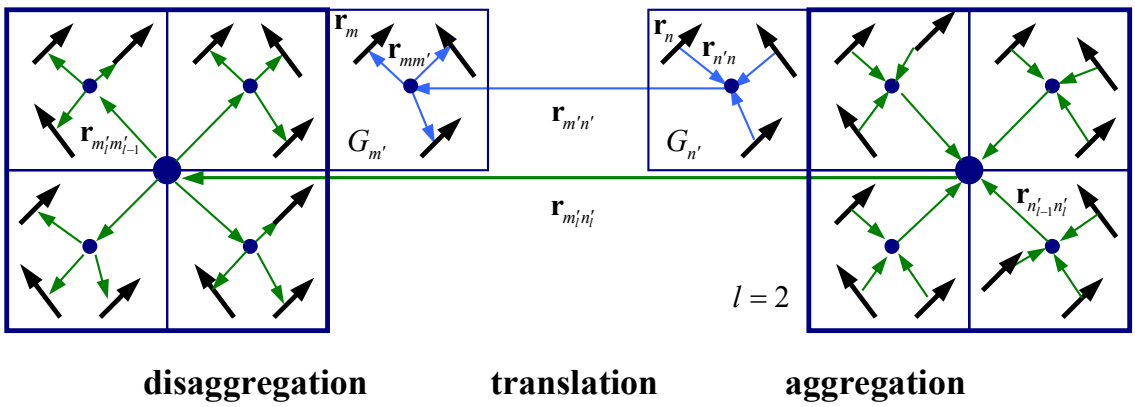

Figure 3.2: Aggregation, translation, and disaggregation process in MLFMM. Subscription for lowest level is neglected.

- Then, the translation and disaggregation process is performed. At each level, translation of radiated field terms from all source groups to the well-separated groups at this particular level is performed. This procedure is done from the lowest level through level $L-2$, which is the highest level on which appropriate group separation is provided. The contributions between non well-separated groups (adjacent groups) are

explicitly evaluated by conventional MoM approaches. Also, starting at level $L-2$, the received contributions are evaluated at lower levels through shifting and anterpolation. Thereby, the receiving pattern of the testing group $G_{m'_{l-1}}$ at the level $l-1$ is obtained by the receiving pattern of the testing group $G_{m'_l}$ at the level l using (3.29). For efficient evaluation of the radiation patterns on the appropriate $\hat{k}$-directions at the level $l-1$, anterpolation is used. This is done because the spectral content of the groups at the level $l-1$ is lower than the spectral content on level l due to smaller group sizes. Hence, less $\hat{k}$-samples are sufficient in this case to represent the radiated fields. More on anterpolation in MLFMM will be discussed in Section 3.2.2. This procedure is performed until the lowest level. There, the received field contributions at the center of the receiving group are finally evaluated at the corresponding testing current elements using the receiving pattern of the appropriate basis functions.

3.2.2 Interpolation and Anterpolation of Group Radiation Patterns

In diagonal MLFMM, the radiation patterns of the source groups are aggregated and disaggregated to obtain the radiation patterns for the groups at higher and lower levels, respectively, as described previously. Thereby, interpolation between known values of the source group radiation patterns at a particular level is used in the aggregation process in order to evaluate the radiation patterns of source groups at additional $\hat{k}$-directions at higher level. In addition, anterpolation is used at the disaggregation process starting from known values of the receiving patterns of testing groups on higher level. The use of interpolation and anterpolation is crucial in MLFMM in order to achieve additional reduction of computational complexity for the BI matrix-vector products. This is because it allows to work with lower sampling rates on lower levels, where the groups are smaller and have lower spectral content. Since the number of small groups is higher, cutting down the workload on lower levels is important for additional reduction of computational complexity.

In order to present the difference between interpolation and anterpolation more clearly, assume that we have a function $f(x)$, whose values are known on sampling points within the range $[x_s, x_l]$ with a particular sampling rate. Then, *interpolation* gives function values on sampling points inside $[x_s, x_l]$ for higher sampling rate than the original. Thus, interpolation increases the sampling rate of $f(x)$ within $[x_s, x_l]$. On the other hand, *anterpolation* states for the adjoint interpolation process. It reduces the sampling rate of the function inside the range $[x_s, x_l]$ and it can be interpreted as a low-pass filtering process. In particular, anterpolation starts from known values of $f(x)$ on sampling points within $[x_s, x_l]$ with some high sampling rate and gives values of $f(x)$ for less sampling points within the same range resulting in smaller sampling rate. It is therefore a down-sampling process, or in other words it is the transpose interpolation. It is noticed, that anterpolation should not be confused with extrapolation, which starts from known values of the function $f(x)$ within $[x_s, x_l]$ and gives function values for a new set of sampling points outside $[x_s, x_l]$.

In this work, *local interpolation* is used, where the radiation pattern at a given direction in the $\hat{k}$-space is interpolated using values at the neighboring directions. Obviously, the same approach is also applied during anterpolation. Local interpolation/anterpolation is easy to implement and it has exponential accuracy. Alternatively, global interpolation can be used, where the radiation pattern at a given direction in the $\hat{k}$-space is interpolated using

values at all directions. This interpolation approach is exact but it is, however, more time consuming than local interpolation. Since radiated three dimensional wave functions are periodic functions of φ, the global interpolation over φ is achieved with an effort of an FFT. The global interpolation over ϑ can be achieved using FFT by forming a periodic function over ϑ [4].

3.2.3 Spherical Harmonics Expansion of the Basis Functions' Far-Fields

The MLFMM is implemented with memory efficiency by expanding the $\hat{k}$-space representation of the basis functions in spherical harmonics as introduced in [26]. Thereby, the far-fields of the basis functions given with the $\hat{k}$-space representations (3.25) are expanded according to

$$\widetilde{\boldsymbol{\beta}}_m(\vartheta,\varphi) = \sum_{p=0}^{P}\sum_{q=-p}^{p} \mathbf{f}_{pq}^{n} Y_{pq}(\vartheta,\varphi), \tag{3.31}$$

where

$$Y_{pq}(\vartheta,\varphi) = \sqrt{\frac{(2p+1)(p-q)!}{4\pi(p+q)!}}\, P_p^q(\cos\vartheta) e^{jq\varphi}\,, \tag{3.32}$$

are the orthonormalized spherical harmonics [87]. Also, P_p^q is the associated Legendre polynomial of degree p and order q. The expansion coefficients are obtained from

$$\mathbf{f}_{pq}^{n} = \oiint \widetilde{\boldsymbol{\beta}}_m(\vartheta,\varphi) Y_{pq}^{*}(\vartheta,\varphi) d\hat{k}^2\,. \tag{3.33}$$

The spherical harmonics expansion coefficients are computed and stored for all basis functions in the initialization step using (3.25) and (3.33).

According to this MLFMM approach, the matrix-vector product computations are performed by first aggregating all spherical harmonics expansion coefficients $\mathbf{f}_{pq}^{n}$ at the center of each MLFMM group at the finest level. After that, the outgoing waves are computed at the quadrature points for all groups on the finest MLFMM level. The translations of outgoing waves into incoming waves as well as the aggregations and disaggregations between different MLFMM levels including interpolation and anterpolation are performed as in standard MLFMM using the numerical quadrature samples. However, when all incoming waves are collected in a certain group on the finest level, the spherical harmonics expansion

$$T_L(\hat{k}\cdot\hat{r}_{m'n'})\left(\bar{\mathbf{I}} - \hat{k}\hat{k}\right)\cdot\widetilde{\boldsymbol{\beta}}_n(\hat{k}) = \sum_{p=0}^{P}\sum_{q=-p}^{p} \mathbf{g}_{pq}^{n} Y_{pq}(\vartheta,\varphi) \tag{3.34}$$

is carried out and by utilizing the orthogonality of the spherical harmonics the closed integral over the Ewald sphere simplifies to the series

$$Z_{mn} = -j\frac{\omega\mu}{4\pi}\sum_{p=0}^{P}\sum_{q=-p}^{p} (\mathbf{f}_{pq}^{m})^{*}\cdot\mathbf{g}_{pq}^{n}\,. \tag{3.35}$$

The number of expansion coefficients needed with this approach is in general less than the corresponding number of quadrature samples for numerical integration in the $\hat{k}$-space resulting in saving of memory requirements without compromising accuracy and numerical speed.

In the present thesis, the FEBI and the MLFMM described in the previous chapters are fully hybridized with the Uniform Geometrical Theory of Diffraction, which will be described briefly in the next chapter.

Chapter 4

The Uniform Geometrical Theory of Diffraction

The *Uniform Geometrical Theory of Diffraction* (UTD) is a field based asymptotic numerical modeling technique, where electromagnetic fields and scattering mechanisms are described according to ray optical concepts, which are accurate for very small wavelengths. It is actually the uniform version of the originally derived Geometrical Theory of Diffraction (GTD) providing continuous field solutions in transition regions around shadow boundaries. The ray optical concepts used to express the fields are based on classical concepts of Geometrical Optics (GO). With UTD, accurate solutions of electromagnetic fields are provided in the high-frequency limit, where the dimensions of the involved objects can be assumed very large as compared to the wavelength. In this chapter, the basic theoretical aspects of UTD will be described.

4.1 Geometrical Optics

The relationship between ray optics and wave propagation is known in physics from earlier days by the works of Huygens in 1690 and Fresnel in 1818. This relationship is the fundamental concept of GO and was formally shown by Luneberg [144] and Kline [145] based on the success of the approach followed by Sommerfeld and Runge [146]. According to this formulation, the transport of energy from one point to another in an isotropic lossless medium is accomplished using the conversation of power flux in a tube of rays. Based on this concept, the GO provides an approximate high-frequency approach for determining the wave propagation for incident and reflected fields by the use of rays as described in the following subsections.

4.1.1 Ray Optical Field Representation

In order to provide ray optical representation of electromagnetic waves within a source free region with lossless and isotropic material properties ε, μ, the Luneberg-Kline asymptotic

expansions [144], [145]

$$\mathbf{E}(\mathbf{r}) = \mathrm{e}^{-jk\Psi(\mathbf{r})} \sum_{n=0}^{\infty} \frac{\mathbf{E}_n(\mathbf{r})}{(j\omega)^n}, \tag{4.1}$$

$$\mathbf{H}(\mathbf{r}) = \mathrm{e}^{-jk\Psi(\mathbf{r})} \sum_{n=0}^{\infty} \frac{\mathbf{H}_n(\mathbf{r})}{(j\omega)^n}. \tag{4.2}$$

are used, where k is the wavenumber in the considered domain given in (3.8) and $\Psi(\mathbf{r})$ is the phase function. In the high-frequency limit as the frequency goes to infinity ($\omega \to \infty \Rightarrow k \to 0$) only the first term ($n = 0$) of the above expansions remains, which is referred to as *ray optical field* (or geometrical optics field). The expressions of these fields are

$$\mathbf{E}_{GO}(\mathbf{r}) = \mathbf{E}_0(\mathbf{r})\mathrm{e}^{-jk\Psi(\mathbf{r})}, \tag{4.3}$$

$$\mathbf{H}_{GO}(\mathbf{r}) = \mathbf{H}_0(\mathbf{r})\mathrm{e}^{-jk\Psi(\mathbf{r})}. \tag{4.4}$$

The Luneberg-Kline expansions (4.1), (4.2) close the gap between ray optics and wave propagation and substituting the expanded fields into Maxwell's equations and the Helmholtz wave equation gives the behavior of ray optical fields in terms of propagation direction, polarization, amplitude as well as phase variation.

In particular, substituting (4.1), (4.2) into Maxwell's equations for the considered domain given in (2.17)-(2.20) shows that $\mathbf{E}_0$, $\mathbf{H}_0$ are both perpendicular to $\nabla\Psi$. Further, evaluating the time-average Poynting vector $\mathcal{S}$ of the ray optical fields for the particular case shows that $\mathcal{S}$ has the direction of $\nabla\Psi$. Also, the phase gradient $\nabla\Psi$ is found to satisfy the *eikonal equation*

$$|\nabla\Psi(\mathbf{r})| = 1. \tag{4.5}$$

Detailed derivations can be found in [147]. Consequently,

$$\hat{e}_s = \nabla\Psi(\mathbf{r}) \tag{4.6}$$

is the unit vector normal to the ray optical fields and it is also the direction in which the power flows. This direction defines the direction of propagation of the ray optical wave. It is noticed, that $\mathbf{E}_0$, $\mathbf{H}_0$ and $\hat{e}_s$ are mutually perpendicular at any point of propagation and there are no field components in the propagation direction. Hence, ray optical fields have a locally plane wave nature. Furthermore, the family of wavefront (equiphase) surfaces, which are normal to the ray optical propagation direction are referred to as *eikonal surfaces* and they satisfy the eikonal equation (4.5). Thus, the unit vector $\hat{e}_s$ is normal to the equiphase surface of constant Ψ, which means that in an isotropic medium the ray optical direction of propagation is everywhere normal to the wavefront. Such highly localized paths of wave propagation, which are directed along the normal to the wavefront are called *rays*. In homogeneous media, the ray trajectories are straight lines, which is not true in the general case of inhomogeneous media, where the ray trajectories are usually curved.

The ray optical field analysis is obtained by considering a bundle of paraxial rays adjacent to the same axial ray, which forms a ray tube. In general, the tube of rays is defined as an *astigmatic ray tube* with general wavefront as shown in Fig. 4.1. The wavefront has a radius of curvature ρ_1 in the principal direction $\hat{X}_1$ and a radius of curvature ρ_2 in the principal

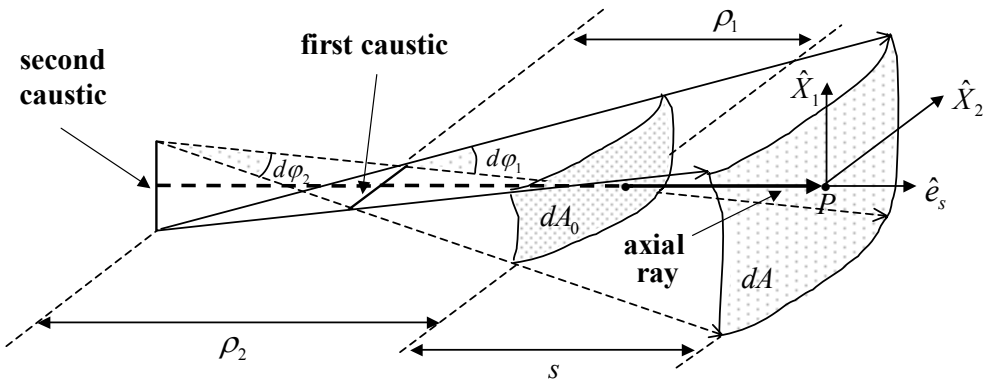

Figure 4.1: Astigmatic ray tube.

direction $\hat{X}_2$. Obviously, the principal directions $\hat{X}_1$, $\hat{X}_2$ are perpendicular to each other and they are also perpendicular to the direction of propagation $\hat{e}_s$. These three unit vectors are defining the two principal planes of curvature of the astigmatic ray tube.

Further, the phase variation of ray optical fields is determined starting from the eikonal equation (4.5) and it is given by

$$\mathrm{e}^{-jk\Psi(s)} = e^{-jk\Psi(0)}\mathrm{e}^{-jks}. \tag{4.7}$$

Thereby,

$$s = |\mathbf{r}_s - \mathbf{r}_0|, \tag{4.8}$$

with $\mathbf{r}_s$ being the position vector of the observation point P and $\mathbf{r}_0$ the position vector of the phase reference point. Detailed derivation can be found in [147].

In addition, amplitude variation and polarization behavior of ray optical fields is determined by substituting (4.1), (4.2) into the Helmholtz wave equation for the electric field

$$\nabla^2\mathbf{E}(\mathbf{r}) + k^2\mathbf{E}(\mathbf{r}) = 0, \tag{4.9}$$

which is derived directly from Maxwell's equations by eliminating $\mathbf{H}$ in the curl equations (2.17) and (2.18). This results in the *transport equation for the ray optical electric field*

$$2(\nabla\Psi\cdot\nabla)\mathbf{E}_0(\mathbf{r}) + (\nabla^2\Psi)\mathbf{E}_0(\mathbf{r}) = 0, \tag{4.10}$$

which is essentially a wave equation for ray optical fields. The solution of the transport equation (4.10) is written as

$$\mathbf{E}_0(s) = \mathbf{E}_0(s_0)\sqrt{\frac{\rho_1\rho_2}{(\rho_1+s)(\rho_2+s)}} \tag{4.11}$$

and using the phase expression (4.7) in the above solution for the phase reference point $s_0 = 0$, the ray optical electric field (4.3) at point P at distance s is given by

$$\mathbf{E}_{GO}(s) = \mathbf{E}(0)\sqrt{\frac{\rho_1\rho_2}{(\rho_1+s)(\rho_2+s)}}e^{-jks}, \tag{4.12}$$

where

$$\mathbf{E}(0) = \mathbf{E}_0(0)e^{-jk\Psi(0)} \tag{4.13}$$

is the ray optical electric field at the reference point, which is assumed to be known. A detailed derivation of this solution can be found in [147]. Also, the expression

$$A(s) = \sqrt{\frac{\rho_1\rho_2}{(\rho_1+s)(\rho_2+s)}} \tag{4.14}$$

gives the amplitude variation of the ray optical field. It expresses the spreading or divergence behavior of the propagating ray tube and is therefore referred to as *spreading* or *divergence factor*. Thereby, ρ_1, ρ_2 are the principal radii of curvature of the reference wavefront $\Psi(0)$ at the point $s_0 = 0$ and $(\rho_1 + s)$, $(\rho_2 + s)$ are the principal radii of curvature of the wavefront at distance s. It is noticed, that for a distance $s = -\rho_1$ or $s = -\rho_2$ the divergence factor becomes infinite, which means that the ray optical field becomes singular. Obviously, these distances are found at the caustics of the ray tube as shown in Fig. 4.1. Thus, GO fails to predict the fields at caustics.

From the physical point of view, the transport equation (4.10) contains divergenceless condition for the power density [147]. Applying Gauss' theorem to this condition for the close surface formed by the section of a ray tube between the reference wavefront dA_0 to dA together with the walls results in

$$|\mathbf{E}_0(s)|^2 dA = |\mathbf{E}_0(0)|^2 dA_0, \tag{4.15}$$

which is a statement of power conservation. This means that the amplitude of the ray optical electric field is given by

$$|\mathbf{E}_0(s)| = |\mathbf{E}_0(0)|\sqrt{\frac{dA_0}{dA}}. \tag{4.16}$$

Thereby, $s_0 = 0$ is assumed as the phase reference point. Further, using simple geometry for the ray tube shown in Fig. 4.1 we have

$$dA_0 = \rho_1\rho_2 d\varphi_1 d\varphi_2 = \frac{d\varphi_1 d\varphi_2}{G_c(0)}, \tag{4.17}$$

$$dA = (\rho_1+s)(\rho_2+s)d\varphi_1 d\varphi_2 = \frac{d\varphi_1 d\varphi_2}{G_c(s)}, \tag{4.18}$$

with G_c denoting Gaussian curvature of the wavefront at P. Thereby, φ_1 and φ_2 are the angles of the ray tube walls focusing at the first and second caustic, respectively, as shown in Fig. 4.1. From the above relations using (4.14) we see that

$$\sqrt{\frac{dA_0}{dA}} = \sqrt{\frac{\rho_1\rho_2}{(\rho_1+s)(\rho_2+s)}} = A(s). \tag{4.19}$$

Comparing the ray optical field expression in (4.12) with (4.16) and (4.19) shows clearly, that the divergence factor represents amplitude variation in the ray tube and in addition, it can be seen that the ray optical expression follows as a consequence of the power conservation law. Particularly, the amplitude variation of the ray optical field is governed by the conservation of power flux within the ray tube and this is typical for ray optical fields.

Finally, the ray optical magnetic field at a point P at distance s from the reference point $s_0 = 0$ is given by

$$\mathbf{H}_{GO}(s) = \frac{1}{Z}\hat{e}_s \times \mathbf{E}_{GO}(s) \tag{4.20}$$

by simply taking into account the locally plane wave nature of the ray optical fields. Thereby, Z is the wave impedance in the considered homogeneous region given by (2.68).

4.1.2 Reflection on Surfaces

The propagation of ray optical fields in homogeneous and isotropic media is performed along straight ray trajectories with amplitude variations, which obey to the conservation law of power flux as far as no obstacles exist in the propagation path of the ray. However, when the ray optical field impinges on an object, fundamental scattering mechanisms are taken place, which are in analogy of the scattering mechanisms of light described in optical physics. This is not surprising, since the ray optical field is an asymptotic representation of electromagnetic waves for the high-frequency limit. Assuming that the ray optical field impinges on a smooth surface the dominant mechanism is reflection, which can be described in a ray optical sense by GO using the field representation discussed in Section 4.1.1. From the geometrical optics point of view, reflection is a *local phenomenon* depending on the *local (critical) reflection point*, which provides the GO reflected field contributions to the direction of the observation point.

Consider a ray optical wave, which propagates towards a generally curved smooth surface by an angle of incidence ϑ^i with respect to the normal unit vector on the surface $\hat{n}$ looking into the direction of the incident field as illustrated in Fig. 4.2. The reflection mechanism for the incident and the reflected ray tube is illustrated in Fig. 4.3 a). The GO reflected electric field at an observation point P on the trajectory of the reflected ray with position vector $\mathbf{r}_s$ is given by the expression

$$\mathbf{E}^r(\mathbf{r}_s) = \bar{\mathbf{R}}^E \cdot \mathbf{E}^i(\mathbf{r}_{Q_R}) A_R(s) \mathrm{e}^{-jks}, \tag{4.21}$$

where $\mathbf{r}_{Q_R}$ is the reflection point on the surface, which is taken as the phase reference point for the reflected ray tube. So, the distance s on the reflected ray trajectory from the phase reference point to the observation point P is given by (4.8) with $\mathbf{r}_0 = \mathbf{r}_{Q_R}$. Also, $\mathbf{E}^i(\mathbf{r}_{Q_R})$ is the incident ray optical electric field at the reflection point $\mathbf{r}_{Q_R}$ on the surface, which is assumed to be known. The direction of reflection to the particular observation point P is determined by *Snell's law of reflection*, which is fully conformal to Fermat's principle as dictated by optical physics. According to this,

$$\vartheta^i = \vartheta^r, \tag{4.22}$$

which means that the angle of ray incidence ϑ^i, defined by $\hat{n}$ and the propagation direction $\hat{e}^i$ of the incident ray, is equal to the angle of reflection ϑ^r, defined by $\hat{n}$ and the propagation direction $\hat{e}^r$ of the reflected ray. Snell's law is derived by applying the boundary condition for the total GO field on the reflection surface.

In addition, $A_R(s)$ is the divergence factor of the reflected ray given by

$$A_R(s) = \sqrt{\frac{\rho_1^r \rho_2^r}{(\rho_1^r + s)(\rho_2^r + s)}}, \tag{4.23}$$

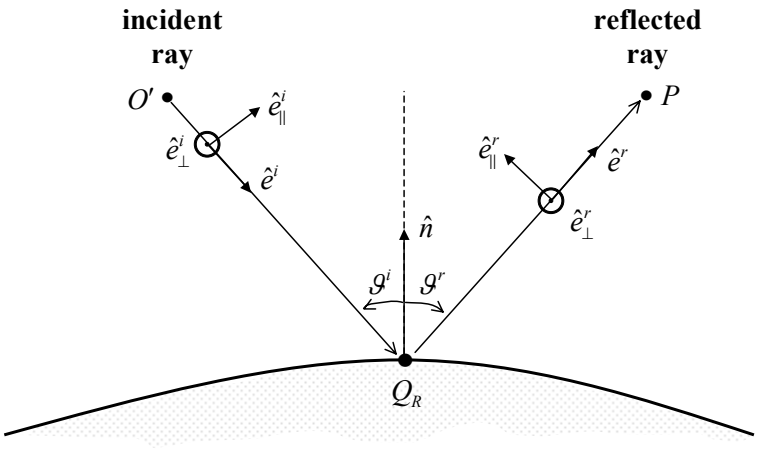

Figure 4.2: Local ray-fixed coordinate system for reflection.

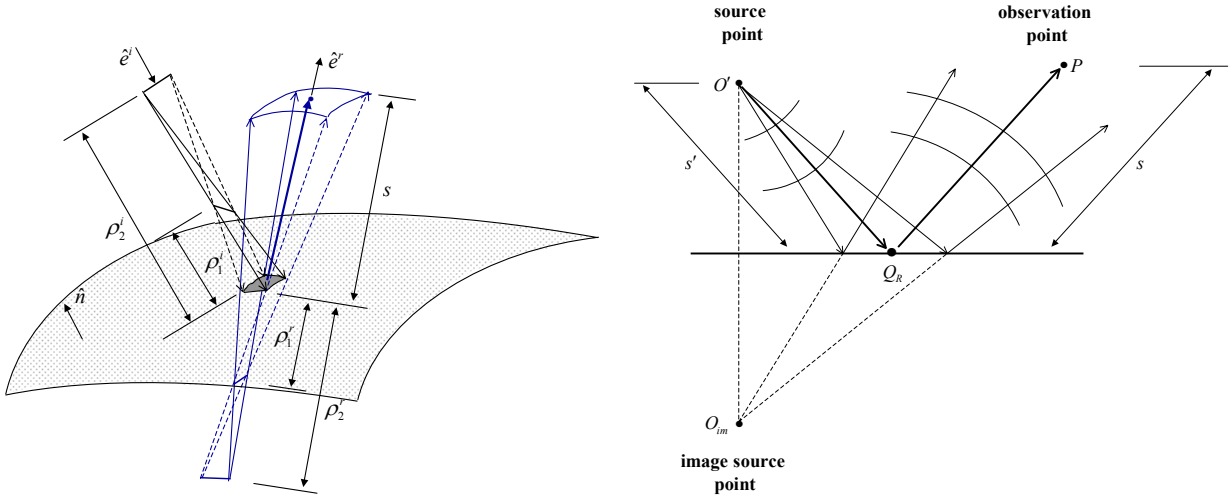

a) b)

Figure 4.3: Astigmatic ray tubes for reflection of ray optical field. a) On smooth curved surface. b) On plane surface.

where ρ^r_1, ρ^r_2 are the principal radii of curvature of the reflected wavefront at the reflection point $\mathbf{r}_{Q_R}$ as illustrated in Fig. 4.3 a). In case of a plane reflection surface, these radii of curvature at $\mathbf{r}_{Q_R}$ are equal to the radii of curvature of the incident wavefront at the same point, thus

$$\rho^r_j = \rho^i_j, \qquad j = 1, 2. \tag{4.24}$$

This can be explained illustratively using image theory as shown in Fig. 4.3 b). For plane reflection surface, the divergence factor of the reflected ray is given by

$$A_R(s) = \begin{cases} 1, & \text{plane wave} \\ \sqrt{\frac{s'}{s'+s}}, & \text{cylindrical wave} \\ \frac{s'}{s'+s}, & \text{spherical wave} \end{cases}, \tag{4.25}$$

which is derived using (4.23) and (4.24) along with the principal radii of curvature for the case of plane ($\rho_1 = \rho_2 = \infty$), cylindrical ($\rho_1 = \infty$, $\rho_2 = s'$), and spherical ($\rho_1 = \rho_2 = s'$) wavefront, respectively. Thereby, s' is the distance from the source point O' to the phase reference point Q_R. In general cases of curved reflection surfaces, the principal radii of curvature of the reflected wavefront at the point of reflection additionally depend on the principal radii of curvature of the reflection surface at the same point. Thereby, the principal planes of curvature of the wavefronts and those of the surface do not necessarily need to coincide. For calculation of ρ_1^r, ρ_2^r, and $A_R(s)$ for curved surfaces the reader is referred to textbooks in literature [27], [28], [147].

Furthermore, $\bar{\mathbf{R}}^E$ is the dyadic reflection coefficient, which gives the relation of the polarization components of the rays before and after reflection in the ray-fixed coordinate system shown in Fig. 4.2. In this local coordinate system the incident and reflected rays are resolved into components that are parallel, with unit vector $\hat{e}_\parallel^{i,r}$, and perpendicular, with unit vector $\hat{e}_\perp^{i,r}$, to the plane of incidence, defined by $\hat{n}$, $\hat{e}^i$, and reflection, defined by $\hat{n}$, $\hat{e}^r$, respectively. The dyadic reflection coefficient for the electric ray optical field is defined in local ray-fixed coordinates as

$$\bar{\mathbf{R}}^E = R_\parallel^E \hat{e}_\parallel^r \hat{e}_\parallel^i + R_\perp^E \hat{e}_\perp^r \hat{e}_\perp^i, \tag{4.26}$$

where $R_\parallel^E$ is the scalar reflection coefficient for the ray optical electric field related to the field components parallel to the plane of incidence and reflection. Similarly, $R_\perp^E$ is the scalar reflection coefficient for the ray optical electric field related to the field components perpendicular to the plane of incidence and reflection. For a PEC reflection surface the scalar reflection coefficients of the ray optical electric field are given by

$$R_\parallel^E = 1, \tag{4.27}$$

$$R_\perp^E = -1, \tag{4.28}$$

and for a dielectric reflection surface with material properties ε_r, μ_r they are given by

$$R_\parallel^E = \frac{\varepsilon_r \cos\vartheta^i - \sqrt{\varepsilon_r\mu_r - \sin^2\vartheta^i}}{\varepsilon_r \cos\vartheta^i + \sqrt{\varepsilon_r\mu_r - \sin^2\vartheta^i}}, \tag{4.29}$$

$$R_\perp^E = \frac{\mu_r \cos\vartheta^i - \sqrt{\varepsilon_r\mu_r - \sin^2\vartheta^i}}{\mu_r \cos\vartheta^i + \sqrt{\varepsilon_r\mu_r - \sin^2\vartheta^i}}. \tag{4.30}$$

The expressions (4.29), (4.30) are derived by satisfying the transition conditions of the tangential ray optical field components across the dielectric interface [27].

For the magnetic field, the dyadic reflection coefficient is given by

$$\bar{\mathbf{R}}^H = -\bar{\mathbf{R}}^E, \tag{4.31}$$

which means that $R_\parallel^H = -R_\parallel^E$ and $R_\perp^H = -R_\perp^E$. This result is expected due to the plane wave nature of the ray optical fields and it is also shown by image theory using electric and magnetic current sources [148]. Finally, the associated ray optical magnetic field at the observation point P is given by

$$\mathbf{H}^r(\mathbf{r}_s) = \frac{1}{Z}\hat{e}^r \times \mathbf{E}^r(\mathbf{r}_s) \tag{4.32}$$

by taking into account the locally plane wave nature of ray optical fields.

4.2 Diffraction on Wedges

The GO reflected field does only contribute to the specular direction as described in Section 4.1, which means that reflected GO rays do exist only in the lit region of illuminated structures. However, in case of finite surfaces, fields are also existing in the shadow region and these fields cannot be predicted by GO. Assuming that a ray optical field impinges on the edge of a finite surface, the corresponding scattering mechanism is diffraction, which is described in a ray optical sense with GTD introduced by Keller in [29]. Thereby, the idea of GO is extended by diffracted rays, which are allowed to exist also in the shadow regions. These fields are evaluated asymptotically for the high-frequency limit. Ray optical diffraction described by GTD is a local phenomenon, similar to GO reflection, depending strongly on the geometry in the immediate vicinity of the *local (critical) diffraction point* on the scattering edge. However, GTD still fails to predict the fields correctly at the transition regions around the shadow boundaries. The UTD introduced by Kouyoumjian and Pathak in [30] provides an uniform extension of GTD enforcing the fields to be continuous across transition regions.

It is assumed that a ray optical field propagates towards a generally curved perfectly conducting wedge by an angle of incidence β_0' with respect to the tangent on the corresponding edge at the local diffraction point Q_D as illustrated in Fig. 4.4 a). The diffraction mechanism for the incident and the diffracted ray tube is illustrated in Fig. 4.5. According to UTD, the diffracted electric field at an observation point P with position vector $\mathbf{r}_s$ is given by the expression

$$\mathbf{E}^d(\mathbf{r}_s) = \bar{\mathbf{D}}^E \cdot \mathbf{E}^i(\mathbf{r}_{Q_D}) A_D(s) \mathrm{e}^{-jks}, \tag{4.33}$$

where $\mathbf{r}_{Q_D}$ is the diffraction point on the edge, which is taken as the phase reference point for the diffracted ray tube. So, the distance s on the diffracted ray trajectory from the phase reference point to the observation point P is given by (4.8) with $\mathbf{r}_0 = \mathbf{r}_{Q_D}$. Also, $\mathbf{E}^i(\mathbf{r}_{Q_D})$ is the incident ray optical electric field at $\mathbf{r}_{Q_D}$ on the edge, which is assumed to be known. The direction of diffraction to the particular observation point P is determined by the *generalized Fermat's principle* introduced by Keller [29]. According to this, the diffracted rays lie on a cone, whose half angle is equal to the angle of incidence β_0'. This results in the *Keller's law of diffraction* given by

$$\hat{e}_{s'} \cdot \hat{e} = \hat{e}_s \cdot \hat{e} \Rightarrow \beta_0' = \beta_0, \tag{4.34}$$

which means that the angle of ray incidence β_0', defined by the unit vector $\hat{e}$ tangent to the edge at the point of diffraction and the propagation direction $\hat{e}_{s'}$ of the incident ray, is equal to the angle of diffraction β_0, defined by $\hat{e}$ and the propagation direction $\hat{e}_s$ of the particular diffracted ray. In contrast to GO reflection, there exist an infinite number of diffracted rays lying on Keller's cone and each of them satisfying the law of diffraction (4.34).

In addition, $A_D(s)$ is the divergence factor of the diffracted ray given by

$$A_D(s) = \sqrt{\frac{\rho_c}{s(\rho_c + s)}}, \tag{4.35}$$

where ρ_c is the ray caustic distance of the diffracted field defined by the distance between the first and the second caustic of the diffracted ray as illustrated in Fig. 4.5. It is noticed, that the first caustic of the diffracted ray tube according to UTD is located at the edge. In

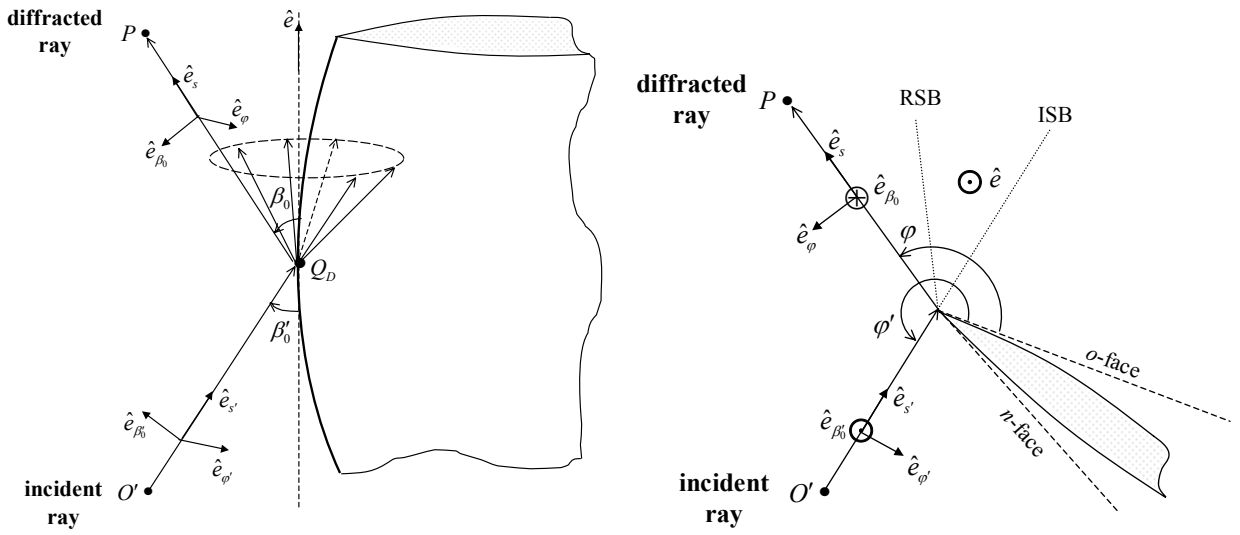

Figure 4.4: Local edge-fixed coordinate system for diffraction. a) 3D view. b) Cross section.

case of a straight wedge, the ray caustic distance is equal to the radius of curvature ρ_c^i of the incident wavefront at Q_D in the plane of incidence defined by $\hat{e}_{s'}$ and $\hat{e}$, thus

$$\rho_c = \rho_c^i. \tag{4.36}$$

Consequently, for a straight wedge the divergence factor of the diffracted ray is given by

$$A_D(s) = \begin{cases} \frac{1}{\sqrt{s}}, & \text{plane wave} \\ \frac{1}{\sqrt{\rho}}, & \text{cylindrical wave} \\ \sqrt{\frac{s'}{s(s'+s)}}, & \text{spherical wave} \end{cases}, \tag{4.37}$$

with $\rho = s \sin\beta_0$, which is derived using (4.35) and (4.36) along with the radius of curvature in the plane of incidence for the case of plane ($\rho_c = \infty$), cylindrical ($\rho_c = \infty$), and spherical ($\rho_c = s'$) wavefront, respectively. Thereby, s' is the distance from the source point O' to the phase reference point Q_D. The one by square root dependence of the divergence factor over distance indicates that diffracted fields have cylindrical wave fronts originating at the edge. Thus, the edge can be assumed as a line source (caustic) for the diffracted fields. In general cases of curved wedges the ray caustic distance of the diffracted field additionally depends on the curvature of the edge. Detailed expressions of ρ_c and $A_D(s)$ for curved wedges can be found in literature [27], [28], [147].

Furthermore, $\overline{\mathbf{D}}^E$ is the dyadic diffraction coefficient, which gives the relation of the polarization components of the rays before and after diffraction in the edge-fixed coordinate system shown in Fig. 4.4 in 3D view and in cross section. In this local coordinate system the incident and diffracted rays are resolved into components that are parallel, with unit vectors $\hat{e}_{\beta_0'}$, $\hat{e}_{\beta_0}$, and perpendicular, with unit vectors $\hat{e}_{\varphi'}$, $\hat{e}_{\varphi}$, to the plane of incidence, defined by $\hat{e}_{s'}$, $\hat{e}$, and diffraction, defined by $\hat{e}_s$, $\hat{e}$, respectively. The unit vectors of the local edge-fixed

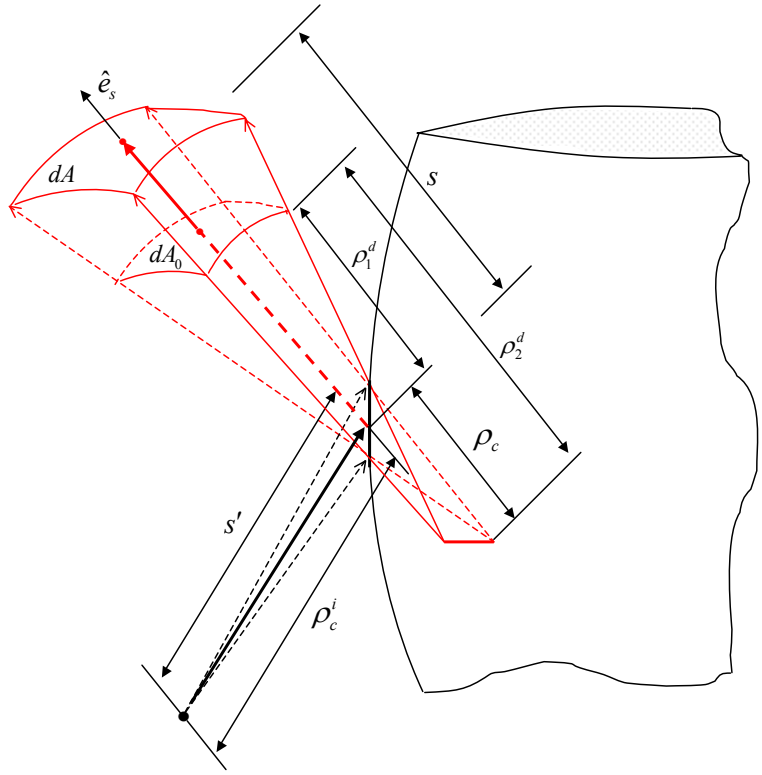

Figure 4.5: Astigmatic ray tubes for diffraction of ray optical field on curved metallic wedge.

coordinate system are connected through

$$\hat{e}_{\varphi'} = \frac{-\hat{e} \times \hat{e}_{s'}}{|\hat{e} \times \hat{e}_{s'}|}, \tag{4.38}$$

$$\hat{e}_{\beta_0'} = \hat{e}_{\varphi'} \times \hat{e}_{s'}, \tag{4.39}$$

$$\hat{e}_{\varphi} = \frac{\hat{e} \times \hat{e}_{s}}{|\hat{e} \times \hat{e}_{s}|}, \tag{4.40}$$

$$\hat{e}_{\beta_0} = \hat{e}_{\varphi} \times \hat{e}_{s}. \tag{4.41}$$

The dyadic diffraction coefficient for the electric UTD field is defined in local edge-fixed coordinates as

$$\bar{\mathbf{D}}^E = -D_{\parallel} \hat{e}_{\beta_0} \hat{e}_{\beta_0'} - D_{\perp} \hat{e}_{\varphi} \hat{e}_{\varphi'}, \tag{4.42}$$

where $D_{\parallel}$ is the scalar diffraction coefficient related to field components parallel to the plane of incidence and diffraction. Similarly, $D_{\perp}$ is the scalar diffraction coefficient related to field components perpendicular to the plane of incidence and diffraction. For a PEC wedge the scalar diffraction coefficients are given by the asymptotic solution of the canonical perfectly conducting wedge problem of infinite extent provided in [30]. They are generally written as the sum of four terms in the form

$$\begin{aligned} D_{\parallel,\perp}(\varphi, \varphi'; F(\cdot)) &= D_1((\varphi, \varphi'; F(\cdot))) + D_2(\varphi, \varphi'; F(\cdot)) \\ &\mp D_3(\varphi, \varphi'; F(\cdot)) + D_4(\varphi, \varphi'; F(\cdot)), \end{aligned} \tag{4.43}$$

where φ', φ are the angles from the reference face of the wedge to the direction of incidence and diffraction, respectively, which are given as reported in [147]. In addition, the functions $F(\cdot)$ are Fresnel functions, which enforce the UTD fields to be continuous across the transition regions in the shadow boundaries defined by the incident ray as well as by the reflected ray in the vicinity of the edge for the given source point. These shadow boundaries are referred to as Incidence Shadow Boundary (ISB) and Reflection Shadow Boundary (RSB), respectively, and are illustrated in Fig. 4.4 b). The Fresnel functions in (4.43) are the *transition functions* of UTD, which approach at the shadow boundaries the value zero at the rate at which the remaining terms of the diffraction coefficients approach infinity. This feature enforce the UTD field to remain bounded in the transition regions as well as continuous across the shadow boundaries and makes the UTD uniform. The terms $D_{1,2}$ in (4.43) are associated with the diffracted field that compensates with the discontinuity of the incident ray optical field when the o-face and n-face of the wedge shown in Fig. 4.4 b) are shadowed, respectively. Also, the terms $D_{3,4}$ in (4.43) are associated with the diffracted field that compensates with the discontinuity of the incident ray optical field when there is reflection from the o-face and n-face of the wedge, respectively. Detailed expressions of the scalar diffraction coefficients and the transition functions along with their arguments are given in [30] and in many literature textbooks like [27], [28], [147].

Similar to GO reflection, the dyadic diffraction coefficient for the magnetic field is given by

$$\bar{\mathbf{D}}^H = -\bar{\mathbf{D}}^E, \tag{4.44}$$

which is expected due to the plane wave nature of the ray optical fields and the definition of the edge-fixed coordinate system according to (4.38)-(4.41). Further, the associated UTD magnetic field at the observation point P is given by

$$\mathbf{H}^d(\mathbf{r}_s) = \frac{1}{Z}\hat{e}_s \times \mathbf{E}^d(\mathbf{r}_s) \tag{4.45}$$

by taking into account the locally plane wave nature of UTD fields. It is finally noticed, that UTD has been extended to dielectric wedges as well as wedges with surfaces described by impedance conditions. For more information on these problems the reader is referred to [149]-[153].

4.3 Limitations of UTD

The major limitation of all ray optical techniques is the failure in predicting fields at the caustics of the ray tubes running the divergence factor of the ray optical fields to infinity. This was described for ray optical field expressions in Section 4.1. For the case of UTD, this means that diffracted fields cannot be predicted for observation points placed directly at the edge. Fields at caustics are computed using source based asymptotic methods like PO or PTD [27], [33]-[35]. Another shortcoming of all ray optical methods, is that they can predict fields only in the ray directions dictated by Fermat's principle. These directions are given by Snell's law for the GO fields and Keller's law for the UTD fields as described in Sections 4.1 and 4.2, respectively. This restricts the applicability of ray optical methods in some cases as e.g. in monostatic computations.

Further, UTD fails to predict the fields at the Edge Diffraction Shadow Boundary (EDSB), which is considered as the Keller's cone at the corners of a finite edge [28]. Across these

boundaries the UTD field abruptly falls to zero. However, this failure is compensated by corner diffraction, which enforces UTD fields to be continuous across EDSBs, in the same way as UTD ensures the continuity of GTD fields across their shadow boundaries [67].

In addition, inside the transition regions UTD fields are not purely ray optical because of the transition functions. In particular, the transition functions depend on specific distance parameters and this dependence results in an amplitude variation which is no more smooth but rather rapid. Consequently, within transition regions the amplitude variation of UTD fields is no more governed by the conservation of power flux within the ray tube as described in Section 4.1.1 and in this sense UTD fields are not purely ray optical within transition regions. However, outside the transition regions the transitions functions become equal to one and the diffracted fields reduce to GTD fields, which are purely ray optical.

Finally, the asymptotic solution of the edge diffraction problem provides a limitation to the distance parameter in the argument of the transition functions. According to this, the source and observation point must be sufficiently away from the edge. For detailed expression of this limitation the reader is referred to the literature [30], [147]. This condition can be violated if s', s become to small or if β_0 is to small, i.e. the incident rays are in the paraxial region close to the edge. For these cases, additional coefficients that extend the validity of UTD in these regions have been developed like in [154].

In this work, the numerical methods presented in Chapters 2 to 4 are fully combined using novel hybrid formulations as described in detail in the following chapters.

Chapter 5

Hybridization of MLFMM with UTD

5.1 Introduction

In the present thesis, the hybrid FEBI-MLFMM method described in Chapter 2 and Chapter 3 is combined with UTD, which was discussed in Chapter 4. The hybridization is performed in both the BIM part of the hybrid method for CFIE formulation by modifying the Green's functions of the problem and the incident field as well as within the matrix-vector multiplications in the various levels of the MLFMM part resulting in a far-field approximation of the translation operator for ray optical contributions. In each case, the Green's function and the incident field are modified according to superposition of all received contributions at an observation point for a given source point. The hybrid formulations provide full coupling between large and composite metallic/dielectric arbitrarily shaped FEBI objects and electrically very large UTD objects within the same environment. Thereby, dielectric regions of FEBI objects are handled conventionally through the efficient combination of BIM with FEM discussed in Section 2.4, which does not affect the hybridization with UTD.

The resulting hybrid method is referred to as hybrid FEBI-MLFMM-UTD method combining for the first time a fast and powerful integral equation method with ray optical techniques [70]-[73]. This provides wide and powerful modeling capabilities especially compared to existing hybridizations of UTD with conventional BI formulations without fast IE solution, which is the case in the hybrid FEBI-UTD method developed in [69]. In that method, modeling flexibility is not good and UTD must often be applied to moderately large objects that should be modeled within the BI part. The hybrid FEBI-MLFMM-UTD method developed in this thesis provides a significant extension to the hybrid FEBI-UTD presented in [69] through novel hybrid formulations, which combine the CFIE as well as the multipole field representations of MLFMM with the ray optical fields of UTD. Thereby, double diffracted ray optical fields at arbitrarily oriented straight metallic edges are included using scalar diffraction coefficients of standard UTD [85], [86]. It is noticed, that to the knowledge of the author the hybrid BIM-UTD field formulations for the MFIE part along with the hybrid MLFMM-UTD formulations are reported in the scientific community for the first time.

In the following, the hybrid field formulations for the FEBI-MLFMM-UTD method are presented and details of the numerical implementation will be discussed.

5.2 Geometrical Configuration

Consider the configuration of Fig. 5.1, where inhomogeneous dielectric FEBI and very large UTD objects exist in the same homogeneous environment such as free space. The FEBI objects are treated according to the formulation presented in Section 2.4 with fast IE solution as reported in Section 3.2. It is obvious, that in the particular configuration the equivalent currents on the boundary surface A radiate in the presence of UTD objects resulting in back coupling to the current distribution itself on the boundary surface of the FEBI objects. Mutual coupling between the objects is taken into account through hybrid field formulations, which will be given in the following sections for clarity only for first order ray optical reflection and diffraction mechanism on UTD objects. However, formulations for higher order ray optical mechanisms are taken into account in the same manner and will be discussed separately in Section 5.5.4 and Section 5.5.5.

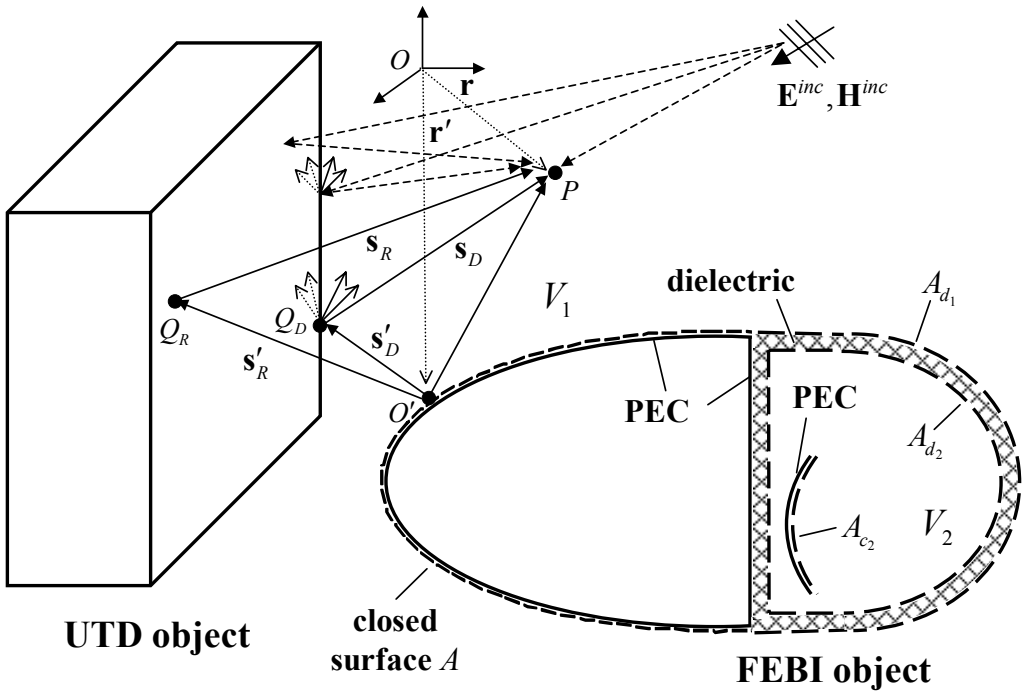

Figure 5.1: Hybrid FEBI-UTD concept.

The hybridization of the FEBI-MLFMM method with UTD is performed in the BI and MLFMM parts by modifying the Green's function and the incident field according to superposition of all received contributions at an observation point for a given source point based on the results presented in [51]. Fields in interior dielectric regions of FEBI objects are treated by FEM as described in Section 2.3. The coupling of FEM with BIM is performed conventionally as described in Section 2.4 particularly through the combination of the basis functions on the boundary surface according to (2.119), which is Green's function independent. Thus, coupling of BIM with FEM does not affect the hybridization with UTD, which is purely performed by Green's function modification. In the following section, the formulation for the hybrid BIM-UTD approach will be given.

5.3 Hybrid BIM-UTD Formulation

The configuration for the hybrid BIM-UTD approach is illustrated in Fig. 5.2. Equivalent surface current densities expressed by (2.39) and (2.40) are placed on the boundary surface A of the FEBI objects according to equivalence principle (see Section 2.1.2) and they radiate in the presence of UTD objects. Through the modification of the Green's function for each current coupling within the MoM procedure the influence of UTD objects on the surface current distribution is taken into account providing full mutual coupling between the objects.

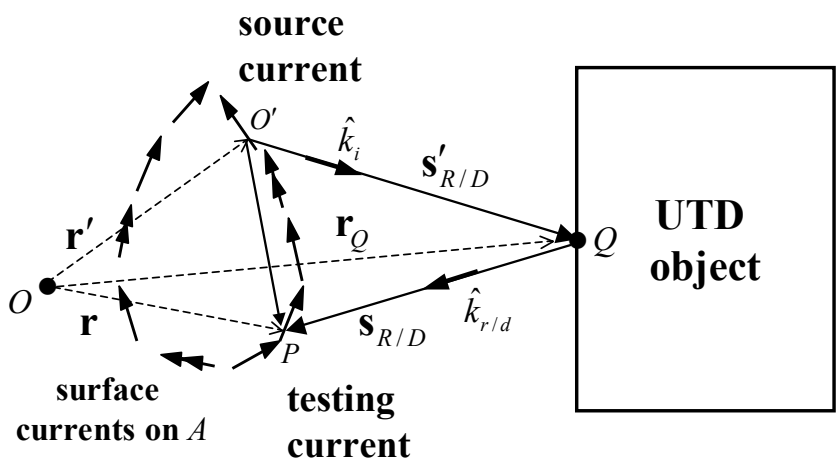

Figure 5.2: Hybrid BIM-UTD concept.

The total Green's functions of the hybrid problem for a given set of source and observation point O' and P with position vector $\mathbf{r}'$ and $\mathbf{r}$, respectively, are expressed as superposition of the direct term of the Green's functions in the absence of UTD objects and all ray optical terms of the Green's functions that arrive due the presence of UTD objects at the particular observation point [69]. This means that

$$\bar{\mathbf{G}}^{E/H}_{J/M,tot}(\mathbf{r},\mathbf{r}') = \bar{\mathbf{G}}^{E/H}_{J/M}(\mathbf{r},\mathbf{r}') + \bar{\mathbf{G}}^{E/H}_{J/M,UTD}(\mathbf{r},\mathbf{r}'), \tag{5.1}$$

where $\bar{\mathbf{G}}^{E/H}_{J,tot}(\mathbf{r},\mathbf{r}')$ and $\bar{\mathbf{G}}^{E/H}_{M,tot}(\mathbf{r},\mathbf{r}')$ are expressing the total Green's functions within the BIM solution domain V of the electric or magnetic field due to electric and magnetic surface currents, respectively. Thereby, $\bar{\mathbf{G}}^{E/H}_{J/M}(\mathbf{r},\mathbf{r}')$ are the direct terms of the Green's functions in the absence of UTD objects given by (2.32)-(2.34) as described in Section 2.1.2. Further, $\bar{\mathbf{G}}^{E/H}_{J/M,UTD}(\mathbf{r},\mathbf{r}')$ are ray optical terms of the Green's functions given by

$$\begin{aligned}\bar{\mathbf{G}}^{E/H}_{J/M,UTD}(\mathbf{r},\mathbf{r}') &= \sum_q \tilde{A}_{R_q}(s_{R_q})\bar{\mathbf{R}}^{E/H}_q \cdot \bar{\mathbf{G}}^{E/H}_{J/M}(\mathbf{r}_{Q_{R_q}},\mathbf{r}') \\ &+ \sum_v \tilde{A}_{D_v}(s_{D_v})\bar{\mathbf{D}}^{E/H}_v \cdot \bar{\mathbf{G}}^{E/H}_{J/M}(\mathbf{r}_{Q_{D_v}},\mathbf{r}') \\ &+ \cdots,\end{aligned} \tag{5.2}$$

where

$$s_{R/D} = |\mathbf{s}_{R/D}| = |\mathbf{r} - \mathbf{r}_{Q_{R/D}}| \tag{5.3}$$

is the distance from the particular reflection/diffraction (local) point $Q_{R/D}$ with position vector $\mathbf{r}_{Q_{R/D}}$ on the UTD object to the observation point. Similarly, the distance from the given source point to the particular local point on the UTD object is given by

$$s'_{R/D} = |\mathbf{s}'_{R/D}| = |\mathbf{r}_{Q_{R/D}} - \mathbf{r}'|. \tag{5.4}$$

Also, the factor

$$\widetilde{A}_{R/D}(s_{R/D}) = A_{R/D}(s_{R/D})\mathrm{e}^{-jks_{R/D}} \tag{5.5}$$

combines the divergence factors $A_{R/D}(s_{R/D})$ of the ray optical mechanisms given in (4.23) and (4.35), respectively, with the appropriate phase factor $\mathrm{e}^{-jks_{R/D}}$. In addition, $\bar{\mathbf{R}}^{E/H}$ are the dyadic reflection coefficients given in (4.26)-(4.31) and $\bar{\mathbf{D}}^{E/H}$ are the dyadic diffraction coefficients given in (4.42)-(4.44). Further, $\bar{\mathbf{G}}^{E/H}_{J/M}(\mathbf{r}_{Q_{R/D}}, \mathbf{r}')$ are field responses at the local points $Q_{R/D}$ on the UTD objects due to a point source placed at $\mathbf{r}'$ and they are evaluated by (2.32)-(2.34) for $\mathbf{r} = \mathbf{r}_{Q_{R/D}}$. These field responses are of ray optical nature in terms of propagation direction, polarization, amplitude and phase variation and they give the incident ray optical fields at the particular local point $\mathbf{r}_{Q_{R/D}}$ on the UTD object. It can be seen that the ray optical terms of the Green's functions are given based on ray optical formulations of reflection and diffraction mechanism given in (4.21) and (4.33) particularly by multiplying the incident field responses at the local points on the UTD objects with the appropriate scalar and dyadic factors of the corresponding ray optical mechanism as described in Section 4.1 and Section 4.2. Finally, direct contributions of the Green's function are not taken into account if the observation point lies in the shadow region of an UTD object.

The hybrid field problem in the solution domain V everywhere outside the FEBI objects is formulated by the surface integral expressions

$$\mathbf{E}(\mathbf{r}) = \iint_A \bar{\mathbf{G}}^{E}_{J,tot}(\mathbf{r}, \mathbf{r}') \cdot \mathbf{J}_A(\mathbf{r}')da' + \iint_A \bar{\mathbf{G}}^{E}_{M,tot}(\mathbf{r}, \mathbf{r}') \cdot \mathbf{M}_A(\mathbf{r}')da' + \mathbf{E}^{inc}_{tot}(\mathbf{r}), \tag{5.6}$$

$$\mathbf{H}(\mathbf{r}) = \iint_A \bar{\mathbf{G}}^{H}_{J,tot}(\mathbf{r}, \mathbf{r}') \cdot \mathbf{J}_A(\mathbf{r}')da' + \iint_A \bar{\mathbf{G}}^{H}_{M,tot}(\mathbf{r}, \mathbf{r}') \cdot \mathbf{M}_A(\mathbf{r}')da' + \mathbf{H}^{inc}_{tot}(\mathbf{r}) \tag{5.7}$$

based on the equivalence principle formulas (2.37) and (2.38) along with the use of the total Green's functions $\bar{\mathbf{G}}^{E/H}_{J,tot}(\mathbf{r}, \mathbf{r}')$ and $\bar{\mathbf{G}}^{E/H}_{M,tot}(\mathbf{r}, \mathbf{r}')$ given in (5.1) and (5.2). Thereby,

$$\mathbf{E}^{inc}_{tot}(\mathbf{r}) = \mathbf{E}^{inc}(\mathbf{r}) + \mathbf{E}^{inc}_{UTD}(\mathbf{r}) \tag{5.8}$$

is the total incident electric field at the observation point $\mathbf{r}$ given by

$$\begin{aligned} \mathbf{E}^{inc}_{tot}(\mathbf{r}) &= \mathbf{E}^{inc}(\mathbf{r}) + \mathbf{E}^{r,inc}(\mathbf{r}) + \mathbf{E}^{d,inc}(\mathbf{r}) + \cdots \\ &= \mathbf{E}^{inc}(\mathbf{r}) + \sum_q \widetilde{A}_{R_q}(s_{R_q})\bar{\mathbf{R}}^{E}_{q} \cdot \mathbf{E}^{inc}(\mathbf{r}_{Q_{R_q}}) \\ &\quad + \sum_v \widetilde{A}_{D_v}(s_{D_v})\bar{\mathbf{D}}^{E}_{v} \cdot \mathbf{E}^{inc}(\mathbf{r}_{Q_{D_v}}) + \cdots, \end{aligned} \tag{5.9}$$

where $\mathbf{E}^{inc}(\mathbf{r})$ is the direct incident electric field received at $\mathbf{r}$, $\mathbf{E}^{inc}_{UTD}(\mathbf{r})$ is the ray optical incident electric field at $\mathbf{r}$ and $\mathbf{E}^{inc}(\mathbf{r}_{Q_{R/D}})$ are the incident electric fields at the particular

point of reflection and diffraction, respectively. It can be seen, that ray optical terms of the incident electric field are evaluated similar to ray optical terms of the Green's function namely by multiplying the incident field at the local points on the UTD objects with the appropriate scalar and dyadic factors of the corresponding ray optical mechanism as described in Section 4.1 and Section 4.2. Furthermore, the total incident magnetic field

$$\mathbf{H}_{tot}^{inc}(\mathbf{r}) = \mathbf{H}^{inc}(\mathbf{r}) + \mathbf{H}_{UTD}^{inc}(\mathbf{r}) \tag{5.10}$$

at $\mathbf{r}$ is written as

$$\begin{aligned}\mathbf{H}_{tot}^{inc}(\mathbf{r}) &= \mathbf{H}^{inc}(\mathbf{r}) + \mathbf{H}^{r,inc}(\mathbf{r}) + \mathbf{H}^{d,inc}(\mathbf{r}) + \cdots \\ &= \mathbf{H}^{inc}(\mathbf{r}) + \frac{1}{Z}\hat{k}_r \times \sum_q \widetilde{A}_{R_q}(s_{R_q})\bar{\mathbf{R}}_q^E \cdot \mathbf{E}^{inc}(\mathbf{r}_{Q_{R_q}}) \\ &\quad + \frac{1}{Z}\hat{k}_d \times \sum_v \widetilde{A}_{D_v}(s_{D_v})\bar{\mathbf{D}}_v^E \cdot \mathbf{E}^{inc}(\mathbf{r}_{Q_{D_v}}) + \cdots\end{aligned} \tag{5.11}$$

by simply taking into account the locally plane wave nature of ray optical fields as described in Section 4.1.1. Thereby, $\mathbf{H}^{inc}(\mathbf{r})$ is the direct incident magnetic field received at $\mathbf{r}$ and Z is the wave impedance in the considered homogeneous region of the BIM solution domain V given by (2.68). Also, $\mathbf{E}^{r/d,inc}(\mathbf{r})$ and $\mathbf{H}^{r/d,inc}(\mathbf{r})$ are the reflected or diffracted terms of the ray optical incident electric or magnetic field at $\mathbf{r}$, respectively, given in (5.9). Finally,

$$\hat{k}_i = \hat{e}^i, \tag{5.12}$$

$$\hat{k}_r = \hat{e}^r, \tag{5.13}$$

$$\hat{k}_d = \hat{e}^d \tag{5.14}$$

are the propagation directions of the incident, reflected, and diffracted rays in the ray-fixed and edge-fixed coordinate system, respectively, as shown in Fig. 5.2. Obviously,

$$\mathbf{s}'_{R/D} = s'_{R/D}\hat{k}_i, \tag{5.15}$$

$$\mathbf{s}_{R/D} = s_{R/D}\hat{k}_{r,d}, \tag{5.16}$$

where the distances $s'_{R/D}$ and $s_{R/D}$ are given in (5.4) and (5.3), respectively.

The IEs of the BIM are derived starting from the surface integral expressions (5.6) and (5.7) and following the same procedure as described in Section 2.2 using the total Green's function (5.1). In particular, substituting the total Green's functions (5.1) with ray optical terms given in (5.2) into (5.6) and applying the procedure reported in Section 2.2.1 we get the *total EFIE* of the hybrid field problem

$$\begin{aligned}\frac{1}{2}\hat{n}(\mathbf{r}) \times \mathbf{M}_A(\mathbf{r}) = \hat{n}(\mathbf{r}) \times \hat{n}(\mathbf{r}) \times \Bigg\{ & j\frac{\omega\mu}{4\pi}\iint_A G(\mathbf{r},\mathbf{r}') \cdot \mathbf{J}_A(\mathbf{r}')da' \\ & + j\frac{1}{4\pi\omega\varepsilon}\nabla\iint_A G(\mathbf{r},\mathbf{r}')\nabla'_A \cdot \mathbf{J}_A(\mathbf{r}')da' + \frac{1}{4\pi}\iint_A \nabla G(\mathbf{r},\mathbf{r}') \times \mathbf{M}_A(\mathbf{r}')da' - \mathbf{E}^{inc}(\mathbf{r}) \\ & + j\frac{\omega\mu}{4\pi}\iint_A \sum_q \widetilde{A}_{R_q}(s_{R_q})\bar{\mathbf{R}}_q^E \cdot \left(\bar{\mathbf{I}} + \frac{1}{k^2}\nabla\nabla'\right) G(\mathbf{r}_{Q_{R_q}},\mathbf{r}') \cdot \mathbf{J}_A(\mathbf{r}')da' \\ & + \frac{1}{4\pi}\iint_A \sum_q \widetilde{A}_{R_q}(s_{R_q})\bar{\mathbf{R}}_q^H \cdot \nabla G(\mathbf{r}_{Q_{R_q}},\mathbf{r}') \times \mathbf{M}_A(\mathbf{r}')da' - \mathbf{E}^{r,inc}(\mathbf{r})\end{aligned}$$

$$
\begin{aligned}
&+j\frac{\omega\mu}{4\pi}\iint\limits_A\sum_v \widetilde{A}_{D_v}(s_{D_v})\bar{\mathbf{D}}_v^E\cdot\left(\bar{\mathbf{I}}+\frac{1}{k^2}\nabla\nabla'\right)G(\mathbf{r}_{Q_{D_v}},\mathbf{r}')\cdot\mathbf{J}_A(\mathbf{r}')da'\\
&+\frac{1}{4\pi}\iint\limits_A\sum_v \widetilde{A}_{D_v}(s_{D_v})\bar{\mathbf{D}}_v^H\cdot\nabla G(\mathbf{r}_{Q_{D_v}},\mathbf{r}')\times\mathbf{M}_A(\mathbf{r}')da'-\mathbf{E}^{d,inc}(\mathbf{r})\\
&+\cdots\Bigg\},\qquad\forall\,\mathbf{r}\in A
\end{aligned}
\tag{5.17}
$$

for the unknown surface current densities $\mathbf{J}_A(\mathbf{r}')$, $\mathbf{M}_A(\mathbf{r}')$. Thereby, the first four terms in the braces of the right hand side of (5.17) are the terms of the direct coupling of the currents in the absence of UTD objects and the remaining terms are all ray optical contributions received at the observation point for a given source point due to the presence of UTD objects according to the configuration shown in Fig. 5.2.

Similarly, substituting the total Green's functions (5.1) with ray optical terms given in (5.2) into (5.7) we get the *total MFIE* of the hybrid field problem

$$
\begin{aligned}
\frac{1}{2}\mathbf{J}_A(\mathbf{r})=\hat{n}(\mathbf{r})\times\Bigg\{&-j\frac{\omega\varepsilon}{4\pi}\iint\limits_A G(\mathbf{r},\mathbf{r}')\cdot\mathbf{M}_A(\mathbf{r}')da'-j\frac{1}{4\pi\omega\mu}\nabla\iint\limits_A G(\mathbf{r},\mathbf{r}')\nabla'_A\cdot\mathbf{M}_A(\mathbf{r}')da'\\
&+\frac{1}{4\pi}\iint\limits_A\nabla G(\mathbf{r},\mathbf{r}')\times\mathbf{J}_A(\mathbf{r}')da'+\mathbf{H}^{inc}(\mathbf{r})\\
&-j\frac{\omega\varepsilon}{4\pi}\iint\limits_A\sum_q \widetilde{A}_{R_q}(s_{R_q})\bar{\mathbf{R}}_q^H\cdot\left(\bar{\mathbf{I}}+\frac{1}{k^2}\nabla\nabla'\right)G(\mathbf{r}_{Q_{R_q}},\mathbf{r}')\cdot\mathbf{M}_A(\mathbf{r}')da'\\
&+\frac{1}{4\pi}\iint\limits_A\sum_q \widetilde{A}_{R_q}(s_{R_q})\bar{\mathbf{R}}_q^E\cdot\nabla G(\mathbf{r}_{Q_{R_q}},\mathbf{r}')\times\mathbf{J}_A(\mathbf{r}')da'+\mathbf{H}^{r,inc}(\mathbf{r})\\
&-j\frac{\omega\varepsilon}{4\pi}\iint\limits_A\sum_v \widetilde{A}_{D_v}(s_{D_v})\bar{\mathbf{D}}_v^H\cdot\left(\bar{\mathbf{I}}+\frac{1}{k^2}\nabla\nabla'\right)G(\mathbf{r}_{Q_{D_v}},\mathbf{r}')\cdot\mathbf{M}_A(\mathbf{r}')da'\\
&+\frac{1}{4\pi}\iint\limits_A\sum_v \widetilde{A}_{D_v}(s_{D_v})\bar{\mathbf{D}}_v^E\cdot\nabla G(\mathbf{r}_{Q_{D_v}},\mathbf{r}')\times\mathbf{J}_A(\mathbf{r}')da'+\mathbf{H}^{d,inc}(\mathbf{r})\\
&+\cdots\Bigg\},\qquad\forall\,\mathbf{r}\in A
\end{aligned}
\tag{5.18}
$$

for the unknown surface current densities $\mathbf{J}_A(\mathbf{r}')$, $\mathbf{M}_A(\mathbf{r}')$. Obviously, the *total CFIE* is formulated by applying (5.17) and (5.18) to the linear combination (2.67).

The solution of the IEs in the hybrid BIM-UTD approach is obtained by MoM according the procedure described in Section 2.2.2. Hence, the boundary surface A is discretized with triangular surface elements and the unknown current densities are expanded in terms of RWG basis functions according to (2.69), (2.70) with unknown expansion coefficients on the discrete triangles. After that, Galerkin's testing approach is applied resulting in a linear system of equations with unknown current expansion coefficients. Particularly, applying this procedure to the total EFIE (5.17) for testing points $\mathbf{r}=\mathbf{r}_m$ and source points $\mathbf{r}'=\mathbf{r}_n$ on the boundary surface A results in hybrid BIM-UTD equation system elements given by the formulas (B.2)-(B.4) in the Appendix B. Similarly, applying the MoM with Galerkin's testing

to the total MFIE (5.18) results in hybrid BIM-UTD equation system elements given by the formulas (B.6)-(B.8). The elements of the system of equations for total CFIE formulation are given by applying the formulas of the Appendix B to the linear combination (2.67). Obviously, through modification of the Green's function within the MoM procedure for each current coupling based on the configuration shown in Fig. 5.2 full back coupling of UTD objects to the equivalent surface currents is provided. Direct contributions in the formulas provided in Appendix B are not taken into account if any UTD object lies between source and testing point. For the evaluation of the elements given in Appendix B operations of dyadic analysis are used as described in Section A.2.1 in the Appendix A. These computations are performed for ray dyad components defined in the global Cartesian coordinate system as described in Section C.3 in the Appendix C.

In the present thesis, UTD is also fully hybridized with MLFMM through novel field formulations, which will be presented and discussed in the following section.

5.4 Hybrid MLFMM-UTD Approach

The hybridization of MLFMM with UTD is performed by approximating ray optical terms of the Green's function with far-field expressions suitable for MLFMM interactions. This results in modification of the translation procedure according to superposition of all received contributions at the receiving groups for all source groups at each MLFMM level, whereas a far-field approximation of the translation operator is used for ray optical contributions. According to this, radiated ray optical fields from the source groups are expressed under far-field conditions using only one $\hat{k}$-direction, which is the direction of ray incidence to the UTD object satisfying Fermat's principle for the particular testing group. That way, the required incident ray optical fields are given at the local points on the UTD objects for each MLFMM interaction. After that, through the use of the appropriate scalar and dyadic factors of the corresponding ray optical mechanism the rays at the receiving groups are finally computed under far-field conditions for only one $\hat{k}$-direction, which is essentially the direction of reflection/diffraction satisfying Fermat's principle. This provides full back coupling of UTD objects to MLFMM groups.

5.4.1 Formulation

The hybrid MLFMM-UTD concept is shown in Fig. 5.3. It is assumed that the source group $G_{n'}$ and the receiving group $G_{m'}$ belong to the FMM model of the FEBI object at a specific level l as described in Section 3.1. Thereby, the direct coupling path from source to testing current for well-separated groups in the absence of UTD objects is written as in (3.9) by intervening the center points of the groups. In that case, the corresponding free space scalar Green's function is expanded in terms of dynamic spherical multipoles based on addition theorem as described in Section 3.1.1. The resulting operator for translating multipoles from the radiating source groups to the receiving testing groups within the pertinent BIM matrix-vector product computations is diagonalized through an expansion of the spherical wave functions into plane waves as described in Section 3.1.2. However, in the hybrid configuration shown in Fig. 5.3 the source groups radiate in the presence of UTD objects and full mutual coupling between MLFMM groups and UTD objects is provided through the presented MLFMM-UTD hybridization.

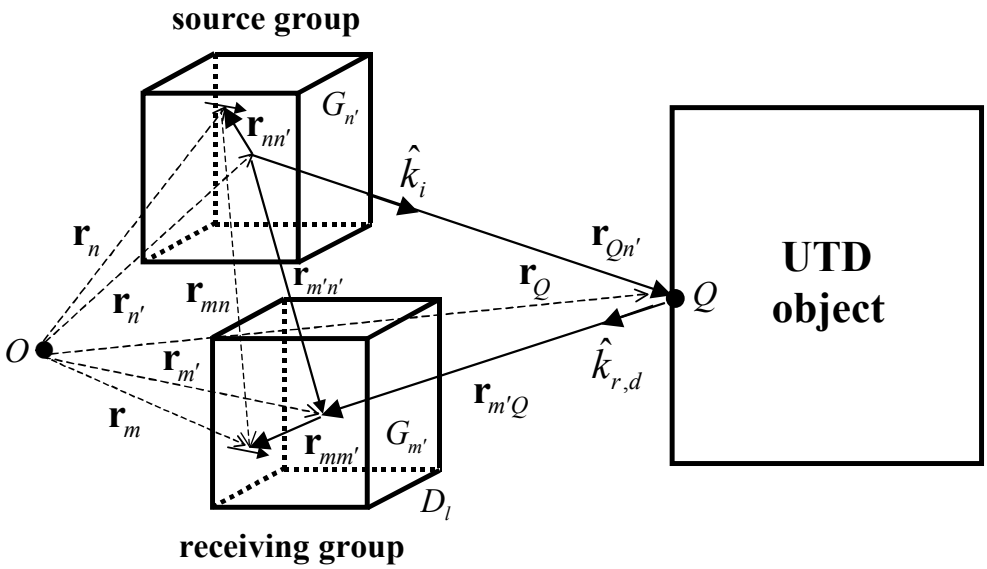

Figure 5.3: Hybrid MLFMM-UTD concept. Ray optical coupling path from source point $\mathbf{r}' = \mathbf{r}_n$ to testing point $\mathbf{r} = \mathbf{r}_m$ is split into four sections $\mathbf{r}_{nn'}$, $\mathbf{r}_{Qn'}$, $\mathbf{r}_{m'Q}$ and $\mathbf{r}_{mm'}$.

In order to take UTD contributions into account in the MLFMM matrix-vector product computations the Green's functions of the problem are modified according to superposition of the direct term associated to interaction of MLFMM groups in the absence of UTD objects and all ray optical terms that arrive due the presence of UTD objects at the receiving groups. Thereby, ray optical terms of the Green's function are approximated by far-field expressions suitable for MLFMM interactions. According to this, the total Green's functions $\bar{\mathbf{G}}^{E/H}_{J/M,tot}(\mathbf{r}_m, \mathbf{r}_n)$ for MLFMM computations from a source current element placed at $\mathbf{r}' = \mathbf{r}_n$ in the source group $G_{n'}$, which is centered at the point $\mathbf{r}_{n'}$, to a testing current element placed at $\mathbf{r} = \mathbf{r}_m$ in the testing group $G_{m'}$, which is centered at the point $\mathbf{r}_{m'}$ as shown in Fig. 5.3, are written as

$$\bar{\mathbf{G}}^{E/H}_{J/M,tot}(\mathbf{r}_m, \mathbf{r}_n) = \bar{\mathbf{G}}^{E/H}_{J/M}(\mathbf{r}_m, \mathbf{r}_n) + \bar{\mathbf{G}}^{E/H}_{J/M,UTD}(\mathbf{r}_m, \mathbf{r}_n), \tag{5.19}$$

where $\bar{\mathbf{G}}^{E/H}_{J/M,UTD}(\mathbf{r}_m, \mathbf{r}_n)$ are ray optical terms of the Green's functions and $\bar{\mathbf{G}}^{E/H}_{J/M}(\mathbf{r}_m, \mathbf{r}_n)$ are direct contributions including the factorized scalar direct term (3.18) in the absence of UTD objects. Thereby, the diagonal translation operator (3.19) is used to translate radiated plane waves from the center of the source group to received plane waves at the center of the testing group over the whole Ewald sphere in the absence of UTD objects as described in Section 3.1.2.

In order to express $\bar{\mathbf{G}}^{E/H}_{J/M,UTD}(\mathbf{r}_m, \mathbf{r}_n)$ in a ray optical sense for MLFMM-UTD computations, the coupling path $\mathbf{r}_{mn} = \mathbf{r}_m - \mathbf{r}_n$ from the source current element to the testing current element over the UTD object is written as

$$\mathbf{r} - \mathbf{r}' = \mathbf{r}_m - \mathbf{r}_n = (\mathbf{r}_m - \mathbf{r}_Q) + (\mathbf{r}_Q - \mathbf{r}_n) = \mathbf{r}_{mQ} + \mathbf{r}_{Qn}, \tag{5.20}$$

by first intervening the local point Q on the UTD object with position vector $\mathbf{r}_Q$. For each of the subpaths in (5.20) the center point of the appropriate group is intervened so that

$$\mathbf{r}_{mQ} = \mathbf{r}_m - \mathbf{r}_Q = (\mathbf{r}_m - \mathbf{r}_{m'}) + (\mathbf{r}_{m'} - \mathbf{r}_Q) = \mathbf{r}_{mm'} + \mathbf{r}_{m'Q}, \tag{5.21}$$

$$\mathbf{r}_{Qn} = \mathbf{r}_Q - \mathbf{r}_n = (\mathbf{r}_Q - \mathbf{r}_{n'}) + (\mathbf{r}_{n'} - \mathbf{r}_n) = \mathbf{r}_{Qn'} + \mathbf{r}_{nn'}. \tag{5.22}$$

Thus, the total path is written as

$$\begin{aligned}\mathbf{r}-\mathbf{r}' = \mathbf{r}_m - \mathbf{r}_n &= (\mathbf{r}_m - \mathbf{r}_{m'}) + (\mathbf{r}_{m'} - \mathbf{r}_Q) + (\mathbf{r}_Q - \mathbf{r}_{n'}) + (\mathbf{r}_{n'} - \mathbf{r}_n) \\ &= \mathbf{r}_{mm'} + \mathbf{r}_{m'Q} + \mathbf{r}_{Qn'} - \mathbf{r}_{nn'}. \end{aligned} \tag{5.23}$$

Further, instead of starting from the addition theorem to represent the Green's functions as it is done in Section 3.1 for conventional MLFMM, a similar procedure as the one used in the Fast Far-Field Approximation (FAFFA) presented in [143] is rather followed. Particularly, it is assumed that the coupling paths from the center of the groups to the local points on the UTD objects $\mathbf{r}_{Qn'}$ and $\mathbf{r}_{m'Q}$ are much larger than the paths within the corresponding groups $\mathbf{r}_{nn'}$ and $\mathbf{r}_{mm'}$, respectively. Under these conditions, each electrical subpath kr_{mQ} and kr_{Qn} in (5.20) is expanded independently in terms of a Taylor series and assuming far-field conditions

$$r_{Qn'} \gg \frac{1}{2}k|\mathbf{r}_{nn'}|^2, \tag{5.24}$$

$$r_{m'Q} \gg \frac{1}{2}k|\mathbf{r}_{mm'}|^2 \tag{5.25}$$

higher order terms of those expansions are neglected. Hence, each electrical subpath in (5.20) is approximated by

$$kr_{mQ} \approx kr_{m'Q} + k\mathbf{r}_{mm'} \cdot \hat{r}_{m'Q}, \tag{5.26}$$

$$kr_{Qn} \approx kr_{Qn'} - k\mathbf{r}_{nn'} \cdot \hat{r}_{Qn'}. \tag{5.27}$$

Using the coupling paths (5.26) and (5.27) in the scalar term (2.34) of the equations (2.32) and (2.33) along with the expressions of ray optical mechanisms on the UTD objects described in Section 4.1 and Section 4.2 the ray optical terms of the Green's functions are written for MLFMM computations with the far-field representations

$$\begin{aligned}\bar{\mathbf{G}}^E_{J,UTD}(\mathbf{r}_m,\mathbf{r}_n) = \frac{\mu}{\varepsilon}\bar{\mathbf{G}}^H_{M,UTD}(\mathbf{r}_m,\mathbf{r}_n) = \\ -j\frac{\omega\mu}{4\pi}\Bigg\{ \sum_q \mathrm{e}^{-j\mathbf{k}_r\cdot\mathbf{r}_{mm'}}\widetilde{A}_{R_q}(s_{R_q})\bar{\mathbf{R}}^{E/H}_q T^{UTD}_L(kr_{Q_{R_q}n'})\cdot\left(\bar{\mathbf{I}}+\frac{1}{k^2}\nabla\nabla'\right)\mathrm{e}^{j\mathbf{k}_i\cdot\mathbf{r}_{nn'}} \\ + \sum_v \mathrm{e}^{-j\mathbf{k}_d\cdot\mathbf{r}_{mm'}}\widetilde{A}_{D_v}(s_{D_v})\bar{\mathbf{D}}^{E/H}_v T^{UTD}_L(kr_{Q_{D_v}n'})\cdot\left(\bar{\mathbf{I}}+\frac{1}{k^2}\nabla\nabla'\right)\mathrm{e}^{j\mathbf{k}_i\cdot\mathbf{r}_{nn'}} \\ + \cdots\Bigg\}\end{aligned} \tag{5.28}$$

and

$$\begin{aligned}\bar{\mathbf{G}}^E_{M,UTD}(\mathbf{r}_m,\mathbf{r}_n) = -\bar{\mathbf{G}}^H_{J,UTD}(\mathbf{r}_m,\mathbf{r}_n) = \\ -\frac{1}{4\pi}\Bigg\{ \sum_q \mathrm{e}^{-j\mathbf{k}_r\cdot\mathbf{r}_{mm'}}\widetilde{A}_{R_q}(s_{R_q})\bar{\mathbf{R}}^{E/H}_q T^{UTD}_L(kr_{Q_{R_q}n'})\cdot\nabla\times\bar{\mathbf{I}}\mathrm{e}^{j\mathbf{k}_i\cdot\mathbf{r}_{nn'}} \\ + \sum_v \mathrm{e}^{-j\mathbf{k}_d\cdot\mathbf{r}_{mm'}}\widetilde{A}_{D_v}(s_{D_v})\bar{\mathbf{D}}^{E/H}_v T^{UTD}_L(kr_{Q_{D_v}n'})\cdot\nabla\times\bar{\mathbf{I}}\mathrm{e}^{j\mathbf{k}_i\cdot\mathbf{r}_{nn'}} \\ + \cdots\Bigg\},\end{aligned} \tag{5.29}$$

where

$$T_L^{UTD}(kr_{Qn'}) = \frac{\mathrm{e}^{-jkr_{Qn'}}}{r_{Qn'}} \tag{5.30}$$

is the *ray optical translation operator*, which translates outgoing ray optical fields from the source groups to incident ray optical fields at the local points on the UTD objects. It is simply the free space scalar Green's function from the center point of the source group to the particular local point on the UTD object. The incident rays at the local points $Q_{R/D}$ on the UTD objects are multiplied with the appropriate scalar factors $\widetilde{A}_{R/D}(s_{R/D})$ and dyadic factors $\overline{\mathbf{R}}^{E/H}$, $\overline{\mathbf{D}}^{E/H}$ of the corresponding ray optical mechanism as described in Section 4.1 and Section 4.2 providing the received ray optical contributions at the center of the receiving groups. Thereby,

$$r_{Qn'} = |\mathbf{r}_Q - \mathbf{r}_{n'}| \tag{5.31}$$

is the distance from the center of the source group to the local point on the UTD object and $s_{R/D}$ is the distance from the particular local point $\mathbf{r}_{Q_{R/D}}$ to the center of the receiving group given by (5.3) for $\mathbf{r} = \mathbf{r}_{m'}$. The terms $\mathrm{e}^{j\mathbf{k}_i\cdot\mathbf{r}_{nn'}}$ and $\mathrm{e}^{-j\mathbf{k}_r\cdot\mathbf{r}_{mm'}}$ are phase shifting factors from the source current to the center of the source group and from the center of the receiving group to the testing current, respectively. They are actually the radiation and receiving pattern of the source and testing current element, respectively. In the present case, only the direction

$$\hat{k}_i = \hat{r}_{Qn'} \tag{5.32}$$

from the working source group to the particular local point is used to represent the radiated fields from the source groups at the working MLFMM level as shown in Fig. 5.3. This direction is essentially the direction of ray incidence from the source group to the UTD object. Similarly, only the direction

$$\hat{k}_{r,d} = \hat{r}_{m'Q} \tag{5.33}$$

from the particular local point to the working receiving group is used to represent the received fields at the receiving groups at the working MLFMM level as shown in Fig. 5.3. This direction is actually the direction of reflection/diffraction from the UTD object to the receiving group. Again, direct contributions of the Green's function are ignored if the receiving group is in the shadow region of an UTD object. It is noticed, that the above ray optical expressions (5.28), (5.29) are valid under far-field conditions with respect to the MLFMM group dimension at the working level. This will be discussed more in detail in Section 5.4.2. A detailed derivation of the ray optical terms of the scalar Green's function (5.28) and (5.29) as well as of the ray optical translation operator (5.30) is given in Section C.1 in the Appendix C.

The hybrid system of equations obtained by MoM solution of CFIE in the BIM-UTD part of the hybrid FEBI-MLFMM-UTD method is written as

$$\left[Z_{J,tot}^{CFIE}\right]\{H\} + \left[Z_{M,tot}^{CFIE}\right]\{E\} = \{b\}, \tag{5.34}$$

where $\{H\}, \{E\}$ are vectors containing the unknown electric and magnetic surface current expansion coefficients, respectively, and $\{b\}$ is the excitation vector. Also, $\left[Z_{J,M,tot}^{CFIE}\right]$ are the

total coupling matrices due to electric and magnetic currents, respectively. For conventional BIM-UTD computations among non well-separated groups the elements of those matrices are given by the equations provided in Appendix B. However, starting from the expressions (5.6) and (5.7) and using the total Green's function (5.19) with ray optical terms given in (5.28) and (5.29) we get for MLFMM computations with CFIE formulation the matrix elements of the hybrid problem due to electric and magnetic currents

$$
\begin{aligned}
Z_{mn,J,tot}^{CFIE} = \\
&+c_1\Bigg\{ \iint\limits_{A}\boldsymbol{\beta}_m(\mathbf{r}_m)\cdot\iint\limits_{A'}\left(\bar{\mathbf{I}}+\frac{1}{k^2}\nabla\nabla'\right)G(\mathbf{r}_m,\mathbf{r}_n)\cdot\boldsymbol{\beta}_n(\mathbf{r}_n)da'da \\
&+\sum_q\iint\limits_{A}\boldsymbol{\beta}_m(\mathbf{r}_m)\mathrm{e}^{-j\mathbf{k}_r\cdot\mathbf{r}_{mm'}}\cdot\iint\limits_{A'}\widetilde{A}_{R_q}(s_{R_q})\bar{\mathbf{R}}_q^E T_L^{UTD}(kr_{Q_{R_q}n'})\cdot\left(\bar{\mathbf{I}}+\frac{1}{k^2}\nabla\nabla'\right) \\
&\qquad\cdot\boldsymbol{\beta}_n(\mathbf{r}_n)\mathrm{e}^{j\mathbf{k}_i\cdot\mathbf{r}_{nn'}}da'da \\
&+\sum_v\iint\limits_{A}\boldsymbol{\beta}_m(\mathbf{r}_m)\mathrm{e}^{-j\mathbf{k}_d\cdot\mathbf{r}_{mm'}}\cdot\iint\limits_{A'}\widetilde{A}_{D_v}(s_{D_v})\bar{\mathbf{D}}_v^E T_L^{UTD}(kr_{Q_{D_v}n'})\cdot\left(\bar{\mathbf{I}}+\frac{1}{k^2}\nabla\nabla'\right) \\
&\qquad\cdot\boldsymbol{\beta}_n(\mathbf{r}_n)\mathrm{e}^{j\mathbf{k}_i\cdot\mathbf{r}_{nn'}}da'da \\
&+\cdots\Bigg\} \\
&+c_2\Bigg\{ \iint\limits_{A}\left[\nabla\times\boldsymbol{\alpha}_m(\mathbf{r}_m)\right]\cdot\iint\limits_{A'}G(\mathbf{r}_m,\mathbf{r}_n)\boldsymbol{\beta}_n(\mathbf{r}_n)da'da \\
&+\sum_q\iint\limits_{A}\left[\nabla\times\boldsymbol{\alpha}_m(\mathbf{r}_m)\mathrm{e}^{-j\mathbf{k}_r\cdot\mathbf{r}_{mm'}}\right]\cdot\iint\limits_{A'}\widetilde{A}_{R_q}(s_{R_q})\bar{\mathbf{R}}_q^E T_L^{UTD}(kr_{Q_{R_q}n'}) \\
&\qquad\cdot\boldsymbol{\beta}_n(\mathbf{r}_n)\mathrm{e}^{j\mathbf{k}_i\cdot\mathbf{r}_{nn'}}da'da \\
&+\sum_v\iint\limits_{A}\left[\nabla\times\boldsymbol{\alpha}_m(\mathbf{r}_m)\mathrm{e}^{-j\mathbf{k}_d\cdot\mathbf{r}_{mm'}}\right]\cdot\iint\limits_{A'}\widetilde{A}_{D_v}(s_{D_v})\bar{\mathbf{D}}_v^E T_L^{UTD}(kr_{Q_{D_v}n'}) \\
&\qquad\cdot\boldsymbol{\beta}_n(\mathbf{r}_n)\mathrm{e}^{j\mathbf{k}_i\cdot\mathbf{r}_{nn'}}da'da \\
&+\cdots\Bigg\}
\end{aligned}
\tag{5.35}
$$

and

$$
\begin{aligned}
Z_{mn,M,tot}^{CFIE} = \\
&+c_3\Bigg\{ \iint\limits_{A}\left[\nabla\times\boldsymbol{\beta}_m(\mathbf{r}_m)\right]\cdot\iint\limits_{A'}G(\mathbf{r}_m,\mathbf{r}_n)\boldsymbol{\beta}_n(\mathbf{r}_n)da'da \\
&+\sum_q\iint\limits_{A}\left[\nabla\times\boldsymbol{\beta}_m(\mathbf{r}_m)\mathrm{e}^{-j\mathbf{k}_r\cdot\mathbf{r}_{mm'}}\right]\cdot\iint\limits_{A'}\widetilde{A}_{R_q}(s_{R_q})\bar{\mathbf{R}}_q^H T_L^{UTD}(kr_{Q_{R_q}n'}) \\
&\qquad\cdot\boldsymbol{\beta}_n(\mathbf{r}_n)\mathrm{e}^{j\mathbf{k}_i\cdot\mathbf{r}_{nn'}}da'da
\end{aligned}
$$

$$
\begin{aligned}
&+\sum_{v}\iint\limits_{A}\left[\nabla\times\boldsymbol{\beta}_m(\mathbf{r}_m)\mathrm{e}^{-j\mathbf{k}_d\cdot\mathbf{r}_{mm'}}\right]\cdot\iint\limits_{A'}\widetilde{A}_{D_v}(s_{D_v})\bar{\mathbf{D}}_v^H T_L^{UTD}(kr_{Q_{D_v}n'})\\
&\qquad\qquad\cdot\boldsymbol{\beta}_n(\mathbf{r}_n)\mathrm{e}^{j\mathbf{k}_i\cdot\mathbf{r}_{nn'}}da'da\\
&+\cdots\Bigg\}\\
&+c_4\Bigg\{\iint\limits_{A}\boldsymbol{\alpha}_m(\mathbf{r}_m)\cdot\iint\limits_{A'}\left(\bar{\mathbf{I}}+\frac{1}{k^2}\nabla\nabla'\right)G(\mathbf{r}_m,\mathbf{r}_n)\cdot\boldsymbol{\beta}_n(\mathbf{r}_n)da'da\\
&+\sum_{q}\iint\limits_{A}\boldsymbol{\alpha}_m(\mathbf{r}_m)\mathrm{e}^{-j\mathbf{k}_r\cdot\mathbf{r}_{mm'}}\cdot\iint\limits_{A'}\widetilde{A}_{R_q}(s_{R_q})\bar{\mathbf{R}}_q^H T_L^{UTD}(kr_{Q_{R_q}n'})\cdot\left(\bar{\mathbf{I}}+\frac{1}{k^2}\nabla\nabla'\right)\\
&\qquad\qquad\cdot\boldsymbol{\beta}_n(\mathbf{r}_n)\mathrm{e}^{j\mathbf{k}_i\cdot\mathbf{r}_{nn'}}da'da\\
&+\sum_{v}\iint\limits_{A}\boldsymbol{\alpha}_m(\mathbf{r}_m)\mathrm{e}^{-j\mathbf{k}_d\cdot\mathbf{r}_{mm'}}\cdot\iint\limits_{A'}\widetilde{A}_{D_v}(s_{D_v})\bar{\mathbf{D}}_v^H T_L^{UTD}(kr_{Q_{D_v}n'})\cdot\left(\bar{\mathbf{I}}+\frac{1}{k^2}\nabla\nabla'\right)\\
&\qquad\qquad\cdot\boldsymbol{\beta}_n(\mathbf{r}_n)\mathrm{e}^{j\mathbf{k}_i\cdot\mathbf{r}_{nn'}}da'da\\
&+\cdots\Bigg\},
\end{aligned}
\tag{5.36}
$$

respectively, with $m,n=1,2,\ldots,N$ and $\mathbf{r}_m,\mathbf{r}_n\in A$. Thereby, the coefficients c_1 to c_4 are given in (3.4)-(3.7). Also, $\boldsymbol{\beta}(\mathbf{r})$ and $\boldsymbol{\alpha}(\mathbf{r})$ are the RWG basis functions of the BIM part given in (2.71) and the edge element basis functions of the FEM part given in (2.98), respectively. Substituting the factorized direct scalar Green's function in the absence of UTD objects given in (3.18) into (5.35) and (5.36) and using the substitution $\nabla\rightarrow-j\mathbf{k}$ similar to the procedure described in Section 3.1.3, we finally get for the hybrid MLFMM-UTD part the matrix elements due to electric and magnetic currents

$$
\begin{aligned}
Z_{mn,J,tot}^{CFIE}=&-j\frac{\omega\mu}{4\pi}\alpha\Bigg\{\oint\!\!\!\oint\tilde{\boldsymbol{\beta}}_m^*(\hat{k})\cdot T_L(\hat{k}\cdot\hat{r}_{m'n'})\left(\bar{\mathbf{I}}-\hat{k}\hat{k}\right)\cdot\tilde{\boldsymbol{\beta}}_n(\hat{k})\,d\hat{k}^2\\
&+\sum_{q}\tilde{\boldsymbol{\beta}}_m^*(\hat{k}_r)\cdot\widetilde{A}_{R_q}(s_{R_q})\bar{\mathbf{R}}_q^E T_L^{UTD}(kr_{Q_{R_q}n'})\cdot\left(\bar{\mathbf{I}}-\hat{k}_r\hat{k}_i\right)\cdot\tilde{\boldsymbol{\beta}}_n(\hat{k}_i)\\
&+\sum_{v}\tilde{\boldsymbol{\beta}}_m^*(\hat{k}_d)\cdot\widetilde{A}_{D_v}(s_{D_v})\bar{\mathbf{D}}_v^E T_L^{UTD}(kr_{Q_{D_v}n'})\cdot\left(\bar{\mathbf{I}}-\hat{k}_d\hat{k}_i\right)\cdot\tilde{\boldsymbol{\beta}}_n(\hat{k}_i)\\
&+\cdots\Bigg\}\\
&+jZ\frac{k}{4\pi}(1-\alpha)\Bigg\{\oint\!\!\!\oint\left[\hat{k}\times\tilde{\boldsymbol{\alpha}}_m^*(\hat{k})\right]\cdot T_L(\hat{k}\cdot\hat{r}_{m'n'})\tilde{\boldsymbol{\beta}}_n(\hat{k})\,d\hat{k}^2\\
&+\sum_{q}\left[\hat{k}_r\times\tilde{\boldsymbol{\alpha}}_m^*(\hat{k}_r)\right]\cdot\widetilde{A}_{R_q}(s_{R_q})\bar{\mathbf{R}}_q^E T_L^{UTD}(kr_{Q_{R_q}n'})\cdot\tilde{\boldsymbol{\beta}}_n(\hat{k}_i)\\
&+\sum_{v}\left[\hat{k}_d\times\tilde{\boldsymbol{\alpha}}_m^*(\hat{k}_d)\right]\cdot\widetilde{A}_{D_v}(s_{D_v})\bar{\mathbf{D}}_v^E T_L^{UTD}(kr_{Q_{D_v}n'})\cdot\tilde{\boldsymbol{\beta}}_n(\hat{k}_i)\\
&+\cdots\Bigg\}
\end{aligned}
\tag{5.37}
$$

and

$$
\begin{aligned}
Z^{CFIE}_{mn,M,tot} = j\frac{k}{4\pi}\alpha\Bigg\{ & \oiint \left[\hat{k}\times\tilde{\boldsymbol{\beta}}^{*}_{m}(\hat{k})\right]\cdot T_L(\hat{k}\cdot\hat{r}_{m'n'})\tilde{\boldsymbol{\beta}}_{n}(\hat{k})\,d\hat{k}^2 \\
& + \sum_{q}\left[\hat{k}_r\times\tilde{\boldsymbol{\beta}}^{*}_{m}(\hat{k}_r)\right]\cdot\tilde{A}_{R_q}(s_{R_q})\bar{\mathbf{R}}^{H}_{q}T^{UTD}_{L}(kr_{Q_{R_q}n'})\cdot\tilde{\boldsymbol{\beta}}_{n}(\hat{k}_i) \\
& + \sum_{v}\left[\hat{k}_d\times\tilde{\boldsymbol{\beta}}^{*}_{m}(\hat{k}_d)\right]\cdot\tilde{A}_{D_v}(s_{D_v})\bar{\mathbf{D}}^{H}_{v}T^{UTD}_{L}(kr_{Q_{D_v}n'})\cdot\tilde{\boldsymbol{\beta}}_{n}(\hat{k}_i) \\
& + \cdots\Bigg\} \\
& + jZ\frac{\omega\varepsilon}{4\pi}(1-\alpha)\Bigg\{ \oiint \tilde{\boldsymbol{\alpha}}^{*}_{m}(\hat{k})\cdot T_L(\hat{k}\cdot\hat{r}_{m'n'})\left(\bar{\mathbf{I}}-\hat{k}\hat{k}\right)\cdot\tilde{\boldsymbol{\beta}}_{n}(\hat{k})\,d\hat{k}^2 \\
& + \sum_{q}\tilde{\boldsymbol{\alpha}}^{*}_{m}(\hat{k}_r)\cdot\tilde{A}_{R_q}(s_{R_q})\bar{\mathbf{R}}^{H}_{q}T^{UTD}_{L}(kr_{Q_{R_q}n'})\cdot\left(\bar{\mathbf{I}}-\hat{k}_r\hat{k}_i\right)\cdot\tilde{\boldsymbol{\beta}}_{n}(\hat{k}_i) \\
& + \sum_{v}\tilde{\boldsymbol{\alpha}}^{*}_{m}(\hat{k}_d)\cdot\tilde{A}_{D_v}(s_{D_v})\bar{\mathbf{D}}^{H}_{v}T^{UTD}_{L}(kr_{Q_{D_v}n'})\cdot\left(\bar{\mathbf{I}}-\hat{k}_d\hat{k}_i\right)\cdot\tilde{\boldsymbol{\beta}}_{n}(\hat{k}_i) \\
& + \cdots\Bigg\},
\end{aligned}
\tag{5.38}
$$

respectively. Thereby, the $\hat{k}$-space representations of the basis functions $\tilde{\boldsymbol{\beta}}(\hat{k})$ and $\tilde{\boldsymbol{\alpha}}(\hat{k})$ are given in (3.25) and (3.26), respectively, with * denoting complex conjugation. Also, the factor $\tilde{A}_{R/D}(s_{R/D})$ is given by (5.5). Further, $\bar{\mathbf{R}}^{E/H}$ are the dyadic reflection coefficients given in (4.26)-(4.31) and $\bar{\mathbf{D}}^{E/H}$ are the dyadic diffraction coefficients given in (4.42)-(4.44), whereas the particular dyadic coefficient for the electric field is used for electric current sources and the dyadic coefficient for the magnetic field is used for magnetic current sources. Obviously, the first term within each bracket in the right hand side of (5.37) and (5.38) is the term of the direct coupling of the MLFMM groups in the absence of UTD objects and the remaining terms are all ray optical contributions received at the testing groups at the working level due to the presence of UTD objects according to the configuration shown in Fig. 5.3. Direct terms are ignored if the receiving group is in the shadow region of an UTD object. Equations (5.37) and (5.38) are used for interactions among well-separated groups on the various MLFMM levels as described in Section 3.1.3. The coupling terms between nearby groups, which are not well-separated, are computed by conventional MoM approaches, whereas coupling with UTD is obtained as described in Section 5.3 with matrix elements given in the Appendix B. Various issues regarding the numerical implementation of the hybrid MLFMM-UTD approach will be discussed in the following subsections.

5.4.2 Numerical Implementation

In the numerical implementation of conventional MLFMM a limited number of sampling points $\hat{k}_p$ with $p \in [1, 2, ..., K]$ is used to evaluate the $\hat{k}$-space integrals. In general, the ray directions of incidence $\hat{k}_i$, reflection $\hat{k}_r$, or diffraction $\hat{k}_d$ required to fulfil Fermats principle for a particular source and receiving group configuration do not match with any of

these sampling points. For this reason, the required direction of incidence must be interpolated from the neighboring sampling points. Similarly, after reflection or diffraction, the appropriate ray direction must be anterpolated to the neighboring sampling points. Particularly, local Lagrange interpolation/anterpolation is used for this purpose similarly to the procedure described in Section 3.2.2 during aggregation and disaggregation process of conventional MLFMM. Thereby, $K_0 \ll K$ number of interpolation and anterpolation points are used together with the corresponding interpolation and anterpolation weights w_{p_t} and $w_{p_{t'}}$, respectively. According to this, the desired direction of ray incidence $\hat{k}_i$ is interpolated from the close directions of the sampling points $\hat{k}_{i,p_t}$ and the desired direction of reflection or diffraction is anterpolated to the close directions $\hat{k}_{r/d,p_{t'}}$ of the sampling points. The full hybrid matrix-vector product in case of Lagrange interpolation for evaluation of ray optical directions in the UTD part is given in Section C.2 in the Appendix C, whereas the computations are performed for ray dyad components defined in the global spherical coordinate system as described in Section C.3 in the Appendix C. This is done for all ray optical terms except reflections on flat metallic surfaces, which are performed in the global Cartesian coordinate system since the radial component is available through the special treatment of reflection terms described in Section 5.5.2. Finally, for the evaluation of the terms given in Appendix C, operations of dyadic analysis are used as described in Section A.2 in the Appendix A.

The conditions (5.24) and (5.25) are used to derive the ray optical expressions of the Green's functions suitable for MLFMM computations. The worst-case of these conditions arises when the source or the testing current element lies at the corner of the corresponding group, which means that the field path within in the group is the largest possible, namely

$$|\mathbf{r}_{nn'}|_{max} = |\mathbf{r}_{mm'}|_{max} = 0.5\sqrt{3}D_l, \tag{5.39}$$

where

$$D_l = 2^{l-1}D_1 \tag{5.40}$$

is the group dimension at level l with D_1 being the smallest group dimension at the lowest MLFMM level. Thus, using (3.8) the worst-case for condition (5.24) and (5.25) becomes

$$r_{UTD} \geq \frac{1}{2}k(0.5\sqrt{3}D_l)^2 = \frac{\pi(0.5\sqrt{3}D_l)^2}{\lambda}. \tag{5.41}$$

It can be seen, that the required condition for ray optical translations is a far-field condition with respect to the MLFMM group sizes at the working level and corresponds to the criterion for far-field translations according to FAFFA [143]. The condition (5.41) requires the local point on the UTD objects to be in the far-field with respect to the group dimensions at the working level. Thus, the UTD objects must only be in the far-field of the individual basis functions included in the working group similar to conventional hybridizations of BIM with UTD and they do not need to be in the far-field of the whole structures.

According to (5.41), the necessary distances to achieve far-field conditions for performing ray optical translations increase with the square of group dimensions as shown in Fig. 5.4. On the other hand, in conventional MLFMM the smallest possible translation region is used in each direction around the source groups on each level for lowest complexity namely

$$d_{l_{FMM}} = 2^l D_1 + 2D_l = 4D_l. \tag{5.42}$$

Due to the fact that the group dimensions are doubled on each level, there is a linear increase of the translation range with the group dimensions. This means that using on each level the smallest possible translation range leads very fast into difficulties in holding the far-field condition on higher levels. In conventional far-field MLFMM, improved translation under far-field conditions can be achieved by considering additional $\hat{k}$-directions in a cone zone around the primary direction connecting the coupling groups [155]. However, such an approach is not conforming with ray optical translations in the hybrid MLFMM-UTD method. In this case, the ray direction of the radiated field from a given source group over the UTD objects to a specific receiving point must satisfy Fermat's principle and for a given configuration including plane UTD objects this direction is unique.

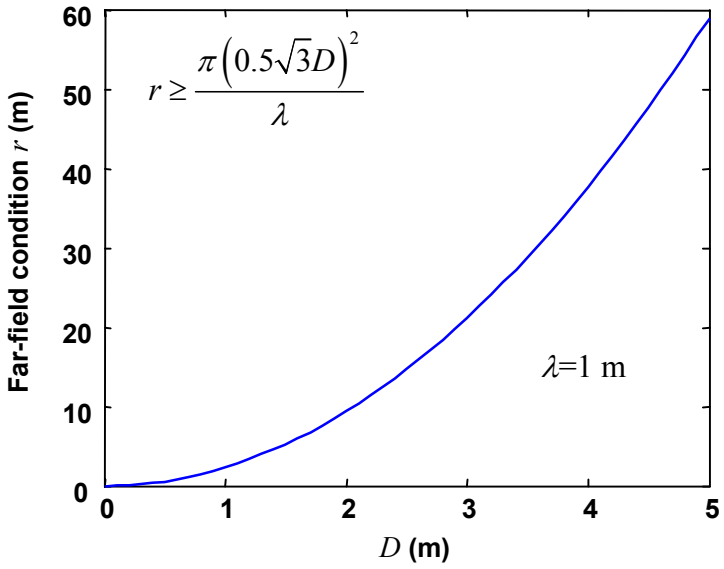

Figure 5.4: Far-field condition with increasing group dimensions.

In the hybrid MLFMM-UTD approach, if on a certain level the far-field condition is not met the corresponding interactions are computed on a finer level. This is achieved by extending the translation range around the source groups with increasing group sizes on coarser levels as shown in Fig. 5.5, where the group dimensions and the corresponding translation ranges on various levels are illustrated with different colors. On the lowest level, standard translation range is used for ray optical translations illustrated with the green region in Fig. 5.5. However, for higher levels the translation range around the source groups for ray optical contributions is extended according to

$$d_{l_{UTD}} = d_{l_{FMM}} + 2(l-1)d_m, \tag{5.43}$$

where the conventional translation range $d_{l_{FMM}}$ is given in (5.42) and d_m is a multiplier controlling the extension width. In Fig. 5.5, the translation region for the second level is illustrated with the red region, where it can be seen that it is extended by two groups. For the third level the extension would be six groups and so on. The translation range extension is applied only for ray optical translations and as a consequence the UTD contributions are evaluated using fewer MLFMM levels than in the case of direct contributions, where the smallest possible translation range is always used.

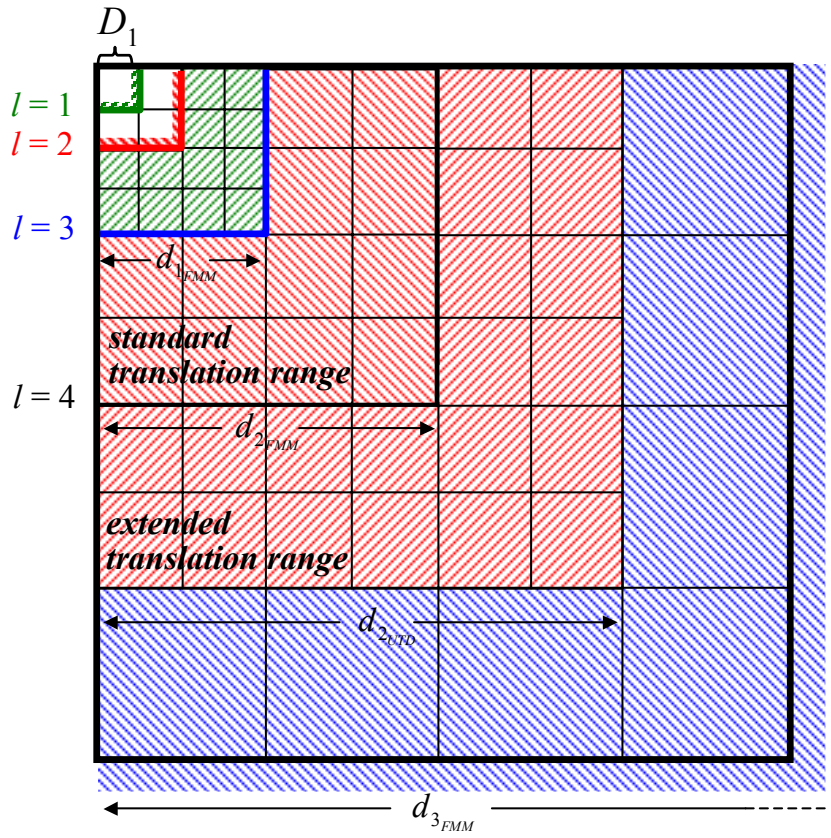

Figure 5.5: Extension of translation range around source groups for ray optical translations in the implementation of the hybrid MLFMM-UTD approach.

5.4.3 Improved Ray Optical Translations

In conventional MLFMM computations, the center points of the groups are used to perform the aggregation and disaggregation of the field contributions as well as the translations at the various levels. In case of using the center points of the groups to perform ray optical translations the resulting ray directions satisfying Fermat's principle for a specific source and testing group configuration are conformal only for current elements lying at those particular points. However, for current elements placed at different locations within the groups, the resulted ray directions with respect to the group center point are slightly different than the actual ray directions corresponding to the individual source and testing current configuration resulting in slightly different local points on the UTD object and producing inadequate results.

In the hybrid FEBI-MLFMM-UTD method presented in this thesis, improved ray optical translations are achieved by using the gravity center of the currents within the groups as source and receiving points for the radiated and received ray optical fields. In this case, the field contributions are aggregated and disaggregated as usual from and to the center points of the groups, respectively. However, translations of radiated ray optical fields at the various MLFMM levels are performed from the gravity center $\mathbf{r}_{g_{n'}}$ of the currents within the source groups to the gravity center $\mathbf{r}_{g_{m'}}$ of the currents in the receiving groups as shown in Fig. 5.6.

The ray optical translation operator for this purpose is written as

$$T_L^{UTD}(kr_{Qg_{n'}}) = \frac{\mathrm{e}^{-jkr_{Qg_{n'}}}}{r_{Qg_{n'}}}, \tag{5.44}$$

where

$$r_{Qg_{n'}} = |\mathbf{r}_Q - \mathbf{r}_{g_{n'}}| \tag{5.45}$$

is the distance from the gravity center of the currents in the source group at the working level to the local point on the UTD objects. Obviously, after reflection/diffraction on the UTD object the distance $s_{R/D}$ used in the divergence and phase factors $\tilde{A}_{R/D}(s_{R/D})$ of the corresponding ray optical mechanism given in (5.5) is defined as the distance from the particular local point $\mathbf{r}_{Q_{R/D}}$ to the gravity center of the currents in the receiving group at the working level and it is given by (5.3) for $\mathbf{r} = \mathbf{r}_{g_{m'}}$.

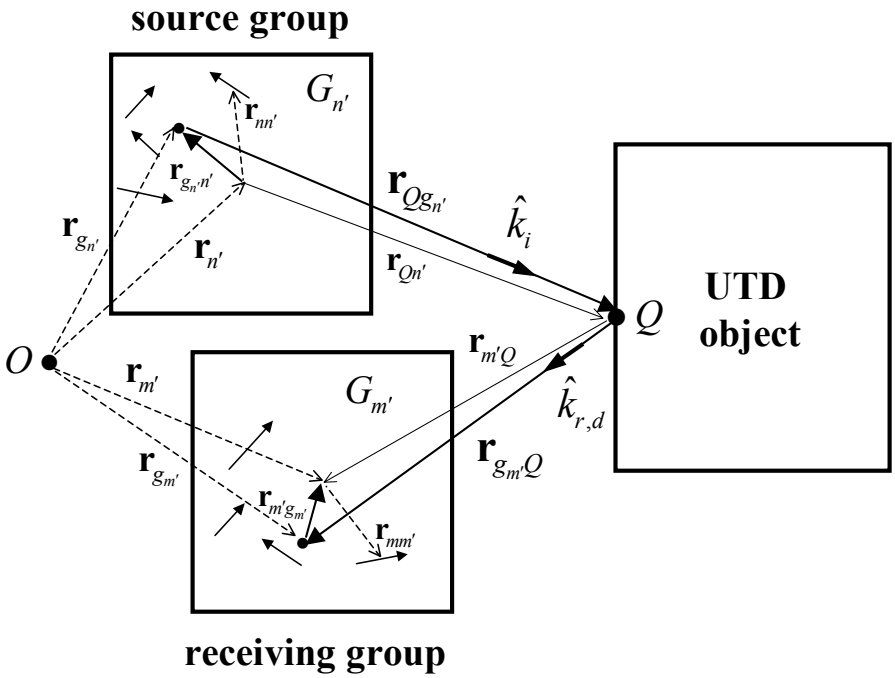

Figure 5.6: Improved ray optical translations using the gravity center of the currents within the groups as source and receiving points.

In addition, in order to be conformal with conventional MLFMM procedure of direct field terms, the aggregated ray optical field contributions are shifted from the center point of the source group to the gravity center of the included currents through the use of the shifting factor $\mathrm{e}^{-j\mathbf{k}_i\cdot\mathbf{r}_{g_{n'}n'}}$ resulting in a $\hat{k}$-space representation of the basis functions given by

$$\tilde{\boldsymbol{\beta}}_n^g(\hat{k}_i) = \mathrm{e}^{-j\mathbf{k}_i\cdot\mathbf{r}_{g_{n'}n'}} \iint\limits_A \boldsymbol{\beta}_n(\mathbf{r}_n)\mathrm{e}^{j\mathbf{k}_i\cdot\mathbf{r}_{nn'}}da', \tag{5.46}$$

$$\tilde{\boldsymbol{\alpha}}_n^g(\hat{k}_i) = \mathrm{e}^{-j\mathbf{k}_i\cdot\mathbf{r}_{g_{n'}n'}} \iint\limits_A \boldsymbol{\alpha}_n(\mathbf{r}_n)\mathrm{e}^{j\mathbf{k}_i\cdot\mathbf{r}_{nn'}}da'. \tag{5.47}$$

Similarly, in the disaggregation process, the received field contributions are shifted from the gravity center of the currents in the receiving group to the corresponding center point through the use of the shifting factor $\mathrm{e}^{j\mathbf{k}_{r,d}\cdot\mathbf{r}_{m'g_{m'}}}$ resulting in a $\hat{k}$-space representation of the basis functions given by

$$\widetilde{\boldsymbol{\beta}}_m^g(\hat{k}_{r,d}) = \mathrm{e}^{j\mathbf{k}_{r,d}\cdot\mathbf{r}_{m'g_{m'}}} \iint_A \boldsymbol{\beta}_m(\mathbf{r}_m)\mathrm{e}^{-j\mathbf{k}_{r,d}\cdot\mathbf{r}_{mm'}}da, \tag{5.48}$$

$$\widetilde{\boldsymbol{\alpha}}_m^g(\hat{k}_{r,d}) = \mathrm{e}^{j\mathbf{k}_{r,d}\cdot\mathbf{r}_{m'g_{m'}}} \iint_A \boldsymbol{\alpha}_m(\mathbf{r}_m)\mathrm{e}^{-j\mathbf{k}_{r,d}\cdot\mathbf{r}_{mm'}}da. \tag{5.49}$$

It is noticed, that translations from the gravity center of the currents within the groups at the various MLFMM levels are used only for ray optical contributions giving more accurate results compared to translations of ray optical fields using directly the center points of the groups. This is true, since using the gravity center of the currents enclosed in each group the computed ray directions satisfying Fermat's principle are closer to the actual directions corresponding to each individual current configuration resulting in a more accurate representation. Translation of contributions related to direct coupling of the groups at the various levels are translated as usual from the center points of the groups in order to apply conventional MLFMM using multipole expansion with respect to the center of the groups based on addition theorem as described in Section 3.1.1.

5.5 Implementation of Ray Optical Concepts

In the implementation of the hybrid FEBI-MLFMM-UTD method presented in this thesis, single and multiple reflections on flat metallic or dielectric objects are considered as well as single and double diffractions on straight metallic edges. Also, combinations of reflected and single diffracted contributions up to the fourth order can be taken into account. Thereby, the corresponding local points on the UTD objects are evaluated through numerical realization of Fermat's principle. More on the implementation of ray optical concepts will be discussed in the following subsections.

5.5.1 Reflection Point on Planar Surfaces

In order to determine the amplitude and phase variation as well as polarization of the reflected ray, first the reflection point on the surface must be determined. It is essentially the point on the surface satisfying Snell's law of reflection (4.22) for a particular source and observation point configuration as a direct consequence of Fermat's principle (see Section 4.1.2). For flat surfaces the reflection point is numerically determined using image theory, which is also fully conformal to Fermat's principle. According to this, the image of the source (or observation) point with respect to the planar surface is created as shown in Fig. 5.7. The image point is connected with the observation (or source) point and the reflection point is the point where this connection line cuts the flat surface. In this case, determination of the reflection point reduces into finding the cutting point between the ray propagating in the direction from image source point to the observation point (or from the source point to the image observation point) with the planar surface.

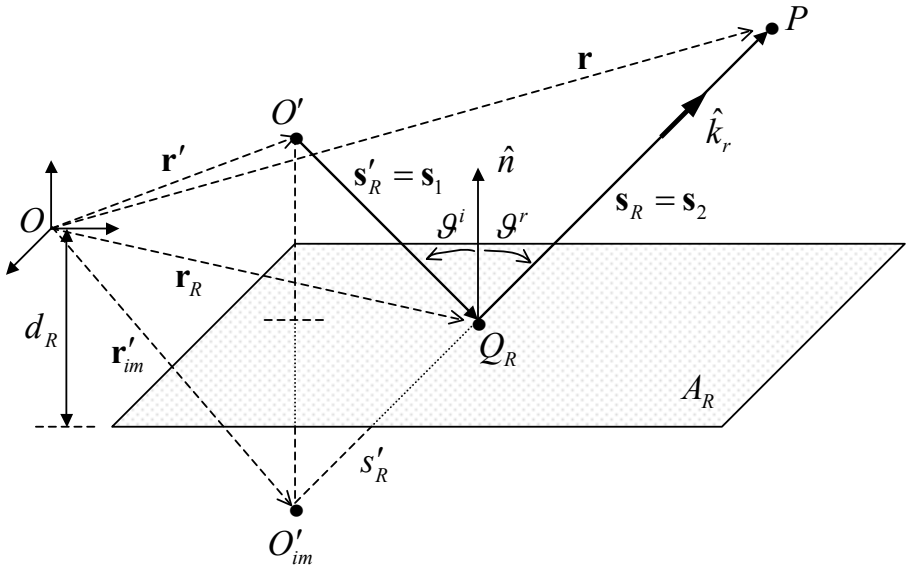

Figure 5.7: Numerical determination of reflection point on plane surfaces based on image theory.

In particular, assuming the configuration illustrated in Fig. 5.7 the ray from the image source point O'_{im} with position vector $\mathbf{r}'_{im}$ to the observation point P with position vector $\mathbf{r}$ propagates with respect to the equation

$$\mathbf{r} = \mathbf{r}'_{im} + p_R(s'_R + s_R)\hat{k}_r, \tag{5.50}$$

where the distances s_R, s'_R and the direction of reflection $\hat{k}_r$ are given by (5.3), (5.4) and (5.13), respectively. Thereby, p_R is a parameter defined on the ray trajectory. The equation of the planar surface A_R is in general

$$\mathbf{r} \cdot \hat{n} + d_R = 0, \qquad \forall\, \mathbf{r} \in A_R, \tag{5.51}$$

where $\hat{n}$ is the normal vector on the surface looking in the direction of the source point and d_R is the distance of the reflection surface from the origin of the coordinate system. From equations (5.50) and (5.51) we get

$$p_R = -\frac{d_R + \mathbf{r}'_{im} \cdot \hat{n}}{(s'_R + s_R)\hat{k}_r \cdot \hat{n}}. \tag{5.52}$$

When the direction of propagation $\hat{k}_r$ is not perpendicular to the normal vector of the surface, thus when $\hat{k}_r \cdot \hat{n} \neq 0$, the cutting point is given by

$$\mathbf{r}_R = \mathbf{r}'_{im} + p_R(s'_R + s_R)\hat{k}_r, \tag{5.53}$$

where p_R is given in (5.52). The point determined by (5.53) is the reflection point for the particular configuration. The expressions (5.52) and (5.53) are valid for all ray directions except grazing direction to the plane of reflection. For finite reflection surfaces, after finding the reflection point it is tested whether the determined cutting point is actually lying within the surface.

5.5.2 Special Treatment of Reflection Terms

In the previous Section 5.5.1 the determination of reflection points on planar surfaces using image theory was described. However, image theory is also used for reflection treatment on flat surfaces in terms of polarization of the reflected ray as well as amplitude variation of terms associated to the gradient of the scalar Green's function with dependence $1/r$ and $1/r^2$.

Particularly, in the special case of flat metallic surfaces it is assumed that the dyadic reflection coefficient has additionally radial components in the local ray-fixed coordinate system according to

$$\bar{\mathbf{R}} = R_{\parallel}\hat{e}^r_{\parallel}\hat{e}^i_{\parallel} + R_{\perp}\hat{e}^r_{\perp}\hat{e}^i_{\perp} + R_r\hat{e}^r\hat{e}^i, \tag{5.54}$$

where the scalar reflection coefficients $R_{\parallel}$ and $R_{\perp}$ associated to field components parallel and perpendicular to the plane of incidence/reflection are given by (4.27) and (4.28), respectively, as described in Section 4.1.2. The additional scalar reflection coefficient R_r related to radial field components, which are parallel to the ray direction of incidence $\hat{e}^i$ and reflection $\hat{e}^r$ in the local ray-fixed coordinate system shown in Fig. 4.2, is given by

$$R_r = 1, \tag{5.55}$$

which is obtained applying the image principle shown in Fig. 5.7 to the local ray-fixed coordinate system configuration [61].

Furthermore, in the hybrid BIM-UTD part of the method reflected terms on flat surfaces associated to the gradient of the ray optical scalar Green's function with dependence $1/r$ and $1/r^2$ are separated and treated by different divergence factors according to image theory similar to the approaches presented in [156], [157]. According to this, the amplitude and phase factors of the ray optical scalar Green's function for reflection in case of an incident ray with spherical wavefront is given by

$$G_R(\mathbf{r},\mathbf{r}') = G(\mathbf{r}_{Q_R},\mathbf{r}')\widetilde{A}(s) = G(\mathbf{r}_{Q_R},\mathbf{r}')\frac{s_1}{s_1+s_2}\mathrm{e}^{-jks_2} \tag{5.56}$$

based on equations (5.2), (5.5) along with (4.25). Thereby, the distances $s_1 = s'_R$ and $s_2 = s_R$ are given by (5.4) and (5.3), respectively assuming the configuration shown in Fig. 5.7. Also, the field response $G(\mathbf{r}_{Q_R},\mathbf{r}')$ at the local reflection point $\mathbf{r}_{Q_R}$ due to a point source placed at $\mathbf{r}'$ is given by

$$G(\mathbf{r}_{Q_R},\mathbf{r}') = \frac{\mathrm{e}^{-jks_1}}{s_1} \tag{5.57}$$

with a gradient given by

$$\begin{aligned}\nabla G(\mathbf{r}_{Q_R},\mathbf{r}') &\overset{(5.57)}{=} \nabla\left(\frac{\mathrm{e}^{-jks_1}}{s_1}\right) = -\left(\frac{1}{s_1}+jk\right)\frac{\mathrm{e}^{-jks_1}}{s_1}\hat{e}^i \\ &= -jk\frac{\mathrm{e}^{-jks_1}}{s_1}\hat{e}^i - \frac{\mathrm{e}^{-jks_1}}{s_1^2}\hat{e}^i.\end{aligned} \tag{5.58}$$

The gradient of (5.56) is written as

$$\begin{aligned}\nabla G_R(\mathbf{r},\mathbf{r}') &= \nabla G(\mathbf{r}_{Q_R},\mathbf{r}')\tilde{A}(s) + G(\mathbf{r}_{Q_R},\mathbf{r}')\nabla\tilde{A}(s)\\ &\overset{(5.58)}{=} -jk\frac{\mathrm{e}^{-jks_1}}{s_1}\frac{s_1}{s_1+s_2}\mathrm{e}^{-jks_2}\hat{e}^i - \frac{\mathrm{e}^{-jks_1}}{s_1^2}\frac{s_1}{s_1+s_2}\mathrm{e}^{-jks_2}\hat{e}^i\\ &\quad + \frac{\mathrm{e}^{-jks_1}}{s_1}\frac{s_2}{(s_1+s_2)^2}\mathrm{e}^{-jks_2}\hat{e}^i\\ &= -jk\frac{\mathrm{e}^{-jks_1}}{s_1}\tilde{A}_{1/r}(s) - \frac{\mathrm{e}^{-jks_1}}{s_1^2}\tilde{A}_{1/r^2}(s). \end{aligned} \tag{5.59}$$

Consequently, terms of the gradient of the ray optical scalar Green's function for reflection on flat surfaces with dependence $1/r$ are multiplied with divergence and phase factors given by

$$\tilde{A}_{1/r}(s) = \frac{s_1}{s_1+s_2}\mathrm{e}^{-jks_2}, \tag{5.60}$$

whereas terms with dependence $1/r^2$ are multiplied with divergence and phase factors given by

$$\tilde{A}_{1/r^2}(s) = \left(\frac{s_1}{s_1+s_2}\right)^2 \mathrm{e}^{-jks_2}. \tag{5.61}$$

This result is fully conformal to image theory. In particular, the scalar Green's function from the image source $\mathbf{r}'_{im}$ to the observation point $\mathbf{r}$ referred to Fig. 5.7 is given by

$$G(\mathbf{r},\mathbf{r}'_{im}) = \frac{\mathrm{e}^{-jk|\mathbf{r}-\mathbf{r}'_{im}|}}{|\mathbf{r}-\mathbf{r}'_{im}|} = \frac{\mathrm{e}^{-jk(s_1+s_2)}}{s_1+s_2} \tag{5.62}$$

with a gradient given by

$$\nabla G(\mathbf{r},\mathbf{r}'_{im}) = -jk\frac{\mathrm{e}^{-jk(s_1+s_2)}}{s_1+s_2}\hat{e}^r - \frac{\mathrm{e}^{-jk(s_1+s_2)}}{(s_1+s_2)^2}\hat{e}^r. \tag{5.63}$$

According to image theory, the scalar Green's function associated to the image problem is equal to the ray optical scalar Green's function for reflection. Thus, (5.59) and (5.63) must be equal and by rewriting (5.63) like

$$\nabla G(\mathbf{r},\mathbf{r}'_{im}) = -jk\frac{\mathrm{e}^{-jks_1}}{s_1}\frac{s_1}{s_1+s_2}\mathrm{e}^{-jks_2}\hat{e}^r - \frac{\mathrm{e}^{-jks_1}}{s_1^2}\frac{s_1^2}{(s_1+s_2)^2}\mathrm{e}^{-jks_2}\hat{e}^r \tag{5.64}$$

finally results in the factors (5.60) and (5.61). It is noticed, that this approach is applied only for reflections on planar metallic surfaces for which image theory is applicable and results in more accurate results in near-field regions, where field components with dependence $1/r^2$ are significant. In all other cases standard ray optical divergence and phase factors are used as described in Chapter 4.

5.5.3 Diffraction Point on Straight Wedges

In order to determine the diffracted ray on a wedge, first the diffraction point on the corresponding edge must be determined. It is essentially the point on the edge satisfying Keller's law of diffraction (4.34) for a particular source and observation point configuration as a direct consequence of the generalized Fermat's principle (see Section 4.2). For straight edges the diffraction point Q_D on the edge is numerically determined by a three-dimensional parametric realization of the generalized Fermat's principle. According to this, the position vector of the diffraction point are expressed in terms of a parameter defined on the edge as

$$\mathbf{r}_D = \mathbf{r}_{v_1} + p_D l_e \hat{e}, \tag{5.65}$$

where $\mathbf{r}_{v_1}$ and l_e are the position vector of the first vertex and the length of the edge, respectively. The parameter p_D is defined on the edge and takes values between $[0, 1]$. Also, $\hat{e}$ is the unit vector along the edge defined from the first to the second vertex.

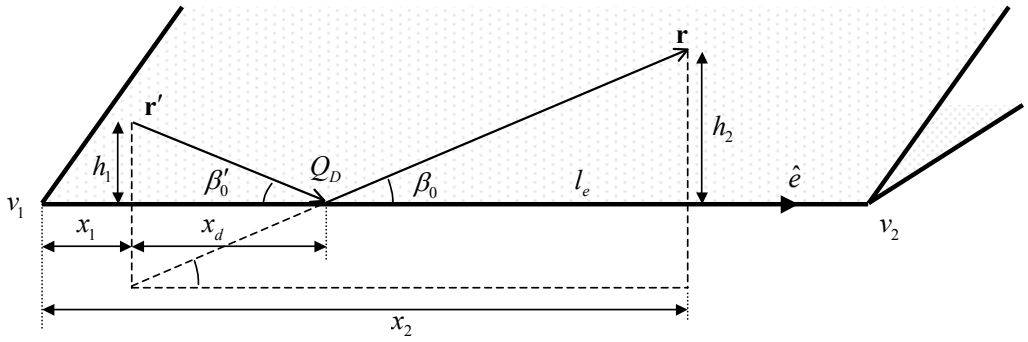

Figure 5.8: Numerical determination of diffraction point on straight edges.

The diffraction point $\mathbf{r}_D$ on the edge is computed using (5.65) for a given set of source and observation point, whereas the parameter p_D is determined in closed form. In particular, considering the configuration shown in Fig. 5.8 it can be seen that

$$\tan\beta_0' = \frac{h_1}{x_d} \Rightarrow x_d = \frac{h_1}{\tan\beta_0'}, \tag{5.66}$$

where β_0' is the angle of ray incidence given in (4.34), h_1 is the distance of the source point from the edge, and x_d is the distance of the projection of the source point from the diffraction point as shown in Fig. 5.8. For the same configuration it can also be seen that

$$\tan\beta_0' = \frac{h_1 + h_2}{x_2 - x_1}, \tag{5.67}$$

where h_2 is the distance of the observation point from the edge and x_1, x_2 are the distances of the projection of source and observation point from the first vertex of the edge, respectively, as shown in Fig. 5.8. From (5.66) and (5.67) we get

$$x_d = \frac{h_1}{h_1 + h_2}(x_2 - x_1). \tag{5.68}$$

Obviously, based on the geometry of the configuration shown in Fig. 5.8 the parameter p_D is written as

$$p_D = \frac{x_d + x_1}{l_e} \tag{5.69}$$

with x_d given by (5.68).

5.5.4 Higher Order Ray Optical Mechanisms

In the hybrid FEBI-MLFMM-UTD method presented in this thesis combination of multiple reflections on flat surfaces and single diffractions on straight metallic edges up the fourth order are considered according to the configuration illustrated in Fig. 5.9. In general, assuming U electrically large UTD objects, the ray optical electric field at the observation point $\mathbf{r}$ for a source point $\mathbf{r}'$ is written as

$$\mathbf{E}_{UTD}(\mathbf{r}) = \bar{\mathbf{X}}_1^E \cdot \bar{\mathbf{X}}_2^E \cdot \ldots \bar{\mathbf{X}}_U^E \cdot \mathbf{E}^i(\mathbf{r}_{Q_1}) \tilde{A}_{tot}(s), \tag{5.70}$$

where $\bar{\mathbf{X}} = \bar{\mathbf{R}}, \bar{\mathbf{D}}$ according to the appropriate ray optical mechanism taken place on the particular UTD object. It is noticed, that at this point only single diffractions on UTD objects are taken into account, which means that no successive dyadic diffraction coefficients are applied in (5.70). In other words, before and after any dyadic diffraction coefficient $\bar{\mathbf{D}}$ in (5.70) the corresponding dyadic reflection coefficient $\bar{\mathbf{R}}$ is found. It is noticed, that ray optical dyadic operations are performed at this point as described in Section A.2 and Section C.3 in the Appendix A and Appendix C, respectively.

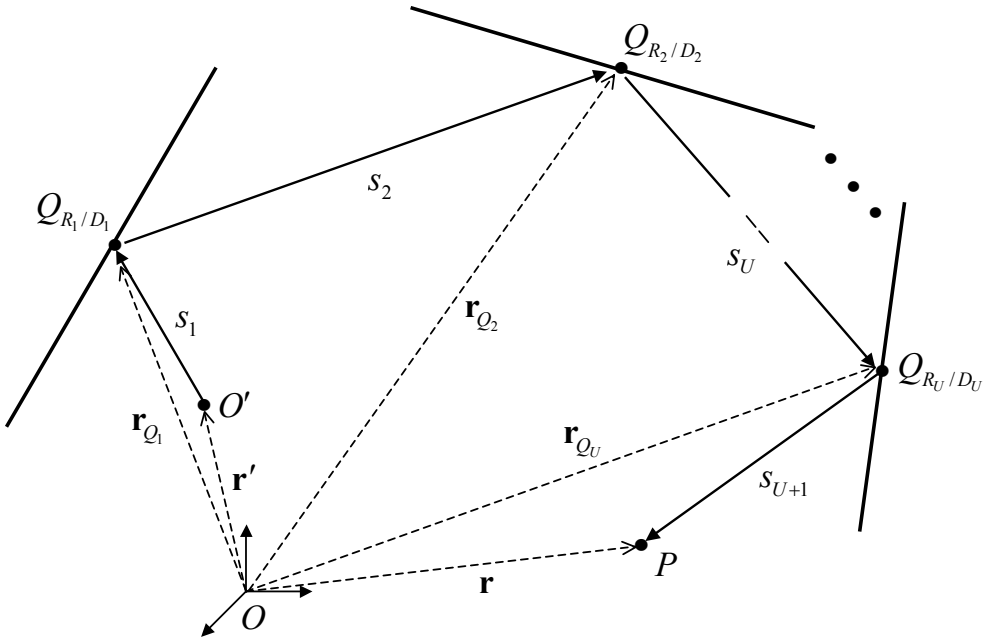

Figure 5.9: Configuration for higher order ray optical mechanisms.

In addition, $\tilde{A}_{tot}(s)$ incorporates the total divergence and phase factor of the ray for the complete ray path and is given by

$$\tilde{A}_{tot}(s) = \left(\prod_{u=1}^{U} A_{R_u,D_u}(s) \right) \mathrm{e}^{-jk \sum_{u=2}^{U+1} s_u}, \tag{5.71}$$

where $A_{R_u,D_u}(s)$ are the divergence factors of each particular reflection or diffraction on the UTD objects given by (4.25) and (4.37), respectively, assuming spherical ray wavefront. For each reflection, the local point on the corresponding UTD object is determined as described

in Section 5.5.1 using the previous and the next interaction point as source and observation point, respectively. Also, in case of single diffraction the corresponding local point is found in the same manner using the procedure described in Section 5.5.3. The resulting divergence and phase factors for the most important higher order ray optical mechanisms implemented in the present thesis can be found in Table 5.1.

Table 5.1: Divergence and phase factors of the most important higher order ray optical mechanisms implemented in the present thesis.

Ray Mechanism	Description	$\underset{\sim}{A}_{tot}(s)$
RR	Double Reflection	$\frac{s_1}{s_1+s_2+s_3}\mathrm{e}^{-jk(s_2+s_3)}$
RD	Reflection - Diffraction	$\frac{s_1}{\sqrt{(s_1+s_2)s_3(s_1+s_2+s_3)}}\mathrm{e}^{-jk(s_2+s_3)}$
DR	Diffraction - Reflection	$\sqrt{\frac{s_1}{(s_2+s_3)(s_1+s_2+s_3)}}\mathrm{e}^{-jk(s_2+s_3)}$
RRR	Triple Reflection	$\frac{s_1}{s_1+s_2+s_3+s_4}\mathrm{e}^{-jk(s_2+s_3+s_4)}$
RRD	Double Reflection - Diffraction	$\frac{s_1}{\sqrt{(s_1+s_2+s_3)s_4(s_1+s_2+s_3+s_4)}}\mathrm{e}^{-jk(s_2+s_3+s_4)}$
DRR	Diffraction - Double Reflection	$\sqrt{\frac{s_1}{(s_2+s_3+s_4)(s_1+s_2+s_3+s_4)}}\mathrm{e}^{-jk(s_2+s_3+s_4)}$
RRRD	Triple Reflection - Diffraction	$\frac{s_1}{\sqrt{(s_1+s_2+s_3+s_4)s_5(s_1+s_2+s_3+s_4+s_5)}}\mathrm{e}^{-jk(s_2+s_3+s_4+s_5)}$

5.5.5 Double Diffraction on Arbitrarily Oriented Straight Metallic Wedges

In addition to multiple ray optical mechanisms described in Section 5.5.4 double diffraction on pairs of straight metallic arbitrarily oriented edges is considered in the present thesis. The double diffracted fields are formulated using scalar diffraction coefficients of standard UTD as described in Section 4.2. Thereby, the diffraction points on the pair of edges are determined by an iterative three-dimensional parametric realization of the generalized Fermat's principle allowing treatment of non-coplanar and arbitrarily oriented edges. Further, for divergence factor determination of the double diffracted field, the ray caustic distance for the second diffraction is determined by linear interpolation between the radii of curvature in the two principal planes of the incident astigmatic ray tube on the second edge [85], [86]. It is noticed that for configurations in which the second diffraction point is in the transition region of the first, the scalar diffraction coefficients of UTD are not valid since the incident field on the second edge is not purely ray optical by means of rapid spatial variations due to the Fresnel transition functions in the diffraction coefficients of the first edge as described in Section 4.3. Double diffracted field formulations, which are valid in transition regions of the first edge have been developed in [158]-[162] using several approaches such as a spectral extension of UTD or spherical spectral synthesis.

Double diffracted UTD field contributions on pairs of edges are taken into account according to the configuration shown in Fig. 5.10. The edges of the pair can be in general non-coplanar and skewed by an angle α_d. The diffraction points Q_{D_1} on edge 1 with position vector $\mathbf{r}_{Q_{D_1}}$ and Q_{D_2} on edge 2 with position vector $\mathbf{r}_{Q_{D_2}}$ are numerically determined by an iterative three-dimensional parametric realization of the generalized Fermat's principle. According to this, the diffraction points for each single diffraction are determined parametrically as described in Section 5.5.3. In case of double diffraction this procedure is repeated iteratively for every edge using each time a point on the other edge as source or observation point, respectively, until the law of diffraction is satisfied on both edges with desired accuracy [160]. This is typically achieved after only few iterations.

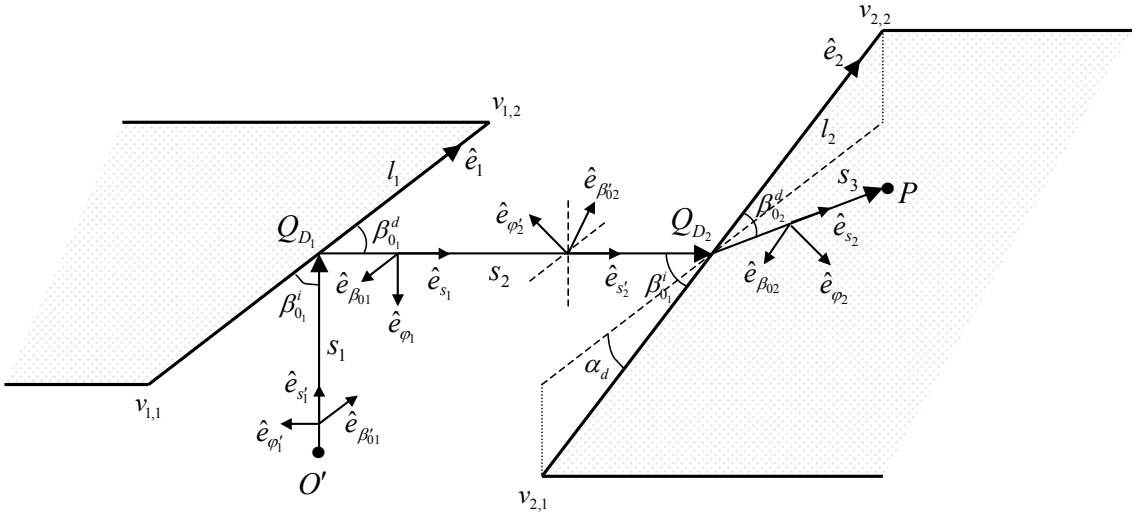

Figure 5.10: Double diffraction edge configuration.

The double diffracted field at the observation point P with position vector $\mathbf{r}$ has the form

$$\mathbf{E}^{dd}(\mathbf{r}) = \bar{\mathbf{D}}_2^E \cdot \bar{\mathbf{D}}_1^E \cdot \mathbf{E}^i(\mathbf{r}_{Q_{D_1}}) A_1(s) A_2(s) \mathrm{e}^{-jk(s_2+s_3)}, \tag{5.72}$$

where $\mathbf{E}^i(\mathbf{r}_{Q_{D_1}})$ is the incident field at Q_{D_1} and

$$\bar{\mathbf{D}}_j^E = -D_{\parallel_j} \hat{e}_{\beta_{0j}} \hat{e}_{\beta'_{0j}} - D_{\perp_j} \hat{e}_{\varphi_j} \hat{e}_{\varphi'_j}, \qquad j = 1, 2 \tag{5.73}$$

are the dyadic diffraction coefficients, in which $\hat{e}_{\beta'_{01,2}}$,$\hat{e}_{\varphi'_{1,2}}$ and $\hat{e}_{\beta_{01,2}}$,$\hat{e}_{\varphi_{1,2}}$ are the transversal components in the edge-fixed coordinate system of incidence and diffraction on edge 1 or edge 2, respectively, as shown in Fig. 5.10. The double diffracted field is formulated with the scalar diffraction coefficients $D_\parallel$, $D_\perp$ of UTD as described in Section 4.2. In addition,

$$A_1(s) = \sqrt{\frac{s_1}{s_2(s_2+s_1)}} \tag{5.74}$$

is the divergence factor of the diffracted field at edge 1. In that, the ray caustic distance ρ_{e_1} is assumed to be equal to s_1, which stands for the case of incident spherical wavefront on a straight edge. Further,

$$A_2(s) = \sqrt{\frac{\rho_{e_2}}{s_3(s_3+\rho_{e_2})}} \tag{5.75}$$

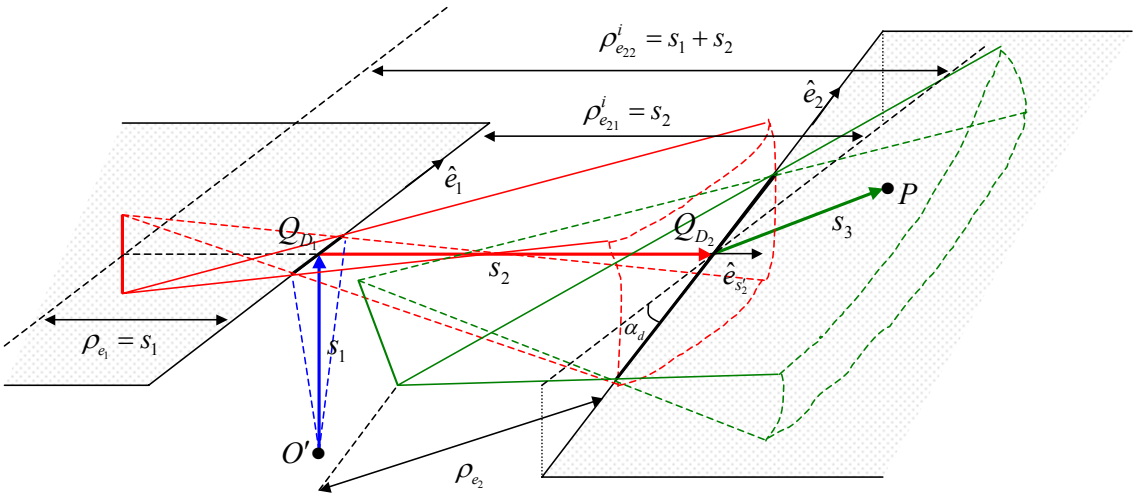

Figure 5.11: Ray tubes of double diffraction.

is the divergence factor of the diffracted field at edge 2. The incident field on edge 2 is the diffracted field at edge 1, which is an astigmatic ray field, as shown in Fig. 5.11.

The ray caustic distance ρ_{e_2} of the diffracted field at edge 2 is determined from the radius of curvature of the incident field in the plane of incidence, defined by $\hat{e}_{s_2'}$ and $\hat{e}_2$. In case of non-coplanar and arbitrarily oriented edges, the plane of incidence at edge 2 is in general somewhere in between the two principal planes of the incident astigmatic ray tube. Consequently, the ray caustic distance ρ_{e_2} depends on the radii of curvature $\rho^i_{e_{21}}$, $\rho^i_{e_{22}}$ of the incident wavefront in both principal planes, which correspond to the first and second caustic of the incident ray field at edge 2, respectively. It is obvious, that for coplanar edges ($\alpha_d = 0$) the plane of incidence at edge 2 coincides with the principal plane corresponding to the second caustic of the incident ray tube and $\rho_{e_2}\big|_{\alpha_d=0} = \rho^i_{e_{22}} = s_1 + s_2$. Also, for perpendicular edges ($\alpha_d = \frac{\pi}{2}$), the plane of incidence at edge 2 coincides with the principal plane corresponding to the first caustic of the incident ray tube, which lies on edge 1, and $\rho_{e_2}\big|_{\alpha_d=\frac{\pi}{2}} = \rho^i_{e_{21}} = s_2$. The ray caustic distance ρ_{e_2} for values of α_d between 0 and $\frac{\pi}{2}$ is determined by linear interpolation between these two principal values of ρ_{e_2} resulting in

$$\rho_{e_2} = s_1 + s_2 - \frac{2\alpha_d}{\pi} s_1, \tag{5.76}$$

where α_d is given in radians. Consequently, the divergence factor of the diffracted field at edge 2 is given by

$$A_2(s) = \sqrt{\frac{s_1 + s_2 - \frac{2\alpha_d}{\pi} s_1}{s_3(s_3 + s_1 + s_2 - \frac{2\alpha_d}{\pi} s_1)}}. \tag{5.77}$$

In addition to the hybrid BIM-UTD and MLFMM-UTD formulations described this chapter, acceleration of near-field computations based on known BI currents was also performed in the present thesis and will be presented in the following chapter.

Chapter 6

Fast Near-Field Computations

6.1 Introduction

In the previous chapters of the present thesis the hybrid FEBI-MLFMM-UTD method for the solution of large and complex radiation and scattering problems was presented. In general, numerical solution of electromagnetic problems using BI based methods provides the desired amplitudes of the expansion of the equivalent current densities on the discrete elements all over the boundary surfaces on the involved BI objects. In case of hybrid approaches with ray optical methods mutual coupling with electrically very large UTD objects is incorporated in the current solution based on hybrid formulations like those presented in this thesis. In order to compute the electromagnetic fields produced by the equivalent currents at observation points in the near-field region of the involved objects, integration of the current densities over the entire boundary surfaces must be performed in the postprocessing stage. Such computations are needed in many applications like EMC investigations in cars or for safety assessment in the vicinity of mobile communications base station antennas. The complexity of evaluating near-field integrals in the postprocessing stage using conventional numerical integration rules is $O(NP)$, where N is the number of equivalent current elements (BI unknowns) and P the number of observation points. If UTD objects are present in the same environment ray optical contributions must additionally be taken into account during integrations of the known equivalent surface currents. It is obvious that postprocessing computations become extremely time consuming in case of large BI objects and large number of observation points.

In this chapter, acceleration of near-field integrations of known equivalent current densities over boundary surfaces is presented using a postprocessing MLFMM approach [74]-[78]. According to this, the BI-MLFMM domain of the equivalent currents is extended to also include nearby observation points and in addition to non empty groups containing source currents also non empty groups containing observation points are collected at each level. Near-field MLFMM translations are performed from source groups including currents to receiving groups including observation points. For far-away observation points no grouping is performed and the field contributions are computed using far-field MLFMM translations, which are performed for each observation point at the coarsest level on which far-field condition is still satisfied. The optimum level for far-field translations is found for each observation point in the initialization step in a worst-case sense using its shortest distance to the BI-MLFMM domain. In both domains ray optical contributions due to the presence

of electrically very large UTD objects are taken into account according to the previously presented hybridization of MLFMM with UTD [79], [80]. The resulting hybrid approach is referred to as P-MLFMM-UTD in order to distinguish the realization of MLFMM-UTD in the postprocessing stage from the one used in the fast BI solution. This approach was applied in the postprocessing stage of the FEBI-MLFMM-UTD technique presented in Chapters 2 to 5. It is noticed, that to the knowledge of the author the combination of near-field and far-field MLFMM translations for fast postprocessing computations in BI based approaches is reported in the scientific community for the first time.

In the following, formulations of the postprocessing MLFMM approach including ray optical contributions will be presented and details of the numerical implementation will be discussed.

6.2 Geometrical Configuration

Consider the configuration shown in Fig. 6.1, where electric $\mathbf{J}_A(\mathbf{r}')$ and magnetic $\mathbf{M}_A(\mathbf{r}')$ current densities are given all over the closed boundary surface A according to equivalence principle. It is assumed that these current densities are known from the solution of any BI based method like the FEBI-MLFMM-UTD method presented in Chapters 2 to 5. Thereby, full back coupling of UTD objects being in the same environment is incorporated in the current solution through hybrid formulations like the formulations presented in Chapter 5. Particularly, in the present implementation it is assumed that equivalent currents of the form (2.39) and (2.40) are available on a boundary surface A in a known expansion using RWG vector basis functions on triangular surface elements according to (2.69) and (2.70) as described in Section 2.2.2. In addition, ray optical contributions are taken into account in the current solution by modifying the Green's functions in the different stages of the method. However, the postprocessing acceleration presented in this chapter can be applied to any kind of BI based implementation.

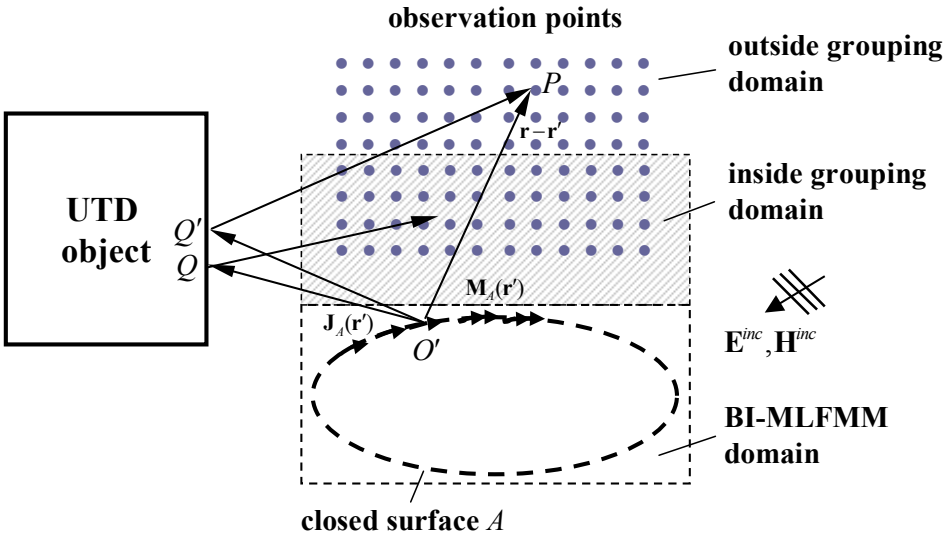

Figure 6.1: Configuration for postprocessing computations of BI based methods.

The electric and magnetic fields produced by the surface currents at particular observation points are given according to equivalence principle formulations as described in Section 2.1.2

using the total Green's functions of the problem, which are expressed in the same sense as in Chapter 5 namely as superposition of the direct terms from the surface currents to the observation points in the absence of UTD objects and all ray optical terms that arrive due the presence of UTD objects at the observation points. In particular, the total electromagnetic fields $\mathbf{E}_{tot}(\mathbf{r}_m)$ and $\mathbf{H}_{tot}(\mathbf{r}_m)$ produced by source currents at an observation point P with position vector $\mathbf{r} = \mathbf{r}_m$ are given by the integral expressions

$$\begin{aligned}\mathbf{E}_{tot}(\mathbf{r}_m) &= \mathbf{E}_P(\mathbf{r}_m) + \mathbf{E}_{UTD}(\mathbf{r}_m) \\ &= \mathbf{E}_{J/M,P}(\mathbf{r}_m) + \mathbf{E}^{inc}(\mathbf{r}_m) + \mathbf{E}_{J/M,UTD}(\mathbf{r}_m) + \mathbf{E}^{inc}_{UTD}(\mathbf{r}_m) \\ &= \iint\limits_A \bar{\mathbf{G}}^E_{J,tot}(\mathbf{r}_m, \mathbf{r}_n) \cdot \mathbf{J}_A(\mathbf{r}_n) da' + \iint\limits_A \bar{\mathbf{G}}^E_{M,tot}(\mathbf{r}_m, \mathbf{r}_n) \cdot \mathbf{M}_A(\mathbf{r}_n) da' \\ &\quad + \mathbf{E}^{inc}_{tot}(\mathbf{r}_m) \end{aligned} \tag{6.1}$$

and

$$\begin{aligned}\mathbf{H}_{tot}(\mathbf{r}_m) &= \mathbf{H}_P(\mathbf{r}_m) + \mathbf{H}_{UTD}(\mathbf{r}_m) \\ &= \mathbf{H}_{J/M,P}(\mathbf{r}_m) + \mathbf{H}^{inc}(\mathbf{r}_m) + \mathbf{H}_{J/M,UTD}(\mathbf{r}_m) + \mathbf{H}^{inc}_{UTD}(\mathbf{r}_m) \\ &= \iint\limits_A \bar{\mathbf{G}}^H_{J,tot}(\mathbf{r}_m, \mathbf{r}_n) \cdot \mathbf{J}_A(\mathbf{r}_n) da' + \iint\limits_A \bar{\mathbf{G}}^H_{M,tot}(\mathbf{r}_m, \mathbf{r}_n) \cdot \mathbf{M}_A(\mathbf{r}_n) da' \\ &\quad + \mathbf{H}^{inc}_{tot}(\mathbf{r}_m) \end{aligned} \tag{6.2}$$

based on the equivalence principle formulas (5.6) and (5.7), respectively, with $\mathbf{r}' = \mathbf{r}_n$ being the position vector of the source point O'. Thereby, $\mathbf{E}_P(\mathbf{r}_m)$, $\mathbf{H}_P(\mathbf{r}_m)$ represent direct field contributions in the absence of UTD objects and $\mathbf{E}_{UTD}(\mathbf{r}_m)$, $\mathbf{H}_{UTD}(\mathbf{r}_m)$ represent ray optical field contributions. In addition, the total Green's functions of the problem are expressed by

$$\bar{\mathbf{G}}^{E/H}_{J/M,tot}(\mathbf{r}_m, \mathbf{r}_n) = \bar{\mathbf{G}}^{E/H}_{J/M}(\mathbf{r}_m, \mathbf{r}_n) + \bar{\mathbf{G}}^{E/H}_{J/M,UTD}(\mathbf{r}_m, \mathbf{r}_n), \tag{6.3}$$

where $\bar{\mathbf{G}}^{E/H}_{J/M}(\mathbf{r}_m, \mathbf{r}_n)$ are direct terms of the Green's functions in the absence of UTD objects and $\bar{\mathbf{G}}^{E/H}_{J/M,UTD}(\mathbf{r}_m, \mathbf{r}_n)$ are ray optical contributions. Also,

$$\mathbf{E}^{inc}_{tot}(\mathbf{r}_m) = \mathbf{E}^{inc}(\mathbf{r}_m) + \mathbf{E}^{inc}_{UTD}(\mathbf{r}_m), \tag{6.4}$$

$$\mathbf{H}^{inc}_{tot}(\mathbf{r}_m) = \mathbf{H}^{inc}(\mathbf{r}_m) + \mathbf{H}^{inc}_{UTD}(\mathbf{r}_m) \tag{6.5}$$

are the total incident electric and magnetic field at the observation point $\mathbf{r}$ given by (5.9) and (5.11), respectively. In order to perform accelerated field computations in the postprocessing stage based on (6.1) and (6.2) the terms of the total Green's functions (6.3) are properly expressed as described in detail in the following sections.

6.3 Formulation Inside Grouping Domain

The evaluation of the field contributions in (6.1) and (6.2) for observation points in the near-field of the involved objects is accelerated using MLFMM. According to this, the MLFMM domain of the BI currents is extended to also include nearby observation points as shown

in Fig. 6.1. For the extended domain, a new grouping is performed and in addition to non empty groups containing source currents also non empty groups containing observation points are collected and numbered at each level. Thereby, empty groups that may arise are ignored at each level. Also, the lowest level is labeled with 1 and the highest level is labeled with L. Groups containing currents are considered as source groups and those containing observation points are considered as receiving groups. The influence of UTD objects to the field solution is taken into account using the hybridization of MLFMM with UTD presented in Section 5.4.

The concept for fast postprocessing computations inside the grouping domain is shown in Fig. 6.2 similar to the configuration shown in Fig. 5.3 in Section 5.4.1 including in this case observation points in the receiving groups rather than testing currents. For the configuration illustrated in Fig. 6.2 the total Green's functions are given by (6.3).

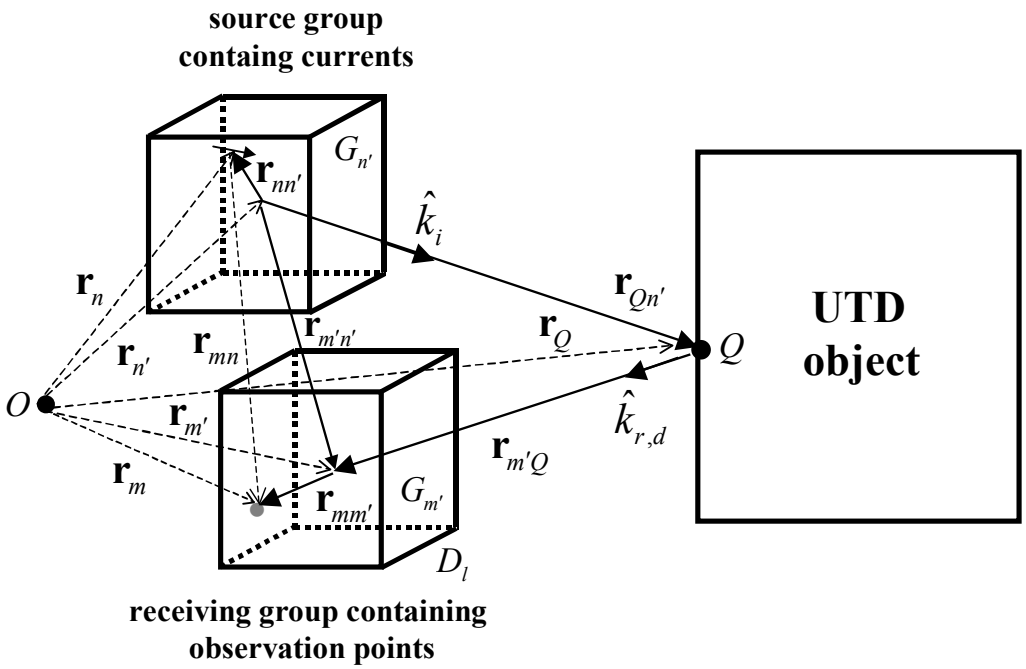

Figure 6.2: Hybrid P-MLFMM-UTD concept inside grouping domain. Direct field path from source point $\mathbf{r}' = \mathbf{r}_n$ to observation point $\mathbf{r} = \mathbf{r}_m$ in the absence of UTD objects is split into three sections $\mathbf{r}_{nn'}$, $\mathbf{r}_{m'n'}$ and $\mathbf{r}_{mm'}$. In addition, ray optical field path from $\mathbf{r}_n$ to $\mathbf{r}_m$ over the UTD object is split into four sections $\mathbf{r}_{nn'}$, $\mathbf{r}_{Qn'}$, $\mathbf{r}_{m'Q}$ and $\mathbf{r}_{mm'}$.

6.3.1 Direct Near-Field Translations

Direct field contributions in the configuration shown in Fig. 6.2 from source groups to non well-separated receiving groups in the absence of UTD objects are evaluated conventionally by numerical integration rules. Source and receiving groups are assumed to be well-separated, if they are separated by at least one group, so that the addition theorem criterion (3.13) remains valid. This group can be either a source group containing currents or a receiving group containing observation points.

For all other direct interactions between well-separated source and receiving groups in the

absence of UTD objects the field contributions are given by the expressions

$$\begin{aligned}\mathbf{E}_P(\mathbf{r}_m) &= -j\frac{\omega\mu}{4\pi}\iint\limits_A\left(\bar{\mathbf{I}}+\frac{1}{k^2}\nabla\nabla'\right)G(\mathbf{r}_m,\mathbf{r}_n)\cdot\mathbf{J}_A(\mathbf{r}_n)da' \\ &- \frac{1}{4\pi}\iint\limits_A\nabla\times G(\mathbf{r}_m,\mathbf{r}_n)\mathbf{M}_A(\mathbf{r}_n)da' \\ &+ \mathbf{E}^{inc}(\mathbf{r}_m) \end{aligned} \tag{6.6}$$

and

$$\begin{aligned}\mathbf{H}_P(\mathbf{r}_m) &= \frac{1}{4\pi}\iint\limits_A\nabla\times G(\mathbf{r}_m,\mathbf{r}_n)\mathbf{J}_A(\mathbf{r}_n)da' \\ &- j\frac{\omega\varepsilon}{4\pi}\iint\limits_A\left(\bar{\mathbf{I}}+\frac{1}{k^2}\nabla\nabla'\right)G(\mathbf{r}_m,\mathbf{r}_n)\cdot\mathbf{M}_A(\mathbf{r}_n)da' \\ &+ \mathbf{H}^{inc}(\mathbf{r}_m), \end{aligned} \tag{6.7}$$

which are obtained starting from equations (6.1) and (6.2) and using the Green's functions in the absence of UTD objects given by (2.32)-(2.34) as described in Section 2.1.2. Thereby, $G(\mathbf{r}_m,\mathbf{r}_n)$ is the scalar term of the direct Green's function in the postprocessing stage and it is expressed following the same procedure as in conventional MLFMM for fast IE solution, which is described in Sections 3.1 and 3.2. According to this, the field path $\mathbf{r}_{mn}=\mathbf{r}_m-\mathbf{r}_n$ from a source current placed at $\mathbf{r}'=\mathbf{r}_n$ within group $G_{n'}$ at the lowest level, which is centered at the point $\mathbf{r}_{n'}$, to an observation point placed at $\mathbf{r}=\mathbf{r}_m$ within group $G_{m'}$ at the lowest level, which is centered at the point $\mathbf{r}_{m'}$, is given by (3.9) as shown in Fig. 6.2. In addition, the free space scalar Green's function from a source current to an observation point is expanded in terms of spherical wave functions including dynamic multipoles located at the center of the corresponding groups according to (3.10). Also, the included spherical wave functions are expanded in terms of plane waves using (3.15) resulting in the factorized expression

$$G(\mathbf{r}_m,\mathbf{r}_n)\approx\oiint \mathrm{e}^{-j\mathbf{k}\cdot\mathbf{r}_{mm'}}T_L(\hat{k}\cdot\hat{r}_{m'n'})\mathrm{e}^{j\mathbf{k}\cdot\mathbf{r}_{nn'}}d\hat{k}^2, \tag{6.8}$$

where $T_L(\hat{k}\cdot\hat{r}_{m'n'})$ is the conventional FMM diagonal translation operator given in (3.19) with $\mathbf{r}_{m'n'}$ being the vector connecting the centers of source and receiving group as shown in Fig. 6.2. This diagonal operator translates radiated plane waves from the center of the source group containing currents to received plane waves at the center of the receiving group containing observation points in the absence of UTD objects.

Substituting the direct factorized free space scalar Green's function representation (6.8) in the near-field expressions (6.6) and (6.7) and using (2.69) and (2.70) for the surface current expressions as well as (3.23) and (3.24) for the corresponding constants we get in the absence of UTD objects for the electric and magnetic near-field at the observation point $\mathbf{r}=\mathbf{r}_m$ due

to electric and magnetic currents the fast multipole representations

$$\begin{aligned}\mathbf{E}_P(\mathbf{r}_m) = &- j\frac{\omega\mu}{4\pi}\oiint e^{-j\mathbf{k}\cdot\mathbf{r}_{mm'}}T_L(\hat{k}\cdot\hat{r}_{m'n'})\left(\bar{\mathbf{I}}-\hat{k}\hat{k}\right)\cdot\sum_n H_n\tilde{\boldsymbol{\beta}}_n(\hat{k})\,d\hat{k}^2\\ &- j\frac{k}{4\pi}\oiint \hat{k}\times e^{-j\mathbf{k}\cdot\mathbf{r}_{mm'}}T_L(\hat{k}\cdot\hat{r}_{m'n'})\sum_n E_n\tilde{\boldsymbol{\beta}}_n(\hat{k})\,d\hat{k}^2\\ &+ \mathbf{E}^{inc}(\mathbf{r}_m)\end{aligned} \tag{6.9}$$

and

$$\begin{aligned}\mathbf{H}_P(\mathbf{r}_m) = &- j\frac{k}{4\pi}\oiint \hat{k}\times e^{-j\mathbf{k}\cdot\mathbf{r}_{mm'}}T_L(\hat{k}\cdot\hat{r}_{m'n'})\sum_n H_n\tilde{\boldsymbol{\beta}}_n(\hat{k})\,d\hat{k}^2\\ &+ j\frac{\omega\varepsilon}{4\pi}\oiint e^{-j\mathbf{k}\cdot\mathbf{r}_{mm'}}T_L(\hat{k}\cdot\hat{r}_{m'n'})\left(\bar{\mathbf{I}}-\hat{k}\hat{k}\right)\cdot\sum_n E_n\tilde{\boldsymbol{\beta}}_n(\hat{k})\,d\hat{k}^2\\ &+ \mathbf{H}^{inc}(\mathbf{r}_m),\end{aligned} \tag{6.10}$$

respectively, where $\tilde{\boldsymbol{\beta}}_n(\hat{k})$ is the $\hat{k}$-space representation of the basis function given in (3.25). Thereby, the substitution $\nabla \rightarrow -j\mathbf{k}$ was used, which is valid for application of the ∇ operator on elementary plane wave functions $\mathrm{e}^{-j\mathbf{k}\cdot\mathbf{r}}$ in the $\hat{k}$-space. Using this representation, radiated fields from groups containing currents are translated to received fields at groups containing observation points through the translation operator $T_L(\hat{k}\cdot\hat{r}_{m'n'})$.

This procedure is here referred to as *near-field MLFMM translation*, by means of plane wave representation of the radiated fields of source groups containing currents with integration over the Ewald sphere in the absence of UTD objects as in conventional MLFMM for matrix-vector multiply acceleration. Thereby, the well-known processes of the MLFMM described in Section 3.1 and Section 3.2 are found. In particular, in the aggregation stage first the radiation patterns of the source groups at the lowest level are computed in the center points using the spherical harmonics expansion of the current basis functions described in Section 3.2.3. The radiated plane waves are translated to received field contributions at the receiving groups. After disaggregation at the lowest level the received field contributions are shifted from the center of the receiving groups to the observation points and are integrated. During aggregation and disaggregation process, the radiation and receiving patterns of the groups are shifted to higher and lower levels, respectively, using (3.29) as shown in Fig. 6.3. Thereby, local interpolation/anterpolation is used as described in Section 3.2.2. Finally, direct terms are ignored if the receiving group is in the shadow region of an UTD object.

6.3.2 Ray Optical Translations Inside Grouping Domain

Inside the domain covered by MLFMM groups ray optical field contributions due to the presence of UTD objects are taken into account according to the hybridization of MLFMM with UTD presented in Section 5.4. Thereby, ray optical terms of the Green's function are approximated with far-field expressions suitable for MLFMM interactions and this results in modification of the translation procedure according to superposition of all received contributions at the receiving groups for all source groups at each MLFMM level, whereas a far-field approximation of the translation operator is used for ray optical contributions.

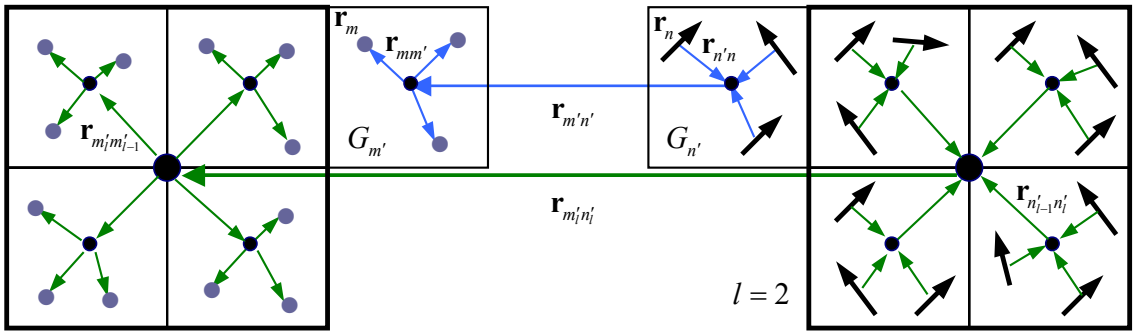

Figure 6.3: Translation of field contributions inside the grouping domain. Radiation and receiving patterns of the groups are shifted to higher and lower levels during aggregation and disaggregation, respectively. Subscription for lowest level is neglected.

Assuming the configuration illustrated in Fig. 6.2 and following the same procedure as described in Section C.1 in the Appendix C the ray optical terms of the Green's functions $\bar{\mathbf{G}}^{E/H}_{J/M,UTD}(\mathbf{r}_m, \mathbf{r}_n)$ in (6.3) are given by (5.28) and (5.29). Thereby, far-field conditions with respect to the group dimensions at the working level are assumed according to (5.41) for representing the radiated fields from the source groups containing currents to local points on the UTD objects using only one $\hat{k}$-direction, which is essentially the direction of ray incidence on the UTD object satisfying Fermat's principle for the particular receiving group. That way, the required incident ray optical fields are given at the local points on the UTD objects for each postprocessing MLFMM interaction. After that, through the use of the appropriate scalar and dyadic factors of the corresponding ray optical mechanism the rays at the receiving groups are finally computed under far-field conditions for only one $\hat{k}$-direction, which is essentially the direction of reflection/diffraction satisfying Fermat's principle.

Substituting (5.28) and (5.29) into equations (6.1) and (6.2) we get for the ray optical terms of the electric and magnetic fields inside the grouping domain the expressions

$$
\begin{aligned}
&\mathbf{E}_{UTD}(\mathbf{r}_m) = \\
&\quad -j\frac{\omega\mu}{4\pi}\Bigg\{ \sum_q e^{-j\mathbf{k}_r\cdot\mathbf{r}_{mm'}} \tilde{A}_{R_q}(s_{R_q}) \bar{\mathbf{R}}^E_q T^{UTD}_L(kr_{Q_{R_q}n'}) \cdot \left(\bar{\mathbf{I}} - \hat{k}_r\hat{k}_i\right) \cdot \sum_n H_n \tilde{\boldsymbol{\beta}}_n(\hat{k}_i) \\
&\quad + \sum_v e^{-j\mathbf{k}_d\cdot\mathbf{r}_{mm'}} \tilde{A}_{D_v}(s_{D_v}) \bar{\mathbf{D}}^E_v T^{UTD}_L(kr_{Q_{D_v}n'}) \cdot \left(\bar{\mathbf{I}} - \hat{k}_d\hat{k}_i\right) \cdot \sum_n H_n \tilde{\boldsymbol{\beta}}_n(\hat{k}_i) \\
&\quad + \cdots \Bigg\} \\
&\quad -j\frac{k}{4\pi}\Bigg\{ \sum_q \hat{k}_r \times e^{-j\mathbf{k}_r\cdot\mathbf{r}_{mm'}} \tilde{A}_{R_q}(s_{R_q}) \bar{\mathbf{R}}^H_q T^{UTD}_L(kr_{Q_{R_q}n'}) \cdot \sum_n E_n \tilde{\boldsymbol{\beta}}_n(\hat{k}_i)
\end{aligned}
$$

$$
\begin{aligned}
&+\sum_{v} \hat{k}_d \times e^{-j\mathbf{k}_d\cdot\mathbf{r}_{mm'}} \widetilde{A}_{D_v}(s_{D_v}) \bar{\mathbf{D}}_v^H T_L^{UTD}(kr_{Q_{D_v}n'}) \cdot \sum_n E_n \widetilde{\boldsymbol{\beta}}_n(\hat{k}_i) \\
&+\cdots \Bigg\} \\
&+\mathbf{E}_{UTD}^{inc}(\mathbf{r}_m)
\end{aligned} \tag{6.11}
$$

and

$$
\begin{aligned}
&\mathbf{H}_{UTD}(\mathbf{r}_m) = \\
&-j\frac{k}{4\pi}\Bigg\{ \sum_{q} \hat{k}_r \times e^{-j\mathbf{k}_r\cdot\mathbf{r}_{mm'}} \widetilde{A}_{R_q}(s_{R_q}) \bar{\mathbf{R}}_q^E T_L^{UTD}(kr_{Q_{R_q}n'}) \cdot \sum_n H_n \widetilde{\boldsymbol{\beta}}_n(\hat{k}_i) \\
&+\sum_{v} \hat{k}_d \times e^{-j\mathbf{k}_d\cdot\mathbf{r}_{mm'}} \widetilde{A}_{D_v}(s_{D_v}) \bar{\mathbf{D}}_v^E T_L^{UTD}(kr_{Q_{D_v}n'}) \cdot \sum_n H_n \widetilde{\boldsymbol{\beta}}_n(\hat{k}_i) \\
&+\cdots \Bigg\} \\
&+j\frac{\omega\varepsilon}{4\pi}\Bigg\{ \sum_{q} e^{-j\mathbf{k}_r\cdot\mathbf{r}_{mm'}} \widetilde{A}_{R_q}(s_{R_q}) \bar{\mathbf{R}}_q^H T_L^{UTD}(kr_{Q_{R_q}n'}) \cdot \left(\bar{\mathbf{I}} - \hat{k}_r\hat{k}_i\right) \cdot \sum_n E_n \widetilde{\boldsymbol{\beta}}_n(\hat{k}_i) \\
&+\sum_{v} e^{-j\mathbf{k}_d\cdot\mathbf{r}_{mm'}} \widetilde{A}_{D_v}(s_{D_v}) \bar{\mathbf{D}}_v^H T_L^{UTD}(kr_{Q_{D_v}n'}) \cdot \left(\bar{\mathbf{I}} - \hat{k}_d\hat{k}_i\right) \cdot \sum_n E_n \widetilde{\boldsymbol{\beta}}_n(\hat{k}_i) \\
&+\cdots \Bigg\} \\
&+\mathbf{H}_{UTD}^{inc}(\mathbf{r}_m),
\end{aligned} \tag{6.12}
$$

respectively, where $T_L^{UTD}(kr_{Qn'})$ is the ray optical translation operator given in (5.30) translating outgoing ray optical fields from source groups containing currents to incident ray optical fields at the local points on the UTD objects. Also, $\hat{k}_i$ and $\hat{k}_{r,d}$ are the direction of ray incidence from the source group to the UTD object as well as the direction of reflection/diffraction from the UTD object to the receiving group as shown in Fig. 6.2 and are given by (5.32) and (5.33), respectively. The incident rays at the local points on the UTD objects are multiplied with the appropriate scalar factors $\widetilde{A}_{R/D}(s_{R/D})$ and dyadic factors $\bar{\mathbf{R}}^{E/H}$, $\bar{\mathbf{D}}^{E/H}$ of the corresponding ray optical mechanism as described in Section 4.1 and Section 4.2 providing the received ray optical contributions at the center of the receiving groups. Thereby, $s_{R/D}$ is given in (5.3) for $\mathbf{r} = \mathbf{r}_{m'}$. The terms $\mathrm{e}^{j\mathbf{k}_i\cdot\mathbf{r}_{nn'}}$ and $\mathrm{e}^{-j\mathbf{k}_{r,d}\cdot\mathbf{r}_{mm'}}$ are phase shifting factors from the source current to the center of the source group and from the center of the receiving group to the testing current, respectively. Finally,

$$
\begin{aligned}
\mathbf{E}_{UTD}^{inc}(\mathbf{r}) &= \sum_{q} \widetilde{A}_{R_q}(s_{R_q}) \bar{\mathbf{R}}_q^E \cdot \mathbf{E}^{inc}(\mathbf{r}_{Q_{R_q}}) \\
&+ \sum_{v} \widetilde{A}_{D_v}(s_{D_v}) \bar{\mathbf{D}}_v^E \cdot \mathbf{E}^{inc}(\mathbf{r}_{Q_{D_v}}) + \cdots
\end{aligned} \tag{6.13}
$$

and

$$\begin{aligned}\mathbf{H}^{inc}_{UTD}(\mathbf{r}) &= \frac{1}{Z}\hat{k}_r \times \sum_q \widetilde{A}_{R_q}(s_{R_q})\bar{\mathbf{R}}^E_q \cdot \mathbf{E}^{inc}(\mathbf{r}_{Q_{R_q}}) \\ &+ \frac{1}{Z}\hat{k}_d \times \sum_v \widetilde{A}_{D_v}(s_{D_v})\bar{\mathbf{D}}^E_v \cdot \mathbf{E}^{inc}(\mathbf{r}_{Q_{D_v}}) + \cdots \end{aligned} \tag{6.14}$$

are ray optical contributions of the incident electric and magnetic field, respectively, at the observation point $\mathbf{r}_m$.

6.4 Formulation Outside Grouping Domain

The extension of near-field MLFMM translations to all observation points can be extremely memory consuming. Therefore, in order to achieve optimum performance the near-field MLFMM translation domain is not necessarily extended to include all observation points but it is applied only to nearby observation points. On the other hand, far away observation points that lie outside the MLFMM grouping domain are preferably treated in a different manner using a far-field approximation of the translation operator for the direct field terms. The influence of UTD objects to the field solution is taken into account in the same manner as inside the grouping domain particularly using the ray optical translation operator presented in Section 5.4. In both cases the approach for performing translations is valid under far-field conditions with respect to the source group dimensions at the working level based on the procedure used in FAFFA [143].

The concept for fast postprocessing computations outside the grouping domain is shown in Fig. 6.4, for which the total Green's functions are given by (6.3). In this case, no grouping is performed at the reception side and the field contributions are computed from the various source groups to each observation point separately.

6.4.1 Direct Far-Field Translations

Referring to the configuration shown in Fig. 6.4, direct terms of the Green's functions are represented using (2.32)-(2.34) as described in Section 2.1.2, which results in field expressions given by (6.6) and (6.7) similar to the procedure applied inside the grouping domain as described in Section 6.3.1. However, in order to express the direct scalar term $G(\mathbf{r}_m, \mathbf{r}_n)$ of the Green's function outside the grouping domain the direct field path $\mathbf{r}_{mn} = \mathbf{r}_m - \mathbf{r}_n$ from the source point $\mathbf{r}' = \mathbf{r}_n$ within the group $G_{n'}$, which is centered at the point $\mathbf{r}_{n'}$, to the observation point $\mathbf{r} = \mathbf{r}_m$ in the absence of UTD objects is written as

$$\mathbf{r} - \mathbf{r}' = \mathbf{r}_m - \mathbf{r}_n = (\mathbf{r}_m - \mathbf{r}_{n'}) + (\mathbf{r}_{n'} - \mathbf{r}_n) = \mathbf{r}_{mn'} - \mathbf{r}_{nn'}, \tag{6.15}$$

by intervening the center point of the source group in the field path. In this case, a similar procedure is used as the one presented in Section 5.4.1 for ray optical representations within MLFMM interactions. Particularly, instead of starting from the addition theorem to represent the scalar direct Green's function as it is done inside the grouping domain (see Section 6.3.1), it is rather assumed that the direct field paths from the center of the source groups to the observation points $\mathbf{r}_{mn'}$ are much larger than the paths $\mathbf{r}_{nn'}$ within the

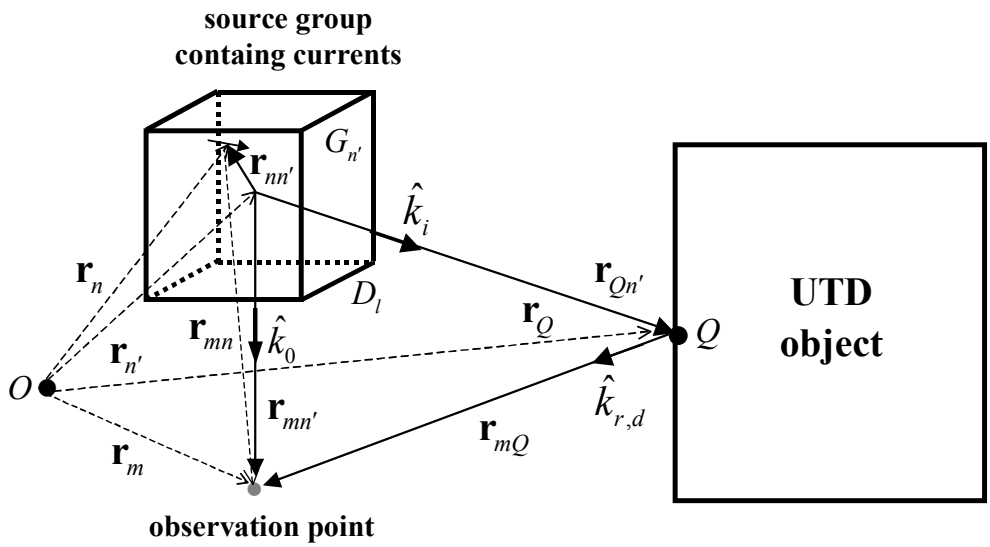

Figure 6.4: Hybrid P-MLFMM-UTD concept outside grouping domain. Direct field path from source point $\mathbf{r}_n$ to observation point $\mathbf{r}_m$ in the absence of UTD objects is split into two sections $\mathbf{r}_{nn'}$ and $\mathbf{r}_{mn'}$. In addition, ray optical field path from $\mathbf{r}_n$ to $\mathbf{r}_m$ over the UTD object is split into three sections $\mathbf{r}_{nn'}$, $\mathbf{r}_{Qn'}$, and $\mathbf{r}_{mQ}$.

source groups. Under this condition, the electrical path kr_{mn} from the source current to the observation point is expanded in terms of a Taylor series and assuming the far-field condition

$$r_{mn'} \gg \frac{1}{2}k|\mathbf{r}_{nn'}|^2 \tag{6.16}$$

higher order terms of this expansion are neglected. Hence, the electrical path from the source current to the observation point in the absence of UTD objects is written as

$$kr_{mn} = k|\mathbf{r}_m - \mathbf{r}_n| \approx kr_{mn'} - k\mathbf{r}_{nn'} \cdot \hat{r}_{mn'}. \tag{6.17}$$

In this case, only the direction

$$\hat{k}_0 = \hat{r}_{mn'} \tag{6.18}$$

from the source group to the particular observation point is used to represent the radiated fields from the source groups at the working MLFMM level as shown in Fig. 6.4. Applying the field path (6.17) in the appropriate free space scalar Greens' function (2.34) for $\mathbf{r} = \mathbf{r}_m$ and $\mathbf{r}' = \mathbf{r}_n$ results in the far-field representation

$$G(\mathbf{r}_m, \mathbf{r}_n) = \frac{\mathrm{e}^{-jk|\mathbf{r}_m - \mathbf{r}_n|}}{|\mathbf{r}_m - \mathbf{r}_n|} = \mathrm{e}^{j\mathbf{k}_0 \cdot \mathbf{r}_{nn'}} T_L^{FF}(kr_{mn'}), \tag{6.19}$$

where

$$T_L^{FF}(kr_{mn'}) = \frac{\mathrm{e}^{-jkr_{mn'}}}{r_{mn'}} \tag{6.20}$$

is the *direct far-field translation operator* used to perform direct translations outside the grouping domain. This operator translates the radiated field from the source group to

received field at the observation point in the absence of UTD objects with $\mathbf{k}_0 = k\hat{k}_0 = k\hat{r}_{mn'}$. The direct far-field translation operator is simply the free space scalar Green's function from the center point of the source group to the particular receiving point. The term $e^{j\mathbf{k}_0\cdot\mathbf{r}_{nn'}}$ is the shifting factor of the field contribution from the source current point to the center point of the source group and it is actually the radiation pattern of the source current element. A detailed derivation of the direct far-field translation operator can be found in Section D.1 in the Appendix D. It is noticed, that the direct far-field translation operator (6.20) has the same form as the ray optical translation operator (5.30) used to perform translations of ray optical terms in the hybrid MLFMM-UTD approach in the IE solution presented in Section 5.4 and in the postprocessing stage presented in Section 6.3.2. Both operators are derived in the same manner using similar far-field conditions and they are simply the free space scalar Green's function from the center point of the source group to the particular receiving point namely the local point on the UTD object and the observation point outside the grouping domain, respectively. However, in the present thesis different notations are used for the various far-field translation operators in order to distinguish the corresponding application.

Finally, substituting the expression (6.19) into equations (6.6) and (6.7) we get in the absence of UTD objects for observation points being outside the MLFMM grouping domain the electric and magnetic near-fields due to electric and magnetic currents

$$\begin{aligned}\mathbf{E}_P(\mathbf{r}_m) = &- j\frac{\omega\mu}{4\pi}T_L^{FF}(kr_{mn'})\left(\bar{\mathbf{I}} - \hat{k}_0\hat{k}_0\right)\cdot\sum_n H_n\tilde{\boldsymbol{\beta}}_n(\hat{k}_0)\\ &- j\frac{k}{4\pi}\hat{k}_0\times T_L^{FF}(kr_{mn'})\sum_n E_n\tilde{\boldsymbol{\beta}}_n(\hat{k}_0)\\ &+ \mathbf{E}^{inc}(\mathbf{r}_m)\end{aligned} \tag{6.21}$$

and

$$\begin{aligned}\mathbf{H}_P(\mathbf{r}_m) = &- j\frac{k}{4\pi}\hat{k}_0\times T_L^{FF}(kr_{mn'})\sum_n H_n\tilde{\boldsymbol{\beta}}_n(\hat{k}_0)\\ &+ j\frac{\omega\varepsilon}{4\pi}T_L^{FF}(kr_{mn'})\left(\bar{\mathbf{I}} - \hat{k}_0\hat{k}_0\right)\cdot\sum_n E_n\tilde{\boldsymbol{\beta}}_n(\hat{k}_0)\\ &+ \mathbf{H}^{inc}(\mathbf{r}_m),\end{aligned} \tag{6.22}$$

respectively, where $T_L^{FF}(kr_{mn'})$ is the direct far-field translation operator in the direction $\hat{k}_0$ given in (6.20).

This procedure is referred to as *far-field MLFMM translation*, by means of approximation of the direct translation operator by a far-field representation only for the direction $\hat{k}_0$ from the source group to the particular observation point outside the grouping domain in the absence of UTD objects. Thereby, it is assumed that the observation point lies in the far-field of the individual source group being still in the near-field with respect to the dimensions of the involved objects. Finally, direct terms are ignored if the observation point is in the shadow region of an UTD object.

6.4.2 Ray Optical Translations Outside Grouping Domain

Outside the domain covered by MLFMM groups ray optical field contributions due to the presence of UTD objects are taken into account in the same manner as presented in Section 5.4.1 and Section 6.3.2 namely through modification of the Green's function according to superposition of all received field contributions resulting in modification of the translation procedure, whereas a far-field approximation of the translation operator is used for ray optical contributions. However, in this particular case the resulting ray optical terms of the Green's function have a slightly different form since at the reception side no grouping is performed.

The assumed configuration is illustrated in Fig. 6.4 and in order to express the ray optical terms of the Green's function $\bar{\mathbf{G}}^{E/H}_{J/M,UTD}(\mathbf{r}_m, \mathbf{r}_n)$ the coupling path $\mathbf{r}_{mn} = \mathbf{r}_m - \mathbf{r}_n$ from the source current element to the observation point placed outside the grouping domain over the UTD object is written as

$$\mathbf{r} - \mathbf{r}' = \mathbf{r}_m - \mathbf{r}_n = (\mathbf{r}_m - \mathbf{r}_Q) + (\mathbf{r}_Q - \mathbf{r}_n) = \mathbf{r}_{mQ} + \mathbf{r}_{Qn}, \tag{6.23}$$

by first intervening the local point Q on the UTD object with position vector $\mathbf{r}_Q$. Then, for the subpath $\mathbf{r}_{Qn}$ in (6.23) the center point of the source group is intervened resulting in the expression (5.22). Thus, the total path is written as

$$\begin{aligned} \mathbf{r} - \mathbf{r}' = \mathbf{r}_m - \mathbf{r}_n &= (\mathbf{r}_m - \mathbf{r}_Q) + (\mathbf{r}_Q - \mathbf{r}_{n'}) + (\mathbf{r}_{n'} - \mathbf{r}_n) \\ &= \mathbf{r}_{mQ} + \mathbf{r}_{Qn'} - \mathbf{r}_{nn'}. \end{aligned} \tag{6.24}$$

Further, it is assumed that the field path from the center of the source group to the local point on the UTD object $\mathbf{r}_{Qn'}$ is much larger than the paths $\mathbf{r}_{nn'}$ within the source group. Under this condition, the electrical subpath kr_{Qn} in (6.23) is expanded in terms of a Taylor series and assuming the far-field condition (5.24) higher order terms of this expansion are neglected. Hence, the electrical subpath from the source current to the local UTD point is approximated by (5.27). Using this coupling path in the scalar term (2.34) of the equations (2.32) and (2.33) along with the expressions of ray optical mechanisms on the UTD objects described in Section 4.1 and Section 4.2 the ray optical terms of the Green's functions outside the grouping domain are written with the far-field representations

$$\begin{aligned} &\bar{\mathbf{G}}^{E}_{J,UTD}(\mathbf{r}_m, \mathbf{r}_n) = \frac{\mu}{\varepsilon} \bar{\mathbf{G}}^{H}_{M,UTD}(\mathbf{r}_m, \mathbf{r}_n) = \\ &\quad -j\frac{\omega\mu}{4\pi} \Bigg\{ \sum_q \widetilde{A}_{R_q}(s_{R_q}) \bar{\mathbf{R}}^{E/H}_q T^{UTD}_L(kr_{Q_{R_q}n'}) \cdot \left(\bar{\mathbf{I}} + \frac{1}{k^2} \nabla\nabla' \right) \mathrm{e}^{j\mathbf{k}_i \cdot \mathbf{r}_{nn'}} \\ &\quad + \sum_v \widetilde{A}_{D_v}(s_{D_v}) \bar{\mathbf{D}}^{E/H}_v T^{UTD}_L(kr_{Q_{D_v}n'}) \cdot \left(\bar{\mathbf{I}} + \frac{1}{k^2} \nabla\nabla' \right) \mathrm{e}^{j\mathbf{k}_i \cdot \mathbf{r}_{nn'}} \\ &\quad + \cdots \Bigg\} \end{aligned} \tag{6.25}$$

and

$$\begin{aligned}\bar{\mathbf{G}}^{E}_{M,UTD}(\mathbf{r}_m,\mathbf{r}_n) = -\bar{\mathbf{G}}^{H}_{J,UTD}(\mathbf{r}_m,\mathbf{r}_n) = \\ -\frac{1}{4\pi}\Bigg\{ \sum_q \widetilde{A}_{R_q}(s_{R_q})\bar{\mathbf{R}}^{E/H}_q T^{UTD}_L(kr_{Q_{R_q}n'})\cdot\nabla\times\bar{\mathbf{I}}\mathrm{e}^{j\mathbf{k}_i\cdot\mathbf{r}_{nn'}} \\ +\sum_v \widetilde{A}_{D_v}(s_{D_v})\bar{\mathbf{D}}^{E/H}_v T^{UTD}_L(kr_{Q_{D_v}n'})\cdot\nabla\times\bar{\mathbf{I}}\mathrm{e}^{j\mathbf{k}_i\cdot\mathbf{r}_{nn'}} \\ +\cdots\Bigg\},\end{aligned} \tag{6.26}$$

where $T^{UTD}_L(kr_{Qn'})$ is the ray optical translation operator given in (5.30), which translates outgoing ray optical fields from the source groups to incident ray optical fields at the local points on the UTD objects. As usual, the incident rays at the local points $Q_{R/D}$ on the UTD objects are multiplied with the appropriate scalar factors $\widetilde{A}_{R/D}(s_{R/D})$ and dyadic factors $\bar{\mathbf{R}}^{E/H}$, $\bar{\mathbf{D}}^{E/H}$ of the corresponding ray optical mechanism (see Section 4.1 and Section 4.2) providing the received ray optical contributions at the center of the receiving groups. Thereby, $r_{Qn'}$ is given by (5.31) and $s_{R/D}$ is given by (5.3), which in this case coincides with $\hat{k}_{r,d}$ given in (5.33). The term $\mathrm{e}^{j\mathbf{k}_i\cdot\mathbf{r}_{nn'}}$ is the phase shifting factor from the source current to the center of the source group. It is noticed, that no phase shifting is performed at reception since outside the grouping domain the field contributions are evaluated to each observation point separately. Also, $\hat{k}_i$ is given by (5.32) as shown in Fig. 6.4. Again, direct contributions of the Green's function are ignored if the observation point is in the shadow region of an UTD object. It is also noticed, that the above ray optical expressions (6.25) and (6.26) are valid under far-field conditions with respect to the MLFMM group dimension at the working level. A detailed derivation of the ray optical terms of the scalar Green's function (6.25) and (6.26) outside the grouping domain is given in Section D.2 in the Appendix D.

Finally, substituting the expressions (6.25) and (6.26) into equations (6.1) and (6.2) we get for the ray optical terms of the electric and magnetic fields outside the grouping domain the expressions

$$\begin{aligned}\mathbf{E}_{UTD}(\mathbf{r}_m) = \\ -j\frac{\omega\mu}{4\pi}\Bigg\{ \sum_q \widetilde{A}_{R_q}(s_{R_q})\bar{\mathbf{R}}^{E}_q T^{UTD}_L(kr_{Q_{R_q}n'})\cdot\Big(\bar{\mathbf{I}}-\hat{k}_r\hat{k}_i\Big)\cdot\sum_n H_n\widetilde{\boldsymbol{\beta}}_n(\hat{k}_i) \\ +\sum_v \widetilde{A}_{D_v}(s_{D_v})\bar{\mathbf{D}}^{E}_v T^{UTD}_L(kr_{Q_{D_v}n'})\cdot\Big(\bar{\mathbf{I}}-\hat{k}_d\hat{k}_i\Big)\cdot\sum_n H_n\widetilde{\boldsymbol{\beta}}_n(\hat{k}_i) \\ +\cdots\Bigg\} \\ -j\frac{k}{4\pi}\Bigg\{ \sum_q \hat{k}_r\times\widetilde{A}_{R_q}(s_{R_q})\bar{\mathbf{R}}^{H}_q T^{UTD}_L(kr_{Q_{R_q}n'})\cdot\sum_n E_n\widetilde{\boldsymbol{\beta}}_n(\hat{k}_i)\end{aligned}$$

$$
\begin{aligned}
&+\sum_{v} \hat{k}_d \times \tilde{A}_{D_v}(s_{D_v}) \bar{\mathbf{D}}_v^H T_L^{UTD}(kr_{Q_{D_v}n'}) \cdot \sum_{n} E_n \tilde{\boldsymbol{\beta}}_n(\hat{k}_i) \\
&+\cdots \Bigg\} \\
&+\mathbf{E}_{UTD}^{inc}(\mathbf{r}_m)
\end{aligned} \tag{6.27}
$$

and

$$
\begin{aligned}
&\mathbf{H}_{UTD}(\mathbf{r}_m) = \\
&-j\frac{k}{4\pi}\Bigg\{ \sum_{q} \hat{k}_r \times \tilde{A}_{R_q}(s_{R_q}) \bar{\mathbf{R}}_q^E T_L^{UTD}(kr_{Q_{R_q}n'}) \cdot \sum_{n} H_n \tilde{\boldsymbol{\beta}}_n(\hat{k}_i) \\
&+\sum_{v} \hat{k}_d \times \tilde{A}_{D_v}(s_{D_v}) \bar{\mathbf{D}}_v^E T_L^{UTD}(kr_{Q_{D_v}n'}) \cdot \sum_{n} H_n \tilde{\boldsymbol{\beta}}_n(\hat{k}_i) \\
&+\cdots \Bigg\} \\
&+j\frac{\omega\varepsilon}{4\pi}\Bigg\{ \sum_{q} \tilde{A}_{R_q}(s_{R_q}) \bar{\mathbf{R}}_q^H T_L^{UTD}(kr_{Q_{R_q}n'}) \cdot \left(\bar{\mathbf{I}} - \hat{k}_r \hat{k}_i \right) \cdot \sum_{n} E_n \tilde{\boldsymbol{\beta}}_n(\hat{k}_i) \\
&+\sum_{v} \tilde{A}_{D_v}(s_{D_v}) \bar{\mathbf{D}}_v^H T_L^{UTD}(kr_{Q_{D_v}n'}) \cdot \left(\bar{\mathbf{I}} - \hat{k}_d \hat{k}_i \right) \cdot \sum_{n} E_n \tilde{\boldsymbol{\beta}}_n(\hat{k}_i) \\
&+\cdots \Bigg\} \\
&+\mathbf{H}_{UTD}^{inc}(\mathbf{r}_m),
\end{aligned} \tag{6.28}
$$

respectively, where $T_L^{UTD}(kr_{Qn'})$ is the ray optical translation operator given in (5.30) and $\hat{k}_{r,d}$ is given in (5.33).

Various issues regarding the numerical implementation of the P-MLFMM-UTD approach will be discussed in the following section.

6.5 Numerical Implementation

Similar to the numerical implementation of the hybrid MLFMM-UTD approach presented in Section 5.4.2, a limited number of sampling points are used to represent the basis functions in the $\hat{k}$-space and to perform the integration over the Ewald sphere in the postprocessing stage. In general, the required directions $\hat{k}_0$ for the direct part and $\hat{k}_i$, $\hat{k}_{r,d}$ for the UTD part are not present as sampling points. So, these directions are computed from the neighboring sampling points of the numerical integration in the $\hat{k}$-space using local interpolation and anterpolation, respectively, as described in Section 5.4.2.

Similar to ray optical translation presented in Section 5.4.2, the worst-case for the condition (6.16) used to derive the far-field translation operator arises when the source current lies at the corner of the source group. Thus, the worst-case for condition (6.16) becomes

$$
r_{far} \geq \frac{1}{2} k |\mathbf{r}_{nn'}|_{max}^2 = \frac{\pi(0.5\sqrt{3}D_l)^2}{\lambda} \overset{(5.41)}{=} r_{UTD}, \tag{6.29}
$$

where D_l is the group dimension at level l and λ is the wavelength. The condition (6.29) enforces both the observation point outside the grouping domain as well as the local point on the UTD object to be in the far-field with respect to the group dimensions at the working level. Thus, observation points and UTD objects must only be in the far-field of the working source group at the particular level and not in the far-field of the whole structure.

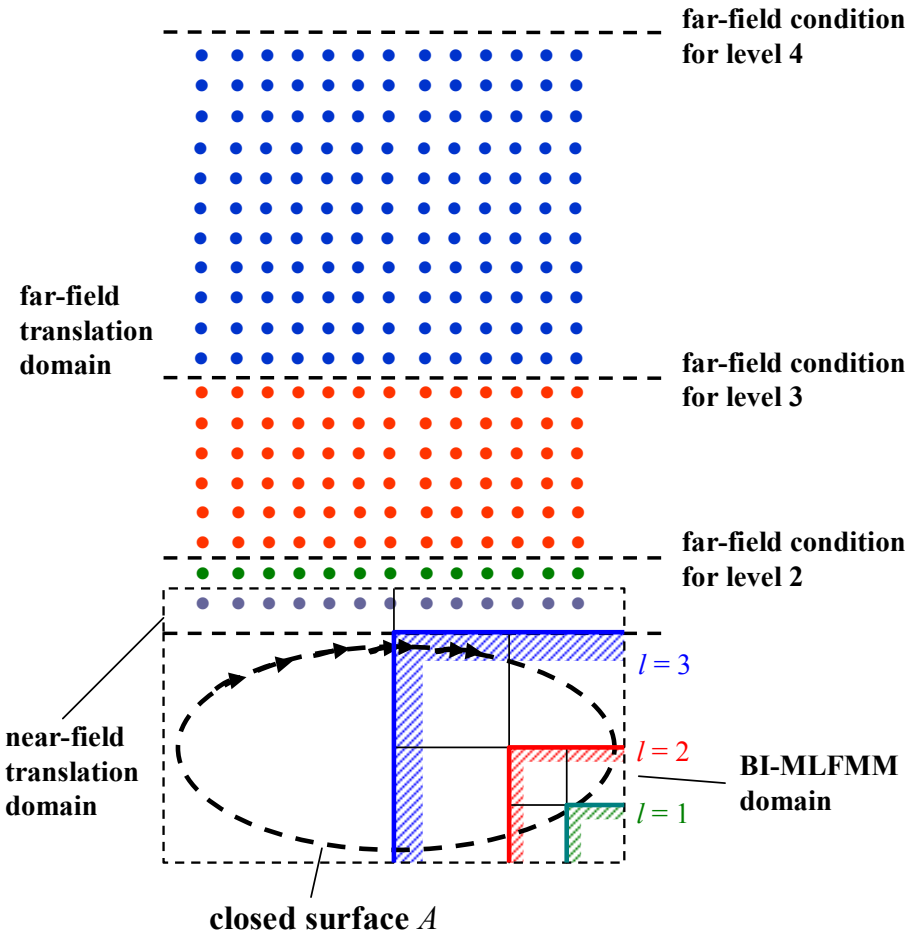

Figure 6.5: Optimum far-field translation level for each observation point.

Especially for the direct part of the implementation, for each observation point, far-field translations are performed at the coarsest level l, at which condition (6.29) is still satisfied. This level does not necessarily have to be the same for all observation points. Actually, for each observation point, the optimum level is found for far-field translations as shown in Fig. 6.5, where the group dimensions and the corresponding far-field conditions on various levels are illustrated with different colors. Particularly, the green region is the translation domain of the finest level, the red region is the translation domain of level 2 and the blue region is the translation domain of level 3. For instance, in case of observation points within the red region direct far-field translations are performed at the second level but not on the third level, where the condition (6.29) is valid at the blue region. In order to save computation time, the optimum level is found in the initialization step for each observation point in a worst-case sense using its shortest distance to the BI-MLFMM domain. Improved accuracy is provided by choosing a more stringent far-field condition.

On the other hand, in the UTD part of the implementation improved ray optical translations are achieved by using the gravity center of the currents within the groups as source and

receiving points for the radiated and received ray optical fields as described in Section 5.4.3. Also, in the present implementation it is required that the UTD objects do not cut the grouping domain in order to compute correctly ray optical contributions to the receiving groups containing observation points. Alternatively, the proposed approach could be implemented for UTD object that lie within the postprocessing grouping domain, however, in this case special treatment is required for accurate results such as additional bookkeeping of groups that are interrupted by UTD objects, which requires significant amount of additional implementation and computational effort.

For the evaluation of ray optical contributions given in (6.11), (6.12) inside the grouping domain and (6.27), (6.28) outside the grouping domain operations of dyadic analysis are used as described in Section A.2 in the Appendix A. These computations are performed for ray dyad components defined in the global spherical coordinate system as described in Section C.3 in the Appendix C. This is done for all ray optical terms except reflections on flat metallic surfaces, which are performed in the global Cartesian coordinate system since the radial component is available through the special treatment of reflection terms described in Section 5.5.2. The complete field expressions in the postprocessing stage of the hybrid FEBI-MLFMM-UTD method are summarized in Section D.3 in the Appendix D.

In addition to hybrid formulations and postprocessing accelerations described in the previous chapters, far-field scattering computations were also performed in the present thesis by applying planar near-field scanning techniques to ray optical field contributions. This approach will be presented in the following chapter.

Chapter 7

Far-Field Scattering Computations

7.1 Introduction

In addition to fast near-field computations presented in the previous Chapter 6 also far-field scattering computations including ray optical fields are performed with the hybrid FEBI-MLFMM-UTD method presented in this thesis. Thereby, special treatment is required for ray optical terms of the scattered field in the far-field region of flat finite objects since the finiteness of the objects is not considered in the formulations. Particularly, ray optical formulations in field based asymptotic methods are derived asymptotically assuming structures of infinite extent. For accurate scattering computations in the far-field of flat finite objects those methods cannot be used directly, since the finiteness of the objects is not considered in the ray optical formulations. Although it is possible to apply GO to calculate the scattered far-field of doubly curved surfaces, this is not possible for finite flat objects [27]. In the case of an incident plane wave on a finite flat plate, the reflected far-field according to GO is also a plane wave, which is only true in case of an infinite plane. Also, GO allows computation of fields in the specular direction only. Taking into account UTD contributions at the edges of the finite structures, the scattered field becomes more accurate. However, correct amplitude variations with the distance from the objects are obtained only at distances that are in the near-field with respect to the lengths of the straight edges. This is due to the fact, that the UTD scattering coefficients are derived for a canonical wedge problem of infinite extent.

Usually, ray optical far-field scattering computations are performed either using approximations of the Radar Cross Section (RCS) formula as in [163] resulting in restricted applicability or by combining ray optical methods with source based asymptotic approaches as in [164], [49], [50] resulting in the necessity to integrate over the objects, which can be inefficient for large scale problems. In this thesis, the drawbacks of ray optical methods in predicting scattered far-fields are efficiently overcome using an approach, which has some similarities with the well-known Shooting and Bouncing Rays (SBR) technique [165]. According to this, all ray optical field contributions are collected in an appropriate Huygens' surface and the far-fields are obtained by integrating the resulting equivalent Huygens' sources. In particular, we work with planar apertures and we use Near-Field to Far-Field Transformations (NFFFTs) based on planar near-field scanning techniques [166]-[171], which are widely used in antenna near-field measurement approaches. Thereby, scattered ray optical fields are first computed in a scanning plane in the near-field region of the involved objects and are afterwards transformed into the far-field using field expansions in terms of spectrum density

functions of outgoing waves resulting in relatively small computational effort. These functions are components of the plane wave spectrum associated with TE and TM fields and are determined from the tangential components of the scattered ray optical near-fields in the scanning plane by Fourier transforms. The computation of the fields in the scanning planes are accelerated using MLFMM as presented in the previous Chapter 6. However, direct field contributions (without UTD like interaction) to the observation points are computed directly in the far-field region using conventional fast techniques. Thus, only ray optical components of the scattered field are sampled, so that no evanescent waves are present in the scanning plane. Consequently, sampling rates higher than the Nyquist sampling rate of $\lambda_0/2$ are not required for any distance of the scanning plane from the involved objects. Sampling rates of $\lambda_0/2$ are used for grazing directions of observation to the scanning plane, whereas sampling rates less than $\lambda_0/2$ are used for restricted angle range around the normal direction to the scanning plane. Far-field solutions for large observation angle ranges are obtained by combining the far-fields of several scanning planes [81]-[84]. It is noticed, that to the knowledge of the author the use of NFFFTs to overcome the drawbacks of ray optical methods in predicting scattered far-fields is reported in the scientific community for the first time.

In the following, the formulation of the proposed approach within the hybrid framework will be presented and details of the numerical implementation will be discussed.

7.2 Configuration

Consider the configuration shown in Fig. 7.1 consisting of electrically large flat metallic UTD objects illuminated by plane wave, which may be in the same environment with composite metallic/dielectric arbitrarily shaped FEBI objects. It is assumed that the equivalent surface currents are known all over the Huygens' surfaces from the hybrid FEBI-MLFMM-UTD solution of the problem as described in Chapters 2 to 5, where mutual coupling among the involved objects is incorporated in the solution. The scattered electric field $\mathbf{E}^s_{tot}(\mathbf{r})$ produced by the equivalent surface currents at an observation point $\mathbf{r}$ is given by superposition of direct $\mathbf{E}^s(\mathbf{r})$ and ray optical $\mathbf{E}^{s,tot}_{UTD}(\mathbf{r})$ contributions according to the integral expression

$$\begin{aligned}\mathbf{E}^s_{tot}(\mathbf{r}) &= \mathbf{E}^s(\mathbf{r}) + \mathbf{E}^{s,tot}_{UTD}(\mathbf{r}) \\ &= \iint\limits_A \Big[\bar{\mathbf{G}}^E_{J,tot}(\mathbf{r},\mathbf{r}')\cdot\mathbf{J}_A(\mathbf{r}') + \bar{\mathbf{G}}^E_{M,tot}(\mathbf{r},\mathbf{r}')\cdot\mathbf{M}_A(\mathbf{r}')\Big]\,da', \end{aligned} \tag{7.1}$$

where $\bar{\mathbf{G}}^E_{J,tot}(\mathbf{r},\mathbf{r}')$ and $\bar{\mathbf{G}}^E_{M,tot}(\mathbf{r},\mathbf{r}')$ are the total Green's functions of the electric field due to electric and magnetic surface currents, respectively, given by (6.3). These consist of direct terms in the absence of UTD objects and all ray optical fields received at the observation point $\mathbf{r}$ for a given source point $\mathbf{r}'$ due to the presence of UTD objects. Also, A is the boundary surface enclosing the FEBI object according to the equivalence principle. The equivalent currents on A are assumed to be available in an expansion using RWG vector basis functions on triangular surface elements according to (2.69) and (2.70) as described in Section 2.2.2. The formulation for the magnetic field can be given by duality.

For far-field scattering computations in the postprocessing stage, direct and ray optical terms are treated in a different manner. In particular, direct field contributions in (7.1) in

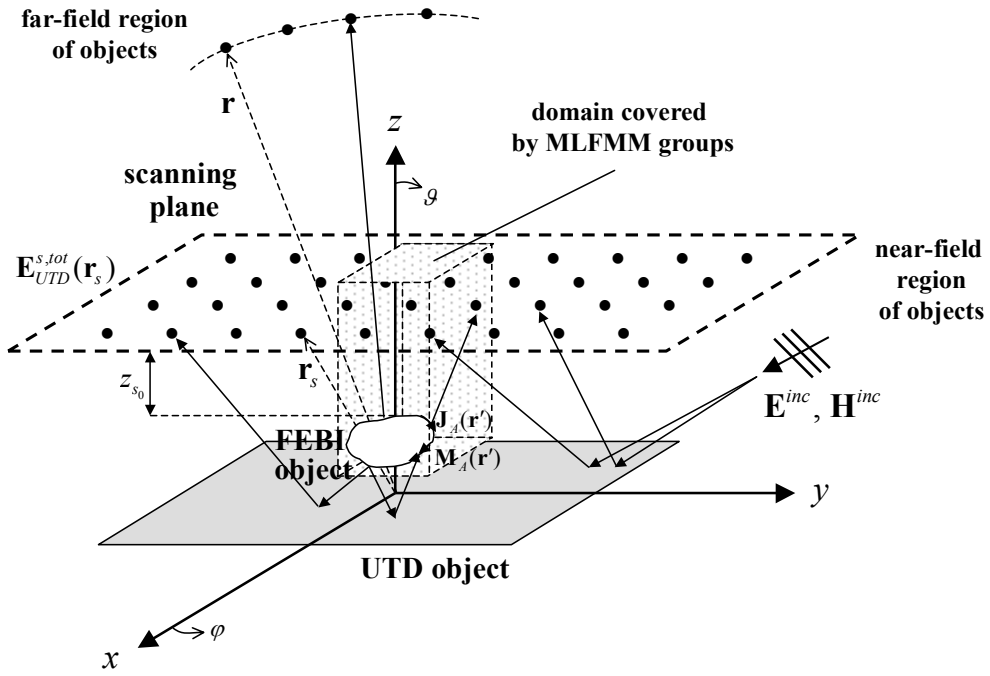

Figure 7.1: Configuration for ray optical far-field scattering treatment in the postprocessing stage of the hybrid FEBI-MLFMM-UTD method using planar NFFFTs. Scattered ray optical fields are first sampled on a scanning plane in the near-field region. These computations are accelerated by MLFMM. Then, the sampled near-fields are transformed into the far-field using plane wave expansions. Direct field terms are evaluated directly in the far-field of the involved objects using conventional fast techniques. Total far-fields are found by superposition.

the absence of UTD objects are evaluated directly in the far-field, whereas scattered ray optical field terms in (7.1) due to the presence of UTD objects are first computed in a scanning plane placed in the near-field region of the structures. Then, the corresponding far-fields are obtained by NFFFTs and the total far-fields are found by superposition. In the present thesis the proposed approach is applied for electric near-field scanning on a plane perpendicular to the z-axis for $z = z_{s_0}$ as shown in Fig. 7.1. However, plane wave spectrum expansions can be performed in the same way using magnetic near-field scanning as well as for scanning planes with any orientation. Thereby, formulations for magnetic fields can be given by duality.

7.3 Formulation

Direct field terms in (7.1) in the absence of UTD objects are evaluated directly in the far-field of the involved objects by MLFMM as reported in [4]. In particular, the radiation patterns of source groups containing BI currents are aggregated by conventional MLFMM up to the highest level, where the whole FEBI object is enclosed in one group. This source contribution corresponds to the scattered far-field of the FEBI object and using the appropriate far-field translation operator the received field contribution for the particular $\hat{k}$-direction to the far-field observation point is evaluated. Thus, direct contributions of electric and magnetic

currents to the scattered electric far-field in (7.1) are given by

$$\begin{aligned}\mathbf{E}^s(\mathbf{r}) = &- j\frac{\omega\mu}{4\pi}T_L^{FF}(kr)\left(\bar{\mathbf{I}}-\hat{k}_s\hat{k}_s\right)\cdot\sum_n\widetilde{\mathbf{J}}_n(\hat{k}_s)\\ &- j\frac{k}{4\pi}\hat{k}_s\times T_L^{FF}(kr)\sum_n\widetilde{\mathbf{M}}_n(\hat{k}_s)\end{aligned} \tag{7.2}$$

where

$$T_L^{FF}(kr)=\frac{e^{-jkr}}{r} \tag{7.3}$$

is the far-field translation operator in the direction $\hat{k}_s=\hat{r}$. Further, n is the total number of surface current elements and

$$\widetilde{\mathbf{J}}_n(\hat{k})=H_n\widetilde{\boldsymbol{\beta}}_n(\hat{k})=H_n\iint_A\boldsymbol{\beta}_n(\mathbf{r}_n)\mathrm{e}^{j\mathbf{k}\cdot\mathbf{r}_{nn'}}da', \tag{7.4}$$

$$\widetilde{\mathbf{M}}_n(\hat{k})=E_n\widetilde{\boldsymbol{\beta}}_n(\hat{k})=E_n\iint_A\boldsymbol{\beta}_n(\mathbf{r}_n)\mathrm{e}^{j\mathbf{k}\cdot\mathbf{r}_{nn'}}da' \tag{7.5}$$

are the $\hat{k}$-space representation of the electric and magnetic current densities on the surface elements. Also, $\mathbf{k}_s=k\hat{k}_s$ is the direction to the observation point in the far-field of the involved structures with k being the wavenumber of free-space given in (3.8) and $r=|\mathbf{r}|$.

On the other hand, ray optical contributions in (7.1) due to the presence of UTD objects are first computed in a scanning plane in the near-field region of the involved structures. Thereby, near-field computations are accelerated by the MLFMM approach illustrated in Fig. 7.2 similar to the one presented in Chapter 6 considering in this case only ray optical interactions with UTD objects. This means that only ray optical translations are needed using the corresponding ray optical translation operator $T_L^{UTD}(kr_{Qn'})$ given in (5.30). Thus, the total scattered ray optical electric near-field at a sampling point $\mathbf{r}_s=x_s\hat{x}+y_s\hat{y}+z_{s_0}\hat{z}$ in the scanning plane is given by

$$\begin{aligned}\mathbf{E}_{UTD}^{s,tot}(\mathbf{r}_s) &= \mathbf{E}_{UTD}^{s}(\mathbf{r}_s)+\mathbf{E}_{UTD}^{inc}(\mathbf{r}_s)\\ &= E_x(\mathbf{r}_s)\hat{x}+E_y(\mathbf{r}_s)\hat{y}+E_z(\mathbf{r}_s)\hat{z},\end{aligned} \tag{7.6}$$

where $\mathbf{E}_{UTD}^{inc}(\mathbf{r}_s)$ are ray optical contributions of the incident electric field received at the sampling point $\mathbf{r}_s$ given by (6.13). Also, $\mathbf{E}_{UTD}^{s}(\mathbf{r}_s)$ are ray optical scattering contributions of surface currents given by (6.11) and (6.27) depending on whether the sampling point is inside or outside the grouping domain, respectively.

The scattered ray optical near-field computed in the scanning plane is transformed into the far-field by standard plane wave spectrum expansions [166], [167] using the scattering matrix notation in [168]. In particular, the fields are expanded in terms of spectrum density functions of outgoing waves $T_1(\mathbf{k}_s)$ and $T_2(\mathbf{k}_s)$, which are components of the plane wave spectrum $\mathbf{A}(\mathbf{k}_s)$ associated with TE and TM fields with respect to z, respectively. In a two-port network representation, these functions are transmission coefficients of TE and TM field components in the positive z-direction. It is noticed, that the plane wave spectrum is the vector amplitude of the uniform plane wave

$$\mathbf{A}(\mathbf{k}_s)e^{-j\mathbf{k}_s\cdot\mathbf{r}} \tag{7.7}$$

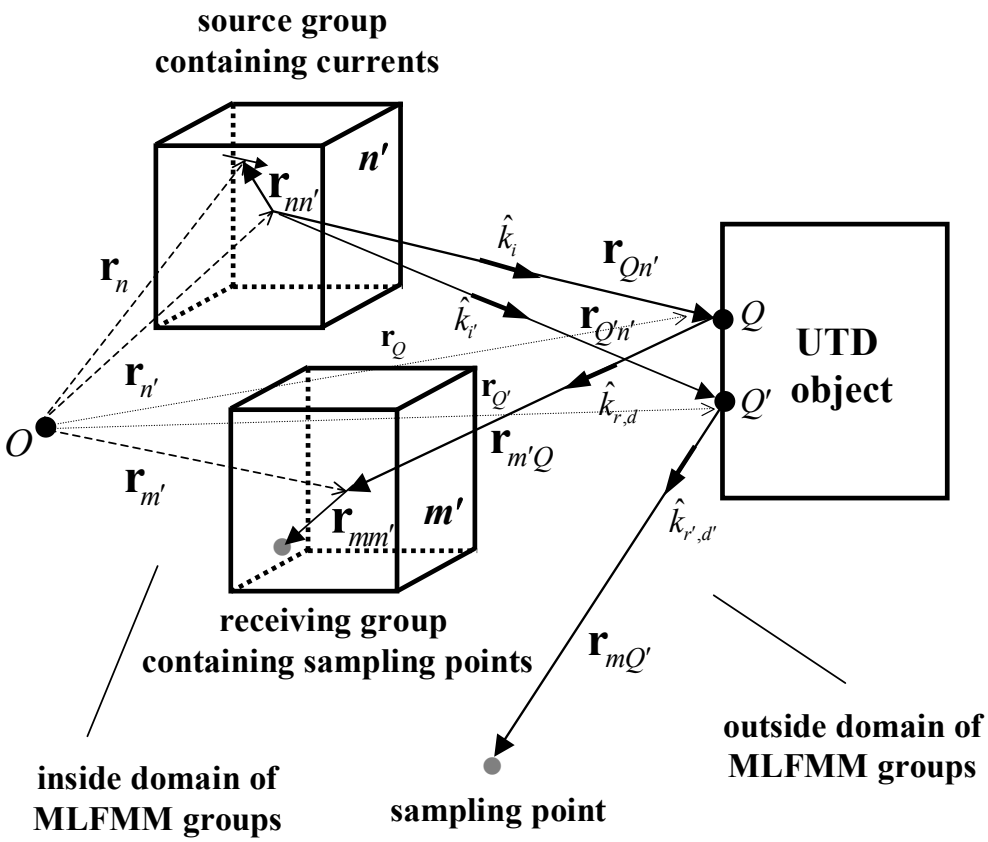

Figure 7.2: Configuration for accelerated ray optical computations in the scanning plane.

propagating in the direction

$$\mathbf{k}_s = k\hat{k}_s = k_{s_x}\hat{x} + k_{s_y}\hat{y} + k_{s_z}\hat{z} \tag{7.8}$$

with wavenumber

$$k = \sqrt{k_{s_x}^2 + k_{s_y}^2 + k_{s_z}^2}, \tag{7.9}$$

where k_{s_x} and k_{s_y} are the real-valued independent variables of the plane wave spectrum expansion. Also, $e^{-j\mathbf{k}_s\cdot\mathbf{r}}$ is the elementary planar scalar wave function. The scattered field at the observation point $\mathbf{r} = x\hat{x} + y\hat{y} + z\hat{z}$ in the far-field region of the involved structures is given in the spherical coordinate system by the asymptotic approximation

$$\mathbf{E}(\mathbf{r}) = j2\pi k\cos\theta\left[jT_1(\mathbf{k}_s)\hat{\varphi} - T_2(\mathbf{k}_s)\hat{\vartheta}\right]\frac{e^{-jkr}}{r}, \tag{7.10}$$

where the spectrum density functions of outgoing waves $T_1(\mathbf{k}_s)$ and $T_2(\mathbf{k}_s)$ are related to the independent Cartesian components $A_x(\mathbf{k}_s)$ and $A_y(\mathbf{k}_s)$ of the plane wave spectrum by

$$T_1(\mathbf{k}_s) = \frac{1}{j4\pi k_r^2}\left[A_y(\mathbf{k}_s)k_{s_x} - A_x(\mathbf{k}_s)k_{s_y}\right], \tag{7.11}$$

$$T_2(\mathbf{k}_s) = -\frac{k}{4\pi k_{s_z}k_r}\left[A_x(\mathbf{k}_s)k_{s_x} + A_y(\mathbf{k}_s)k_{s_y}\right], \tag{7.12}$$

respectively, where

$$k_r = \sqrt{k_{s_x}^2 + k_{s_y}^2} \tag{7.13}$$

so that

$$k_{s_z} = \sqrt{k^2 - k_r^2}. \tag{7.14}$$

Using Fourier transforms of the tangential components $E_x(\mathbf{r}_s)$, $E_y(\mathbf{r}_s)$ of the scattered ray optical electric near-fields in the scanning plane, the independent Cartesian components of the plane wave spectrum are given by

$$A_x(\mathbf{k}_s) = e^{jk_{s_z}z} \int_{-\infty}^{\infty}\int_{-\infty}^{\infty} E_x(\mathbf{r}_s) e^{-j(k_{s_x}x_s + k_{s_y}y_s)}\, dx_s dy_s, \tag{7.15}$$

$$A_y(\mathbf{k}_s) = e^{jk_{s_z}z} \int_{-\infty}^{\infty}\int_{-\infty}^{\infty} E_y(\mathbf{r}_s) e^{-j(k_{s_x}x_s + k_{s_y}y_s)}\, dx_s dy_s, \tag{7.16}$$

which are evaluated with low effort compared to total computation time [168].

7.4 Numerical Implementation and Discussion

In the numerical implementation, first the $\hat{k}$-space representation of the radiated fields is computed at the various MLFMM levels. Then, the field contributions to the observation points in the scanning plane are computed via ray optical translations from an appropriate level guaranteeing that the critical points on the UTD objects are in the far-field of both the source group and the receiving group, in which the sample point is located, according to the far-field criterion (5.41). For observation points located outside of the domain covered by the MLFMM groups, the far-field criterion (5.41) needs only to be checked for the source group.

In near-field measurement approaches, where planar scanning techniques are typically used, the sampled near-field contains evanescent wave components requiring special treatment such as higher spatial sampling rates than the Nyquist rate in combination with sufficient distance z_{s_0} of the scanning plane [167]-[170]. However, in the present approach only ray optical components of the scattered field are sampled, which are purely propagating waves, so that no evanescent modes are present in the scanning plane. Consequently, the dependent variable k_{s_z} of the plane wave spectrum expansion is always real-valued and the independent variables are bounded according to

$$k_r = \sqrt{k_{s_x}^2 + k_{s_y}^2} \leq k. \tag{7.17}$$

Thus, the plane wave spectrum has always an upper limit at the wavenumber of free-space $k = \frac{2\pi}{\lambda_0}$. Consequently, sampling rates higher than the Nyquist sampling rate of $\lambda_0/2$ are not required for any distance of the scanning plane from the involved objects.

Rays with grazing incidence to the scanning plane contribute to the scattered field in grazing directions ($\vartheta = \pm 90°$) and are found at the upper limit of the plane wave spectrum, so that

$\lambda_0/2$ sampling rate is required to transform them into the far-field. However, as the direction of ray incidence to the scanning plane goes towards the normal direction the corresponding ray contributions are moving away from the upper limit of the plane wave spectrum towards smaller values and the effective wavelength in the scanning plane increases, so that sampling rates less than $\lambda_0/2$ are sufficient to transform them into the far-field. In the limiting case of ray incidence normal to the scanning plane, the ray contribution is found at the origin of the plane wave spectrum and the effective wavelength in the scanning plane goes to infinity, which means that no sampling limit exists at all.

Using sampling rates less than $\lambda_0/2$, computation time is reduced but on the other hand accuracy becomes worse towards near-grazing directions of observation due to aliasing. This results in reduced angular coverage around the normal direction to the scanning plane. Also, the angular coverage depends on the dimensions of the scanning plane, on the dimensions of the involved objects, and on the distance z_{s_0} between scanning plane and the involved objects [172], [173]. In the numerical implementation, the scanning plane is truncated resulting in reduced angular coverage around the normal direction to the scanning plane. Using scanning planes with larger dimensions, accuracy towards grazing directions is improved but at the price of longer computation time. The drawback of reduced accuracy at grazing directions of observation is efficiently overcome by combining the solutions obtained from scanning planes with different angle ranges. Alternatively, angular limitations due to scanning plane truncation can be overcome using cylindrical or spherical scanning techniques [170] or relieved by methods as discussed in [171]. In the present thesis planar scanning planes were applied, since their implementation is very efficient and a restricted angle range is sufficient for many applications.

The accuracy of scattering far-field computations with the hybrid FEBI-MLFMM-UTD method basically depends on the applicability of the UTD part, since the FEBI-MLFMM part produces numerically exact results directly in the far-field for arbitrarily shaped composite metallic/dielectric objects. The UTD is in general applicable for electrically very large and relatively simple objects and it is responsible for the accuracy of the sampled fields in the scanning plane. More on the applicability of UTD can be found in Chapter 4. Furthermore, the accuracy of the NFFFT part in the postprocessing stage of the hybrid method depends on scanning plane dimensions and sampling spacings as discussed above and it is independent of geometry and sizes of the involved objects as long as the requirements for the scanning plane are fulfilled.

Using the hybrid FEBI-MLFMM-UTD method including the postprocessing features presented in the previous chapters large scale radiation and scattering problems including arbitrarily shaped and electrically very large objects can be handled efficiently by saving a large amount in computation time and memory requirements. This is demonstrated very clearly with numerical examples presented in the next chapter.

Chapter 8

Numerical Examples

In this chapter, numerical examples are presented for validation of the presented hybrid field formulations as well as for demonstration of the applicability and the efficiency of the hybrid method presented in this thesis. Numerical results for various scattering and radiation problems are shown, where excellent agreement and significant saving in computational resources compared to reference solutions can be observed.

8.1 Scattering Problems

8.1.1 Dielectric Cube over Plate

The first numerical example consists of a dielectric cube with 1 m edge length placed in front of a flat metallic square plate with 6 m edge length as shown in Fig. 8.1 a). The cube was filled with a lossy dielectric material with $\varepsilon_r = 2.5 - j0.01$ and the system was excited with an x-polarized plane wave traveling in $-z$-direction with $|E_0| = 1$ V/m and $f = 500$ MHz. As a reference the full FEBI-MLFMM solution was used, in which the surfaces were discretized with 35356 and the dielectric volume with 41611 unknowns. The magnitude of the equivalent surface current distribution resulting from the reference solution is illustrated in Fig. 8.1 b), where strong mutual coupling between both objects can be clearly seen. For the hybrid FEBI-MLFMM-UTD solution the same mesh was used for the cube and the influence of the plate was taken into account by UTD.

In the postprocessing stage of the hybrid computation, the bistatic RCS was computed with the approach described in Chapter 7 by evaluating the scattered ray optical electric near-field on 1681 sampling points in a scanning plane perpendicular to the z-axis with dimensions $20\lambda_0 \times 20\lambda_0$, which corresponds to a sampling rate of $\lambda_0/2$, and for $z_{s_0} = \lambda_0$ as shown in Fig. 8.1 a), where λ_0 is the free space wavelength. Further, the bistatic RCS was computed with the hybrid approach by evaluating ray optical contributions at observation points directly in the far-field of the whole structure particularly for $r = 1000$ m. The resulting copolar bistatic RCS in the xz-plane is shown in Fig. 8.2 a), where excellent agreement compared to the reference solution can be seen using the hybrid method presented in this thesis for a wide angle range of observation. Also, strong deviations from the reference solution can be observed in case of direct evaluation of ray optical contributions in the far-field with the hybrid method due to failure of ray optical techniques to predict scattered far-fields.

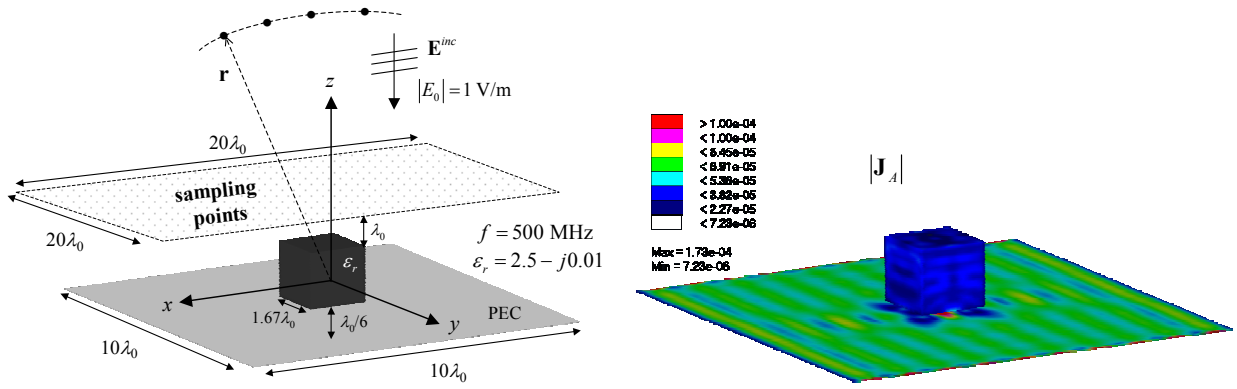

a) b)

Figure 8.1: Dielectric cube with 1 m edge length placed in front of a flat metallic square plate with 6 m edge length. a) Configuration. b) Magnitude of equivalent surface currents from reference solution.

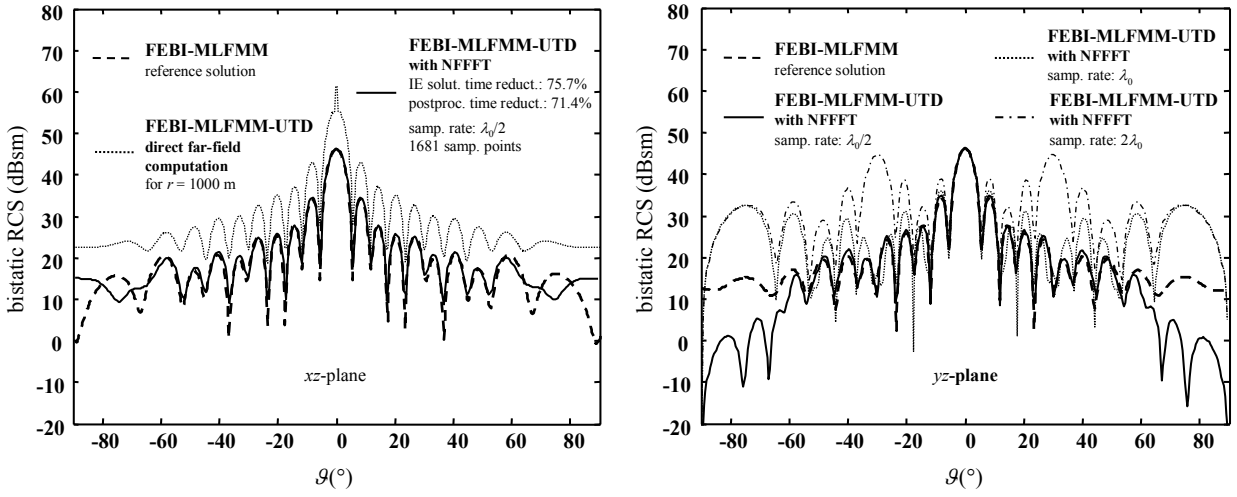

a) b)

Figure 8.2: Copolar bistatic RCS of configuration shown in Fig. 8.1. a) In the xz-plane for $\lambda_0/2$ sampling rate. The reduction in computation time is in comparison with the reference solution. b) In the yz-plane for sampling rates of $\lambda_0/2$, λ_0, and $2\lambda_0$.

Obviously, special treatment of UTD contributions according to the proposed approach is essential for accurate far-field scattering results. In the same figure, the improvement in computation time using the hybrid method compared to the reference solution is shown for both the IE solution as well as postprocessing computations. Thereby, saving of large amount in computation time in each case can be seen.

Finally, the bistatic RCS was computed for different sampling rates using the same scanning plane dimensions and the same distance to the dielectric cube. The results in the yz-plane are shown in Fig. 8.2 b), where it can be observed, that for decreasing sampling rate deviations towards grazing directions to the scanning plane become stronger and the field of view is reduced about the normal direction to the scanning plane. For $2\lambda_0$ sampling rate the bistatic

RCS is predicted well with the hybrid method for an angle range of about $\pm 10°$ around the normal direction.

8.1.2 Cone-Cylinder within Corner Reflectors

The second example consists of a conducting cone-cylinder placed inside of two different kind of corner reflectors. First, the cone-cylinder was placed within a 90° dihedral conducting corner reflector at a distance of $1.5\lambda_0$ in x-direction as shown in Fig. 8.3 a). The problem was excited by a z-polarized plane wave traveling in $-x$-direction with $|E_0| = 100$ V/m and $f_0 = 15$ GHz. Again, the numerical exact BI-MLFMM solution of the problem was used as a reference, where both objects were discretized with a triangular surface mesh resulting in a model with 786391 unknowns. For the full hybrid BI-MLFMM-UTD computation the same mesh was used for the cone-cylinder and second order rays were additionally taken into account in order to have sufficient treatment of the corner reflector by UTD. In this case, the total number of unknowns was 42408.

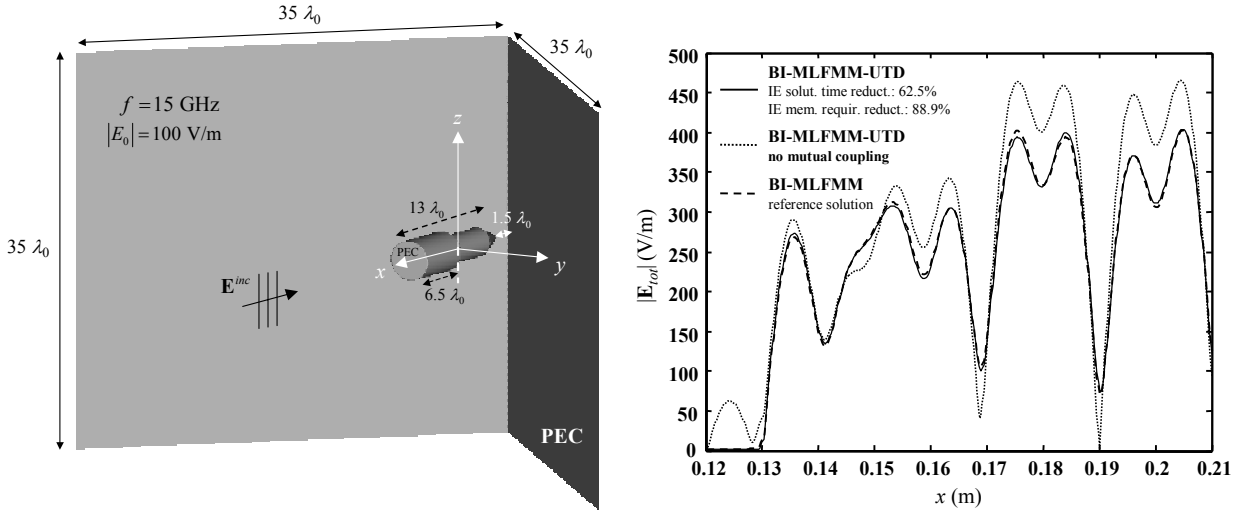

a) b)

Figure 8.3: Conducting cone-cylinder within 90° dihedral corner reflector. a) Configuration. b) Magnitude of total electric field along direction of propagation. The reduction in computational resources is in comparison with the reference solution.

Further, computations were done without taking into account mutual coupling between equivalent surface currents and corner reflector. In this case, only the incident field of the problem was modified by UTD contributions and this BI solution was used afterwards to compute the field distributions including UTD. Results of the total electric field along the direction of propagation compared to the numerical exact solution and the solution without mutual coupling are shown in Fig. 8.3 b). For the full hybrid computation including mutual coupling the results show excellent agreement with the reference solution. It can be clearly seen that mutual coupling according to the hybrid FEBI-MLFMM-UTD method presented in this thesis is important for accurate hybrid results. In addition, significant savings of IE solution time and memory requirements compared to the reference solutions is provided by the full hybrid computation as shown in Fig. 8.3 b).

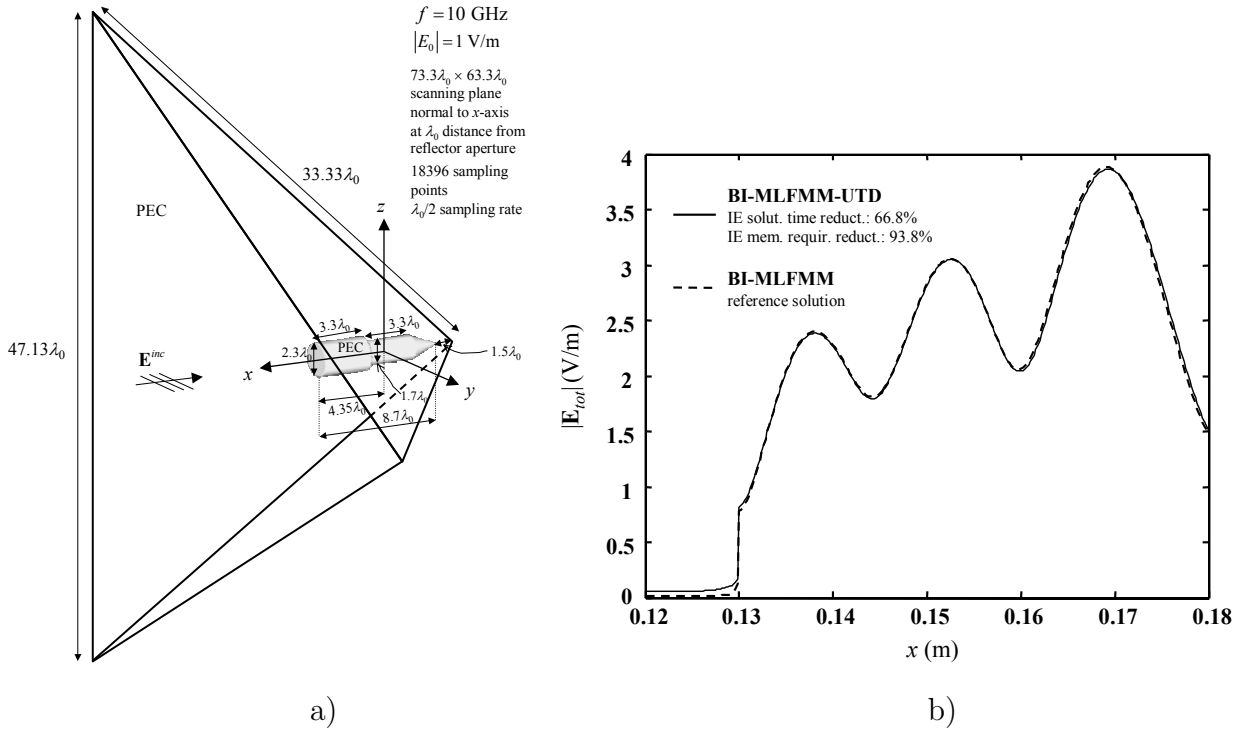

a) b)

Figure 8.4: Conducting cone-cylinder within 90° trihedral corner reflector. a) Configuration. b) Magnitude of total electric field along direction of propagation. The reduction in computational resources is in comparison with the reference solution.

Second, the same cone-cylinder was placed within a 90° trihedral corner reflector as shown in Fig. 8.4 a). In this case, the problem was excited with a y-polarized plane wave traveling in $-x$-direction with $|E_0| = 1$ V/m and $f = 10$ GHz. Again, the numerically exact solution was used as a reference, where 621912 unknowns were used to discretize the surfaces of the objects. In the hybrid computation, the corner reflector was treated by UTD using higher order ray optical contributions and in the postprocessing stage first the total electric field was computed along the direction of propagation. The magnitude of the resulted total electric field is shown in Fig. 8.4 b), where excellent agreement of the hybrid result can be observed compared to the reference solution. In the same figure reduction of computational resources compared to the reference solution is shown. It is obvious, that significant amount of computation time and memory requirements are saved in the IE solution stage using the hybrid method presented in this thesis.

After that, a $73.3\lambda_0 \times 63.3\lambda_0$ scanning plane perpendicular to the x-axis was used to compute the bistatic RCS with 18396 sampling points, which corresponds to a sampling rate of $\lambda_0/2$. The scanning plane was placed at a distance of λ_0 from the reflector aperture. The computed copolar bistatic RCS is shown in Fig. 8.5 a) and Fig. 8.5 b) for the xy- and the xz-plane, respectively, where very good agreement with the reference solution can be seen for a wide angle range of observation. The reason for lower degree of accuracy observed in the results of Fig. 8.5 b) compared to the other examples, especially in the fine structure of nulls, can be found in the scanning plane dimension in z-direction. Due to this, a considerable amount of UTD rays, which significantly contribute in the xz-plane for the particular directions, is not received at the scanning plane. In the same figures the computation time reduction

compared to the reference solution for the postprocessing stage is shown. Thereby, significant savings in the postprocessing computations can be observed using the hybrid method. Using a larger scanning plane, accuracy towards grazing observation directions can be improved, but computation time suffers. However, excellent and efficient results for the whole angle range are achieved combining solutions provided by additional scanning planes as it will be demonstrated in the next example.

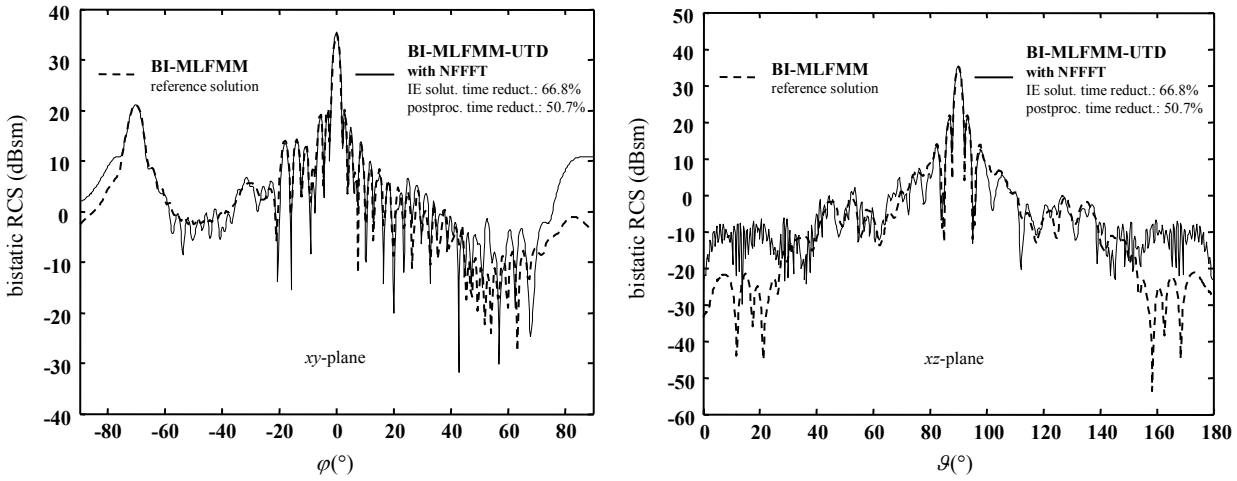

a) b)

Figure 8.5: Copolar bistatic RCS of configuration shown in Fig. 8.4. a) In the xy-plane. b) In the xz-plane. The reduction in computation time is in comparison with the reference solution.

8.1.3 Cylinder with Coated Top over Plate

Next example is a conducting cylinder with a coated metallic hemispherical top placed over a flat metallic plate and excited by plane wave as shown in Fig. 8.6. Again the full FEBI-MLFMM was used as a reference and for the hybrid solution, the same mesh was used for the cylinder with hemispherical top and the plate was treated by UTD.

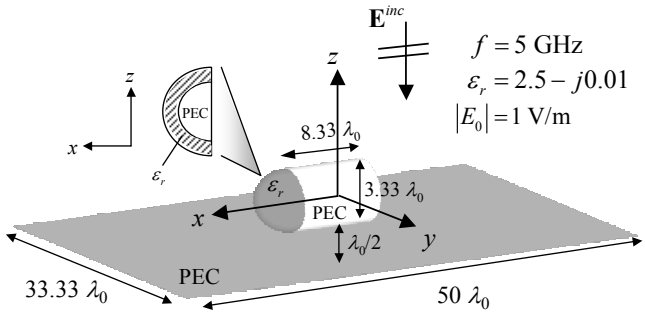

Figure 8.6: Conducting cylinder with coated metallic hemispherical top over flat metallic plate.

In the postprocessing stage of the hybrid solution, a scanning plane perpendicular to the z-axis was first used to compute the bistatic RCS using 15251 sampling points. The computed

copolar bistatic RCS in the yz-plane is shown in Fig. 8.7 a), where excellent agreement with the reference solution can be observed for an angle range of about $\pm 45°$ from the normal direction to the scanning plane.

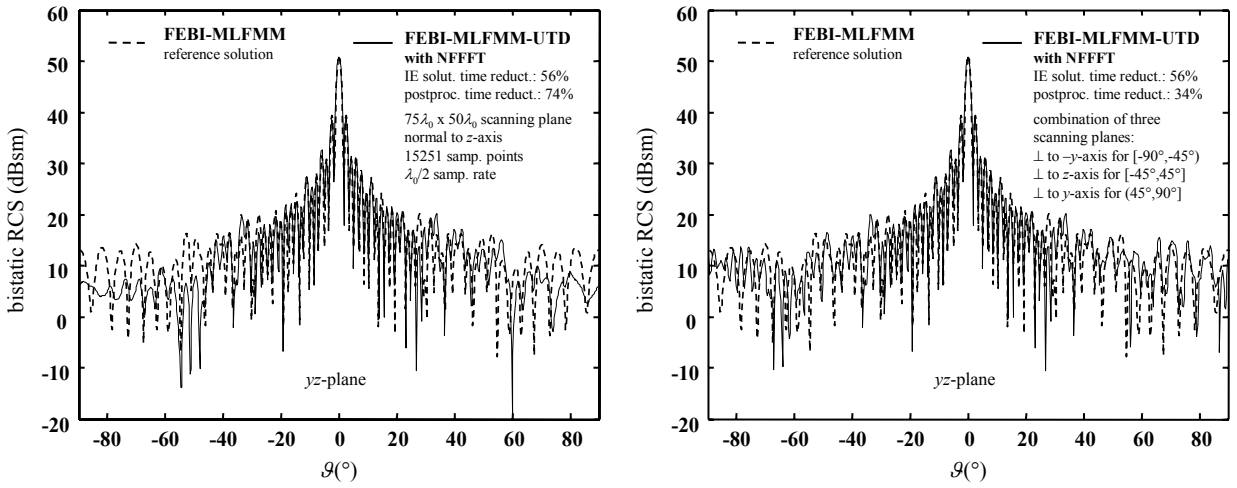

a) b)

Figure 8.7: Copolar bistatic RCS of configuration shown in Fig. 8.6. a) In the yz-plane for a scanning plane perpendicular to the z-axis. b) In the yz-plane combining the solutions of three scanning planes for the complete angle range. The reduction in computation time is in comparison with the reference solution.

After that, two additional scanning planes were used in order to overcome low accuracy at grazing observation angles by combining the solutions. In particular, a scanning plane perpendicular to the $-y$-axis was used to compute the bistatic RCS for the observation angles in the range $[-90°, -45°)$ as well as a scanning plane perpendicular to the y-axis for the observation range $[45°, 90°)$. The resulting copolar bistatic RCS can be seen in Fig. 8.7 b), where excellent agreement for the complete angle range can be observed. Again, a large amount in computation time is saved in each case using the hybrid method. In the combined hybrid solution of Fig. 8.7 b), computation time increases as compared to the hybrid solution of Fig. 8.7 a). However, it is still significantly lower than the computation time of the numerically exact solution providing excellent results for $\pm 90°$.

8.1.4 General Example

The configuration shown in Fig. 8.8 a) represents a more general example, where full combination of the hybrid FEBI-MLFMM-UTD method proposed in the present thesis is clearly demonstrated. The dimensions of the flat metallic plates (UTD objects) are $28.5\lambda_0 \times 60\lambda_0$. The lossy dielectric structure with $\varepsilon_r = 2.5 - j0.005$ is mounted in a metallic cavity. The mixed metallic/dielectric body has a square cross section in the xy-plane and the metallic torus is rotationally symmetric around the z-axis. All objects were placed symmetrically with respect to both the xz- and the yz-plane. The problem was excited by a y-polarized plane wave traveling in $-z$-direction with $|E_0| = 100$ V/m and $f_0 = 30$ GHz. In the hybrid computation the metallic torus and the mixed metallic/dielectric structure were discretized with tetrahedral elements within the dielectric volume and triangles on the surfaces resulting

in a model with 113049 BI unknowns. The electrically large plates were treated by UTD. The results are compared to the full FEBI-MLFMM solution, where all objects were discretized with 1715195 BI unknowns. In Fig. 8.8 b), the total electric near-field along the direction of propagation is shown for both computations. It can be seen that results with the hybrid method show excellent agreement with the exact numerical solution.

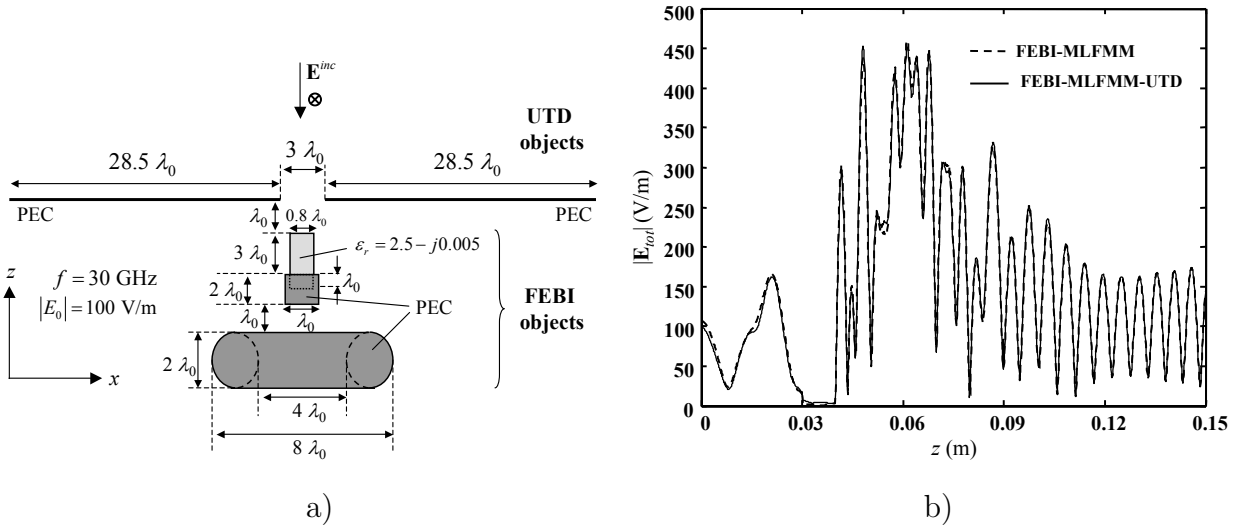

a) b)

Figure 8.8: General problem of two FEBI and two UTD objects. a) Configuration. b) Magnitude of total electric field along direction of propagation.

8.2 Radiation Problems

8.2.1 Log-Periodic Antenna in Front of Plates

First radiation example consists of a log-periodic dipole antenna radiating in the neighborhood of flat metallic plates as shown in Fig. 8.9 a) for 900 MHz operating frequency. The dipoles were simulated by infinitely thin metallic strips and the antenna was excited by a delta-gap voltage source. As a reference, the full BI-MLFMM solution was used, where all objects were discretized with 81483 BI unknowns using EFIE. For the hybrid computation the same mesh was used for the antenna and the flat plates were treated by UTD resulting into 1683 unknowns. In Fig. 8.9 a), the computation time and memory requirements for both simulations can be seen, where saving of significant amount in computational resources can be observed using the hybrid method.

The radiation pattern of the antenna in the xy-plane can be seen in Fig. 8.9 b), where in comparison with the radiation pattern of the antenna in free space strong influence of the environment in the radiation can be observed in all directions. The hybrid solution shows excellent agreement to the reference result needing much less computational resources. This makes the hybrid method presented in this thesis very attractive for numerical simulation of configurations including environment effects by taking environment objects into account very efficiently with UTD. The influence of the environment in the radiation characteristic of the log-periodic antenna can also be seen very clearly in Fig. 8.10, where the instantaneous electric field for $t = 0$ sec is shown in the xy-plane. It is noticed, that instantaneous fields

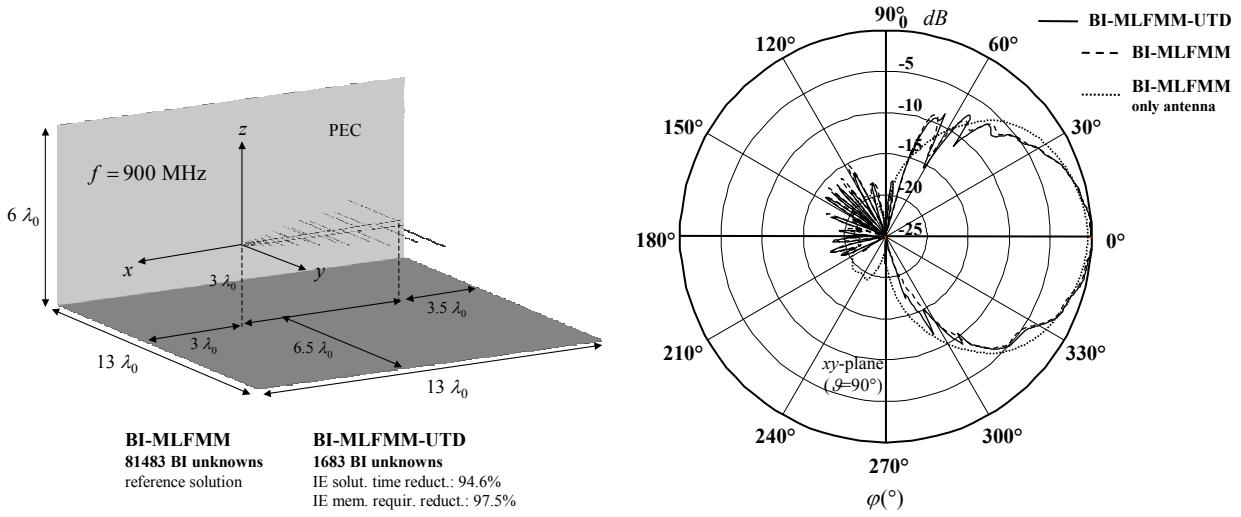

a) b)

Figure 8.9: Log-periodic antenna radiating in the neighborhood of flat plates. a) Configuration. The reduction in computation time is in comparison with the reference solution. b) Total field radiation pattern in the xy-plane.

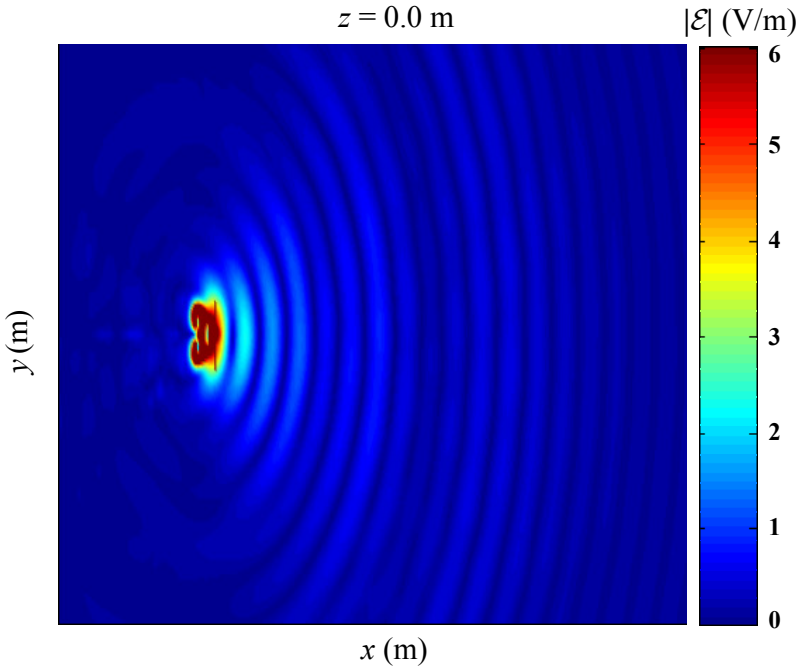

Figure 8.10: Instantaneous electric field for $t = 0$ sec in the xy-plane for the antenna shown in Fig. 8.9 a).

are referred to the physical time-dependent field quantities and are functions of both spatial and time variables. On the other hand, complex fields are functions of only spatial variables and the time delay due to the finite speed of propagation is expressed by phase. In case of

time-harmonic $e^{j\omega t}$ dependence, the physical quantities are understood to be the real part of the corresponding complex quantity.

8.2.2 Dielectric Rod Antenna in Front of Arbitrarily Oriented Plates

In this example a dielectric rod antenna is radiating in front of two arbitrarily oriented flat plates placed as shown in Fig. 8.11 a). The operating frequency of the antenna was 10 GHz and a delta-gap voltage source was used for excitation. The length of the rod was $3\lambda_0$ with $\varepsilon_r = 2.5$ and a metallic mounting was used to hold the rod. The small radius of the rod was $0.24\lambda_0$ and the large radius at the connection point with the metallic mounting was $0.45\lambda_0$. As a reference, the full FEBI-MLFMM solution is used and with the hybrid approach two simulations where performed for both with and without double diffracted contributions on the nearby edges. In Fig. 8.11 b), the computational effort for each case is shown, where the saving in computation time and memory requirements using the hybrid method can be clearly seen.

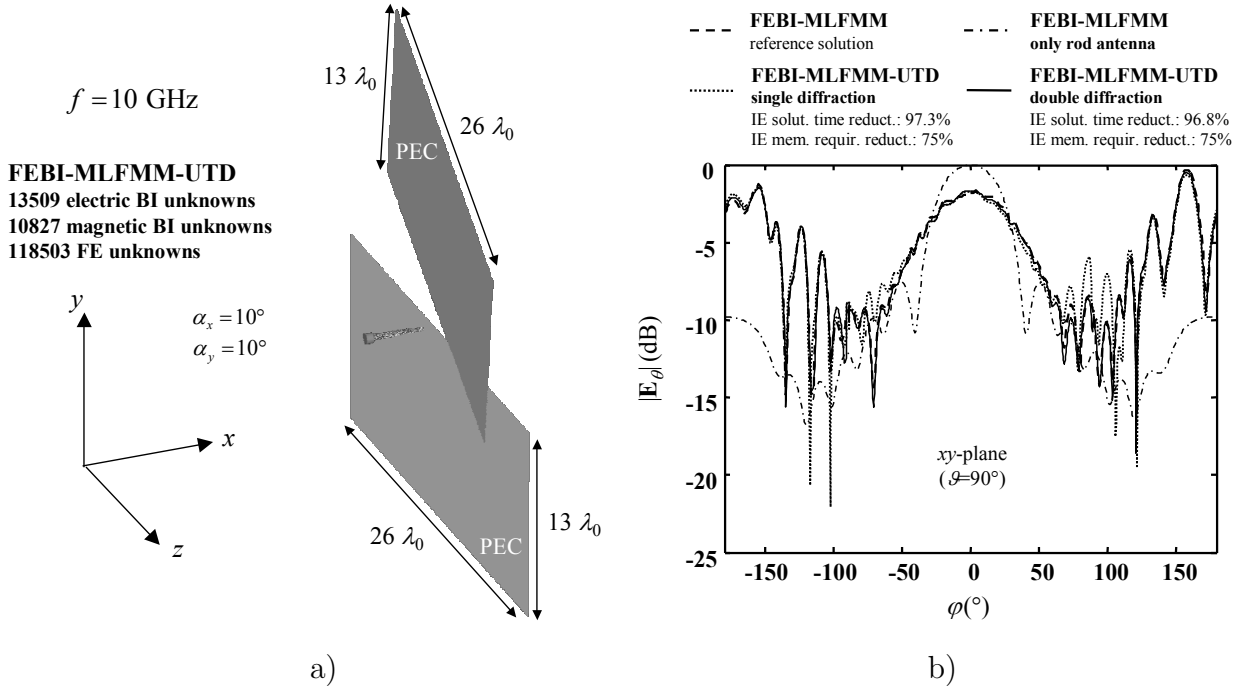

a) b)

Figure 8.11: Dielectric rod antenna radiating in front of arbitrarily oriented flat plates. a) Configuration. b) Total field radiation pattern in the xy-plane. The reduction in computation time is in comparison with the reference solution.

In the same figure, the radiation pattern of the antenna in the xy-plane cutting through the antenna in the middle is shown. It can be seen, that the hybrid result including double diffraction shows excellent agreement with the reference solution. The double diffracted field on the edges of the slot becomes significant for near-grazing directions to the plates (around $\pm 90°$). The simulations are also compared to the radiation pattern of the antenna radiating in free space. The influence of the slot on the radiation of the antenna is obvious. The deformation of the main lobe can be seen as well as significant increase of the radiation in

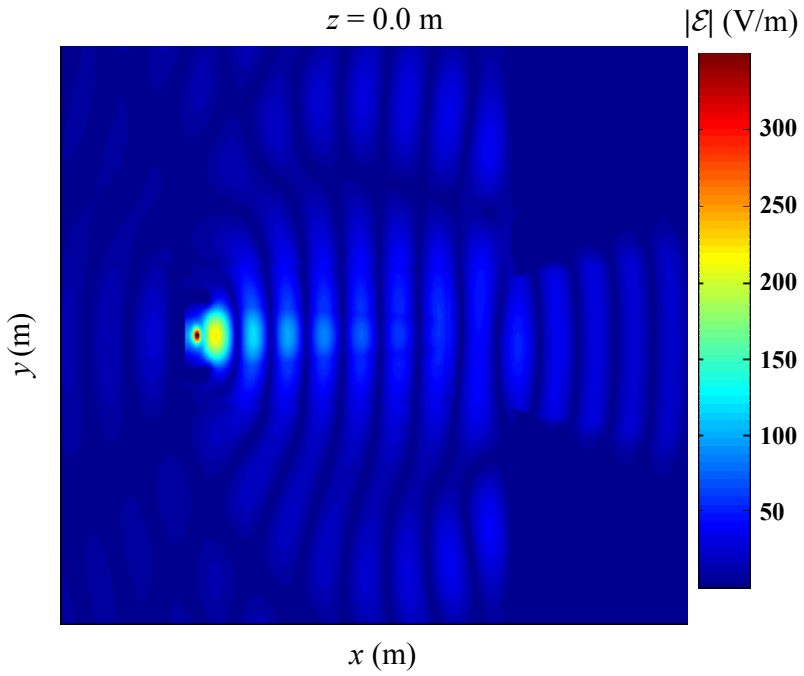

Figure 8.12: Instantaneous electric field for $t = 0$ sec in the xy-plane for the antenna shown in Fig. 8.11 a).

backward direction. A disturbance of the symmetric radiation can also be observed. The same result can be seen in Fig. 8.12, where the instantaneous electric field for $t = 0$ sec is shown in the xy-plane. The influence of the environment in the near-field distribution of the antenna can be clearly seen.

8.2.3 Cylindrical Parabolic Reflector Antenna

The next problem is a cylindrical parabolic reflector antenna excited by an X-Band pyramidal horn for 10 GHz as shown in Fig. 8.13 a). The full BI-MLFMM model results in a computation with 830280 unknowns, whereas for the BI-MLFMM-UTD simulation the parabolic reflector was approximated with plates and the total number of unknowns was 36326. Three computations were made with 6, 10, and 20 plates by taking into account second order rays as well. The corresponding computation times can be seen in Fig. 8.13 b). Results of the total electric near field along the z-axis compared to the reference solution are shown in the same figure. Further, results of the copolar radiation pattern in the principal E-plane compared to the reference solution are shown in Fig. 8.14 a). For 6 and 10 plates there are significant deviations from the reference results, whereas for 20 plates the results agree very well still providing faster computation than the exact solution.

Finally, the influence of the reflector on the frequency behavior of the input impedance of the excitation horn is shown in Fig. 8.14 b). Full BI-MLFMM and BI-MLFMM-UTD computations agree very well and show the fine oscillations to be expected when compared to the input impedance of the horn without the reflector. It is noticed, that the pyramidal

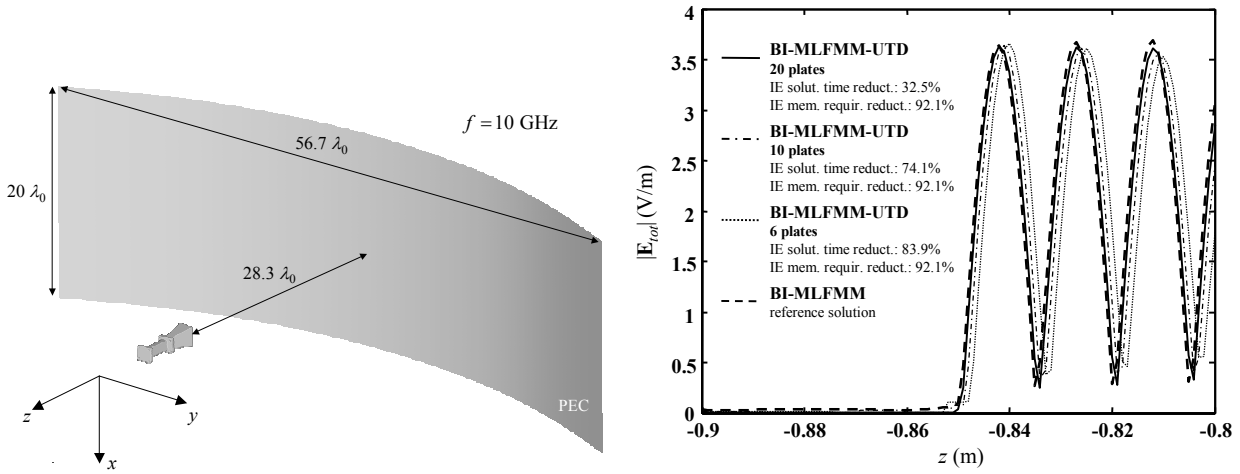

a) b)

Figure 8.13: Cylindrical parabolic reflector antenna with X-band pyramidal horn excitation. a) Configuration. b) Total electric field along the z-axis. The reduction in computation time is in comparison with the reference solution.

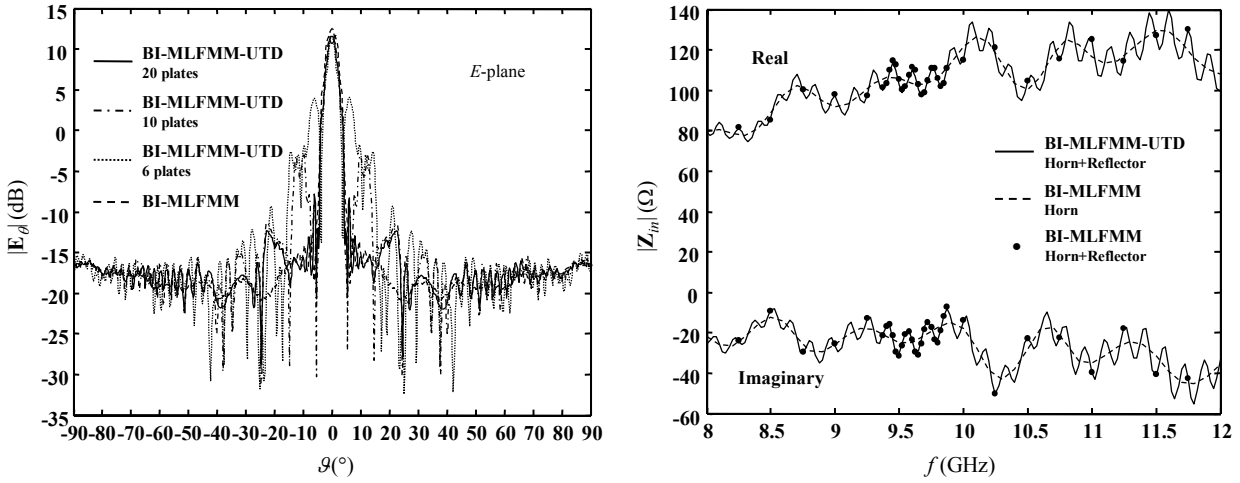

a) b)

Figure 8.14: a) Copolar radiation pattern on E-plane for cylindrical parabolic reflector antenna shown in Fig. 8.13 a). b) Influence of the cylindrical parabolic reflector on the input impedance of the X-band pyramidal excitation horn illustrated in Fig. 8.13 a).

horn was modeled as a closed object with thick metallic walls using 24221 surface triangular elements and employing CFIE. The feed of the horn was realized by a flat metal strip placed symmetrically with respect to the side walls and at a $\lambda_g/4$ distance from the back wall of the supporting rectangular waveguide, where λ_g is the wavelength inside the waveguide. The flat metal strip was modeled by EFIE and was excited by a delta-gap voltage source with an internal 50 Ω resistor.

8.2.4 Monopole Antenna on Truck over Ground

In this example, the radiation performance of a $\lambda/4$-monopole antenna installed at the top of a full-scale truck over ground is simulated as shown in Fig. 8.15 a). The operating frequency of the antenna was $f = 1.5$ GHz and it was excited at the low end using a delta-gap voltage source. The ground plane was assumed to be clay soil with $\varepsilon_r = 2.38 - j0.0048$ and it was placed at $z = 0.0$ m.

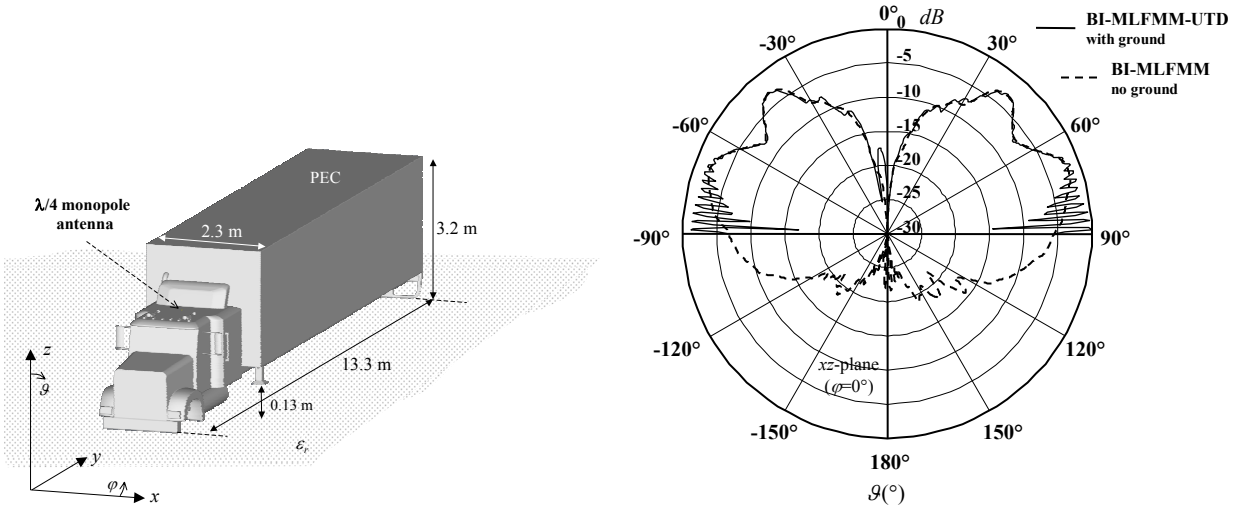

Figure 8.15: Monopole antenna installed at the top of full-scale truck over ground. a) Configuration. b) Copolar radiation pattern in the xz-plane.

The objects were placed symmetrically with respect to all three principal planes of the Cartesian coordinate system. First, the radiation of the installed monopole antenna was simulated numerically exact by activating only the BI-MLFMM part of the hybrid code. Thereby, the surfaces of the antenna and the truck were discretized with 1124859 unknowns employing mixed CFIE/EFIE. It is noticed, that the monopole antenna was realized by a flat metallic strip and was modeled by EFIE. Then, the whole radiating structure was simulated over ground with the BI-MLFMM-UTD method, whereas the ground plane was treated ray optically through reflections on the dielectric surface. The resulted radiation patterns of the monopole antenna in the xz-plane are shown in Fig. 8.15 b). For the first case (dashed line) it can be clearly seen that the platform of the truck strongly influences the overall radiation of the antenna. Particularly, the radiation pattern is strongly deformed in all directions due to the presence of the platform. Also, additional strong deformation can be seen due to the ground (solid line). This influence is basically found for near-grazing directions to the ground plane. Similar results could be observed in the yz-plane, whereas the radiation pattern of the monopole antenna is no longer symmetric in that principal plane as expected when looking at the position of the monopole antenna on the truck platform.

Chapter 9

Summary and Conclusions

In the present thesis, the hybrid FEBI-MLFMM-UTD numerical method was presented for the solution of very large and complex radiation and scattering electromagnetic problems. The presented hybrid approach combines for the first time a local method, a global fast IE method, and ray optical asymptotic techniques. The hybridization with UTD is performed in both the BIM part, where the Green's function and the incident field are appropriately modified for CFIE, as well as within the matrix-vector multiplications in the various levels of the MLFMM part resulting in a far-field approximation of the translation operator for ray optical contributions. In each case, the Green's function and the incident field are modified according to superposition of all received field contributions. Dielectric regions of FEBI objects are handled efficiently through conventional combination of BIM with FEM, which does not affect the hybridization with UTD.

The hybridization of MLFMM with UTD is performed by approximating ray optical terms of the Green's function with far-field expressions suitable for MLFMM interactions. This results in modification of the translation procedure according to superposition of all received contributions at the receiving groups for all source groups at each MLFMM level, whereas a far-field approximation of the translation operator is used for ray optical contributions. Improved ray optical translations are achieved by using the gravity center of the currents within the groups as source and receiving points for the radiated and received ray optical fields. Also, for higher MLFMM levels groups become larger and the far-field condition used to derive the ray optical translation operator is more difficult to be satisfied. This problem is overcome by extending the translation range around the source groups for the UTD contributions with increasing group size, while for direct contributions the smallest possible translation range is used.

In the UTD part, single and multiple reflections on flat metallic or dielectric objects are considered as well as single and double diffractions on straight metallic edges. Also, combinations of reflected and single diffracted contributions up to the fourth order can be taken into account. Thereby, the corresponding local points on the UTD objects are evaluated through numerical realization of Fermat's principle. For reflections on flat surfaces special treatment based on image theory is used in terms of polarization of the reflected ray as well as amplitude variation of terms associated to the gradient of the scalar Green's function with dependence $1/r$ and $1/r^2$. Double diffracted fields are formulated with the hard and soft scalar diffraction coefficients of UTD, where diffraction points are determined by an iterative three-dimensional parametric realization of the generalized Fermat's principle. Also, the ray

caustic distance of the diffracted field at the second edge is determined by linear interpolation between the two principal radii of curvature of the incident astigmatic ray tube.

Further, postprocessing near-field computations in the proposed hybrid method are accelerated using MLFMM, whereas the grouping domain of the equivalent currents is extended to also include nearby observation points. In addition to non empty groups containing source currents also non empty groups containing observation points are collected at each level. Near-field MLFMM translations are performed from source groups including currents to receiving groups including observation points. For far-away observation points no grouping is performed and the field contributions are computed using far-field MLFMM translations, which are performed for each observation point at the coarsest level on which far-field condition is still satisfied. The optimum level for far-field translations is found for each observation point in the initialization step in a worst-case sense using its shortest distance to the BI-MLFMM domain. In both domains ray optical contributions due to the presence of UTD objects are taken into account according to hybridization of MLFMM with UTD.

In addition, far-field scattering computations are performed by applying NFFFTs in the postprocessing stage based on planar near-field scanning techniques. Particularly, the scattered ray optical electric field is first computed in a scanning plane in the near-field region of the involved objects and it is then transformed into far-field regions using field expansions in terms of spectrum density functions of outgoing waves. These functions are components of the plane wave spectrum associated with TE and TM fields and are evaluated with low effort compared to total computation time from the tangential components of the scattered ray optical near-fields in the scanning plane by Fourier transforms. Thereby, computations in the near-field are accelerated using the postprocessing MLFMM. Direct field contributions from equivalent surface currents to observation points in the far-field region are computed directly and no evanescent waves are present in the scanning plane, so that sampling rates higher than $\lambda_0/2$ are not required for any distance of the scanning plane from the involved objects. Sampling rates of $\lambda_0/2$ are used for grazing directions of observation to the scanning plane, whereas sampling rates less than $\lambda_0/2$ are used for restricted angle range around the normal direction to the scanning plane. Reduced accuracy at grazing directions of observation is overcome by combining solutions provided by several scanning planes.

Using the hybrid FEBI-MLFMM-UTD method large scale problems including arbitrarily shaped and electrically very large objects can be handled very efficiently saving a large amount in computation and memory requirements, which was demonstrated very clearly with the presented numerical examples. A wide range of practical problems can be computed with the hybrid method presented in this thesis, like analysis of mobile communications base station antennas or computation of near field distributions for EMC investigations. Further, the environment in radiation and scattering problems can be taken into account very efficiently, by treating (whenever necessary) objects in the neighborhood of the radiation or scattering structures by UTD. It becomes also possible to efficiently compute radiated and scattered numerically exact electromagnetic field distributions including ray optical fields for large objects on observation planes, which gives an illustrative insight of complex radiation and scattering mechanisms. The presented method is best suited for problems including relatively few and large UTD objects, since computation time increases more than linearly with the number of UTD objects. This means that growing number of UTD objects quickly results in large computation times. Using many of them, e.g. to approximate curved surfaces, can even become more time expensive than a full FEBI-MLFMM solution. However, memory requirements are almost independent from the "small" number of UTD objects allowing

solutions of problems with electrically very large objects in direct neighborhood of arbitrarily shaped objects, for which full FEBI-MLFMM solutions are not possible at all with currently available computational resources.

As an outlook, implementation of ray optical mechanisms for curved surfaces will significantly extend the proposed approach. Thereby, the critical points on the UTD objects can be evaluated through parametric realization of Fermat's principle and the necessary surface radii of curvature on the critical points can be computed from the parametric expressions using differential geometry approaches. In addition, extension of hybridization to directly connected FEBI and UTD objects will also provide significant enhancement of the hybrid method. Thereby, coupling contributions of UTD objects with basis functions lying within non well-separated MLFMM groups near the junction could be treated efficiently by image theory. With these implementations the applicability of the hybrid approach can be further extended, so that the overall simulation tool could be applied efficiently to even more radiation and scattering configurations.

Appendix A

Mathematical Details

A.1 Definitions from Linear Algebra

In the following, basic definitions from linear algebra are given, which are often found in numerical analysis [17]. The definitions are related to matrices and in each case, the corresponding operators generating these matrices also carry the same definition. Additional definitions and descriptions can be found in [174], [175].

- The matrix $[A]$ is *symmetric*, if

  $$[A]^T = [A],$$

  otherwise it is *asymmetric*. In case of

  $$[A^*]^T = [A],$$

  where $[A^*]^T$ denotes conjugate transpose of $[A]$, the matrix is said to be *Hermitian* or *self-adjoint*.

- The *nullspace* of a matrix $[A]$ is a set of vectors $\{u\}$, for which

  $$[A]\{u\} = 0.$$

- The *condition number* $\kappa(A)$ of a square $(n \times n)$ matrix $[A]$ is defined as

  $$\kappa(A) = \|A\|\|A^{-1}\|,$$

  where $\|\cdot\|$ is any valid matrix norm. For the special case of the norm $\|\cdot\|_2$ (Euclidean norm), the matrix condition number is proportional to the ratio of the largest to the smallest eigenvalue of the matrix. Matrices with condition number near one are said to be well-conditioned. Matrices with condition number much greater than one are said to be ill-conditioned.

- Any square $(n \times n)$ matrix $[A]$ is *singular*, if its rows and columns are not linearly independent. This means that the determinant of the matrix is zero and the matrix is not invertible. Therefore, the condition number of a singular matrix is infinite.

- The matrix $[A]$ is *positive definite*, if

  $$\{u^*\}^T[A]\{u\} > 0,$$

  where $\{u\}$ is any nonzero complex vector. The most important property of a positive definite matrix $[A]$ is that its determinant is always positive, which means that $[A]$ is always a nonsingular and invertible matrix. A Hermitian (or symmetric) matrix is positive definite if all its eigenvalues are positive, which is true if all diagonal elements of the matrix are positive. If all eigenvalues are nonnegative (positive or zero) the Hermitian matrix is *positive semidefinite*. The definitions for *negative definite* and *negative semidefinite* matrices are given in the same way.

- The matrix $[A]$ is *indefinite*, if

  $$(\{u^*\}^T[A]\{u\})(\{v^*\}^T[A]\{v\}) > 0,$$

  where $\{u\}$ and $\{u\}$ are any nonzero complex vectors. A Hermitian indefinite matrix has eigenvalues, and thus diagonal elements, that can be both, positive and negative.

A.2 Dyadic Analysis

A.2.1 Operations in Cartesian Coordinates

Dyad Components

In the global Cartesian coordinate system a *dyad* (or a second rank tensor) is defined as

$$\bar{\mathbf{F}} = \mathbf{F}_x\hat{x} + \mathbf{F}_y\hat{y} + \mathbf{F}_z\hat{z}, \tag{A.1}$$

where the Cartesian components $\mathbf{F}_x$, $\mathbf{F}_y$, and $\mathbf{F}_z$ are vectors defined by

$$\mathbf{F}_x = F_{xx}\hat{x} + F_{yx}\hat{y} + F_{zx}\hat{z}, \tag{A.2}$$
$$\mathbf{F}_y = F_{xy}\hat{x} + F_{yy}\hat{y} + F_{zy}\hat{z}, \tag{A.3}$$
$$\mathbf{F}_z = F_{xz}\hat{x} + F_{yz}\hat{y} + F_{zz}\hat{z}. \tag{A.4}$$

Therefore,

$$\begin{aligned}\bar{\mathbf{F}} &= F_{xx}\hat{x}\hat{x} + F_{yx}\hat{y}\hat{x} + F_{zx}\hat{z}\hat{x} \\ &+ F_{xy}\hat{x}\hat{y} + F_{yy}\hat{y}\hat{y} + F_{zy}\hat{z}\hat{y} \\ &+ F_{xz}\hat{x}\hat{z} + F_{yz}\hat{y}\hat{z} + F_{zz}\hat{z}\hat{z},\end{aligned} \tag{A.5}$$

which contains nine independent Cartesian components.

The *unit dyad* is defined as

$$\bar{\mathbf{I}} = \hat{x}\hat{x} + \hat{y}\hat{y} + \hat{z}\hat{z} \tag{A.6}$$

and

$$\mathbf{C}\cdot\bar{\mathbf{I}} = \bar{\mathbf{I}}\cdot\mathbf{C} = \mathbf{C}. \tag{A.7}$$

Vector-Dyad Dot Product

$$\begin{aligned}\mathbf{b}\cdot\bar{\mathbf{F}} &= (b_xF_{xx} + b_yF_{yx} + b_zF_{zx})\hat{x} \\ &+ (b_xF_{xy} + b_yF_{yy} + b_zF_{zy})\hat{y} \\ &+ (b_xF_{xz} + b_yF_{yz} + b_zF_{zz})\hat{z}\end{aligned} \tag{A.8}$$

with

$$\mathbf{b} = b_x\hat{x} + b_y\hat{y} + b_z\hat{z}. \tag{A.9}$$

Dyad-Vector Dot Product

$$\begin{aligned}\bar{\mathbf{F}}\cdot\mathbf{b} &= (b_xF_{xx} + b_yF_{xy} + b_zF_{xz})\hat{x} \\ &+ (b_xF_{yx} + b_yF_{yy} + b_zF_{yz})\hat{y} \\ &+ (b_xF_{zx} + b_yF_{zy} + b_zF_{zz})\hat{z}.\end{aligned} \tag{A.10}$$

Dyad-Dyad Dot Product

$$\begin{aligned}
\bar{\mathbf{F}} \cdot \bar{\mathbf{H}} &= (F_{xx}H_{xx} + F_{xy}H_{yx} + F_{xz}H_{zx})\hat{x}\hat{x} \\
&+ (F_{xx}H_{xy} + F_{xy}H_{yy} + F_{xz}H_{zy})\hat{x}\hat{y} \\
&+ (F_{xx}H_{xz} + F_{xy}H_{yz} + F_{xz}H_{zz})\hat{x}\hat{z} \\
&+ (F_{yx}H_{xx} + F_{yy}H_{yx} + F_{yz}H_{zx})\hat{y}\hat{x} \\
&+ (F_{yx}H_{xy} + F_{yy}H_{yy} + F_{yz}H_{zy})\hat{y}\hat{y} \\
&+ (F_{yx}H_{xz} + F_{yy}H_{yz} + F_{yz}H_{zz})\hat{y}\hat{z} \\
&+ (F_{zx}H_{xx} + F_{zy}H_{yx} + F_{zz}H_{zx})\hat{z}\hat{x} \\
&+ (F_{zx}H_{xy} + F_{zy}H_{yy} + F_{zz}H_{zy})\hat{z}\hat{y} \\
&+ (F_{zx}H_{xz} + F_{zy}H_{yz} + F_{zz}H_{zz})\hat{z}\hat{z}. \qquad \text{(A.11)}
\end{aligned}$$

Vector-Dyad Cross Product

$$\begin{aligned}
\mathbf{b} \times \bar{\mathbf{F}} &= (b_yF_{xz} - b_zF_{xy})\hat{x}\hat{x} + (b_yF_{yz} - b_zF_{yy})\hat{x}\hat{y} + (b_yF_{zz} - b_zF_{zy})\hat{x}\hat{z} \\
&+ (b_zF_{xx} - b_xF_{xz})\hat{y}\hat{x} + (b_zF_{yx} - b_xF_{yz})\hat{y}\hat{y} + (b_zF_{zx} - b_xF_{zz})\hat{y}\hat{z} \\
&+ (b_xF_{xy} - b_yF_{xx})\hat{z}\hat{x} + (b_xF_{yy} - b_yF_{yx})\hat{z}\hat{y} + (b_xF_{zy} - b_yF_{zx})\hat{z}\hat{z}. \qquad \text{(A.12)}
\end{aligned}$$

Dyad-Vector Cross Product

$$\begin{aligned}
\bar{\mathbf{F}} \times \mathbf{b} &= (\mathbf{F}_x \times \mathbf{b})\hat{x} + (\mathbf{F}_y \times \mathbf{b})\hat{y} + (\mathbf{F}_z \times \mathbf{b})\hat{z} \\
&= -(\mathbf{b} \times \mathbf{F}_x)\hat{x} - (\mathbf{b} \times \mathbf{F}_y)\hat{y} - (\mathbf{b} \times \mathbf{F}_z)\hat{z} \\
&= -\mathbf{b} \times \bar{\mathbf{F}}. \qquad \text{(A.13)}
\end{aligned}$$

A.2.2 Operations in Spherical Coordinates

Dyad Components

In the global spherical coordinate system the dyad is expressed as

$$\bar{\mathbf{F}} = \mathbf{F}_r\hat{r} + \mathbf{F}_\vartheta\hat{\vartheta} + \mathbf{F}_\varphi\hat{\varphi}, \tag{A.14}$$

where the spherical vector components $\mathbf{F}_r$, $\mathbf{F}_\vartheta$, and $\mathbf{F}_\varphi$ are connected to the Cartesian vector components by

$$\mathbf{F}_r = \mathbf{F}_x \sin\vartheta\cos\varphi + \mathbf{F}_y \sin\vartheta\sin\varphi + \mathbf{F}_z\cos\vartheta, \tag{A.15}$$
$$\mathbf{F}_\vartheta = \mathbf{F}_x \cos\vartheta\cos\varphi + \mathbf{F}_y \cos\vartheta\sin\varphi - \mathbf{F}_z\sin\vartheta, \tag{A.16}$$
$$\mathbf{F}_\varphi = -\mathbf{F}_x \sin\varphi + \mathbf{F}_y\cos\varphi, \tag{A.17}$$

with

$$\mathbf{F}_x = F_{xr}\hat{r} + F_{x\vartheta}\hat{\vartheta} + F_{x\varphi}\hat{\varphi}, \tag{A.18}$$
$$\mathbf{F}_y = F_{yr}\hat{r} + F_{y\vartheta}\hat{\vartheta} + F_{y\varphi}\hat{\varphi}, \tag{A.19}$$
$$\mathbf{F}_z = F_{zr}\hat{r} + F_{z\vartheta}\hat{\vartheta} + F_{z\varphi}\hat{\varphi}. \tag{A.20}$$

Therefore,

$$\begin{aligned}\bar{\mathbf{F}} &= F_{rr}\hat{r}\hat{r} + F_{\vartheta r}\hat{\vartheta}\hat{r} + F_{\varphi r}\hat{\varphi}\hat{r} \\ &+ F_{r\vartheta}\hat{r}\hat{\vartheta} + F_{\vartheta\vartheta}\hat{\vartheta}\hat{\vartheta} + F_{\varphi\vartheta}\hat{\varphi}\hat{\vartheta} \\ &+ F_{r\varphi}\hat{r}\hat{\varphi} + F_{\vartheta\varphi}\hat{\vartheta}\hat{\varphi} + F_{\varphi\varphi}\hat{\varphi}\hat{\varphi},\end{aligned} \tag{A.21}$$

where the nine independent spherical components are connected to the Cartesian components by

$$F_{rr} = F_{xr}\sin\vartheta\cos\varphi + F_{yr}\sin\vartheta\sin\varphi + F_{zr}\cos\vartheta, \tag{A.22}$$
$$F_{\vartheta r} = F_{x\vartheta}\sin\vartheta\cos\varphi + F_{y\vartheta}\sin\vartheta\sin\varphi + F_{z\vartheta}\cos\vartheta, \tag{A.23}$$
$$F_{\varphi r} = F_{x\varphi}\sin\vartheta\cos\varphi + F_{y\varphi}\sin\vartheta\sin\varphi + F_{z\varphi}\cos\vartheta, \tag{A.24}$$
$$F_{r\vartheta} = F_{xr}\cos\vartheta\cos\varphi + F_{yr}\cos\vartheta\sin\varphi - F_{zr}\sin\vartheta, \tag{A.25}$$
$$F_{\vartheta\vartheta} = F_{x\vartheta}\cos\vartheta\cos\varphi + F_{y\vartheta}\cos\vartheta\sin\varphi - F_{z\vartheta}\sin\vartheta, \tag{A.26}$$
$$F_{\varphi\vartheta} = F_{x\varphi}\cos\vartheta\cos\varphi + F_{y\varphi}\cos\vartheta\sin\varphi - F_{z\varphi}\sin\vartheta, \tag{A.27}$$
$$F_{r\varphi} = -F_{xr}\sin\varphi + F_{yr}\cos\varphi, \tag{A.28}$$
$$F_{\vartheta\varphi} = -F_{x\vartheta}\sin\varphi + F_{y\vartheta}\cos\varphi, \tag{A.29}$$
$$F_{\varphi\varphi} = -F_{x\varphi}\sin\varphi + F_{y\varphi}\cos\varphi, \tag{A.30}$$

with

$$F_{xr} = F_{xx}\sin\vartheta\cos\varphi + F_{yx}\sin\vartheta\sin\varphi + F_{zx}\cos\vartheta, \tag{A.31}$$
$$F_{x\vartheta} = F_{xx}\cos\vartheta\cos\varphi + F_{yx}\cos\vartheta\sin\varphi - F_{zx}\sin\vartheta, \tag{A.32}$$
$$F_{x\varphi} = -F_{xx}\sin\varphi + F_{yx}\cos\varphi, \tag{A.33}$$
$$F_{yr} = F_{xy}\sin\vartheta\cos\varphi + F_{yy}\sin\vartheta\sin\varphi + F_{zy}\cos\vartheta, \tag{A.34}$$
$$F_{y\vartheta} = F_{xy}\cos\vartheta\cos\varphi + F_{yy}\cos\vartheta\sin\varphi - F_{zy}\sin\vartheta, \tag{A.35}$$
$$F_{y\varphi} = -F_{xy}\sin\varphi + F_{yy}\cos\varphi, \tag{A.36}$$
$$F_{zr} = F_{xz}\sin\vartheta\cos\varphi + F_{yz}\sin\vartheta\sin\varphi + F_{zz}\cos\vartheta, \tag{A.37}$$
$$F_{z\vartheta} = F_{xz}\cos\vartheta\cos\varphi + F_{yz}\cos\vartheta\sin\varphi - F_{zz}\sin\vartheta, \tag{A.38}$$
$$F_{z\varphi} = -F_{xz}\sin\varphi + F_{yz}\cos\varphi. \tag{A.39}$$

Vector-Dyad Dot Product

$$\begin{aligned}\mathbf{b}\cdot\bar{\mathbf{F}} &= (b_rF_{rr} + b_\vartheta F_{\vartheta r} + b_\varphi F_{\varphi r})\hat{r} \\ &+ (b_rF_{r\vartheta} + b_\vartheta F_{\vartheta\vartheta} + b_\varphi F_{\varphi\vartheta})\hat{\vartheta} \\ &+ (b_rF_{r\varphi} + b_\vartheta F_{\vartheta\varphi} + b_\varphi F_{\varphi\varphi})\hat{\varphi},\end{aligned} \tag{A.40}$$

with

$$\mathbf{b} = b_r\hat{r} + b_\vartheta\hat{\vartheta} + b_\varphi\hat{\varphi}. \tag{A.41}$$

Dyad-Vector Dot Product

$$\begin{aligned}\bar{\mathbf{F}}\cdot\mathbf{b} &= (b_rF_{rr} + b_\vartheta F_{r\vartheta} + b_\varphi F_{r\varphi})\hat{r} \\ &+ (b_rF_{\vartheta r} + b_\vartheta F_{\vartheta\vartheta} + b_\varphi F_{\vartheta\varphi})\hat{\vartheta} \\ &+ (b_rF_{\varphi r} + b_\vartheta F_{\varphi\vartheta} + b_\varphi F_{\varphi\varphi})\hat{\varphi}.\end{aligned} \tag{A.42}$$

Appendix B

Hybrid BIM-UTD Formulations

In the following, the MoM matrix elements for the hybrid BIM-UTD part of the method presented in this thesis will be given for EFIE and MFIE formulation assuming testing points $\mathbf{r} = \mathbf{r}_m$ and source points $\mathbf{r}' = \mathbf{r}_n$ on the boundary surface A. The matrix elements for CFIE formulation are obtained using the linear combination (2.67).

B.1 Equation System Elements of Electric Field Integral Equation Part

The system of equations for the total EFIE is written in matrix form as

$$\left[B^{EFIE}_{J,tot}\right]\{H\} + \left[B^{EFIE}_{M,tot}\right]\{E\} = \{b^{EFIE}_{tot}\}, \tag{B.1}$$

with matrix elements given by

$$\begin{aligned}
B^{EFIE}_{mn,J,tot} = \\
&+j\frac{\omega\mu}{4\pi}\iint\limits_{A}\boldsymbol{\beta}_m(\mathbf{r}_m)\cdot\iint\limits_{A'}G(\mathbf{r}_m,\mathbf{r}_n)\boldsymbol{\beta}_n(\mathbf{r}_n)da'da \\
&+j\frac{1}{4\pi\omega\varepsilon}\iint\limits_{A}\nabla_A\cdot\boldsymbol{\beta}_m(\mathbf{r}_m)\iint\limits_{A'}G(\mathbf{r}_m,\mathbf{r}_n)\nabla'_A\cdot\boldsymbol{\beta}_n(\mathbf{r}_n)da'da \\
&+j\frac{\omega\mu}{4\pi}\Bigg\{\sum_q\iint\limits_{A}\boldsymbol{\beta}_m(\mathbf{r}_m)\cdot\iint\limits_{A'}\widetilde{A}_{R_q}(s_{R_q})\bar{\mathbf{R}}^E_q\cdot\left(\bar{\mathbf{I}}+\frac{1}{k^2}\nabla\nabla'\right)G(\mathbf{r}_{Q_{R_q}},\mathbf{r}_n)\cdot\boldsymbol{\beta}_n(\mathbf{r}_n)da'da \\
&+\sum_v\iint\limits_{A}\boldsymbol{\beta}_m(\mathbf{r}_m)\cdot\iint\limits_{A'}\widetilde{A}_{D_v}(s_{D_v})\bar{\mathbf{D}}^E_v\cdot\left(\bar{\mathbf{I}}+\frac{1}{k^2}\nabla\nabla'\right)G(\mathbf{r}_{Q_{D_v}},\mathbf{r}_n)\cdot\boldsymbol{\beta}_n(\mathbf{r}_n)da'da \\
&+\cdots\Bigg\},
\end{aligned} \tag{B.2}$$

$$
\begin{aligned}
B^{EFIE}_{mn,M,tot} = \frac{1}{2}\iint\limits_{A}\boldsymbol{\beta}_m(\mathbf{r}_m)\cdot\big[\boldsymbol{\beta}_n(\mathbf{r}_n)\times\hat{n}(\mathbf{r}_m)\big]da \\
+\frac{1}{4\pi}\Bigg\{\iint\limits_{A}\boldsymbol{\beta}_m(\mathbf{r}_m)\cdot\iint\limits_{A'}\nabla G(\mathbf{r}_m,\mathbf{r}_n)\times\boldsymbol{\beta}_n(\mathbf{r}_n)da'da \\
+\sum_q\iint\limits_{A}\boldsymbol{\beta}_m(\mathbf{r}_m)\cdot\iint\limits_{A'}\widetilde{A}_{R_q}(s_{R_q})\bar{\mathbf{R}}^H_q\cdot\nabla G(\mathbf{r}_{Q_{R_q}},\mathbf{r}_n)\times\boldsymbol{\beta}_n(\mathbf{r}_n)da'da \\
+\sum_v\iint\limits_{A}\boldsymbol{\beta}_m(\mathbf{r}_m)\cdot\iint\limits_{A'}\widetilde{A}_{D_v}(s_{D_v})\bar{\mathbf{D}}^H_v\cdot\nabla G(\mathbf{r}_{Q_{D_v}},\mathbf{r}_n)\times\boldsymbol{\beta}_n(\mathbf{r}_n)da'da \\
+\cdots\Bigg\},
\end{aligned}
\tag{B.3}
$$

$$
\begin{aligned}
b^{EFIE}_{m,tot} = \iint\limits_{A}\boldsymbol{\beta}_m(\mathbf{r}_m)\cdot\mathbf{E}^{inc}(\mathbf{r}_m)da \\
+\sum_q\iint\limits_{A}\boldsymbol{\beta}_m(\mathbf{r}_m)\cdot\widetilde{A}_{R_q}(s_{R_q})\bar{\mathbf{R}}^E_q\cdot\mathbf{E}^{inc}(\mathbf{r}_{Q_{R_q}}) \\
+\sum_v\iint\limits_{A}\boldsymbol{\beta}_m(\mathbf{r}_m)\cdot\widetilde{A}_{D_v}(s_{D_v})\bar{\mathbf{D}}^E_v\cdot\mathbf{E}^{inc}(\mathbf{r}_{Q_{D_v}})+\cdots,
\end{aligned}
\tag{B.4}
$$

$\forall\ \mathbf{r}_m,\mathbf{r}_n\in A$, where m,n are the testing and source edge, respectively, with $m=1,2,\ldots,N$. Thereby, the factor $\widetilde{A}_{R/D}(s_{R/D})$ combines the divergence and phase factors of the corresponding ray optical mechanism and is given by (5.5).

B.2 Equation System Elements of Magnetic Field Integral Equation Part

The system of equations for the total MFIE is written in matrix form as

$$\left[B_{J,tot}^{MFIE}\right]\{H\} + \left[B_{M,tot}^{MFIE}\right]\{E\} = \{b_{tot}^{MFIE}\}, \tag{B.5}$$

with matrix elements given by

$$\begin{aligned}
B_{mn,J,tot}^{MFIE} = {} & \frac{1}{2}\iint_{A}\boldsymbol{\beta}_m(\mathbf{r}_m)\cdot\boldsymbol{\beta}_n(\mathbf{r}_n)da \\
& -\frac{1}{4\pi}\Bigg\{\iint_{A}\left[\hat{n}(\mathbf{r}_m)\times\boldsymbol{\beta}_m(\mathbf{r}_m)\right]\cdot\iint_{A'}\nabla G(\mathbf{r}_m,\mathbf{r}_n)\times\boldsymbol{\beta}_n(\mathbf{r}_n)da'da \\
& +\sum_q\iint_{A}\left[\hat{n}(\mathbf{r}_m)\times\boldsymbol{\beta}_m(\mathbf{r}_m)\right]\cdot\iint_{A'}\widetilde{A}_{R_q}(s_{R_q})\bar{\mathbf{R}}_q^E\cdot\nabla G(\mathbf{r}_{Q_{R_q}},\mathbf{r}_n)\times\boldsymbol{\beta}_n(\mathbf{r}_n)da'da \\
& +\sum_v\iint_{A}\left[\hat{n}(\mathbf{r}_m)\times\boldsymbol{\beta}_m(\mathbf{r}_m)\right]\cdot\iint_{A'}\widetilde{A}_{D_v}(s_{D_v})\bar{\mathbf{D}}_v^E\cdot\nabla G(\mathbf{r}_{Q_{D_v}},\mathbf{r}_n)\times\boldsymbol{\beta}_n(\mathbf{r}_n)da'da \\
& +\cdots\Bigg\},
\end{aligned} \tag{B.6}$$

$$\begin{aligned}
B_{mn,M,tot}^{MFIE} = {} & \\
& +\jmath\frac{\omega\varepsilon}{4\pi}\iint_{A}\left[\hat{n}(\mathbf{r}_m)\times\boldsymbol{\beta}_m(\mathbf{r}_m)\right]\cdot\iint_{A'}G(\mathbf{r}_m,\mathbf{r}_n)\boldsymbol{\beta}_n(\mathbf{r}_n)da'da \\
& +\jmath\frac{1}{4\pi\omega\mu}\iint_{A}\nabla_A\cdot\left[\hat{n}(\mathbf{r}_m)\times\boldsymbol{\beta}_m(\mathbf{r}_m)\right]\iint_{A'}G(\mathbf{r}_m,\mathbf{r}_n)\nabla'_A\cdot\boldsymbol{\beta}_n(\mathbf{r}_n)da'da \\
& +\jmath\frac{\omega\varepsilon}{4\pi}\Bigg\{\sum_q\iint_{A}\left[\hat{n}(\mathbf{r}_m)\times\boldsymbol{\beta}_m(\mathbf{r}_m)\right]\cdot\iint_{A'}\widetilde{A}_{R_q}(s_{R_q})\bar{\mathbf{R}}_q^H\cdot\left(\bar{\mathbf{I}}+\frac{1}{k^2}\nabla\nabla'\right)G(\mathbf{r}_{Q_{R_q}},\mathbf{r}_n) \\
& \qquad\cdot\boldsymbol{\beta}_n(\mathbf{r}_n)da'da \\
& +\sum_v\iint_{A}\left[\hat{n}(\mathbf{r}_m)\times\boldsymbol{\beta}_m(\mathbf{r}_m)\right]\cdot\iint_{A'}\widetilde{A}_{D_v}(s_{D_v})\bar{\mathbf{D}}_v^H\cdot\left(\bar{\mathbf{I}}+\frac{1}{k^2}\nabla\nabla'\right)G(\mathbf{r}_{Q_{D_v}},\mathbf{r}_n) \\
& \qquad\cdot\boldsymbol{\beta}_n(\mathbf{r}_n)da'da \\
& +\cdots\Bigg\},
\end{aligned} \tag{B.7}$$

$$
\begin{aligned}
b_{m,tot}^{MFIE} = & \iint_A \big[\hat{n}(\mathbf{r}_m) \times \boldsymbol{\beta}_m(\mathbf{r}_m)\big] \cdot \mathbf{H}^{inc}(\mathbf{r}_m) da \\
& + \frac{1}{Z} \sum_q \iint_A \big[\hat{n}(\mathbf{r}_m) \times \boldsymbol{\beta}_m(\mathbf{r}_m)\big] \cdot \hat{k}_r \times \widetilde{A}_{R_q}(s_{R_q}) \bar{\mathbf{R}}_q^E \cdot \mathbf{E}^{inc}(\mathbf{r}_{Q_{R_q}}) da \\
& + \frac{1}{Z} \sum_v \iint_A \big[\hat{n}(\mathbf{r}_m) \times \boldsymbol{\beta}_m(\mathbf{r}_m)\big] \cdot \hat{k}_d \times \widetilde{A}_{D_v}(s_{D_v}) \bar{\mathbf{D}}_v^E \cdot \mathbf{E}^{inc}(\mathbf{r}_{Q_{D_v}}) da + \cdots ,
\end{aligned} \tag{B.8}
$$

$\forall\, \mathbf{r}_m, \mathbf{r}_n \in A$, with $m = 1, 2, \ldots, N$. Thereby, $\widetilde{A}_{R/D}(s_{R/D})$ is given by (5.5).

Appendix C

Hybrid MLFMM-UTD Formulations

In the following, first the derivation of the ray optical terms of the Green's functions and the ray optical translation operator used in the hybrid MLFMM-UTD approach will be given. After that, the matrix elements for the hybrid MLFMM-UTD part of the method presented in this thesis will be given for CFIE formulation assuming testing points $\mathbf{r} = \mathbf{r}_m$ and source points $\mathbf{r}' = \mathbf{r}_n$ placed in the testing group $G_{m'}$ centered at $\mathbf{r}_{m'}$ and in the source group $G_{n'}$ centered at the point $\mathbf{r}_{n'}$, respectively.

C.1 Ray Optical Translation Operator

The configuration shown in Fig. 5.3 is assumed, where the coupling path from the source current element to the testing current element is written as

$$\mathbf{r} - \mathbf{r}' = \mathbf{r}_m - \mathbf{r}_n = (\mathbf{r}_m - \mathbf{r}_Q) + (\mathbf{r}_Q - \mathbf{r}_n) = \mathbf{r}_{mQ} + \mathbf{r}_{Qn}, \tag{C.1}$$

by first intervening the local point Q on the UTD object with position vector $\mathbf{r}_Q$. For each of the subpaths in (C.1) the center point of the appropriate group is intervened so that

$$\mathbf{r}_{mQ} = \mathbf{r}_m - \mathbf{r}_Q = (\mathbf{r}_m - \mathbf{r}_{m'}) + (\mathbf{r}_{m'} - \mathbf{r}_Q) = \mathbf{r}_{mm'} + \mathbf{r}_{m'Q}, \tag{C.2}$$

$$\mathbf{r}_{Qn} = \mathbf{r}_Q - \mathbf{r}_n = (\mathbf{r}_Q - \mathbf{r}_{n'}) + (\mathbf{r}_{n'} - \mathbf{r}_n) = \mathbf{r}_{Qn'} + \mathbf{r}_{nn'}. \tag{C.3}$$

Thus, the total path is written as

$$\begin{aligned} \mathbf{r} - \mathbf{r}' = \mathbf{r}_m - \mathbf{r}_n &= (\mathbf{r}_m - \mathbf{r}_{m'}) + (\mathbf{r}_{m'} - \mathbf{r}_Q) + (\mathbf{r}_Q - \mathbf{r}_{n'}) + (\mathbf{r}_{n'} - \mathbf{r}_n) \\ &= \mathbf{r}_{mm'} + \mathbf{r}_{m'Q} + \mathbf{r}_{Qn'} - \mathbf{r}_{nn'}. \end{aligned} \tag{C.4}$$

In order to express ray optical terms of the Green's function in a suitable way for MLFMM computations, it is assumed that the coupling paths from the center of the groups to the local points on the UTD objects $\mathbf{r}_{Qn'}$ and $\mathbf{r}_{m'Q}$ are much larger than the paths within the corresponding groups $\mathbf{r}_{nn'}$ and $\mathbf{r}_{mm'}$, respectively, thus

$$|\mathbf{r}_{Qn'}| \gg |\mathbf{r}_{nn'}|, \tag{C.5}$$

$$|\mathbf{r}_{m'Q}| \gg |\mathbf{r}_{mm'}|. \tag{C.6}$$

The electrical path kr_{Qn} from the source current to the local point on the UTD object is alternatively written as

$$\begin{aligned} kr_{Qn} &\overset{(C.3)}{=} k\sqrt{(\mathbf{r}_{Qn'} - \mathbf{r}_{nn'}) \cdot (\mathbf{r}_{Qn'} - \mathbf{r}_{nn'})} \\ &= k\sqrt{|\mathbf{r}_{Qn'}|^2 - 2\mathbf{r}_{Qn'} \cdot \mathbf{r}_{nn'} + |\mathbf{r}_{Qn'}|^2} \\ &= kr_{Qn'}\sqrt{1 - 2\frac{\mathbf{r}_{Qn'} \cdot \mathbf{r}_{nn'}}{r_{Qn'}^2} + \frac{r_{nn'}^2}{r_{Qn'}^2}}. \end{aligned} \tag{C.7}$$

When the condition (C.5) holds for the source group, the expression (C.7) is expanded in terms of a Taylor series as

$$kr_{Qn} \approx kr_{Qn'} - k\mathbf{r}_{nn'} \cdot \hat{r}_{Qn'} + \frac{\sin^2 \vartheta_{Qn'}}{2r_{Qn'}} kr_{nn'}^2, \tag{C.8}$$

where $\vartheta_{Qn'}$ is the angle between $\mathbf{r}_{Qn'}$ and $\mathbf{r}_{nn'}$. Under the condition

$$r_{Qn'} \gg \frac{1}{2}k|\mathbf{r}_{nn'}|^2 \tag{C.9}$$

the higher-order term of the expansion (C.8) is neglected and the electrical path kr_{Qn} is simplified as

$$kr_{Qn} = k|\mathbf{r}_Q - \mathbf{r}_n| \approx kr_{Qn'} - k\mathbf{r}_{nn'} \cdot \hat{r}_{Qn'}. \tag{C.10}$$

Applying the same procedure for the electrical path kr_{mQ} from the local point on the UTD object to the testing current we get

$$\begin{aligned} kr_{mQ} &\overset{(C.2)}{=} k\sqrt{(\mathbf{r}_{mm'} + \mathbf{r}_{m'Q}) \cdot (\mathbf{r}_{mm'} + \mathbf{r}_{m'Q})} \\ &= k\sqrt{|\mathbf{r}_{mm'}|^2 + 2\mathbf{r}_{m'Q} \cdot \mathbf{r}_{mm'} + |\mathbf{r}_{m'Q}|^2} \\ &= kr_{m'Q}\sqrt{1 + 2\frac{\mathbf{r}_{m'Q} \cdot \mathbf{r}_{mm'}}{r_{m'Q}^2} + \frac{r_{mm'}^2}{r_{m'Q}^2}} \\ &\overset{(C.6)}{\Rightarrow} \\ kr_{mQ} &\approx kr_{m'Q} + k\mathbf{r}_{mm'} \cdot \hat{r}_{m'Q} + \frac{\sin^2 \vartheta_{m'Q}}{2r_{Qn'}} kr_{mm'}^2, \end{aligned}$$

where $\vartheta_{m'Q}$ is the angle between $\mathbf{r}_{m'Q}$ and $\mathbf{r}_{mm'}$. Under the condition

$$r_{m'Q} \gg \frac{1}{2}k|\mathbf{r}_{mm'}|^2 \tag{C.11}$$

we finally get

$$kr_{mQ} = k|\mathbf{r}_m - \mathbf{r}_Q| \approx kr_{m'Q} + k\mathbf{r}_{mm'} \cdot \hat{r}_{m'Q}. \tag{C.12}$$

Using the electrical coupling path expressions (C.10) and (C.12) the scalar term of the ray optical Green's function from the source to the testing current is alternatively written as

$$G_{UTD}(\mathbf{r}_m, \mathbf{r}_n) = \mathrm{e}^{-j\mathbf{k}_{r,d} \cdot \mathbf{r}_{mm'}} \frac{\mathrm{e}^{-jk(r_{Qn'} + r_{m'Q})}}{r_{Qn'} + r_{m'Q}} \mathrm{e}^{j\mathbf{k}_i \cdot \mathbf{r}_{nn'}}, \tag{C.13}$$

where the directions $\hat{k}_i$ and $\hat{k}_{r,d}$ are given by (5.32) and (5.33), respectively. Finally, representing the term $\frac{\mathrm{e}^{-jk(r_{Qn'}+r_{m'Q})}}{r_{Qn'}+r_{m'Q}}$ from the center of the source group to the center of the receiving group over the UTD object in a ray optical sense (see Section 4.1 and Section 4.2) the ray optical terms of the Green's functions (2.32) and (2.33) are written with the far-field representations

$$\begin{aligned}\bar{\mathbf{G}}^{E}_{J,UTD}(\mathbf{r}_m,\mathbf{r}_n) &= \frac{\mu}{\varepsilon}\bar{\mathbf{G}}^{H}_{M,UTD}(\mathbf{r}_m,\mathbf{r}_n) = \\ &-j\frac{\omega\mu}{4\pi}\Bigg\{\sum_q \mathrm{e}^{-j\mathbf{k}_r\cdot\mathbf{r}_{mm'}}\widetilde{A}_{R_q}(s_{R_q})\bar{\mathbf{R}}^{E/H}_q T^{UTD}_L(kr_{Q_{R_q}n'})\cdot\left(\bar{\mathbf{I}}+\frac{1}{k^2}\nabla\nabla'\right)\mathrm{e}^{j\mathbf{k}_i\cdot\mathbf{r}_{nn'}} \\ &+\sum_v \mathrm{e}^{-j\mathbf{k}_d\cdot\mathbf{r}_{mm'}}\widetilde{A}_{D_v}(s_{D_v})\bar{\mathbf{D}}^{E/H}_v T^{UTD}_L(kr_{Q_{D_v}n'})\cdot\left(\bar{\mathbf{I}}+\frac{1}{k^2}\nabla\nabla'\right)\mathrm{e}^{j\mathbf{k}_i\cdot\mathbf{r}_{nn'}} \\ &+\cdots\Bigg\}\end{aligned} \tag{C.14}$$

and

$$\begin{aligned}\bar{\mathbf{G}}^{E}_{M,UTD}(\mathbf{r}_m,\mathbf{r}_n) &= -\bar{\mathbf{G}}^{H}_{J,UTD}(\mathbf{r}_m,\mathbf{r}_n) = \\ &-\frac{1}{4\pi}\Bigg\{\sum_q \mathrm{e}^{-j\mathbf{k}_r\cdot\mathbf{r}_{mm'}}\widetilde{A}_{R_q}(s_{R_q})\bar{\mathbf{R}}^{E/H}_q T^{UTD}_L(kr_{Q_{R_q}n'})\cdot\nabla\times\bar{\mathbf{I}}\mathrm{e}^{j\mathbf{k}_i\cdot\mathbf{r}_{nn'}} \\ &+\sum_v \mathrm{e}^{-j\mathbf{k}_d\cdot\mathbf{r}_{mm'}}\widetilde{A}_{D_v}(s_{D_v})\bar{\mathbf{D}}^{E/H}_v T^{UTD}_L(kr_{Q_{D_v}n'})\cdot\nabla\times\bar{\mathbf{I}}\mathrm{e}^{j\mathbf{k}_i\cdot\mathbf{r}_{nn'}} \\ &+\cdots\Bigg\},\end{aligned} \tag{C.15}$$

where

$$T^{UTD}_L(kr_{Qn'}) = \frac{\mathrm{e}^{-jkr_{Qn'}}}{r_{Qn'}} \tag{C.16}$$

is the *ray optical translation operator*. It is actually a far-field translation operator like in [143], however, here it is used to translate outgoing ray optical fields from the source groups to incident ray optical fields at the local points on the UTD objects. It can be seen, that this operator is simply the free space scalar Green's function from the center point of the source group to the particular local point on the UTD object. The incident rays at the local points on the UTD objects are multiplied with the appropriate scalar factors $\widetilde{A}_{R/D}(s_{R/D})$ and dyadic factors $\bar{\mathbf{R}}^{E/H}$, $\bar{\mathbf{D}}^{E/H}$ of the corresponding ray optical mechanism (see Section 4.1 and Section 4.2) providing the received ray optical contributions at the center of the receiving groups. Thereby, $s_{R/D}$ is given in (5.3) for $\mathbf{r}=\mathbf{r}_{m'}$. The terms $\mathrm{e}^{j\mathbf{k}_i\cdot\mathbf{r}_{nn'}}$ and $\mathrm{e}^{-j\mathbf{k}_{r,d}\cdot\mathbf{r}_{mm'}}$ are phase shifting factors from the source current to the center of the source group and from the center of the receiving group to the testing current, respectively. Also, $\hat{k}_i=\hat{r}_{Qn'}$ is the direction of ray incidence from the source group to the UTD object and $\hat{k}_{r,d}=\hat{r}_{m'Q}$ is the direction of reflection/diffraction from the UTD object to the receiving group as shown in Fig. 5.3.

The conditions to perform ray optical translations are given in (C.9) and (C.11). In the worst-case, where source or testing current element lies at the corner of the corresponding group, these conditions become

$$r_{UTD} \geq \frac{1}{2}k(0.5\sqrt{3}D_l)^2 = \frac{\pi(0.5\sqrt{3}D_l)^2}{\lambda}, \tag{C.17}$$

where D_l is the group dimension at level l as described in Section 5.4.2. This is the condition for performing ray optical translations and it corresponds to a far-field condition with respect to the MLFMM group dimensions at the working level. Thus, this condition enforces the local point on the UTD object to be in the far-field of the working source and receiving group in order to perform valid ray optical translations. This means that the UTD object does not need to be in the far-field with respect to the dimensions of the whole structure but rather in the far-field of the individual basis functions similar to hybrid BIM-UTD formulations.

C.2 Hybrid Matrix-Vector Product

The full matrix-vector product for the equation system (5.34) of the hybrid FEBI-MLFMM-UTD method is written for electric currents as

$$
\begin{aligned}
\sum_{n=1}^{N} Z_{mn,J,tot}^{CFIE} H_n = & \sum_{n' \in G_{Bn'}} \sum_{n \in G_{n'}} Z_{mn,J,tot}^{MoM} H_n \\
& -j\frac{\omega\mu}{4\pi}\alpha \Bigg\{ \oiint \tilde{\boldsymbol{\beta}}_m^*(\hat{k}) \cdot \sum_{n' \notin G_{Bn'}} T_L(\hat{k}\cdot\hat{r}_{m'n'}) \left(\bar{\mathbf{I}} - \hat{k}\hat{k} \right) \cdot \sum_{n \in G_{n'}} H_n \tilde{\boldsymbol{\beta}}_n(\hat{k})\, d\hat{k}^2 \\
& + \sum_{q} \sum_{t'}^{K_0} w_{p_{t'}} \tilde{\boldsymbol{\beta}}_m^*(\hat{k}_{r,p_{t'}}) \cdot \sum_{t}^{K_0} w_{p_t} \tilde{A}_{R_q}(s_{R_q}) \bar{\mathbf{R}}_q^E \sum_{n' \notin G_{Bn'}} T_L^{UTD}(kr_{Q_{R_q}n'}) \\
& \qquad \cdot \left(\bar{\mathbf{I}} - \hat{k}_{r,p_{t'}} \hat{k}_{i,p_t} \right) \cdot \sum_{n \in G_{n'}} H_n \tilde{\boldsymbol{\beta}}_n(\hat{k}_{i,p_t}) \\
& + \sum_{v} \sum_{t'}^{K_0} w_{p_{t'}} \tilde{\boldsymbol{\beta}}_m^*(\hat{k}_{d,p_{t'}}) \cdot \sum_{t}^{K_0} w_{p_t} \tilde{A}_{D_v}(s_{D_v}) \bar{\mathbf{D}}_v^E \sum_{n' \notin G_{Bn'}} T_L^{UTD}(kr_{Q_{D_v}n'}) \\
& \qquad \cdot \left(\bar{\mathbf{I}} - \hat{k}_{d,p_{t'}} \hat{k}_{i,p_t} \right) \cdot \sum_{n \in G_{n'}} H_n \tilde{\boldsymbol{\beta}}_n(\hat{k}_{i,p_t}) \\
& + \cdots \Bigg\} \\
& + jZ\frac{k}{4\pi}(1-\alpha) \Bigg\{ \oiint \left[\hat{k} \times \tilde{\boldsymbol{\alpha}}_m^*(\hat{k}) \right] \cdot \sum_{n' \notin G_{Bn'}} T_L(\hat{k}\cdot\hat{r}_{m'n'}) \sum_{n \in G_{n'}} H_n \tilde{\boldsymbol{\beta}}_n(\hat{k})\, d\hat{k}^2 \\
& + \sum_{q} \sum_{t'}^{K_0} w_{p_{t'}} \left[\hat{k}_{r,p_{t'}} \times \tilde{\boldsymbol{\alpha}}_m^*(\hat{k}_{r,p_{t'}}) \right] \cdot \sum_{t}^{K_0} w_{p_t} \tilde{A}_{R_q}(s_{R_q}) \bar{\mathbf{R}}_q^E \sum_{n' \notin G_{Bn'}} T_L^{UTD}(kr_{Q_{R_q}n'}) \\
& \qquad \cdot \sum_{n \in G_{n'}} H_n \tilde{\boldsymbol{\beta}}_n(\hat{k}_{i,p_t}) \\
& + \sum_{v} \sum_{t'}^{K_0} w_{p_{t'}} \left[\hat{k}_{d,p_{t'}} \times \tilde{\boldsymbol{\alpha}}_m^*(\hat{k}_{d,p_{t'}}) \right] \cdot \sum_{t}^{K_0} w_{p_t} \tilde{A}_{D_v}(s_{D_v}) \bar{\mathbf{D}}_v^E \sum_{n' \notin G_{Bn'}} T_L^{UTD}(kr_{Q_{D_v}n'}) \\
& \qquad \cdot \sum_{n \in G_{n'}} H_n \tilde{\boldsymbol{\beta}}_n(\hat{k}_{i,p_t}) \\
& + \cdots \Bigg\}
\end{aligned}
\tag{C.18}
$$

and for magnetic currents as

$$
\begin{aligned}
\sum_{n=1}^{N} Z^{CFIE}_{mn,M,tot} E_n = & \sum_{n' \in G_{Bn'}} \sum_{n \in G_{n'}} Z^{MoM}_{mn,M,tot} E_n \\
& + j\frac{k}{4\pi}\alpha \Bigg\{ \oiint \left[\hat{k} \times \widetilde{\boldsymbol{\beta}}^{*}_{m}(\hat{k}) \right] \cdot \sum_{n' \notin G_{Bn'}} T_L(\hat{k} \cdot \hat{r}_{m'n'}) \sum_{n \in G_{n'}} E_n \widetilde{\boldsymbol{\beta}}_n(\hat{k}) \, d\hat{k}^2 \\
& + \sum_{q} \sum_{t'}^{K_0} w_{p_{t'}} \left[\hat{k}_{r,p_{t'}} \times \widetilde{\boldsymbol{\beta}}^{*}_{m}(\hat{k}_{r,p_{t'}}) \right] \cdot \sum_{t}^{K_0} w_{p_t} \widetilde{A}_{R_q}(s_{R_q}) \bar{\mathbf{R}}^{H}_{q} \sum_{n' \notin G_{Bn'}} T^{UTD}_{L}(kr_{Q_{R_q}n'}) \\
& \qquad \cdot \sum_{n \in G_{n'}} E_n \widetilde{\boldsymbol{\beta}}_n(\hat{k}_{i,p_t}) \\
& + \sum_{v} \sum_{t'}^{K_0} w_{p_{t'}} \left[\hat{k}_{d,p_{t'}} \times \widetilde{\boldsymbol{\beta}}^{*}_{m}(\hat{k}_{d,p_{t'}}) \right] \cdot \sum_{t}^{K_0} w_{p_t} \widetilde{A}_{D_v}(s_{D_v}) \bar{\mathbf{D}}^{H}_{v} \sum_{n' \notin G_{Bn'}} T^{UTD}_{L}(kr_{Q_{D_v}n'}) \\
& \qquad \cdot \sum_{n \in G_{n'}} E_n \widetilde{\boldsymbol{\beta}}_n(\hat{k}_{i,p_t}) \\
& + \cdots \Bigg\} \\
& + jZ\frac{\omega\varepsilon}{4\pi}(1-\alpha) \Bigg\{ \oiint \widetilde{\boldsymbol{\alpha}}^{*}_{m}(\hat{k}) \cdot \sum_{n' \notin G_{Bn'}} T_L(\hat{k} \cdot \hat{r}_{m'n'}) \left(\bar{\mathbf{I}} - \hat{k}\hat{k} \right) \cdot \sum_{n \in G_{n'}} E_n \widetilde{\boldsymbol{\beta}}_n(\hat{k}) \, d\hat{k}^2 \\
& + \sum_{q} \sum_{t'}^{K_0} w_{p_{t'}} \widetilde{\boldsymbol{\alpha}}^{*}_{m}(\hat{k}_{r,p_{t'}}) \cdot \sum_{t}^{K_0} w_{p_t} \widetilde{A}_{R_q}(s_{R_q}) \bar{\mathbf{R}}^{H}_{q} \sum_{n' \notin G_{Bn'}} T^{UTD}_{L}(kr_{Q_{R_q}n'}) \\
& \qquad \cdot \left(\bar{\mathbf{I}} - \hat{k}_{r,p_{t'}} \hat{k}_{i,p_t} \right) \cdot \sum_{n \in G_{n'}} E_n \widetilde{\boldsymbol{\beta}}_n(\hat{k}_{i,p_t}) \\
& + \sum_{v} \sum_{t'}^{K_0} w_{p_{t'}} \widetilde{\boldsymbol{\alpha}}^{*}_{m}(\hat{k}_{d,p_{t'}}) \cdot \sum_{t}^{K_0} w_{p_t} \widetilde{A}_{D_v}(s_{D_v}) \bar{\mathbf{D}}^{H}_{v} \sum_{n' \notin G_{Bn'}} T^{UTD}_{L}(kr_{Q_{D_v}n'}) \\
& \qquad \cdot \left(\bar{\mathbf{I}} - \hat{k}_{d,p_{t'}} \hat{k}_{i,p_t} \right) \cdot \sum_{n \in G_{n'}} E_n \widetilde{\boldsymbol{\beta}}_n(\hat{k}_{i,p_t}) \\
& + \cdots \Bigg\},
\end{aligned}
\tag{C.19}
$$

for $m \in G_{m'}$, where $G_{m'}$ is the m'-th testing group. Also, $G_{Bn'}$ denotes all nearby (not well-separated) groups of the n'-th source group $G_{n'}$ including itself. Thereby, $Z^{MoM}_{mn,J/M,tot}$ are the total hybrid near coupling matrix elements for CFIE between non well-separated groups due to electric and magnetic currents, respectively, which are evaluated by conventional MoM using the equations in Appendix B. Further, K_0 is the number of interpolation and anterpolation points for evaluation of ray optical directions in the UTD part with $K_0 \ll K$ and w_{p_t}, $w_{p_{t'}}$ are the interpolation and anterpolation weights, respectively. Finally, $\hat{k}_{i,p_t}$ is the direction of the sampling point close to the direction of ray incidence and $\hat{k}_{r/d,p_{t'}}$ is the direction of the sampling point close to direction of reflection or diffraction.

C.3 Ray Optical Dyad Components

The ray optical dyadic coefficients for reflection and diffraction are given in the corresponding local coordinate system by expressions of the form

$$\bar{\mathbf{K}} = K_{\parallel}\hat{e}_{\parallel}^{r,d}\hat{e}_{\parallel}^{i} + K_{\perp}\hat{e}_{\perp}^{r,d}\hat{e}_{\perp}^{i}, \tag{C.20}$$

where $\bar{\mathbf{K}} = \bar{\mathbf{R}}, \bar{\mathbf{D}}$ and $K_{\parallel,\perp} = R_{\parallel,\perp}, D_{\parallel,\perp}$ in case of reflection or diffraction. Particularly, the above expressions connect the local components of the incident and reflected/diffracted rays through (4.26) in the local ray-fixed coordinate system in case of reflection and through (4.42) in the local edge-fixed coordinate system in case of diffraction as described in Section 4.1.2 and Section 4.2, respectively.

The local components of the ray optical dyadic coefficients are connected to the global Cartesian components through

$$\begin{aligned}
\hat{e}_{\parallel,\perp}^{r,d}\hat{e}_{\parallel,\perp}^{i} &= \hat{e}_{\parallel,\perp x}^{r,d}\hat{e}_{\parallel,\perp x}^{i}\hat{x}^{r,d}\hat{x}^{i} + \hat{e}_{\parallel,\perp x}^{r,d}\hat{e}_{\parallel,\perp y}^{i}\hat{x}^{r,d}\hat{y}^{i} + \hat{e}_{\parallel,\perp x}^{r,d}\hat{e}_{\parallel,\perp z}^{i}\hat{x}^{r,d}\hat{z}^{i} \\
&+ \hat{e}_{\parallel,\perp y}^{r,d}\hat{e}_{\parallel,\perp x}^{i}\hat{y}^{r,d}\hat{x}^{i} + \hat{e}_{\parallel,\perp y}^{r,d}\hat{e}_{\parallel,\perp y}^{i}\hat{y}^{r,d}\hat{y}^{i} + \hat{e}_{\parallel,\perp y}^{r,d}\hat{e}_{\parallel,\perp z}^{i}\hat{y}^{r,d}\hat{z}^{i} \\
&+ \hat{e}_{\parallel,\perp z}^{r,d}\hat{e}_{\parallel,\perp x}^{i}\hat{z}^{r,d}\hat{x}^{i} + \hat{e}_{\parallel,\perp z}^{r,d}\hat{e}_{\parallel,\perp y}^{i}\hat{z}^{r,d}\hat{y}^{i} + \hat{e}_{\parallel,\perp z}^{r,d}\hat{e}_{\parallel,\perp z}^{i}\hat{z}^{r,d}\hat{z}^{i}
\end{aligned} \tag{C.21}$$

based on the dyad definitions given in Section A.2.1 in the Appendix A. So, the Cartesian components of the ray optical dyadic coefficients are

$$K_{xx} = K_{\parallel}\hat{e}_{\parallel x}^{r,d}\hat{e}_{\parallel x}^{i} + K_{\perp}\hat{e}_{\perp x}^{r,d}\hat{e}_{\perp x}^{i}, \tag{C.22}$$
$$K_{xy} = K_{\parallel}\hat{e}_{\parallel x}^{r,d}\hat{e}_{\parallel y}^{i} + K_{\perp}\hat{e}_{\perp x}^{r,d}\hat{e}_{\perp y}^{i}, \tag{C.23}$$
$$K_{xz} = K_{\parallel}\hat{e}_{\parallel x}^{r,d}\hat{e}_{\parallel z}^{i} + K_{\perp}\hat{e}_{\perp x}^{r,d}\hat{e}_{\perp z}^{i}, \tag{C.24}$$
$$K_{yx} = K_{\parallel}\hat{e}_{\parallel y}^{r,d}\hat{e}_{\parallel x}^{i} + K_{\perp}\hat{e}_{\perp y}^{r,d}\hat{e}_{\perp x}^{i}, \tag{C.25}$$
$$K_{yy} = K_{\parallel}\hat{e}_{\parallel y}^{r,d}\hat{e}_{\parallel y}^{i} + K_{\perp}\hat{e}_{\perp y}^{r,d}\hat{e}_{\perp y}^{i}, \tag{C.26}$$
$$K_{yz} = K_{\parallel}\hat{e}_{\parallel y}^{r,d}\hat{e}_{\parallel z}^{i} + K_{\perp}\hat{e}_{\perp y}^{r,d}\hat{e}_{\perp z}^{i}, \tag{C.27}$$
$$K_{zx} = K_{\parallel}\hat{e}_{\parallel z}^{r,d}\hat{e}_{\parallel x}^{i} + K_{\perp}\hat{e}_{\perp z}^{r,d}\hat{e}_{\perp x}^{i}, \tag{C.28}$$
$$K_{zy} = K_{\parallel}\hat{e}_{\parallel z}^{r,d}\hat{e}_{\parallel y}^{i} + K_{\perp}\hat{e}_{\perp z}^{r,d}\hat{e}_{\perp y}^{i}, \tag{C.29}$$
$$K_{zz} = K_{\parallel}\hat{e}_{\parallel z}^{r,d}\hat{e}_{\parallel z}^{i} + K_{\perp}\hat{e}_{\perp z}^{r,d}\hat{e}_{\perp z}^{i}. \tag{C.30}$$

In case of reflection on flat metallic surfaces, the radial components $\hat{e}_k^r\hat{e}_l^i$, $k,l = x,y,z$ are added to each of the above components according to special treatment of reflection terms described in Section 5.5.2.

The ray optical dyadic coefficients are transformed into the global spherical coordinate sys-

tem according to

$$
\begin{aligned}
\bar{\mathbf{K}} = & \\
& \Bigg\{ \Big(K_{xx} \sin\vartheta_i \cos\varphi_i + K_{xy} \sin\vartheta_i \sin\varphi_i + K_{xz} \cos\vartheta_i \Big) \sin\vartheta_{r,d} \cos\varphi_{r,d} \\
& \quad + \Big(K_{yx} \sin\vartheta_i \cos\varphi_i + K_{yy} \sin\vartheta_i \sin\varphi_i + K_{yz} \cos\vartheta_i \Big) \sin\vartheta_{r,d} \sin\varphi_{r,d} \\
& \quad + \Big(K_{zx} \sin\vartheta_i \cos\varphi_i + K_{zy} \sin\vartheta_i \sin\varphi_i + K_{zz} \cos\vartheta_i \Big) \cos\vartheta_{r,d} \\
& \qquad \Bigg\} \hat{r}\hat{r} \\
& + \Bigg\{ \Big(K_{xx} \cos\vartheta_i \cos\varphi_i + K_{xy} \cos\vartheta_i \sin\varphi_i - K_{xz} \sin\vartheta_i \Big) \sin\vartheta_{r,d} \cos\varphi_{r,d} \\
& \quad + \Big(K_{yx} \cos\vartheta_i \cos\varphi_i + K_{yy} \cos\vartheta_i \sin\varphi_i - K_{yz} \sin\vartheta_i \Big) \sin\vartheta_{r,d} \sin\varphi_{r,d} \\
& \quad + \Big(K_{zx} \cos\vartheta_i \cos\varphi_i + K_{zy} \cos\vartheta_i \sin\varphi_i - K_{zz} \sin\vartheta_i \Big) \cos\vartheta_{r,d} \\
& \qquad \Bigg\} \hat{r}\hat{\vartheta} \\
& + \Bigg\{ \Big(- K_{xx} \sin\varphi_i + K_{xy} \cos\varphi_i \Big) \sin\vartheta_{r,d} \cos\varphi_{r,d} \\
& \quad + \Big(- K_{yx} \sin\varphi_i + K_{yy} \cos\varphi_i \Big) \sin\vartheta_{r,d} \sin\varphi_{r,d} \\
& \quad + \Big(- K_{zx} \sin\varphi_i + K_{zy} \cos\varphi_i \Big) \cos\vartheta_{r,d} \\
& \qquad \Bigg\} \hat{r}\hat{\varphi} \\
& + \Bigg\{ \Big(K_{xx} \sin\vartheta_i \cos\varphi_i + K_{xy} \sin\vartheta_i \sin\varphi_i + K_{xz} \cos\vartheta_i \Big) \cos\vartheta_{r,d} \cos\varphi_{r,d} \\
& \quad + \Big(K_{yx} \sin\vartheta_i \cos\varphi_i + K_{yy} \sin\vartheta_i \sin\varphi_i + K_{yz} \cos\vartheta_i \Big) \cos\vartheta_{r,d} \sin\varphi_{r,d} \\
& \quad - \Big(K_{zx} \sin\vartheta_i \cos\varphi_i + K_{zy} \sin\vartheta_i \sin\varphi_i + K_{zz} \cos\vartheta_i \Big) \sin\vartheta_{r,d} \\
& \qquad \Bigg\} \hat{\vartheta}\hat{r}
\end{aligned}
$$

$$
\begin{aligned}
&+\Bigg\{\Big(K_{xx}\cos\vartheta_i\cos\varphi_i + K_{xy}\cos\vartheta_i\sin\varphi_i - K_{xz}\sin\vartheta_i\Big)\cos\vartheta_{r,d}\cos\varphi_{r,d}\\
&\quad+\Big(K_{yx}\cos\vartheta_i\cos\varphi_i + K_{yy}\cos\vartheta_i\sin\varphi_i - K_{yz}\sin\vartheta_i\Big)\cos\vartheta_{r,d}\sin\varphi_{r,d}\\
&\quad-\Big(K_{zx}\cos\vartheta_i\cos\varphi_i + K_{zy}\cos\vartheta_i\sin\varphi_i - K_{zz}\sin\vartheta_i\Big)\sin\vartheta_{r,d}\\
&\qquad\Bigg\}\hat{\vartheta}\hat{\vartheta}\\
&+\Bigg\{\Big(-K_{xx}\sin\varphi_i + K_{xy}\cos\varphi_i\Big)\cos\vartheta_{r,d}\cos\varphi_{r,d}\\
&\quad+\Big(-K_{yx}\sin\varphi_i + K_{yy}\cos\varphi_i\Big)\cos\vartheta_{r,d}\sin\varphi_{r,d}\\
&\quad-\Big(-K_{zx}\sin\varphi_i + K_{zy}\cos\varphi_i\Big)\sin\vartheta_{r,d}\\
&\qquad\Bigg\}\hat{\vartheta}\hat{\varphi}\\
&+\Bigg\{-\Big(K_{xx}\sin\vartheta_i\cos\varphi_i + K_{xy}\sin\vartheta_i\sin\varphi_i + K_{xz}\cos\vartheta_i\Big)\sin\varphi_{r,d}\\
&\quad+\Big(K_{yx}\sin\vartheta_i\cos\varphi_i + K_{yy}\sin\vartheta_i\sin\varphi_i + K_{yz}\cos\vartheta_i\Big)\cos\varphi_{r,d}\\
&\qquad\Bigg\}\hat{\varphi}\hat{r}\\
&+\Bigg\{-\Big(K_{xx}\cos\vartheta_i\cos\varphi_i + K_{xy}\cos\vartheta_i\sin\varphi_i - K_{xz}\sin\vartheta_i\Big)\sin\varphi_{r,d}\\
&\quad+\Big(K_{yx}\cos\vartheta_i\cos\varphi_i + K_{yy}\cos\vartheta_i\sin\varphi_i - K_{yz}\sin\vartheta_i\Big)\cos\varphi_{r,d}\\
&\qquad\Bigg\}\hat{\varphi}\hat{\vartheta}\\
&+\Bigg\{-\Big(-K_{xx}\sin\varphi_i + K_{xy}\cos\varphi_i\Big)\sin\varphi_{r,d}\\
&\quad+\Big(-K_{yx}\sin\varphi_i + K_{yy}\cos\varphi_i\Big)\cos\varphi_{r,d}\\
&\qquad\Bigg\}\hat{\varphi}\hat{\varphi},
\end{aligned}
\tag{C.31}
$$

which is based on the transformation of dyad components into the spherical coordinate system as described in Section A.2.2 in the Appendix A using the Cartesian components given in (C.22)-(C.30). Thereby, ϑ_i, φ_i are spherical coordinates of the ray incidence direction $\hat{k}_i$, whereas $\vartheta_{r,d}, \varphi_{r,d}$ are spherical coordinates of the ray directions $\hat{k}_{r,d}$ of reflection and diffraction, respectively.

Appendix D

Hybrid Postprocessing Formulations

In the following, first the derivation of the direct far-field translation operator as well as the derivation of the ray optical terms of the Green's function outside the grouping domain will be presented. After that, the total electric and magnetic field contributions for postprocessing computations will be summarized assuming observation points $\mathbf{r} = \mathbf{r}_m$ and source points $\mathbf{r}' = \mathbf{r}_n$.

D.1 Direct Far-Field Translation Operator Outside Grouping Domain

The configuration shown Fig. 6.4 is assumed, where the field path from the source point $\mathbf{r}' = \mathbf{r}_n$ to the observation point $\mathbf{r} = \mathbf{r}_m$ is written as

$$\mathbf{r} - \mathbf{r}' = \mathbf{r}_m - \mathbf{r}_n = (\mathbf{r}_m - \mathbf{r}_{n'}) + (\mathbf{r}_{n'} - \mathbf{r}_n) = \mathbf{r}_{mn'} - \mathbf{r}_{nn'}, \tag{D.1}$$

by intervening the center point of the source group in the field path. In order to express the appropriate free space scalar Green's function (2.34) from the source to the observation point, it is assumed that the field path from the center of the source group to the observation point $\mathbf{r}_{mn'}$ is much larger than the paths $\mathbf{r}_{nn'}$ within the source groups, thus

$$|\mathbf{r}_{mn'}| \gg |\mathbf{r}_{nn'}|. \tag{D.2}$$

The electrical path kr_{mn} from the source current to the observation point is alternatively written as

$$\begin{aligned} kr_{mn} &\overset{(D.1)}{=} k\sqrt{(\mathbf{r}_{mn'} - \mathbf{r}_{nn'}) \cdot (\mathbf{r}_{mn'} - \mathbf{r}_{nn'})} \\ &= k\sqrt{|\mathbf{r}_{mn'}|^2 - 2\mathbf{r}_{mn'} \cdot \mathbf{r}_{nn'} + |\mathbf{r}_{nn'}|^2} \\ &= kr_{mn'}\sqrt{1 - 2\frac{\mathbf{r}_{mn'} \cdot \mathbf{r}_{nn'}}{r_{mn'}^2} + \frac{r_{nn'}^2}{r_{mn'}^2}}. \end{aligned} \tag{D.3}$$

When the condition (D.2) holds for the source group, the expression (D.3) is expanded in terms of a Taylor series as

$$kr_{mn} \approx kr_{mn'} - k\mathbf{r}_{nn'} \cdot \hat{r}_{mn'} + \frac{\sin^2 \vartheta_{mn'}}{2r_{mn'}} kr_{nn'}^2, \tag{D.4}$$

where $\vartheta_{mn'}$ is the angle between $\mathbf{r}_{mn'}$ and $\mathbf{r}_{nn'}$. Under the condition

$$r_{mn'} \gg \frac{1}{2}k|\mathbf{r}_{nn'}|^2, \tag{D.5}$$

the higher-order term of the expansion (D.3) is neglected and the electrical path kr_{mn} is further simplified as

$$kr_{mn} = k|\mathbf{r}_m - \mathbf{r}_n| \approx kr_{mn'} - k\mathbf{r}_{nn'} \cdot \hat{r}_{mn'}. \tag{D.6}$$

So, the free space scalar Greens's function (2.34) for $\mathbf{r} = \mathbf{r}_m$ and $\mathbf{r}' = \mathbf{r}_n$ becomes

$$\begin{aligned} G_P(\mathbf{r}_m, \mathbf{r}_n) &= \frac{\mathrm{e}^{-jk|\mathbf{r}_m - \mathbf{r}_n|}}{|\mathbf{r}_m - \mathbf{r}_n|} = \frac{\mathrm{e}^{-jkr_{mn}}}{r_{mn}} \\ &= \frac{\mathrm{e}^{-j(kr_{mn'} - k\mathbf{r}_{nn'} \cdot \hat{r}_{mn'})}}{r_{mn'} - \mathbf{r}_{nn'} \cdot \hat{r}_{mn'}} \\ &\overset{(D.2)}{=} \mathrm{e}^{j\mathbf{k}_0 \cdot \mathbf{r}_{nn'}} \frac{\mathrm{e}^{-jkr_{mn'}}}{r_{mn'}}, \end{aligned} \tag{D.7}$$

since $\hat{k}_0 = \hat{r}_{mn'}$ as shown in Fig. 6.4 with $\mathbf{k}_0 = k\hat{k}_0$. Thereby,

$$T_L^{FF}(kr_{mn'}) = \frac{\mathrm{e}^{-jkr_{mn'}}}{r_{mn'}} \tag{D.8}$$

is the *direct far-field translation operator*, which translates the outgoing wave from the source group to an incoming wave at the observation point for the direction $\hat{k}_0$. The term $\mathrm{e}^{j\mathbf{k}_0 \cdot \mathbf{r}_{nn'}}$ is a phase shifting factor from the source current point to the center point of the source group. It is noticed, that the direct far-field translation operator derived in this section has the same form as the ray optical translation operator derived in Section C.1. Both operators are derived in the same manner using similar far-field conditions. In the present thesis, however, different notations are used for these far-field translation operators in order to distinguish the corresponding application.

Furthermore, the condition used to perform direct far-field translations in the direct part and ray optical translations in the UTD part is

$$r_{far} \geq \frac{1}{2}k|\mathbf{r}_{nn'}|^2_{max} = \frac{\pi(0.5\sqrt{3}D_l)^2}{\lambda} \overset{(C.17)}{=} r_{UTD} \tag{D.9}$$

as described in Section 6.5. Thereby, D_l is the group dimension at level l given in (5.40) and λ is the wavelength. This condition corresponds to a far-field condition with respect to the group dimension at the working level and it enforces the observation point outside the grouping domain as well as the local point on the UTD object to be in the far-field of the working source group.

D.2 Ray Optical Terms of Green's Function Outside Grouping Domain

The configuration shown in Fig. 6.4 is assumed, where the coupling path from the source current element to the observation point outside the grouping domain is written as

$$\mathbf{r}-\mathbf{r}'=\mathbf{r}_m-\mathbf{r}_n=(\mathbf{r}_m-\mathbf{r}_Q)+(\mathbf{r}_Q-\mathbf{r}_n)=\mathbf{r}_{mQ}+\mathbf{r}_{Qn}, \tag{D.10}$$

by first intervening the local point Q on the UTD object with position vector $\mathbf{r}_Q$. Then, for the subpath $\mathbf{r}_{Qn}$ in (D.10) the center point of the source group is intervened resulting in the expression (C.3). Thus, the total path is written as

$$\begin{aligned}\mathbf{r}-\mathbf{r}'=\mathbf{r}_m-\mathbf{r}_n &= (\mathbf{r}_m-\mathbf{r}_Q)+(\mathbf{r}_Q-\mathbf{r}_{n'})+(\mathbf{r}_{n'}-\mathbf{r}_n)\\ &= \mathbf{r}_{mQ}+\mathbf{r}_{Qn'}-\mathbf{r}_{nn'}.\end{aligned} \tag{D.11}$$

In order to express ray optical terms of the Green's function in a suitable way for MLFMM computations, the condition (C.5) is assumed, which means that the field path from the center of the source group to the local point on the UTD objects $\mathbf{r}_{Qn'}$ is much larger than the paths within the source groups $\mathbf{r}_{nn'}$. The electrical path kr_{Qn} from the source current to the local point on the UTD object is alternatively written as in (C.7) and following the same procedure as in Section C.1 through the use of the same conditions (C.5) and (C.9) the electrical path kr_{Qn} is simplified as in (C.10).

Using the electrical coupling path expressions (C.10) together with the remaining path kr_{mQ} the scalar Green's function from the source current to the observation point outside the grouping domain is alternatively written as

$$G_{UTD}(\mathbf{r}_m,\mathbf{r}_n)=\frac{\mathrm{e}^{-jk(r_{Qn'}+r_{mQ})}}{r_{Qn'}+r_{mQ}}\mathrm{e}^{j\mathbf{k}_i\cdot\mathbf{r}_{nn'}}, \tag{D.12}$$

where the direction $\hat{k}_i$ is given by (5.32). Finally, representing the term $\frac{\mathrm{e}^{-jk(r_{Qn'}+r_{mQ})}}{r_{Qn'}+r_{mQ}}$ from the center of the source group to the observation point over the UTD object in a ray optical sense (see Section 4.1 and Section 4.2) the ray optical terms of the Green's functions (2.32) and (2.33) are written with the far-field representations

$$\begin{aligned}\bar{\mathbf{G}}^{E}_{J,UTD}(\mathbf{r}_m,\mathbf{r}_n)=\frac{\mu}{\varepsilon}\bar{\mathbf{G}}^{H}_{M,UTD}(\mathbf{r}_m,\mathbf{r}_n)=\\ -j\frac{\omega\mu}{4\pi}\Bigg\{\sum_q \widetilde{A}_{R_q}(s_{R_q})\bar{\mathbf{R}}^{E/H}_q T^{UTD}_L(kr_{Q_{R_q}n'})\cdot\left(\bar{\mathbf{I}}+\frac{1}{k^2}\nabla\nabla'\right)\mathrm{e}^{j\mathbf{k}_i\cdot\mathbf{r}_{nn'}}\\ +\sum_v \widetilde{A}_{D_v}(s_{D_v})\bar{\mathbf{D}}^{E/H}_v T^{UTD}_L(kr_{Q_{D_v}n'})\cdot\left(\bar{\mathbf{I}}+\frac{1}{k^2}\nabla\nabla'\right)\mathrm{e}^{j\mathbf{k}_i\cdot\mathbf{r}_{nn'}}\\ +\cdots\Bigg\}\end{aligned} \tag{D.13}$$

and

$$\begin{aligned}\bar{\mathbf{G}}^{E}_{M,UTD}(\mathbf{r}_m,\mathbf{r}_n) = -\bar{\mathbf{G}}^{H}_{J,UTD}(\mathbf{r}_m,\mathbf{r}_n) = \\ -\frac{1}{4\pi}\Bigg\{ \sum_q \widetilde{A}_{R_q}(s_{R_q})\bar{\mathbf{R}}^{E/H}_q T^{UTD}_L(kr_{Q_{R_q}n'})\cdot\nabla\times\bar{\mathbf{I}}\mathrm{e}^{j\mathbf{k}_i\cdot\mathbf{r}_{nn'}} \\ +\sum_v \widetilde{A}_{D_v}(s_{D_v})\bar{\mathbf{D}}^{E/H}_v T^{UTD}_L(kr_{Q_{D_v}n'})\cdot\nabla\times\bar{\mathbf{I}}\mathrm{e}^{j\mathbf{k}_i\cdot\mathbf{r}_{nn'}} \\ +\cdots\Bigg\},\end{aligned} \tag{D.14}$$

where $T^{UTD}_L(kr_{Qn'})$ is the ray optical translation operator given in (5.30), which is used to translate outgoing ray optical fields from the source groups to incident ray optical fields at the local points on the UTD objects. Similar to the approach in Section C.1, the incident rays at the local points $Q_{R/D}$ on the UTD objects are multiplied with the appropriate scalar factors $\widetilde{A}_{R/D}(s_{R/D})$ and dyadic factors $\bar{\mathbf{R}}^{E/H}$, $\bar{\mathbf{D}}^{E/H}$ of the corresponding ray optical mechanism (see Section 4.1 and Section 4.2) providing the received ray optical contributions at the center of the receiving groups. Thereby, $r_{Qn'}$ is given by (5.31) and $s_{R/D}$ is given by (5.3), which in this case it coincides with $\hat{k}_{r,d}$ given in (5.33). The term $\mathrm{e}^{j\mathbf{k}_i\cdot\mathbf{r}_{nn'}}$ is the phase shifting factor from the source current to the center of the source group. It is noticed, that no phase shifting is performed at the reception since outside the grouping domain the field contributions are evaluated to each observation point separately. Also, $\hat{k}_i$ is given by (5.32) as shown in Fig. 6.4.

D.3 Total Field Contributions

The complete expressions for the electric and magnetic field in the postprocessing stage of the hybrid method are

$$
\begin{aligned}
&\mathbf{E}_{tot}(\mathbf{r}_m) = \\
&\quad -j\frac{\omega\mu}{4\pi}\Bigg\{ \oiint e^{-j\mathbf{k}\cdot\mathbf{r}_{mm'}} T_L(\hat{k}\cdot\hat{r}_{m'n'}) \left(\bar{\mathbf{I}} - \hat{k}\hat{k}\right) \cdot \sum_n H_n \tilde{\boldsymbol{\beta}}_n(\hat{k})\, d\hat{k}^2 \\
&\quad + \sum_q e^{-j\mathbf{k}_r\cdot\mathbf{r}_{mm'}} \widetilde{A}_{R_q}(s_{R_q}) \bar{\mathbf{R}}_q^E T_L^{UTD}(kr_{Q_{R_q}n'}) \cdot \left(\bar{\mathbf{I}} - \hat{k}_r\hat{k}_i\right) \cdot \sum_n H_n \tilde{\boldsymbol{\beta}}_n(\hat{k}_i) \\
&\quad + \sum_v e^{-j\mathbf{k}_d\cdot\mathbf{r}_{mm'}} \widetilde{A}_{D_v}(s_{D_v}) \bar{\mathbf{D}}_v^E T_L^{UTD}(kr_{Q_{D_v}n'}) \cdot \left(\bar{\mathbf{I}} - \hat{k}_d\hat{k}_i\right) \cdot \sum_n H_n \tilde{\boldsymbol{\beta}}_n(\hat{k}_i) \\
&\quad + \cdots \Bigg\} \\
&\quad -j\frac{k}{4\pi}\Bigg\{ \oiint \hat{k} \times e^{-j\mathbf{k}\cdot\mathbf{r}_{mm'}} T_L(\hat{k}\cdot\hat{r}_{m'n'}) \sum_n E_n \tilde{\boldsymbol{\beta}}_n(\hat{k})\, d\hat{k}^2 \\
&\quad + \sum_q \hat{k}_r \times e^{-j\mathbf{k}_r\cdot\mathbf{r}_{mm'}} \widetilde{A}_{R_q}(s_{R_q}) \bar{\mathbf{R}}_q^H T_L^{UTD}(kr_{Q_{R_q}n'}) \cdot \sum_n E_n \tilde{\boldsymbol{\beta}}_n(\hat{k}_i) \\
&\quad + \sum_v \hat{k}_d \times e^{-j\mathbf{k}_d\cdot\mathbf{r}_{mm'}} \widetilde{A}_{D_v}(s_{D_v}) \bar{\mathbf{D}}_v^H T_L^{UTD}(kr_{Q_{D_v}n'}) \cdot \sum_n E_n \tilde{\boldsymbol{\beta}}_n(\hat{k}_i) + \cdots \Bigg\} \\
&\quad -j\frac{\omega\mu}{4\pi}\Bigg\{ T_L^{FF}(kr_{mn'}) \left(\bar{\mathbf{I}} - \hat{k}_0\hat{k}_0\right) \cdot \sum_n H_n \tilde{\boldsymbol{\beta}}_n(\hat{k}_0) \\
&\quad + \sum_q \widetilde{A}_{R_q}(s_{R_q}) \bar{\mathbf{R}}_q^E T_L^{UTD}(kr_{Q_{R_q}n'}) \cdot \left(\bar{\mathbf{I}} - \hat{k}_r\hat{k}_i\right) \cdot \sum_n H_n \tilde{\boldsymbol{\beta}}_n(\hat{k}_i) \\
&\quad + \sum_v \widetilde{A}_{D_v}(s_{D_v}) \bar{\mathbf{D}}_v^E T_L^{UTD}(kr_{Q_{D_v}n'}) \cdot \left(\bar{\mathbf{I}} - \hat{k}_d\hat{k}_i\right) \cdot \sum_n H_n \tilde{\boldsymbol{\beta}}_n(\hat{k}_i) + \cdots \Bigg\} \\
&\quad -j\frac{k}{4\pi}\Bigg\{ \hat{k}_0 \times T_L^{FF}(kr_{mn'}) \sum_n E_n \tilde{\boldsymbol{\beta}}_n(\hat{k}_0) \\
&\quad + \sum_q \hat{k}_r \times \widetilde{A}_{R_q}(s_{R_q}) \bar{\mathbf{R}}_q^H T_L^{UTD}(kr_{Q_{R_q}n'}) \cdot \sum_n E_n \tilde{\boldsymbol{\beta}}_n(\hat{k}_i) \\
&\quad + \sum_v \hat{k}_d \times \widetilde{A}_{D_v}(s_{D_v}) \bar{\mathbf{D}}_v^H T_L^{UTD}(kr_{Q_{D_v}n'}) \cdot \sum_n E_n \tilde{\boldsymbol{\beta}}_n(\hat{k}_i) + \cdots \Bigg\} \\
&\quad + \mathbf{E}^{inc}(\mathbf{r}_m) \\
&\quad + \sum_q \widetilde{A}_{R_q}(s_{R_q}) \bar{\mathbf{R}}_q^E \cdot \mathbf{E}^{inc}(\mathbf{r}_{Q_{R_q}}) \\
&\quad + \sum_v \widetilde{A}_{D_v}(s_{D_v}) \bar{\mathbf{D}}_v^E \cdot \mathbf{E}^{inc}(\mathbf{r}_{Q_{D_v}}) + \cdots
\end{aligned}
\tag{D.15}
$$

and

$$
\begin{aligned}
&\mathbf{H}_{tot}(\mathbf{r}_m) = \\
&\quad -j\frac{k}{4\pi}\Bigg\{ \oiint \hat{k} \times e^{-j\mathbf{k}\cdot\mathbf{r}_{mm'}} T_L(\hat{k}\cdot\hat{r}_{m'n'}) \sum_n H_n \widetilde{\boldsymbol{\beta}}_n(\hat{k})\, d\hat{k}^2 \\
&\quad + \sum_q \hat{k}_r \times e^{-j\mathbf{k}_r\cdot\mathbf{r}_{mm'}} \widetilde{A}_{R_q}(s_{R_q}) \bar{\mathbf{R}}_q^E T_L^{UTD}(kr_{Q_{R_q}n'}) \cdot \sum_n H_n \widetilde{\boldsymbol{\beta}}_n(\hat{k}_i) \\
&\quad + \sum_v \hat{k}_d \times e^{-j\mathbf{k}_d\cdot\mathbf{r}_{mm'}} \widetilde{A}_{D_v}(s_{D_v}) \bar{\mathbf{D}}_v^E T_L^{UTD}(kr_{Q_{D_v}n'}) \cdot \sum_n H_n \widetilde{\boldsymbol{\beta}}_n(\hat{k}_i) + \cdots \Bigg\} \\
&\quad + j\frac{\omega\varepsilon}{4\pi}\Bigg\{ \oiint e^{-j\mathbf{k}\cdot\mathbf{r}_{mm'}} T_L(\hat{k}\cdot\hat{r}_{m'n'}) \left(\bar{\mathbf{I}} - \hat{k}\hat{k}\right) \cdot \sum_n E_n \widetilde{\boldsymbol{\beta}}_n(\hat{k})\, d\hat{k}^2 \\
&\quad + \sum_q e^{-j\mathbf{k}_r\cdot\mathbf{r}_{mm'}} \widetilde{A}_{R_q}(s_{R_q}) \bar{\mathbf{R}}_q^H T_L^{UTD}(kr_{Q_{R_q}n'}) \cdot \left(\bar{\mathbf{I}} - \hat{k}_r\hat{k}_i\right) \cdot \sum_n E_n \widetilde{\boldsymbol{\beta}}_n(\hat{k}_i) \\
&\quad + \sum_v e^{-j\mathbf{k}_d\cdot\mathbf{r}_{mm'}} \widetilde{A}_{D_v}(s_{D_v}) \bar{\mathbf{D}}_v^H T_L^{UTD}(kr_{Q_{D_v}n'}) \cdot \left(\bar{\mathbf{I}} - \hat{k}_d\hat{k}_i\right) \cdot \sum_n E_n \widetilde{\boldsymbol{\beta}}_n(\hat{k}_i) \\
&\quad + \cdots \Bigg\} \\
&\quad -j\frac{k}{4\pi}\Bigg\{ \hat{k}_0 \times T_L^{FF}(kr_{mn'}) \sum_n H_n \widetilde{\boldsymbol{\beta}}_n(\hat{k}_0) \\
&\quad + \sum_q \hat{k}_r \times \widetilde{A}_{R_q}(s_{R_q}) \bar{\mathbf{R}}_q^E T_L^{UTD}(kr_{Q_{R_q}n'}) \cdot \sum_n H_n \widetilde{\boldsymbol{\beta}}_n(\hat{k}_i) \\
&\quad + \sum_v \hat{k}_d \times \widetilde{A}_{D_v}(s_{D_v}) \bar{\mathbf{D}}_v^E T_L^{UTD}(kr_{Q_{D_v}n'}) \cdot \sum_n H_n \widetilde{\boldsymbol{\beta}}_n(\hat{k}_i) + \cdots \Bigg\} \\
&\quad + j\frac{\omega\varepsilon}{4\pi}\Bigg\{ T_L^{FF}(kr_{mn'}) \left(\bar{\mathbf{I}} - \hat{k}_0\hat{k}_0\right) \cdot \sum_n E_n \widetilde{\boldsymbol{\beta}}_n(\hat{k}_0) \\
&\quad + \sum_q \widetilde{A}_{R_q}(s_{R_q}) \bar{\mathbf{R}}_q^H T_L^{UTD}(kr_{Q_{R_q}n'}) \cdot \left(\bar{\mathbf{I}} - \hat{k}_r\hat{k}_i\right) \cdot \sum_n E_n \widetilde{\boldsymbol{\beta}}_n(\hat{k}_i) \\
&\quad + \sum_v \widetilde{A}_{D_v}(s_{D_v}) \bar{\mathbf{D}}_v^H T_L^{UTD}(kr_{Q_{D_v}n'}) \cdot \left(\bar{\mathbf{I}} - \hat{k}_d\hat{k}_i\right) \cdot \sum_n E_n \widetilde{\boldsymbol{\beta}}_n(\hat{k}_i) + \cdots \Bigg\} \\
&\quad + \mathbf{H}^{inc}(\mathbf{r}_m) \\
&\quad + \frac{1}{Z}\hat{k}_r \times \mathbf{E}^{r,inc}(\mathbf{r}_m) \\
&\quad + \frac{1}{Z}\hat{k}_d \times \mathbf{E}^{d,inc}(\mathbf{r}_m) + \cdots ,
\end{aligned}
\tag{D.16}
$$

respectively.

Bibliography

[1] R. Mittra, *Computer Techniques for Electromagnetics,* Pergamon Press, New York, 1973.

[2] R. Mittra, *Numerical and Asymptotic Techniques in Electromagnetics,* Springer Verlag, New York, 1975.

[3] N.K. Uzunoglou, K.S. Nikita, D.I. Kaklamani, *Applied Computational Electromagnetics: State of the Art and Future Trends,* Springer Verlag, Berlin, 1997.

[4] W.C. Chew, J.-M. Jin, E. Michielssen, *Fast and Efficient Algorithms in Computational Electromagnetics,* Artech House, Boston, 2001.

[5] T.F. Eibert, *Numerische Berechnung von Antennen und Streuproblemen,* Skriptum zur Vorlesung, TU Darmstadt, 2002.

[6] V.A. Fock, *Electromagnetic Diffraction and Propagation Problems,* ch. 11-14, Pergamon Press, New York, 1965.

[7] G.D. Dockery, "Modeling electromagnetic wave propagation in the troposphere using the parabolic equation," *IEEE Trans. Antennas Propagat.,* vol. 36, no. 10, pp. 1464-1470, Oct. 1988.

[8] A.E. Barrios, "Parabolic equation modeling in horizontally inhomogeneous environments," *IEEE Trans. Antennas Propagat.,* vol. 40, no. 7, pp. 791-797, July 1992.

[9] J.A. Stratton, *Electromagnetic Theory,* McGraw-Hill, Inc., New York, 1941.

[10] K.S. Yee, "Numerical solution of initial boundary value problems involving Maxwell's equations in isotropic media," *IEEE Trans. Antennas Propagat.,* vol. 14, no. 3, pp. 302-307, May 1966.

[11] A. Taflove, *Computational Electrodynamics: The Finite Difference Time Domain Method,* Artech House, Boston, 1995. Springer Verlag, Berlin, 1997.

[12] R. Holland, V.P. Cable, and L.C. Wilson, "Finite-volume time-domain (FVTD) techniques for EM scattering," *IEEE Trans. Electromagn. Compat.,* vol. 33, no. 4, pp. 281-294, Nov. 1991s.

[13] K.S. Yee and J.S. Chen, "The finite-difference time-domain (FDTD) and the finite-volume time-domain (FVTD) methods in solving Maxwell's equations," *IEEE Trans. Antennas Propagat.,* vol. 45, no. 3, pp. 354-363, Mar. 1997.

[14] T. Weiland, "Eine Methode zur Lösung der Maxwellschen Gleichungen für sechskomponentige Felder auf diskreter Basis," *Archiv für Elektronik und Übertragungstechnik (AEÜ),* vol. 31, pp. 116-120, May 1977.

[15] P.P. Silvester, R.L. Ferrari, *Finite Elements for Electrical Engineers,* 2nd Ed., Cambridge University Press, New York, 1990.

[16] J.-M. Jin, *The Finite Element Method in Electromagnetics,* 2nd Ed., John Wiley & Sons, Inc., New York, 2002.

[17] J.L. Volakis, A. Chatterjee, L.-C. Kempel, *Finite Element Method for Electromagnetics,* IEEE Press, Inc., New York, 1998.

[18] R.F. Harrington, *Field Computation by Moment Methods,* The Macmillan Company, New York, 1968.

[19] S.M. Rao, D.R. Wilton, and A.W. Glisson, "Electromagnetic scattering by surfaces of arbitrary shape," *IEEE Trans. Antennas Propagat.,* vol. 30, no. 3, pp. 409-418, May 1982.

[20] R. Gomez Martin, A. Salinas, and A. Rubio Bretones, "Time-domain integral equation methods for transient analysis," *IEEE Antennas Propagat. Mag.,* vol. 34, no. 3, pp. 15-23, June 1992.

[21] E. Bleszynski, M. Bleszynski, and T. Jaroszewicz, "AIM: Adaptive integral method for solving large scale electromagnetic scattering and radiation problems," *Radio Science,* vol. 31, pp. 1225-1251, 1996.

[22] S.D. Gedney, A. Zhu, W.-H. Tang, G. Liu, and P. Petre, "A fast high-order quadrature sampled pre-corrected FFT for electromagnetic scattering," *Microwave Opt. Technology Letters,* vol. 36, no. 5, pp. 343-349, Mar. 2003.

[23] R. Coifman, V. Rokhlin, and S. Wandzura, "The fast multipole method: A pedestrian prescription," *IEEE Antennas Propagat. Mag.,* vol. 35, no. 3, pp. 7-12, June 1993.

[24] J.M. Song and W.C. Chew, "Multilevel fast-multipole algorithm for solving combined field integral equations of electromagnetic scattering," *Microwave Opt. Technology Letters,* vol. 10, no. 1, pp. 14-19, Sep. 1995.

[25] J. Song, C-C. Lu, and W.C. Chew, "Multilevel Fast Multipole Algorithm for Electromagnetic Scattering by Large Complex Objects," *IEEE Trans. Antennas Propagat.,* vol. 45, no. 10, pp. 1488-1493, Oct. 1997.

[26] T.F. Eibert, "A diagonalized multilevel fast multipole method with spherical harmonics expansion of the k-space integrals," *IEEE Trans. Antennas Propagat.,* vol. 53, no. 2, pp. 814-817, Feb. 2005.

[27] C.A. Balanis, *Advanced Engineering Electromagnetics,* John Wiley & Sons, Inc., New York, 1989.

[28] Y.T. Lo and S.W. Lee, *Antenna Handbook Vol.1,* Chapman & Hall, New York, 1993.

[29] J.B. Keller, "Geometrical theory of diffraction," *J. Opt. Soc. America,* vol. 52, no. 2, pp. 116-130, Feb. 1962.

[30] R.G. Kouyoumjian and P.R. Pathak, "A uniform geometrical theory of diffraction for an edge in a perfectly conducting surface," *Proc. IEEE,* vol. 62, no. 11, pp. 1448-1461, Nov. 1974.

[31] P.R. Pathak, "High-frequency techniques for antenna analysis," *Proc. IEEE,* vol. 80, no. 1, pp. 44-65, Jan. 1992.

[32] P.R. Rousseau and P.H. Pathak, "Time-domain uniform geometrical theory of diffraction for a curved wedge," *IEEE Trans. Antennas Propagat.,* vol. 43, no. 12, pp. 1375-1382, Dec. 1995.

[33] P.Ya. Ufimtsev, "Method for edge waves in the physical theory of diffraction," (from the Russian "Metod krayevykh voln v fizicheskoy teorii difratsii," *Izd-vo Sov. Radio,* pp. 1-243, 1962), translation by the U.S. Air Force Foreign Technology Division, Wright-Patterson, Ohio, Sep. 1971.

[34] E.F. Knott and T.B.A. Senior, "Comparison of three high-frequency diffraction techniques," *Proc. IEEE,* vol. 62, no. 11, pp. 1468-1474, Nov. 1974.

[35] A. Michaeli, "Equivalent edge currents for arbitrary aspects of observation," *IEEE Trans. Antennas Propagat.,* vol. 32, no. 3, pp. 252-258, Mar. 1984.

[36] J.-M. Jin and J.L. Volakis, "A finite element-boundary integral formulation for scattering by three-dimensional cavity-backed apertures," *IEEE Trans. Antennas Propagat.,* vol. 39, no. 1, pp. 97-104, Jan. 1991.

[37] T.F. Eibert, *Verknüpfung der Methode der Finiten Elemente mit einem Integralgleichungsverfahren für ebene geschichtete Strukturen,* Dissertation, Universität Wuppertal, 1997.

[38] T. Eibert and V. Hansen, "Calculation of unbounded field problems in free space by a 3D FEM/BEM-hybrid approach," *J. Electromag. Waves Applicat.,* vol. 10, no. 1, pp. 61-78, Jan. 1996.

[39] T.F. Eibert and V. Hansen, "3D FEM/BEM-hybrid approach based on a general formulation of Huygens' principle for planar layered media," *IEEE Trans. Microwave Theory Tech.,* vol. 45, no. 7, pp. 1105-1112, July 1997.

[40] T.F. Eibert and V. Hansen, "3D FEM/BEM-hybrid modeling of surface mounted devices within planar circuits," *IEEE Trans. Microwave Theory Tech.,* vol. 46, no. 9, pp. 1334-1336, Sep. 1998.

[41] T.F. Eibert, "Modelling of integrated antenna - scatterer configurations by hybrid finite element - boundary integral - multilevel fast multipole methods," *Progress in Electromagn. Research Symposium,* Pisa, 2004.

[42] K.S. Yee and J.S. Chen, "Impedance boundary condition simulation in the FDTD/FVTD hybrid," *IEEE Trans. Antennas Propagat.,* vol. 45, no. 6, pp. 921-925, June 1997.

[43] M. Yang, Y. Chen, and R. Mittra, "Hybrid finite-difference/finite-volume time-domain analysis for microwave integrated circuits with curved PEC surfaces using a nonuniform rectangular grid," *IEEE Trans. Microwave Theory Tech.,* vol. 48, no. 6, pp. 969-975, June 1997.

[44] A. Taflove and K. Umashankar, "A hybrid moment method/finite-difference time-domain approach to electromagnetic coupling and aperture penetration into complex geometries," *IEEE Trans. Antennas Propagat.,* vol. 30, no. 4, pp. 617-627, July 1982.

[45] H. Rogier, F. Olyslager, and D. De Zutter, "A new hybrid FDTD-BIE approach to model electromagnetic scattering problems," *IEEE Microwave Guided Wave Lett.,* vol. 8, no. 3, pp. 138-140, Mar. 1998.

[46] Z. Huang, K.R. Demarest, and R.G. Plumb, "An FDTD/MoM hybrid technique for modeling complex antennas in the presence of heterogeneous grounds," *IEEE Geosience and Remote Sensing,* vol. 37, pp. 2692-2698, Nov. 1999.

[47] J.E. Wheeler and D.R. Wilton, "A hybrid FIT/MoM approach for EM analysis involving penetrable objects," *Proc. IEEE Antennas and Propagat. Symp.,* vol. 4, pp. 1762-1765, 1992.

[48] A. Becker and V. Hansen, "A hybrid method combining the FDTD and the time domain boundary-integral equation marching-on-in-time algorithm," *Advances in Radio Science,* vol. 1, pp. 99-104, 2003.

[49] F. Weinmann, "Ray tracing with PO/PTD for RCS modeling of large complex objects," *IEEE Trans. Antennas Propagat.,* vol. 54, no. 6, pp. 1797-1806, June 2006.

[50] F. Weinmann, "Scattering simulations with GO/UTD-PO/PTD ray tracing," *URSI International Symposium on Electromagnetic Theory,* Ottawa, July 2007.

[51] G.A. Thiele and T.H. Newhouse, "A hybrid technique for combining moment methods with the geometrical theory of diffraction," *IEEE Trans. Antennas Propagat.,* vol. 23, no. 1, pp. 62-69, Jan. 1975.

[52] J.N. Sahalos and G.A. Thiele, "On the application of the GTD-MM technique and its limitations," *IEEE Trans. Antennas Propagat.,* vol. 29, no. 5, pp. 780-786, Sep. 1981.

[53] L.W. Henderson and G.A. Thiele, "A hybrid MM-geometrical optics technique for the treatment of wire antennas mounted on a curved surface," *IEEE Trans. Antennas Propagat.,* vol. 30, no. 6, pp. 1257-1261, Nov. 1982.

[54] S. Srikanth, P.H. Pathak, and C.W. Chuang, "Hybrid UTD-MM analysis of the scattering by a perfectly conducting semicircular cylinder," *IEEE Trans. Antennas Propagat.,* vol. 34, no. 10, pp. 1250-1257, Oct. 1986.

[55] G.A. Thiele, "Overview of selected hybrid methods in radiating system analysis," *Proc. IEEE,* vol. 80, no. 1, pp. 66-78, Jan. 1992.

[56] W.L. Stutzman, G.A. Thiele, *Antenna Theory and Design,* John Wiley & Sons, Inc., New York, 1981.

[57] L.M. Medgyesi-Mitschang and D.-S. Wang, "Hybrid methods in computational electromagnetics: A Review," *Computer Phys. Commun.,* vol. 68, pp. 76-94, 1991.

[58] D.P. Bouche, F.A. Molinet, and R. Mittra, "Asymptotic and hybrid techniques for electromagnetic scattering," *Proc. IEEE,* vol. 81, pp. 1658-1684, Dec. 1993.

[59] U. Jakobus and F.M. Landstorfer, "Improved PO-MoM hybrid formulation for scattering from three-dimensional perfectly conducting bodies of arbitrary shape," *IEEE Trans. Antennas Propagat.,* vol. 43, no. 2, pp. 162-169, Feb. 1995.

[60] U. Jakobus and F.M. Landstorfer, "Improvement of the PO-MoM hybrid method by accounting for effects of perfectly conducting wedges," *IEEE Trans. Antennas Propagat.,* vol. 43, no. 10, pp. 1123-1129, Oct. 1995.

[61] I.P. Theron, D.B. Davidson, and U. Jakobus, "Extensions to the hybrid method of moments/uniform GTD formulation for sources located close to a smooth convex surface," *IEEE Trans. Antennas Propagat.,* vol. 48, no. 6, pp. 940-945, July 2000.

[62] T. Özdemir, M.W. Nurnberger, and J.L. Volakis, "A hybridization of finite-element with high-frequency methods for pattern prediction for antennas on aircraft structures," *IEEE Antennas Propagat. Mag.,* vol. 38, no. 3, pp. 28-38, June 1996.

[63] A. Skarlatos, R. Schuhmann, and T. Weiland, "Simulation of scattering problems in time domain using a hybrid FDTD-UTD formulation," *Proc. of the ACES,* pp. 377-382, Monterey, Mar. 2003.

[64] A. Becker and V. Hansen, "A hybrid method combining an efficient TD-MoM with the TD-UTD," *Proc. URSI Intern. Symposium on Electromagn. Theory,* pp. 1245-1247, May 2004.

[65] A. Becker and V. Hansen, "Hybrid$^{(3)}$: Combining the time-domain method of moments, the time-domain geometrical theory of diffraction and the FDTD," *Proc. IEEE Antennas and Propagat. Symp.,* Washington, D.C., July 2005.

[66] A. Becker and V. Hansen, "A hybrid method combining the multitemporal resolution time-domain method of moments with the time-domain geometrical theory of diffraction for thin-wire antenna problems," *IEEE Trans. Antennas Propagat.,* vol. 54, no. 3, pp. 953-960, Mar. 2006.

[67] A. Skarlatos, *Coupling the Finite Integration Technique with the Uniform Geometrical Theory of Diffraction,* Ph.D. dissertation, Technische Universität Darmstadt, 2003.

[68] A. Skarlatos, R. Schuhmann, and T. Weiland, "Solution of radiation and scattering problems in complex environments using a hybrid finite integration technique- uniform theory of diffraction approach," *IEEE Trans. Antennas Propagat.,* vol. 53, no. 10, pp. 3347-3357, Oct. 2005.

[69] M. Alaydrus, V. Hansen, and T.F. Eibert, "Hybrid^2: Combining the three-dimensional hybrid finite element - boundary integral technique for planar multilayered media with the uniform geometrical theory of diffraction," *IEEE Trans. Antennas Propagat.,* vol. 50, no. 1, pp. 67-74, Jan. 2002.

[70] A. Tzoulis and T.F. Eibert, "A hybrid FEBI-MLFMM-UTD method for numerical solutions of electromagnetic problems including arbitrarily shaped and electrically large objects," *IEEE Trans. Antennas Propagat.,* vol. 53, no. 10, pp. 3358-3366, Oct. 2005.

[71] A. Tzoulis and T.F. Eibert, "Hybridization of multilevel fast multipole method and uniform geometrical theory of diffraction for radiation and scattering computations," *Proc. IEEE Antennas and Propagat. Symp.,* Washington, D.C., July 2005.

[72] A. Tzoulis and T.F. Eibert, "Combining the multilevel fast multipole method with the uniform geometrical theory of diffraction," *Advances in Radio Science,* vol. 3, pp. 183-188, 2005.

[73] T.F. Eibert and A. Tzoulis, "The hybrid finite element - boundary integral - multilevel fast multipole - uniform geometrical theory of diffraction method," *XXIX General Assembly of the URSI,* Invited, New Delhi, Oct. 2005.

[74] A. Tzoulis and T.F. Eibert, "Efficient electromagnetic near-field computation by the multilevel fast multipole method employing mixed near-field/far-field translations," *IEEE Antennas Wireless Propag. Lett.,* vol. 4, pp. 449-452, 2005.

[75] A. Tzoulis and T.F. Eibert, "Fast computation of electromagnetic near-fields with the multilevel fast multipole method combining near-field and far-field translations," *Advances in Radio Science,* vol. 4, pp. 111-115, 2006.

[76] T.F. Eibert and A. Tzoulis, "On the formulation of the 3D hybrid finite element - boundary integral technique: ... Still the old one: formulation, solution, results," *8th International Workshop on Finite Elements for Microwave Engineering,* Stellenbosch, May 2006.

[77] T.F. Eibert, A. Tzoulis and T. Vaupel, "Radar cross section modeling results obtained by the hybrid finite element - boundary integral technique," *1st Antenna Measurement Techniques Association Europe Symposium,* Munich, May 2006.

[78] T.F. Eibert and A. Tzoulis, "Some large-scale scattering and near-field results computed by the hybrid finite element - boundary integral - multilevel fast multipole method," *Proc. IEEE Antennas and Propagat. Symp.,* Albuquerque, July 2006.

[79] A. Tzoulis and T.F. Eibert, "Antenna modeling with the hybrid finite element - boundary integral - multilevel fast multipole - uniform geometrical theory of diffraction method," *2nd International ITG Conference on Antennas,* Munich, March 2007.

[80] A. Tzoulis and T.F. Eibert, "Advances in hybrid finite element - boundary integral - multilevel fast multipole - uniform geometrical theory of diffraction method," *Advances in Radio Science,* vol. 5, pp. 101-106, 2007.

[81] A. Tzoulis, T. Vaupel, and T.F. Eibert, "Computation of scattered far-fields in fast hybrid finite element - boundary integral - ray optical method," *URSI International Symposium on Electromagnetic Theory,* Ottawa, July 2007.

[82] T.F. Eibert, H. Buddendick, M.M. Leibfritz, C.S. Schmidt, and A. Tzoulis, "Hybrid electromagnetic field characterization involving high-frequency field representations," *URSI International Symposium on Electromagnetic Theory,* Invited, Ottawa, July 2007.

[83] A. Tzoulis, T. Vaupel, and T.F. Eibert, "Far-field scattering with fast hybrid integral equation based - ray optical method," *2nd European Conference on Antennas and Propagation,* Edinburgh, Nov. 2007.

[84] A. Tzoulis, T. Vaupel, and T.F. Eibert, "Ray optical electromagnetic far-field scattering computations using planar near-field scanning techniques," *IEEE Trans. Antennas Propagat.,* vol. 56, no. 2, pp. 461-468, Feb. 2008.

[85] A. Tzoulis and T.F. Eibert, "Computations for various edge configurations with the hybrid finite element - boundary integral - multilevel fast multipole - uniform geometrical theory of diffraction method including double diffraction," *1st European Conference on Antennas and Propagation,* Nice, Nov. 2006.

[86] A. Tzoulis, Ismatullah, and T.F. Eibert, "Fast multipole accelerated hybrid finite element - boundary integral - ray-optical method including double diffractions," *Electromagnetics,* vol. 28, no. 1, pp. 109-122, Jan. 2008.

[87] R.F. Harrington, *Time-Harmonic Electromagnetic Fields,* McGraw-Hill, Inc., New York, 1961.

[88] S.A. Schelkunoff, "Kirchhoff's formula, its vector analogue, and other field equivalent theorems," *Comm. Pure Appl. Math.,* vol. 4, pp. 43-59, June 1951.

[89] A.E.H. Love, "The integration of the equations of propagation of electric waves," *Phil. Trans. Roy. Soc. London,* vol. 197, ser. A, pp. 1-45, 1901.

[90] K.-M. Chen, "A mathematical formulation of the equivalence principle," *IEEE Trans. Microwave Theory Tech.,* vol. 37, no. 10, pp. 1576-1581, Oct. 1989.

[91] J.C. Monzon, "On surface integral representation: Validity of Huygens' principle and the equivalence principle in inhomogeneous bianisotropic media," *IEEE Trans. Microwave Theory Tech.,* vol. 41, no. 11, pp. 1995-2001, Nov. 1993.

[92] Q.-X. Chu and C.-H. Liang, "The uniqueness theorem of electromagnetic fields in lossless regions," *IEEE Trans. Antennas Propagat.,* vol. 41, no. 2, pp. 245-246, Feb. 1993.

[93] C.A. Balanis, *Antenna Theory, Analysis and Design,* John Wiley & Sons, Inc., New York, 1982.

[94] A.F. Peterson, "The 'interior resonance' problem associated with surface integral equations of electromagnetics: Numerical consequences and a survey of remedies," *Electromagnetics,* vol. 10, no. 3, pp. 293-312, July 1990.

[95] J.R. Mautz and R.F. Harrington, "*H*-field, *E*-field, and combined-field solutions for conducting bodies of revolution," *Int. J. Electron. Commun. (AEÜ),* vol. 32, no. 4, pp. 157-164, April 1978.

[96] J.D. Collins, J.-M. Jin, and J.L. Volakis, "Eliminating interior resonances in finite element-boundary integral methods for scattering," *IEEE Trans. Antennas Propagat.,* vol. 40, no. 12, pp. 1583-1585, Dec. 1992.

[97] A.D. Yaghjian, "Augmented electric and magnetic field integral equations," *Radio Science,* vol. 16, no. 6, pp. 987-1001, Nov. 1981.

[98] J.C. Monzon and N.J. Damaskos, "A scheme for eliminating internal resonances: The parasitic body technique," *IEEE Trans. Antennas Propagat.,* vol. 42, no. 8, pp. 1089-1096, Aug. 1994.

[99] A.F. Peterson and K.R. Aberegg, "Parametric mapping of vector basis functions for surface integral equation formulations," *ACES Journal,* vol. 10, no. 3, pp. 107-115, Nov. 1993.

[100] D.R. Wilton, S.M. Rao, A.W. Glisson, D.H. Schaubert, O.M. Al-Bundak, and C.M. Butler, "Potential integrals for uniform and linear source distributions on polygonal and polyhedral domains," *IEEE Trans. Antennas Propagat.,* vol. 32, no. 3, pp. 276-281, Mar. 1984.

[101] R.D. Graglia, "On the numerical integration of the linear shape functions times the 3-D Greens function or its gradient on a Plane triangle," *IEEE Trans. Antennas Propagat.,* vol. 41, no. 10, pp. 1448-1455, Oct. 1993.

[102] T.F. Eibert and V. Hansen, "On the calculation of potential integrals for linear source distributions on triangular domains," *IEEE Trans. Antennas Propagat.,* vol. 43, no. 12, pp. 1499-1502, Dec. 1995.

[103] D. Sievers, T.F. Eibert and V. Hansen, "Correction to 'On the calculation of potential integrals for linear source distributions on triangular domains'," *IEEE Trans. Antennas Propagat.,* vol. 53, no. 9, pp. 3113-3113, Sep. 2005.

[104] P. Ylä-Oijala and M. Taskinen, "Calculation of CFIE impedance matrix elements with RWG and $n\times$RWG functions," *IEEE Trans. Antennas Propagat.,* vol. 51, no. 8, pp. 1837-1846, Aug. 2003.

[105] M.G. Duffy, "Quadrature over a pyramide or cube of integrands with a singularity at a vertex," *SIAM J. Numer. Anal.,* vol. 19, no. 6, pp. 1260-1262, 1982.

[106] M.A. Khayat and D.R. Wilton, "Numerical evaluation of singular and near-singular potential integrals," *IEEE Trans. Antennas Propagat.,* vol. 53, no. 10, pp. 3180-3190, Oct. 2005.

[107] Ismatullah and T.F. Eibert, "Adaptive singularity cancellation for efficient treatment of near-singular and near-hypersingular integrals in surface integral equation formulations," *IEEE Trans. Antennas Propagat.,* vol. 56, no. 1, pp. 274-278, Jan. 2008.

[108] A. Herschlein, J. v. Hagen and W. Wiesbeck "Methods for the evaluation of regular, weakly singular and strongly singular surface reaction integrals arising in method of moments," *ACES Journal,* vol. 17, no. 1, pp. 63-73, Mar. 2002.

[109] A. Tzoulis and T.F. Eibert, "Review of singular potential integrals for method of moments solutions of surface integral equations," *Advances in Radio Science,* vol. 2, pp. 93-99, 2004.

[110] A. Konrad, "Vector variational formulation of electromagnetic fields in anisotropic media," *IEEE Trans. Microwave Theory Tech.,* vol. 24, no. 9, pp. 553-559, Sep. 1976.

[111] G. Jeng and A. Wexler, "Self-adjoint variational formulation of problems having non-self-adjoint operators," *IEEE Trans. Microwave Theory Tech.,* vol. 26, no. 2, pp. 91-94, Feb. 1978.

[112] C.H. Chen and C.-D. Lien, "The variational principle for non-self-adjoint electromagnetic problems," *IEEE Trans. Microwave Theory Tech.,* vol. 28, no. 8, pp. 878-886, Aug. 1980.

[113] R. Dyczij-Edlinger and O. Biro, "A joint vector and scalar potential formulation for driven high frequency problems using hybrid edge and nodal finite elements," *IEEE Trans. Microwave Theory Tech.*, vol. 44, no. 1, pp. 15-23, Jan. 1996.

[114] R. Dyczij-Edlinger, G. Peng, and J.-F. Lee, "A fast vector-potential method using tangentially continuous vector finite elements," *IEEE Trans. Microwave Theory Tech.*, vol. 46, no. 6, pp. 863-868, Jan. 1996.

[115] A. Bossavit and I. Mayergoyz, "Edge-elements for scattering problems," *IEEE Trans. Magn.*, vol. 25, no. 4, pp. 2816-2821, July 1989.

[116] J.-F. Lee, D.-K. Sun, and Z.J. Cendes, "Full-wave analysis of dielectric waveguides using tangential vector finite elements," *IEEE Trans. Microwave Theory Tech.*, vol. 39, no. 8, pp. 1262-1271, Aug. 1991.

[117] Z.J. Cendes, "Vector finite elements for electromagnetic field computation," *IEEE Trans. Magn.*, vol. 27, no. 5, pp. 3958-3966, Sep. 1991.

[118] J.P. Webb, "Edge elements and what they can do for you," *IEEE Trans. Magn.*, vol. 29, no. 2, pp. 1460-1465, Mar. 1993.

[119] D. Sun, J. Manges, X. Yuan, and Z. Cendes, "Spurious modes in finite-element methods," *IEEE Antennas Propagat. Mag.*, vol. 37, no. 5, pp. 12-24, Oct. 1995.

[120] S.H. Wong and Z.J. Cendes, "Combined finite element-modal solution of three-dimensional eddy current problems," *IEEE Trans. Magn.*, vol. 24, no. 6, pp. 2685-2687, Nov. 1988.

[121] J.M. Jin, J.L. Volakis, C.L. Yu and A.C. Woo, "Modeling of resistive sheets in finite element solutions," *IEEE Trans. Antennas Propagat.*, vol. 40, no. 6, pp. 727-731, June 1992.

[122] H. Xiao-Xiang and X. Jin-Ping, "IBC/FEM analysis of electromagnetic scattering of cavities coated with layered medium," *Front. Electr. Electron. Eng. China*, vol. 1, no. 1, pp. 88-91, Jan. 2006.

[123] T.B.A. Senior, J.L. Volakis, *Approximate Boundary Conditions in Electromagnetics*, IEE Press, London, 1995.

[124] J.M. Jin, J.L. Volakis and V.V. Liepa, "A fictitious absorber for truncating finite element meshes in scattering," *IEE Proc. H*, vol. 139, pp. 472-476, Oct. 1992.

[125] J.-B. Berenger, "A perfectly matched layer for the absorption of electromagnetic waves," *J. Comput. Phys.*, vol. 114, no. 2, pp. 185-200, Feb. 1994.

[126] W.C. Chew and W.H. Weedon, "A 3D perfectly matched medium from modified Maxwell's equations with stretched coordinates," *Microwave Opt. Technology Letters*, vol. 7, pp. 599-604, 1994.

[127] Y. Saad, *Iterative Methods for Sparse Linear Systems*, 2nd Ed., Jan. 2000.

[128] T.F. Eibert, "Iterative near-zone preconditioning of iterative method of moments electric field integral equation solutions," *IEEE Antennas Wireless Propag. Lett.*, vol. 2, pp. 101-102, 2003.

[129] A. Herschlein, *Entwicklung numerischer Verfahren zur Feldberechnung konformer Antennen auf Oberflächen höherer Ordnung,* Dissertation, Universität Karlsruhe, 2002.

[130] X.-Q. Sheng, J.-M. Jin, J. Song, C.-C. Lu, and W.C. Chew, "On the formulation of hybrid finite-element and boundary-integral methods for 3-D scattering," *IEEE Trans. Antennas Propagat.,* vol. 46, no. 3, pp. 303-311, Mar. 1998.

[131] T.F. Eibert and V. Hansen, "Comments on 'On the formulation of hybrid finite-element and boundary-integral methods for 3-D scattering'," *IEEE Trans. Antennas Propagat.,* vol. 48, no. 1, pp. 129-129, Jan. 2000.

[132] L. Greengard and V. Rokhlin, "A fast algorithm for particle simulations," *J. Comput. Phys.,* vol. 73, no. 12, pp. 325-348, Dec. 1987.

[133] V. Rokhlin, "Rapid solution of integral equations of scattering theory in two dimensions," *J. Comput. Phys.,* vol. 86, no. 2, pp. 414-419, Feb. 1990.

[134] N. Engheta, W.D. Murphy, V. Rokhlin, and M.S. Vassiliou, "The fast multipole method (FMM) for electromagnetic scattering problems," *IEEE Trans. Antennas Propagat.,* vol. 40, no. 6, pp. 634-641, June 1992.

[135] J.M. Song and W.C. Chew, "Fast multipole method solution using parametric geometry," *Microwave Opt. Technology Letters,* vol. 7, no. 16, pp. 760-765, Nov. 1994.

[136] G.V. Eleftheriades and J.R. Mosig "On the network characterization of planar passive circuits using the method of moments," *IEEE Trans. Microwave Theory Tech.,* vol. 44, no. 3, pp. 438-445, Mar. 1996.

[137] M. Abramowitz, I.A. Stegun, *Handbook of Mathematical Functions,* 9th Ed., Dover Publications, Inc., New York, 1972.

[138] W.C. Chew, "Computational electromagnetics - the physics of smooth kernel versus oscillatory kernel, and wavelets versus fast multipole," Plenary Invited Talk, *18th Annual Review of Progress in Applied Computational Electromagnetics,* Monterey, Mar. 2002.

[139] V. Rokhlin, "Diagonal forms of translation operators for the Helmholtz equation in three dimensions," *Appl. Comp. Harmonic Analysis,* no. 1, pp. 82-93, 1993.

[140] M.A. Epton and B. Dembart, "Multipole translation theory for the three-dimensional Laplace and Helmholtz equations," *SIAM J. Sci. Comput.,* vol. 16, no. 4, pp. 865-897, July 1995.

[141] W.C. Chew, S. Koc, J.M. Song, C.C. Lu, and E. Michielssen, "A succinct way to diagonalize the translation matrix in three dimensions," *Microwave Opt. Technology Letters,* vol. 15, pp. 144-147, 1997.

[142] S. Koc, J. Song, and W.C. Chew, "Error analysis for the numerical evaluation of the diagonal forms of the scalar spherical addition theorem," *SIAM J. Numer. Anal.,* vol. 36, no. 3, pp. 906-921, 1999.

[143] W.C. Chew, T.J. Cui, and J.M. Song, "A FAFFA-MLFMA algorithm for electromagnetic scattering," *IEEE Trans. Antennas Propagat.,* vol. 50, no. 11, pp. 1641-1649, Nov. 2002.

[144] R.M. Luneberg, *Mathematical Theory of Optics,* Brown University Notes, Providence, RI, 1944.

[145] M. Kline, "An asymptotic solution of Maxwell's equations," *Comm. Pure Appl. Math.,* vol. 4, pp. 225-262, June 1951.

[146] A. Kline and J. Runge, "Anwendung der Vektorrechnung auf die Grundlagen der geometrischen Optik," *Ann. Phys.,* vol. 35, pp. 277-298, 1911.

[147] D.A. McNamara, C.W.I. Pistorius, J.A.G. Malherbe, *Introduction to the Uniform Geometrical Theory of Diffraction,* Artech House, Boston, 1990.

[148] M. Alaydrus and V. Hansen, "Higher order mechanisms and coupling in the hybrid^2 method for calculating near and far fields of complex composite radiating structures," *Proc. IEEE Antennas and Propagat. Symp.,* Salt Lake City, July 2000.

[149] W.D. Burnside and K.W. Burgener, "High-frequency scattering by a thin lossless dielectric slab," *IEEE Trans. Antennas Propagat.,* vol. 31, no. 1, pp. 104-110, Jan. 1983.

[150] R. Tiberio, G. Pelosi, and G. Manara, "A uniform GTD formulation for the diffraction by a wedge with impedance faces," *IEEE Trans. Antennas Propagat.,* vol. 33, no. 8, pp. 867-873, Aug. 1985.

[151] J.L. Volakis, "A uniform geometrical theory of diffraction for an imperfectly conducting half-plane," *IEEE Trans. Antennas Propagat.,* vol. 34, no. 2, pp. 172-180, Feb. 1986.

[152] J.L. Volakis, "Revision of figures in 'A uniform geometrical theory of diffraction for an imperfectly conducting half-plane'," *IEEE Trans. Antennas Propagat.,* vol. 35, no. 6, pp. 742-744, June 1987.

[153] J.L. Volakis and T.B.A. Senior, "Diffraction by a thin dielectric half-plane," *IEEE Trans. Antennas Propagat.,* vol. 35, no. 12, pp. 1483-1487, Dec. 1987.

[154] O.M. Buyukdura, *Radiation from Sources and Scatterers Near the Edge of a Perfectly Conducting Wedge,* Ph.D. dissertation, Ohio State University, 1984.

[155] T.J. Cui, W.C. Chew, G. Chen, and J.M. Song, "Efficient MLFMA, RPFMA, and FAFFA algorithms for EM scattering by very large structures," *IEEE Trans. Antennas Propagat.,* vol. 52, no. 3, pp. 759-770, Mar. 2004.

[156] U. Jakobus, *Intelligente Kombination verschiedener numerischer Berechnungsverfahren zur effizienten Analyse elektromagnetischer Streuprobleme unter besonderer Berücksichtigung der Parallelverarbeitung,* Habilitationsschrift, Universität Stuttgart, 1999.

[157] F. Weinmann, *EMV bei der Nutzung elektrischer Energieverteilnetze als Kommunikationsmedium,* Dissertation, Universität Karlsruhe, 2003.

[158] R. Tiberio, G. Manara, G. Pelosi, and R.G. Kouyoumjian, "High-frequency electromagnetic scattering of plane waves from double wedges," *IEEE Trans. Antennas Propagat.,* vol. 37, no. 9, pp. 1172-1180, Sep. 1989.

[159] M. Schneider and R. Luebbers, "A general, uniform double wedge diffraction coefficient," *IEEE Trans. Antennas Propagat.,* vol. 39, no. 1, pp. 8-14, Jan. 1991.

[160] L.P. Ivrissimtzis and R.J. Marhefka, "Double diffraction at a coplanar skewed edge configuration," *Radio Sci.,* vol. 26, no. 4, pp. 821-830, Aug. 1991.

[161] F. Capolino, M. Albani, S. Maci and R. Tiberio, "Double diffraction at a pair of coplanar skew edges," *IEEE Trans. Antennas Propagat.,* vol. 45, no. 8, pp. 1219-1226, Aug. 1997.

[162] M. Albani, "A uniform double diffraction coefficient for a pair of wedges in arbitrary configuration," *IEEE Trans. Antennas Propagat.,* vol. 53, no. 2, pp. 702-710, Feb. 2005.

[163] R.A. Ross, "Radar cross section of rectangular flat plates as a function of aspect angle," *IEEE Trans. Antennas Propagat.,* vol. 14, no. 3, pp. 329-335, May 1966.

[164] M. Domingo, R.P. Torres, and M.F. Catedra, "Calculation of the RCS from the interaction of edges and facets," *IEEE Trans. Antennas Propagat.,* vol. 42, no. 6, pp. 885-888, June 1994.

[165] H. Ling, R.-C. Chou, S.-W. Lee, "Shooting and bouncing rays: Calculating the RCS of an arbitrarily shaped cavity," *IEEE Trans. Antennas Propagat.,* vol. 37, no. 2, pp. 194-205, Feb. 1989.

[166] D.T. Paris, W.M. Leach, and E.B. Joy, "Basic theory of probe-compensated near-field measurements," *IEEE Trans. Antennas Propagat.,* vol. 26, no. 3, pp. 373-379, May 1978.

[167] J.J.H. Wang, "An examination of the theory and practices of planar near-field measurement," *IEEE Trans. Antennas Propagat.,* vol. 36, no. 6, pp. 746-753, June 1988.

[168] J. Appel-Hansen, "A note on planar near-field scanning techniques," *Technical University of Denmark,* 1979.

[169] E.B. Joy and D.T. Paris, "Spatial sampling and filtering in near-field measurements," *IEEE Trans. Antennas Propagat.,* vol. 20, no. 3, pp. 253-261, June 1972.

[170] A.D. Yaghjian, "An overview of near-field antenna measurements," *IEEE Trans. Antennas Propagat.,* vol. 34, no. 1, pp. 30-45, Jan. 1986.

[171] O.M. Bucci and M.D. Migliore, "A new method for avoiding the truncation error in near-field antennas measurements," *IEEE Trans. Antennas Propagat.,* vol. 54, no. 10, pp. 2940-2952, Oct. 2006.

[172] A.D. Yaghjian, "Upper-bound errors in far-field antenna parameters determined from planar near-field measurements," *National Bureau of Standards,* Technical Note 667, Part 1: Analysis, pp. 1-113, Oct. 1975.

[173] B.E. Fischer, I.J. LaHaie, and G.G. Fliss, "On the use of wavenumber migration for linear SAR image formation and near-field to far-field transformation," *Proceedings of the 23rd Annual Meeting of the Antenna Measurement Techniques Association (AMTA 2001),* Denver, CO, pp. 117-122, 2001.

[174] G.H. Golub, C.F. Van Loan, *Matrix Computations,* 3rd Ed., John Hopkins University Press, Baltimore, MD, 1996.

[175] I.N. Bronstein, K.A. Semendjajew, G. Musiol, H. Mühlig, *Taschenbuch der Mathematik,* Verlag Harri Deutsch, Frankfurt am Main, 1993.

Curriculum Vitae

Andreas Tzoulis

Birthday: 19/7/1976
Birthplace: Munich
Citizenship: Greek

EDUCATION:

2001:	M.Sc. in Electronic Physics (Radioelectrology) - Telecommunications Division, Department of Physics, Aristotle University of Thessaloniki, Greece.
1999:	B.Sc. in Physics, Department of Physics, Aristotle University of Thessaloniki, Greece.
1994:	Graduation (Apolyterium) from 1st Greek Lyceum, Munich, Germany.

PROFESSIONAL EXPERIENCE:

2002 - 2008:	Research assistant in Antennas and Scattering (AuS) Department of the Research Institute of High Frequency Physics and Radar Techniques (FHR) of FGAN e.V. Germany.
2005 - 2007:	Teaching position in "*Laboratory in Computational Electromagnetics*" at University of Applied Sciences Bonn-Rhein-Sieg.
2004 - 2007:	Teaching position in "*Radio Frequency Technology*" at University of Applied Sciences Bonn-Rhein-Sieg.
2001:	Participation in research project titled "*Technical Support to the Greek NTPC (National Telecommunications and Post Commission) on Spectrum Monitoring Issues*".
2001:	Participation in research project titled "*Laboratory Network Certification and Testing of Telecommunications Terminals, Electrical and Electronic Equipment*".

Scientific Publications in Refereed Journals:

1. A. Tzoulis, T. Vaupel, and T.F. Eibert, "Ray Optical Electromagnetic Far-Field Scattering Computations Using Planar Near-Field Scanning Techniques", *IEEE Trans. Antennas Propagat.*, vol. 56, no. 2, pp. 461-468, February 2008.
2. A. Tzoulis, Ismatullah, and T.F. Eibert, "Fast Multipole Accelerated Hybrid Finite Element - Boundary Integral - Ray-Optical Method Including Double Diffractions", *Electromagnetics*, vol. 28, no. 1, pp. 109-122, January 2008.
3. A. Tzoulis and T.F. Eibert, "Advances in Hybrid Finite Element - Boundary Integral - Multilevel Fast Multipole - Uniform Geometrical Theory of Diffraction Method", *Advances in Radio Science* (ISSN: 16849965, EISSN: 16849973), vol. 5, pp. 101-106, 2007.
4. A. Tzoulis and T.F. Eibert, "Fast Computation of Electromagnetic Near-Fields with the Multilevel Fast Multipole Method Combining Near-Field and Far-Field Translations", *Advances in Radio Science* (ISSN: 16849965, EISSN: 16849973), vol. 4, pp. 111-115, 2006.
5. A. Tzoulis and T.F. Eibert, "Combining the Multilevel Fast Multipole Method with the Uniform Geometrical Theory of Diffraction", *Advances in Radio Science* (ISSN: 16849965, EISSN: 16849973), vol. 3, pp. 183-188, 2005.
6. A. Tzoulis and T.F. Eibert, "Efficient Electromagnetic Near-Field Computation by the Multilevel Fast Multipole Method Employing Mixed Near-Field/Far-Field Translations", *IEEE Antennas Wireless Propag. Lett.*, vol. 4, pp. 449-452, 2005.
7. A. Tzoulis and T.F. Eibert, "A Hybrid FEBI-MLFMM-UTD Method for Numerical Solutions of Electromagnetic Problems Including Arbitrarily Shaped and Electrically Large Objects", *IEEE Trans. Antennas Propagat.*, vol. 53, no. 10, pp. 3358-3366, October 2005.
8. A. Tzoulis and T.F. Eibert, "Review of Singular Potential Integrals for Method of Moments Solutions of Surface Integral Equations", *Advances in Radio Science* (ISSN: 16849965, EISSN: 16849973), vol. 2, pp. 93-99, 2004.

Scientific Publications in Refereed Conference Proceedings:

9. T.F. Eibert, C. Schmidt, and A. Tzoulis, "Some Variations of the Multilevel Fast Multipole Method", *International IEEE Mini-Symposium on Electromagnetics and Network Theory and their Microwave Technology Applications*, Munich, Germany, October 2008.
10. A. Tzoulis and T.F. Eibert, "Advances of the Fast Finite Element Boundary Integral Technique Combined with Ray Optical Methods", *9th International Workshop on Finite Elements for Microwave Engineering*, Bonn, Germany, May 2008.
11. F. Weinmann and A. Tzoulis, "Numerical Modeling Results of Radar Signatures for Large and Complex Targets", *IEEE Radar Conference*, Rome, May 2008.
12. A. Tzoulis, T. Vaupel, and T.F. Eibert, "Far-Field Scattering with Fast Hybrid Integral Equation Based - Ray Optical Method", *2nd European Conference on Antennas and Propagation*, Edinburgh, November 2007.
13. T.F. Eibert, H. Buddendick, M.M. Leibfritz, C.S. Schmidt, A. Tzoulis, "Hybrid Electromagnetic Field Characterization Involving High-Frequency Field Representations", *URSI International Symposium on Electromagnetic Theory*, Invited, Ottawa, July 2007.
14. A. Tzoulis, T. Vaupel, and T.F. Eibert, "Computation of Scattered Far-Fields in Fast Hybrid Finite Element - Boundary Integral - Ray Optical Method", *URSI International Symposium on Electromagnetic Theory*, Ottawa, July 2007.

15. A. Tzoulis and T.F. Eibert, "Antenna Modeling with the Hybrid Finite Element - Boundary Integral - Multilevel Fast Multipole - Uniform Geometrical Theory of Diffraction Method", *2nd International ITG Conference on Antennas*, Munich, March 2007.
16. A. Tzoulis and T.F. Eibert, "Computations for Various Edge Configurations with the Hybrid Finite Element - Boundary Integral - Multilevel Fast Multipole - Uniform Geometrical Theory of Diffraction Method Including Double Diffraction", *1st European Conference on Antennas and Propagation*, Nice, November 2006.
17. A. Tzoulis and T.F. Eibert, "Advances in Hybrid Finite Element - Boundary Integral - Multilevel Fast Multipole - Uniform Geometrical Theory of Diffraction Method", *Kleinheubacher Tagung*, September 2006.
18. T.F. Eibert and A. Tzoulis, "Some Large-Scale Scattering and Near-Field Results Computed by the Hybrid Finite Element - Boundary Integral - Multilevel Fast Multipole Method", *IEEE International Antennas and Propagation Symposium*, Albuquerque, July 2006.
19. T.F. Eibert, A. Tzoulis, and T. Vaupel, "Radar Cross Section Modeling Results Obtained by the Hybrid Finite Element - Boundary Integral Technique", *1st Antenna Measurement Techniques Association Europe Symposium*, pp. 147-152, Munich, May 2006.
20. T.F. Eibert and A. Tzoulis, "On the Formulation of the 3D Hybrid Finite Element - Boundary Integral Technique: ... Still the Old One: Formulation, Solution, Results", *8th International Workshop on Finite Elements for Microwave Engineering*, Stellenbosch, South Africa, May 2006.
21. T.F. Eibert and A. Tzoulis, "The Hybrid Finite Element - Boundary Integral - Multilevel Fast Multipole - Uniform Geometrical Theory of Diffraction Method", *XXIX General Assembly of the URSI*, Invited, New Delhi, October 2005.
22. A. Tzoulis and T.F. Eibert, "Fast Computation of Electromagnetic Near-Fields with the Multilevel Fast Multipole Method Combining Near-Field and Far-Field Translations", *Kleinheubacher Tagung*, September 2005.
23. A. Tzoulis and T.F. Eibert, "Hybridization of Multilevel Fast Multipole Method and Uniform Geometrical Theory of Diffraction for Radiation and Scattering Computations", *IEEE International Antennas and Propagation Symposium*, Washington, D.C., July 2005.
24. A. Tzoulis and T.F. Eibert, "Combining the Multilevel Fast Multipole Method with the Uniform Geometrical Theory of Diffraction", *Kleinheubacher Tagung*, September 2004.
25. A. Tzoulis and T.F. Eibert, "Review of Singular Potential Integrals for Method of Moments Solutions of Surface Integral Equations", *Kleinheubacher Tagung*, September 2003.